

**UNIVERSIDADE DE LISBOA**  
**FACULDADE DE MEDICINA DE LISBOA**



**BEYOND RAYLEIGH'S LIMIT:  
ACHIEVING REAL-TIME SUPER-RESOLUTION  
FLUORESCENCE MICROSCOPY**

**RICARDO HENRIQUES**

**DOUTORAMENTO EM CIÊNCIAS BIOMÉDICAS,  
ESPECIALIDADE DE CIÊNCIAS MORFOLÓGICAS**

**2011**



**UNIVERSIDADE DE LISBOA**  
**FACULDADE DE MEDICINA DE LISBOA**



**BEYOND RAYLEIGH'S LIMIT:**  
**ACHIEVING REAL-TIME SUPER-RESOLUTION**  
**FLUORESCENCE MICROSCOPY**

**RICARDO HENRIQUES**

**DOUTORAMENTO EM CIÊNCIAS BIOMÉDICAS,**  
**ESPECIALIDADE DE CIÊNCIAS MORFOLÓGICAS**  
**2011**

**THESIS SUPERVISED BY:**

**DR. MUSA MHLANGA (INSTITUTO DE MEDICINA MOLECULAR, PORTUGAL)**

**DR. ANTÓNIO JACINTO (INSTITUTO DE MEDICINA MOLECULAR, PORTUGAL)**

**A impressão desta dissertação foi aprovada pelo Conselho Científico da Faculdade de Medicina de Lisboa em reunião de 21 de Junho de 2011.**

Todas as afirmações efectuadas no presente documento são da exclusiva responsabilidade do seu autor, não cabendo qualquer responsabilidade à Faculdade de Medicina de Lisboa pelos conteúdos nele apresentados.

*O desenvolvimento e execução gráfica da presente dissertação foram financiados pela Fundação para a Ciência e a Tecnologia (Bolsa SFRH/BD/63680/2009)*



## Resumo

**Palavras-chave:** nanoscopia, super-resolução, *PALM*, *STORM*, *photo-switchable probes*, *molecular-bleacons*, *blinkons*

O presente trabalho teve por objectivo o desenvolvimento de novas ferramentas e aplicações em microscopia de super-resolução por fluorescência, desbloqueando informações estruturais de alta resolução em moléculas como DNA, RNA e proteínas. Estas moléculas, parte do dogma central da biologia, existem como objectos individuais em escalas de poucos nanómetros, para além do poder de resolução da microscopia de fluorescência clássica. Neste contexto, explorámos neste trabalho técnicas de *single-molecule localization microscopy* (SMLM), que mantêm até hoje o recorde em poder de resolução para microscopia óptica. Estas técnicas, têm a capacidade de experimentalmente identificar e localizar moléculas individuais na escala de sub-nanómetros. Nesta família de métodos, *photo-activated localization microscopy* (PALM), *stochastic optical reconstruction microscopy* (STORM) e suas variantes, têm o potencial para resolver estruturas celulares completas com uma precisão nanométrica através da localização de milhares de milhões de fluoróforos individuais no interior de células marcadas. A implementação e utilização destes novos métodos representam um enorme desafio já que estes ainda se encontram no seu “estádio embrionário”. O meu doutoramento teve como objectivo melhorar estes novos métodos em três áreas diferentes. A primeira área sendo a configuração de hardware, nomeadamente através do desenvolvimento de um método que permite converter um microscópio *wide-field* de fluorescência ou de *total internal reflection fluorescence* (TIRF) em um sistema de super-resolução capaz de alcançar nanoscopia 3D. A segunda área focou-se em melhorar os métodos de aquisição e análise de imagem em super-resolução, através do desenvolvimento de “QuickPALM” e ferramentas como o “controle do laser para QuickPALM”. Estes quando integrados com outras bibliotecas de software *open-source*, como o ImageJ ou µManager, constituem um conjunto completo de ferramentas de *software* necessário para controlar o microscópio de super-resolução e analisar em tempo real os dados adquiridos. A terceira área relacionada com o desenvolvimento de novas sondas *photo-switchable* para super-resolução, baseou-se na exploração de interacções

transitórias de fluoróforos "clássicos" com supressores de fluorescência de alta eficiência. Estes desenvolvimentos têm sido aplicados para o estudo de processos biológicos ao nível nanométrico ao longo do meu doutoramento. A secção de resultados da presente tese demonstra uma das implementações mais proeminente, em que temos estudado a interacção espacial de proteínas chave na via de sinalização NF- $\kappa$ B activada após estimulação de receptores como TNF- $\alpha$  e IL-1. No global, o trabalho que desenvolvi durante o meu doutoramento constitui uma contribuição científica original e extremamente relevante para o avanço da microscopia de localização molecular. Pouco tempo após a publicação e disponibilização do QuickPALM à comunidade científica, este tornou-se uma das ferramentas mais utilizadas na detecção de partículas e de reconstrução de imagens para a classe de técnicas de SMLM. Adicionalmente, os meus resultados fornecem uma visão nova no estudo de estruturas celulares a nível molecular e das interacções entre os participantes-chave na biologia molecular.

## Summary

**Keywords:** nanoscopy, super-resolution, PALM, STORM, photo-switchable probes, molecular-beacons, blinkons

This work reports the development of new tools and applications for the visualization of biological macromolecules in the cellular context using super-resolution fluorescence microscopy. DNA, RNA and protein molecules, the central dogma molecules of biology, typically exist at dimensions of a few nanometers, well beyond the resolving power of classical fluorescent microscopy. In this context we have explored single-molecule localization microscopy (SMLM) techniques that to date, hold the record in resolving power for optical microscopy. These have both the capacity to identify and localize individual molecules at scales experimentally demonstrated to be at sub-nanometre level. In this family of methods, photo-activated localization microscopy (PALM) and stochastic optical reconstruction microscopy (STORM) as well as their variants, hold the potential to fully resolve complete cellular structures at the nanoscale by precisely localizing thousands to millions of individual fluorophores within a labelled cell. Confronting these novel methods was highly challenging due to their near embryonic state. My Ph.D. aimed to improve these novel methods in three different areas. First, the hardware configuration, by creating a simple setup method that converts a standard wide-field fluorescence or total-internal reflection fluorescence (TIRF) microscope into a super-resolution system able to achieve 3 dimensional nanoscopy. Second, the super-resolution image acquisition and analysis, by developing “QuickPALM” and tools such as the “Laser control for QuickPALM”, which integrated with other open-source libraries such as ImageJ or  $\mu$ Manager provide a complete set of software tools to achieve super-resolution hardware control and real-time analysis of the acquired data. Third, the discovery of new photo-switchable probes for super-resolution, achieved by the exploitation of the transient interaction of “classical” fluorophores with high-efficiency quenchers. These developments have been applied on to the study of biological processes at the nanometer level throughout my Ph.D. Specifically; the results section of the present thesis demonstrates one of the most prominent implementations, where we have studied the spatial interaction of key proteins of the

NF- $\kappa$ B pathway upon receptor stimulation by TNF- $\alpha$  or IL-1. Altogether, the work I developed during my Ph.D. has provided important and original scientific contributions for the advancement of single molecule localization microscopy. Shortly after QuickPALM was published and made available to the scientific community it became one of the most widely used analytical tools at the core of particle detection and reconstruction for this class of SMLM techniques. Moreover, my results provide a novel view into cellular structure at the molecular level and provide a novel framework to study the interplay of key molecular participants in biology.

## Acknowledgments

Though the following dissertation is an individual work, I could never have reached the end without the help, support, guidance and efforts of several people to whom I want to express my gratitude:

Dr. Musa M Mhlanga for welcoming me as a friend and giving me the opportunity to work in a new promising field. For providing me with excellent working conditions, for the grateful discussions and encouragement throughout the work presented in this dissertation.

Dr. Christophe Zimmer, for hosting me in his lab for the major part of my Ph.D., for being an “unofficial” supervisor and for welcoming me always as a member of his team.

Dr. António Jacinto for both accepting to be my internal supervisor in Faculdade de Medicina Universidade de Lisboa and for being my mentor. It has been a pleasure to share and discuss my work with you.

Dr. Gabriel Martins, member of my thesis committee. Not only for the exciting discussions about my work but also for providing the opportunity to present it to the research community.

Dr. Jost Enninga, for not only being a good friend but also for allowing me to use his “wet-lab” making this Ph.D. possible.

Dr. Fabrice Agou and Dr. Michel Veron, for the exciting collaboration in the NF- $\kappa$ B project and for providing me a position in their unit when otherwise I would not be allowed to stay at Institut Pasteur.

Dr. Jean-Christophe Olivo-Marin and his team, for receiving me at his laboratory when I first came to Paris.

My colleagues in the several Institutes I worked on, Instituto de Medicina Molecular (Lisbon, Portugal), Institut Pasteur (Paris, France) and Council for Scientific and Industrial Research (Pretoria, South Africa). A special thanks to Dr. Mickael Lelek, the optical “geek” without whom I would not have been able to perform my experiments.

Dr. Lionel and Sandrine Gresh for their friendliness and welcoming me in their home during my research in South.

The “Portuguese mafia” at Pasteur in Paris, for adopting me as a member of their family. Notably Miguel Lopes, the most giving and altruistic person I know.

My family for their support. And Cristina, for holding my heart and making me smile even through the hardships of research.

Last but not least, Dr. Nuno Moreno, for pulling me from nuclear physics and giving me the chance to apply my physicist view into the biology world. Both Nuno’s and Gabriel’s passion for microscopy seeded my own. This thesis is dedicated to them.

## **Preface**

The present thesis embraces the data obtained during my Ph.D. research project developed from March 2008 to May 2011.

My Ph.D. was supervised by Dr. Musa Mhlanga and Dr. António Jacinto from Instituto de Medicina Molecular (Lisbon, Portugal). The research work was carried out in Instituto de Medicina Molecular (IMM, Lisboa, Portugal), Institut Pasteur (IP, Paris, France) and Council for Scientific and Industrial Research (CSIR, Pretoria, South Africa). Several other researchers have contributed significantly as supervisors at different phases of my Ph.D., namely: Dr. Jean-Christophe Olivo-Marin (in 2008, Institut Pasteur, Paris, France), Dr. Christophe Zimmer (from 2009 to 2011, Institut Pasteur, Paris, France), Dr. Fabrice Agou and Dr. Michel Veron (2010 to 2011, Institut Pasteur, Paris, France).

My Ph.D. was financially supported from 2008 to 2009 by the European Commission Molecular Imaging program and Fundação para a Ciência e a Tecnologia (ISR/IST plurianual funding). From 2010 onwards by Fundação para a Ciência e Tecnologia, through the Ph.D. fellowship grant SFRH/BD/63680/2009. The Council for Scientific and Industrial Research (Pretoria, South Africa) sponsored research and travel costs in South Africa.

The present thesis is structured in 3 main chapters:

- Chapter 1 (Objectives) – a discussion of the aims of the presented work.
- Chapter 2 (General Introduction) - provides an overall introduction to the work developed. Introduces the concept of super-resolution and explores how it provides a new molecular scale view into the spatial-dynamics of biological systems. It also addresses one of the key dogmas of super-resolution - live-cell imaging - and the necessary steps to overtake this challenge.

This chapter includes text from my published reviews:

- Ricardo Henriques and Musa M. Mhlanga (2009). PALM and STORM: what hides beyond the Rayleigh limit?. Biotechnol. J. vol. 4(6): 846- 57.
- Ricardo Henriques\*, Caron Griffiths\*, E. Hesper Rego and Musa M. Mhlanga (2011). PALM and STORM: unlocking live-cell super-resolution. Biopolymers vol. 95(5): 322-331.
- Chapter 2 (Methods and Results) – Presents my original research in the field of super-resolution. Here you can find as:
  - (2.1) the description of QuickPALM, a software package that when used in conjunction with other open-source libraries as ImageJ and µManager allows real-time processing for super-resolution imaging;
  - (2.2) the development of “blinkons”, a *novel* class of probes able to induce photo-switchable behaviour in “classic” organic dyes by exploring the transient interaction of fluorophores with high-efficiency quenchers and;
  - (2.3) a super-resolution view into the spatial interaction and structural role of the key proteins NEMO, poly-ubiquitin and K63-chains on receptor stimulation upon TNF- $\alpha$  or IL-1 modulation of the NF- $\kappa$ B pathway.

Included in this chapter is my published article:

- Ricardo Henriques, Mickael Lelek, Eugenio F. Fornasiero, Flavia Valtorta, Christophe Zimmer & Musa M. Mhlanga (2010). QuickPALM: 3D real-time photoactivation nanoscopy image processing in ImageJ. Nature Methods 7: 339–340.



- Chapter 3 (General Discussion and Perspectives) – Overviews the significance of the completed work within the field of the biological sciences and opens up a new vista into the future directions in the discipline.

During my Ph.D I have collaborated with several research groups from the Instituto de Medicina Molecular (Lisboa) and Institut Pasteur (Paris). This experience has allowed me to extend my knowledge in both fields of biology and optical microscopy. Although, these results are not included in the present thesis, I would like to mention some of the resultant publications or manuscripts in preparation:

- J.Y. Tinevez, N. Perry, J. Schindelin, R. Henriques, S. Spencer (2011). TrackMate: from single-molecule to full cell tracking made easy. Cytometry Part A, *in preparation*.
- H. Soares, R. Henriques, O. Alarcon, F. Porrot, O. Schwartz, M. Alarcon, M.I. Thoulouze, A. Alcover (2011). HIV unveils calcium and synaptotagmin-7 regulated exocytosis of signaling molecules required for immunological synapse signal amplification, Nature Immunology, *submitted*.
- M. Lelek\*, F.D. Nunzio\*, R. Henriques, P. Charneau, N. Arhel, and C. Zimmer (2011). Super-resolution imaging of HIV in infected cells with FLAsH-PALM. PNAS, *submitted*.
- C. Griffiths\*, R. Henriques\*, M.M. Mhlanga (2011). PALM and STORM: a super-resolution molecular view into living cells. Biotechnology International, Biotechnology International, vol. 23 (1) pp. 8-10.
- C.S.S. Gomes-Santos, M.A. Itoe, C. Afonso, R. Henriques, R. Gardner, N. Sepúlveda, P.D. Simões, H. Raquel, P. Almeida, L.F. Moita, F. Frischknecht and M.M. Mota (2011). Highly dynamic host actin reorganization events around developing plasmodium inside hepatocytes. FASEB Journal, *submitted*.
- J. Caetano-Lopes, A.M. Nery, R. Henriques, H. Canhão, J. Duarte, P.M. Amaral, M. Vale, R.A. Moura, P.A. Pereira, P. Weinmann, S. Abdulghani, M. Souto-Carneiro, P. Rego, J. Monteiro, S. Sakagushi S, M.V. Queiroz, Y.T. Konttinen, L. Graça, M.F. Vaz, J.E. Fonseca (2009). Chronic arthritis directly induces quantitative and qualitative bone disturbances leading to compromised biomechanical properties. Clinical and experimental rheumatology 2009; 27(3): 475-82.
- L.B. Barreiro; R. Henriques; M.M. Mhlanga (2009). High-throughput SNP genotyping: combining tag SNPs and molecular beacons. Methods in molecular biology (Clifton, N.J.) 2009; 578: 255-76.

- J. Rino, J. Braga, R. Henriques, M. Carmo-Fonseca (2009). Frontiers in fluorescence microscopy. The International journal of developmental biology 2009; 53(8-10): 1569-79.



# Table of Contents

<b>Resumo.....</b>	<b>i</b>
<b>Summary.....</b>	<b>iii</b>
<b>Acknowledgments .....</b>	<b>v</b>
<b>Preface.....</b>	<b>vii</b>
<b>Table of Contents .....</b>	<b>xiv</b>
<b>List of Abbreviations .....</b>	<b>xvi</b>
<b>1 Objectives.....</b>	<b>1</b>
<b>2 General Introduction .....</b>	<b>5</b>
<b>2.1 The optical microscopy diffraction limit.....</b>	<b>6</b>
<b>2.2 From micro-to-nano.....</b>	<b>6</b>
<b>2.3 Super-resolution by photo-switching of single-molecules .....</b>	<b>10</b>
2.3.1 Detection & Microscope Optics.....	10
2.3.2 Fluorescent Proteins & Dyes .....	12
2.3.3 Single-molecule analysis and reconstruction.....	24
<b>2.4 Stepping into 3D super-resolution.....</b>	<b>25</b>
<b>2.5 Imaging of molecular structures.....</b>	<b>26</b>
<b>2.6 Breaking through the technological limits.....</b>	<b>27</b>
<b>3 Methods and Results.....</b>	<b>29</b>
<b>3.1 QuickPALM: 3D real-time photo-activation nanoscopy image processing in ImageJ.....</b>	<b>29</b>
3.1.1 Introduction.....	30
3.1.2 Material and Methods .....	31
3.1.3 Results and discussion .....	39
3.1.4 Conclusions and outlook.....	42
<b>3.2 Blinkons: multi-colour tuneable photo-switchable fluorophores for super-resolution microscopy .....</b>	<b>45</b>
3.2.1 Introduction.....	45
3.2.2 Material and Methods .....	52
3.2.3 Results and discussion .....	64

3.2.4	Conclusions and Outlook.....	75
<b>3.3</b>	<b>A sub-cellular super-resolution view on NEMO and NF-<math>\kappa</math>B activation..</b>	<b>77</b>
3.3.1	Introduction.....	77
3.3.2	Material and Methods .....	84
3.3.3	Results and discussion .....	87
3.3.4	Conclusions and outlook.....	100
<b>4</b>	<b>General Discussion and Perspectives .....</b>	<b>101</b>
<b>5</b>	<b>Appendix.....</b>	<b>108</b>
<b>5.1</b>	<b>The Ph.D. research time-line and additional results .....</b>	<b>108</b>
5.1.1	Microscopy challenges.....	109
5.1.2	The rise and fall of ThunderSTORM.....	110
5.1.3	From ThunderSTORM to QuickPALM.....	115
5.1.4	Blinking molecular-beacons .....	118
5.1.5	Super-resolving neuron vesicles .....	119
5.1.6	Looking at NEMO with super-resolution glasses.....	123
5.1.7	One PhD, two continents, five different groups .....	123
<b>5.2</b>	<b>PALM and STORM: What hides beyond the Rayleigh limit? .....</b>	<b>125</b>
<b>5.3</b>	<b>PALM and STORM: Unlocking Live-Cell Super-Resolution .....</b>	<b>138</b>
<b>5.4</b>	<b>QuickPALM: 3D real-time photoactivation nanoscopy image processing in ImageJ.....</b>	<b>149</b>
<b>5.5</b>	<b>Curriculum Vitae .....</b>	<b>164</b>
<b>6</b>	<b>References.....</b>	<b>170</b>

## List of Abbreviations

BP	biplane
CYLD	cylindromatosis (turban tumor syndrome)
DHFR	dihydrofolate reductase
dSTORM	direct STORM
EM	electron microscopy
EM-CCD	electron-multiplying charge-coupled device
FISH	fluorescent in situ hybridization
FPALM	fluorescence photo-activated localization microscopy
FRET	fluorescent resonance energy transfer
FWHM	full-width-half-maximum
HA	hemagglutinin
HILO	highly inclined and laminated optical sheet
IL1	interleukin 1
LAP	lipioic acid ligase
MB	molecular-beacon
MSD	mean-square displacement
NEMO	NF- $\kappa$ B essential modulator
NF- $\kappa$ B	nuclear factor kappa-light-chain-enhancer of activated B cells
NSOM	near-field scanning optical microscopy
PALM	photo-activated localization microscopy
PALMIRA	PALM with independently running acquisition
PBS	phosphate buffered saline
PFA	paraformaldehyde
PSF	point-spread function
PVA	poly-(vinyl-alcohol)
RESOLFT	reversible saturable optical fluorescence transitions
ROS	reactive oxygen species
SIM	structured illumination microscopy
SMI	spatially modulated illumination
SMLM	single-molecule localization microscopy
SNR	signal-to-noise ratio
SPDM	spectral precision distance microscopy
SPT	single-particle tracking
sptPALM	single-particle tracking PALM
SSIM	saturated structured illumination microscopy
STED	stimulated emission depletion
STORM	stochastic optical reconstruction microscopy
TEM	transmission electron microscopy
TIRF	total internal reflection fluorescence
TMP	trimethoprim
TNF	tumor necrosis factor

VSVG	vesicular stomatitis virus G
WmH	width-minus-height



# 1 Objectives

The work presented aims to develop new methods and demonstrate new applications within the single-molecule localization microscopy (SMLM) field by both tackling some of its current limitations and demonstrating results that otherwise could not be achieved without this suite of *novel* methods.

The first challenge tackled was the need for a high-performance method to analyse the data generated by super-resolution photo-activated localization microscopy (PALM) or stochastic optical reconstruction microscopy (STORM) experiments. Typically, these methods can generate up to hundreds of thousands of images within few minutes of acquisition. These need to be processed in order to generate a final super-resolution dataset composed of all the detected individual fluorophores within each acquired image. The entire analysis procedure could typically take a far greater period of time than the acquisition itself. This obliged users of these techniques to only visualize the complete acquired data hours to days after the acquisition itself.

By developing and publishing QuickPALM (see section 3.1) I have aimed to provide the scientific community with new method for both the analysis of PALM, STORM or SMLM type datasets. The algorithm within QuickPALM excels in processing speed, being able to examine the generated multi-dimensional data in few minutes or in parallel to the acquisition procedure itself. QuickPALM today has become one of the standards in PALM and STORM data analysis and has a user-base of over 600 known users.

The development and applications of QuickPALM are discussed in depth in the results section 3.1.

Another aim concerns the development of *novel* super-resolution fluorescent probes. The PALM and STORM methods require the stochastic activation of photo-switchable fluorophores, a class of fluorophores able to transition between light-emitting and non-emitting states (note, photo-switching properties can be partially induced in conventional fluorophores by special embedding mediums). This photo-

switching procedure is at the core of these techniques and without it single-molecule localization in densely labelled samples cannot be achieved.

However, there remains a dearth of multi-color photo-switchable fluorophores with optimal characteristics for these techniques. Through the exploitation of the properties of molecular-beacons, I have been able to develop a new type of photo-switching probes that I termed “blinkons”.

Blinkons are based on an oligo-nucleotide hairpin conformation similar to molecular-beacons, i.e., a fluorophore and a high-efficiency compatible (fluorescence) quencher are set at opposite ends (5'- and 3'- ends) of their sequence. By default, the close proximity between both the quencher and fluorophore will disallow any fluorescence emission. The special property presented by blinkons is their capacity to transiently and reversibly change the hairpin structure and as such, temporarily switch into a light-emitting state. This behaviour induces photo-switching in these probes.

Through application of the blinkon structure to most multi-color fluorophores with known efficient quenchers it is possible to create *novel* fluorescent photo-switching molecules. Moreover, the addition of a biotinylated nucleotide to the blinkon oligo-nucleotide structure allows it to bind to proteins or cellular structures fused with streptavidin.

The description and characterization of the blinkon probes can be found in section 3.2 of the results chapter. Here, we take advantage of QuickPALM to undergo a single-molecule characterization of the blinkons. QuickPALM it is also used to validate the blinkon probes as fluorescent markers conjugated to antibodies by super-resolving bundled microtubules in neuron cells.

The final aim of this thesis was to super-resolve the sub-cellular territories of NEMO (NF- $\kappa$ B Essential **MO**dulator) and its associated binding of poly-ubiquitin chains through the use of dSTORM technique and QuickPALM.

NEMO is a key regulatory protein in the NF- $\kappa$ B pathway. NF- $\kappa$ B represents a family of transcription factors with a key role in immune, inflammatory and anti-apoptotic responses. It stimulates immune cell function and acts in a pro-inflammatory manner by inducing the expression of cytokines, chemokines and their receptors. Furthermore, NF- $\kappa$ B is capable of inhibiting programmed cell death through transcription stimulation of anti-apoptotic genes and as such, can be also a main driver in cancer growth and survival.

Here we show for the first time through super-resolution microscopy that NEMO forms a sub-diffraction nanoscale scaffold structure near the cell membrane. My data suggests that this structure can be modulated by poly-ubiquitin binding to NEMO. Also, both the NF- $\kappa$ B activation through TNF- $\alpha$  or IL-1 stimulation demonstrates a re-arrangement on the NEMO formed scaffold in the vicinity of the corresponding receptors.

An advanced analysis of the NEMO sub-cellular territories can be found on section 3.3 of the results chapter.



## **2 General Introduction**

Modern cell biology depends extensively on fluorescence light microscopy to provide key insights into cellular structure and molecular behaviour. Inherent advantages, such as its non-invasive nature and the ability to use highly specific labelling tools, have made fluorescence light microscopy the preferred strategy for imaging fixed and living cells. The maximum optical resolution of this method is typically restricted to 200-nm laterally and 500-nm axially. This limitation constrains its ability to provide high-resolution structural information on molecules that are central to the dogma of biology, namely DNA, RNA and protein, which exist as single-molecules at scales of few nanometres. The physics-based resolution limit of light microscopes imposed by their optical architecture and the wave nature of light was mathematically described in the 19<sup>th</sup> century by Ernst Abbe (1).

Electron microscopy (EM) has been able to surpass the resolution limit of optical microscopy and for several years was the routine approach to resolve cellular architecture at the ultra-structural or atomic level. However, EM lacks the basic advantages of fluorescence microscopy such as highly specific multi-colour labelling, and live-cell imaging, both of which remain altogether impossible with EM.

In response to this dilemma, recent developments in microscopy have aimed to create techniques able to retain the advantages of fluorescence microscopy while approaching the resolving power of EM. Indeed recent advances in single-molecule localization microscopy (SMLM) have shown resolution below the nanometre (2). Variants such as photo-activated localization microscopy (PALM) (3), fluorescence PALM (FPALM) (4), stochastic optical reconstruction microscopy (STORM) (5), direct STORM (dSTORM) (6) and PALM with independent running acquisition (PALMIRA) (7-9) have emerged at the forefront of the new “super-resolution” methods retaining the labelling advantages of fluorescence imaging.

## **2.1 The optical microscopy diffraction limit**

When observing a single fluorophore on a microscope, the emitted light will be forced to cross several different physical mediums until it reaches the detector. As a result, light scatters throughout the different environments leading to an artificial spatial broadening of the discrete point. In the 19<sup>th</sup> century E. Abbe described analytically this hard limit on optical microscopy by which any point source of light smaller than the diffraction limit of the imaging system would have a fixed observable size (*l*). The observable spatial profile of such spots defines the point-spread function (PSF) of the microscope, also known by the airy diffraction pattern.

Any two fluorescent molecules whose overlapping PSFs are separated by a distance smaller than the PSF width become difficult or impossible to resolve as separate objects. This distance known as the Rayleigh Criterion is given approximately by  $\lambda/(2NA)$  laterally (x-y) and  $2\lambda\eta/(2NA)^2$  axially (z), where  $\lambda$  is the wavelength of the emitted light,  $\eta$  is the index of refraction of the medium and *NA* the numerical aperture of the objective lens(10). In a conventional fluorescence microscope using visible light ( $\lambda$  between 450 and 700nm) and a high numerical aperture objective (*NA*  $\approx$  1.4) the resolution limit given by the Rayleigh Criterion is approximately ~200nm in the focal plane (x,y) and 500-800nm along the optic axis (z).

## **2.2 From micro-to-nano**

For several years electron microscopy (EM) has been the predominant technique for high-resolution nanoscopy of biological samples (11) having an outsized impact on our understanding of ultra-structural biology at scales of just a few nanometres. Nevertheless several limitations arise from the use of this technique such as low labelling efficiency and laborious sample preparation methods that are currently incompatible with live-cell imaging. As a result the vast majority of microscopy research in the life sciences is still carried out with optical light microscopy (12).

By default, fluorescence microscopes are able to detect and position single-molecules with a high accuracy if they present distinct spectral emissions or if their associated PSFs do not spatially overlap extensively (13, 14). The problem arises when

neighbouring markers are excited simultaneously stimulating a coincident emission making the separation of their overlapping PSFs virtually impossible (Figure 2.1).

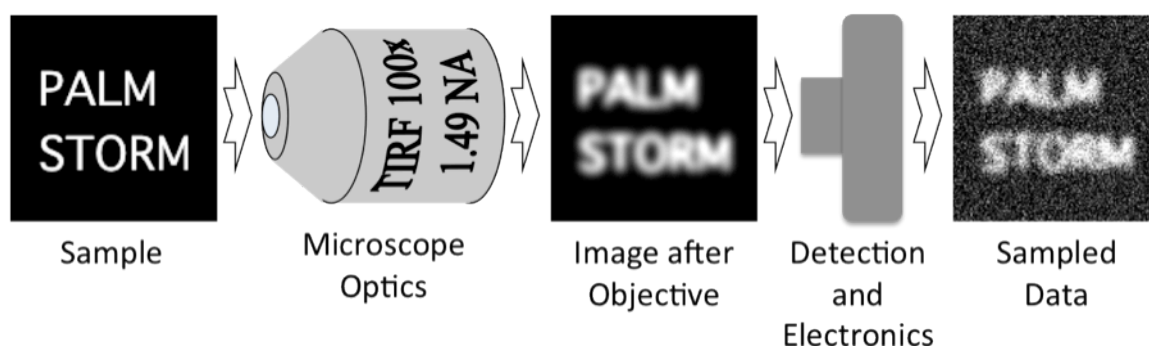


Figure 2.1. Scheme of the distortion created by a fluorescence microscope. Using the words PALM and STORM as an example, as light travels from the emitting molecules through the optics of the imaging system diffraction occurs and the spatial information of the fluorophores becomes blurred. When a light detector acquires this information, noise is introduced into the resulting produced image.

One of the earliest techniques that attempted to tackle this problem was near-field scanning optical microscopy (NSOM) where the detection of non-propagating light waves emanating from a very restricted number of molecules was achieved through scanning with a nanosized tip (15). However this technique is restricted to the imaging of the sample surface and not able to give information about the interior and contents of cells.

Far-field fluorescence nanoscopy arose by cleverly making use of Abbe's formulas; one such way was to reduce the PSF size, for example by increasing the angular aperture of the imaging optics. This concepts have been around since the late seventies, such as in the case of the first 4Pi illumination ideas from the brothers Cremer and Cremer in Heidelberg (16) leading to the development of the 4Pi confocal microscope (17-19) or the wide-field approach I<sup>5</sup>M (20), both the techniques take advantage of opposing objective lenses leading to up to a seven-fold increase in the z-axis resolution. However, using two objectives creates a wave-front that is still non-spherical giving rise to the appearance of unwanted side-lobes on the focal spot that need to be reduced mathematically in post-processing steps (21). Another approach has been achieved by Structured Illumination Microscopy (SIM) (22-25) where a wide-field periodically patterned illumination allows for the expansion of the

frequency space detectable by the microscope, reducing the size of the PSF and allowing a resolution increase of up to a factor of two. The combination of this method with I<sup>5</sup>M allows for a 3D image resolution of around 100 nm (26). By implementing saturated intensities - Saturated Structured Illumination Microscopy (SSIM) is able to use arbitrarily high spatial frequencies to generate an excitation pattern (27). This enables SSIM to achieve an experimentally measured 50 nm in lateral resolution (28). Stimulated Emission Depletion (STED) fluorescence microscopy makes use of two lasers, while a focused excitation laser beam pushes fluorophores to their excited state, a second laser with a doughnut-shaped intensity profile prompts a stimulated emission of the excited fluorophores surrounding the excitation spot impelling them to the ground state (18, 29). This feature confines the fluorescence emission to the non-stimulated region inside the doughnut reducing the size of the PSF and thus achieving a remarkable measured resolutions as high as 20 nm laterally and 30-40nm axially, 40-45 nm can be achieved in any of the three dimensions if STED is combined with a 4Pi setup (30, 31). Recently STED has been shown to be able to produce video-rate images of synaptic vesicles with a resolution of 60 nm in live neuronal cells (32). Thus Abbe's basic insight remains true and is only overcome by "PSF engineering."

A concept observed since the 1980s in biology comes out of the fact that although the size of observed particles is limited by the resolution of the microscope, if a sufficient number of photons is detected, the centre of the particle can be determined precisely (33, 34), unlimited resolution could even be achieved if this number tends to infinity (35). Notwithstanding, two main constraining factors in achieving accurate particle localization exist: Firstly, neighbouring particle PSFs cannot overlap and secondly, the localization accuracy depends heavily on the signal-to-noise ratio of the sampled image. Despite these limitation it has still been possible to conduct far-field microscopy single-particle tracking studies with an astonishing precision as high as 1 nm, as is the case of the work of *Gelles et al.* in the movement of kinesin-coated beads (36) or *Yildiz et al.* on the movement of Myosin V over actin filaments (37). However, in most instances, biological-imaging experiments will encounter the visualization of densely labelled samples. In such cases the overlapping PSFs due to the emission of the densely packed fluorophores prevent their accurate localization (see Figure 2.2).



Researchers have been able to cleverly find methods to circumvent these constraints. In 1995, *E. Betzig* suggested that one might identify individual molecules with differing spectra whose separation is smaller than the PSF width (38), several groups have latter shown the application of these ideas in single-molecule spectral selection sub-diffraction imaging (39). Other ingenious approaches have also been developed such as single-molecule localization through sequential photo-bleaching (40, 41) or through the analysis of the stochastic blinking of quantum dots (42).

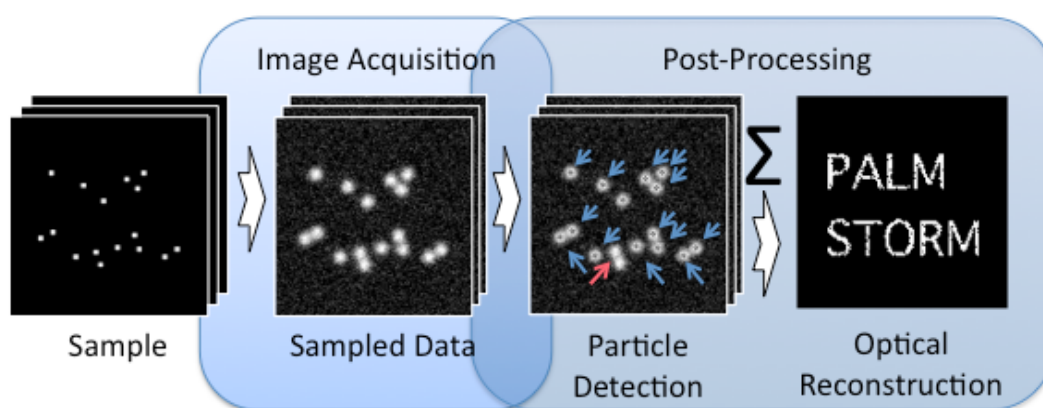


Figure 2.2. PALM and STORM imaging scheme. Several images are acquired where very few emitting molecules are observed in each. Although ultimately images becomes blurred and noisy during acquisition, the low probability of overlapping fluorophores (and PSFs) allows for the detection and localization of the majority of emitting particles inside each image. As this information is integrated in time, the localization of all detected molecules can be matched and a final super-resolution dataset or image is generated.

One of the solutions to these problems that has become popular in the research community emerges through the sequential and stochastic switching ON and OFF of fluorophores therefore minimizing the probability that at any given time two or more fluorophore light emissions (and thus PSFs) spatially overlap. In each imaging cycle most molecules remain dark but a small number are randomly switched on, imaged and localized. This process can then be repeated for numerous iterations until the majority of molecules have been accurately detected and positioned (see Figure 2.2). A consequence of using this method is that thousands of images may need to be acquired to generate one super-resolution dataset. This feature has become the

backbone of techniques such as photo-activation localization microscopy (PALM) (43), fluorescence photo-activation localization microscopy (FPALM) (44), stochastic optical reconstruction microscopy (STORM) (5) and PALM with independently running acquisition (PALMIRA) (7-9).

## **2.3 Super-resolution by photo-switching of single-molecules**

Three key components are required to achieve super-resolution with stochastic photo-switching. They are firstly the microscope optics and the detector that must be able to detect very few photons. Secondly, the fluorescent dyes and proteins that enable photo-switching permitting stochastic activation. Thirdly and perhaps not fully appreciated, analysis of thousands of images and their reconstruction into a super-resolved image.

### **2.3.1 Detection & Microscope Optics**

As isolated emitting diffraction limited spots are imaged, their centroid can be localized with an approximate precision of  $\sigma/\sqrt{N}$ , where  $\sigma$  is the standard deviation of the PSF and  $N$  is the number of detected photons (13). This relationship reveals the importance of the imaging system and fluorophores used. To achieve high localization accuracy, one would want to achieve a small PSF by using a high  $NA$  objective and optical components that minimize the unwanted diffraction. Yet one of the main problems arises from the low photon-detection efficiency in microscopes leading to the need for high-sensitivity and low-noise detectors as is the case with electron-multiplying charge-coupled devices (EM-CCD) cameras and low absorption optics. Labelled biological samples, however, can present a large number of fluorophores in a diffraction-limited region preventing precise single-molecule localization. A solution based on photo-switchable fluorescent molecules – molecules that can be reversibly switched from non-fluorescent (OFF-state) to fluorescent (ON-state) by stimulation of light with specific wavelengths – can be created through the use of activation-deactivation imaging cycles. Importantly the density of activated molecules in each single image must be kept very low, such that the images (in this

case PSFs) of individual fluorophores do not overlap permitting single-particle detection. In each step of this imaging process a small number of molecules is activated, imaged and deactivated, repeating this cycle creates a sequence of images where sequentially most of the photo-switchable population will appear distributed over a large number of temporal-slices allowing for the individual spot detection and localization.

Imaging by itself can be easily implemented on a TIRF or wide-field based system that features a high magnification and numerical aperture objective (100x 1.45 *NA* or better), high-efficiency optics and detector, and an excitation system that is compatible with the photo-switching activation and excitation of the chosen fluorophore (see Figure 2.5) - minor modifications to the setup might be needed in order to achieve 3D information through the introduction of astigmatic lenses or simultaneous double-plane detection (45, 46).

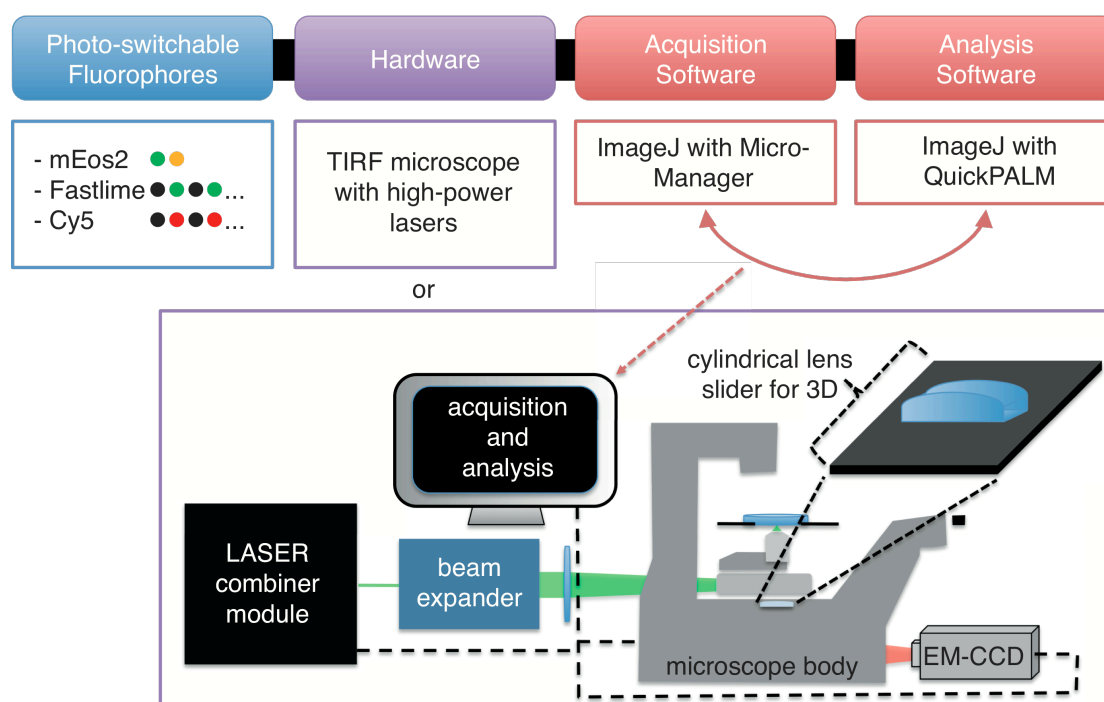


Figure 2.3. Setting up your own SMLM. Aside from the complexities involving fluorophore selection discussed extensively here, assembling a SMLM compatible microscope is both cost-effective and straightforward. TIRF microscopes can easily be adapted for SMLM or a custom system can be set up by combining a commercial microscope body with a high-sensitivity camera and a custom laser excitation system. A cylindrical lens inserted into a slider below the objective revolver can provide

astigmatism characteristics enabling 3D imaging with the system – an extensive list of tutorials on the subject can be found in <http://code.google.com/p/quickpalm>.  $\mu$ Manager constitutes a free, open-source software for hardware control and acquisition compatible with SMLM experiments and can be used in tandem with QuickPALM – a dedicated ImageJ plugin to process SMLM data.

### 2.3.2 Fluorescent Proteins & Dyes

For PALM and STORM, the choice of the right photo-switchable fluorophores is key, as they are critical factors that modulate the speed of acquisition and localization accuracy of the techniques. Desirable fluorescent molecules should be extremely bright in order to allow for the detection of the maximum possible amount of photons per molecule ( $N$ ) - this can be achieved by selecting dyes or fluorescent proteins that have both a large extinction coefficient ( $\epsilon$ ) and quantum yield ( $QY$ ). It is important to maintain a good ratio between the amounts of photons emitted in the fluorescent activated state in comparison with the residual photons emitted in the non-activated state. Acquisition speed is highly dependent on the activation and deactivation rates of the fluorophores as experimental settings need to be optimized in order to prevent unwanted PSF overlapping (this issue comes to the forefront in specific biological examples described later). Thus, by maintaining a good balance between the small number of fluorescent molecules that are activated in each acquired frame and the amount that do not immediately deactivate between consecutive frames allows single-molecule to be achieved.

Several different classes of photo-switchable fluorophores compatible with super-resolution localization have been described (see Table 2.1): *irreversible photo-activation fluorescent proteins* – can only make a single transition from a dark to an emitting state, deactivation is achieved by irreversibly bleaching the molecule. One of the earliest developed and most successful fluorophore of this class is PA-GFP (47) spearheaded by the early work of the A. Diaspro group on restricting the activation of PA-GFP in 3D space through two-photon activation (48) or the recent work of Hess and colleagues with live cell FPALM (49). Due to its low contrast ratio the spatial resolution is severely limited; *irreversible photo-shiftable fluorescent proteins* – are able to do an irreversible shift between two fluorescent colours. These are some of the

most commonly used proteins for super-resolution imaging. mKiKGR has been recently engineered based on the KiKGR tetramer making it a more suitable alternative for cellular protein imaging (50). Of this class, PS-CFP2 is the only green-emitting protein and has successfully been used in multi-color super-resolution imaging (51); *reversible photo-activatable fluorescent proteins* – capable of shifting between active and non-active states multiple times, even though the wavelength of the emission peak of bsDronpa, rsFastLime and Padron are near each other, Andresen et al. (52) has shown that the time-spectral photo-switching characteristics of these fluorophores can be used to differentiate them in multi-color imaging (52); *reversible photo-activatable fluorescent dyes* – non-genetically encoded they are able to undergo several shifts between a fluorescent and non-fluorescent state, in comparison to their analogue photo-switchable proteins the photon output ( $N$ ) of some of these probes is extremely high leading to lateral resolutions in the order of 20 nm achieved in STORM (53). Although some of these dyes are able to photo-switch alone as is the case of Cy5 (6), when paired with a secondary chromophore switching might be improved, this feature greatly increases the colour range of STORM probes (53); *caged fluorophores* – irradiation with UV-light causes the release of a protective group leading to a fluorescence increase of the dye, caging brings a new way to create new photo-switchable probes based on pre-existing fluorophores with desirable photo-physical properties (54); *fluorophores with reversible photo-bleaching* – recently it has been shown that embedding samples in oxygen depleted mediums such as polyvinyl alcohol, glucose oxidase or glycerol, allows conventional fluorophores (such as EGFP, EYFP, ECFP, Alexa488, Alexa568, fluorescein among many others) to switch into dark-states after strong illumination, allowing them after a period of “relaxation” to stochastically switch back to an emitting-state (55-57). This method has permitted the achievement of 30nm resolution by imaging Alexa488 (58).

Fluorophore	Switch	$\lambda( act )$	$\lambda( ex )$	$\lambda( em )$	$\epsilon$	QY	N	Fluorescence Increase	O. State	Ref
Irreversible photo-activation fluorescent proteins										
PA-GFP (Pre)		413	400	515	20.700	0.13	~70	5	Monomer	(54, 59)
PA-GFP (Post)			504	517	17.400	0.79	~300			
PAmCherry (Pre)		405	ND	ND	ND	ND	ND	5000	Monomer	(60)
PAmCherry (Post)			570	596	24.000	0.53	ND			
Irreversible photo-shiftable fluorescent proteins										
PS-CFP2 (Pre)		405	400	468	43.000	0.20	ND	>2000	Monomer	(54, 59, 61)
PS-CFP2 (Post)			490	511	47.000	0.23	~260			
Kaede (Pre)		350-410	508	518	98.800	0.88	ND	2000	Tetramer	(54, 59)
Kaede (Post)			572	580	60.400	0.33	~460			
mKiKGR (Pre)		405	505	519	49.000	0.69	ND	>2000	Monomer	(50)
mKiKGR (Post)			580	591	28.000	0.63	~970			
mEosFP (Pre)		400	505	516	67.200	0.64	ND	ND	Monomer	(54, 59)
mEosFP (Post)			569	581	37.000	0.62	~490			
tdEos (Pre)		405	506	516	84.000	0.91	ND	200	Tandem dimer	(60, 62, 63)
tdEos (Post)			569	581	33.000	0.62	~750			
mEos2 (Pre)		405	506	519	56.000	0.84	ND	ND	Monomer	(62)
mEos2 (Post)			573	584	46.000	0.66	ND			
Dendra-2 (Pre)		405 or 488	490	507	45.000	0.50	ND	300	Monomer	(54, 60, 61)
Dendra-2 (Post)			553	573	35.000	0.55	ND			
Reversible photo-activatable fluorescent proteins										
Photo-switchable EYFP		405	514	527	137.000	0.61	ND	ND	Monomer	(64, 65)
Dronpa		405	503	522	125.000	0.68	120	ND	Monomer	(52, 54, 59)
bsDronpa		405	460	504	45.000	0.50	ND	ND	Monomer	(52)
Padron		496	503	522	43.000	0.64	ND	ND	Monomer	(52, 54)
rsFastLime		405	496	518	46.000	0.60	>2000	ND	Monomer	(8, 52)
Reversible photo-activatable fluorescent dyes										
Photochromic Rhodamine		375	530	620	105.000	0.65	~750	ND	NA	(7, 54)
Alexa Fluor 647*		532*	650	665	240.000	0.33	~6000	ND	NA	(53, 54)
Cy5*		405 or 457 or 532*	649	664	250.000	0.28	~6000	ND	NA	(53, 54)
Cy5.5*		532*	675	694	190.000	0.23	~6000	ND	NA	(53, 54)
Cy7*		532*	747	767	200.000	0.28	~1000	ND	NA	(53, 54)
Photocaged fluorophores										
Caged Q-rhodamine		405	545	575	90.000	0.90	ND	ND	NA	(54)
Caged carboxyfluorescein		405	494	518	29.000	0.93	ND	ND	NA	(54)

\* Pairing this fluorophores with a second activator chromophore greatly increases the photo-switching characteristics, literature described pairs: Cy3-Alexa Fluor 647, Alexa Fluor 405-Cy5, Cy2-Cy5, Cy3-Cy5, Cy3-Cy5.5, Cy3-Cy7 (53).

Table 2.1. Photo-switchable fluorophores for super-resolution imaging:  $\lambda(act)$  - photo-activation wavelength in nm,  $\lambda(ex)$  - excitation wavelength in nm,  $\lambda(em)$  - emission wavelength in nm,  $\epsilon$  - extinction coefficient in  $M^{-1}cm^{-1}$ ,  $QY$  – fluorescence quantum yield,  $N$  – emitted number of photons per molecule,  $O. State$  – oligomeric state.

### 2.3.2.1 Genetically encoded fluorophores

Perhaps the greatest advantage of genetically-encoded fluorescent proteins is the capacity to specifically label molecules in a non-invasive and live-cell compatible manner when compared to other methods such as immuno-fluorescence staining. Furthermore, cell-friendly mediums can be applied as opposed to the photo-switching buffers commonly used in STORM and dSTORM.

Interestingly, it has been known for many years that GFP itself switches between a fluorescent state and a dark state in response to light (66). However, it was the engineering of proteins to change their spectral properties upon illumination with light of specific wavelengths that allowed for the possibility of SMLM to become a widely used tool in cell biology. There are now numerous examples of these proteins each with slightly different photo-physical characteristics. Photo-activatable proteins, such as PA-GFP, undergo a single transition from a non-fluorescent to a fluorescent state upon light-induced activation; reversible photo-switchable fluorophores are capable of multiple cycles of activation from a dark to a fluorescent state and return to a dark state, as in the case of Dronpa; photo-shiftable proteins, exemplified by mEos2, can be stimulated to convert between two spectrally distinct fluorescent forms (colours) by activating irradiation. These switching processes are manipulated by careful control of the imaging environment in tandem with the activation and excitation light intensities. This procedure permits for small subsets of fluorophores to be activated and rapidly extinguished while capturing a sequence of images.

Most of the published literature on live-cell SMLM has genetically-encoded fluorophores. Yet care needs to be taken when approaching these methods. Most photo-modulatable fluorophores require activation by near-UV light, which is toxic to the majority of cells. The Dendra2 fluorophore is a minor exception, since it can be activated at wavelengths close to a 488nm wavelength - reviewed in (67). In most

experiments it is also desirable that fluorophores immediately bleach following activation in order to eliminate their presence from multiple acquired images where they would augment the probability of particle spatial-overlap. A strong excitation light is then applied to bleach the fluorophores but the penalty is increased photo-toxicity.

For live-cell imaging in SMLM the photo-toxicity challenge can be partially overcome by using lower excitation intensities. This can be used to analyze the motility of the activated portion of fluorophores over a small sequence of images until the population is bleached, a process that can be repeated several times. If the fluorophores are confined to a specific cellular structure or location and motility is sufficiently slow so as not to cause blur artifacts (which degrade particle localization), then it becomes possible to reconstruct the domains where the fluorophores have been captured. This process uses each fluorophore multiple times to landmark their enclosing territory and causes less cell damage due to the reduction in the illumination intensity. Similarly, this strategy can also be used to study and map single-molecule motion as demonstrated by the single-particle tracking PALM (sptPALM) technique that combines single-particle tracking with PALM microscopy (68) (see Figure 2.4).

The emergence of proteins with different emission spectra, such as rsCherry, a monomeric red photo-switchable fluorescent protein (60), has made multi-colour time-lapse SMLM imaging possible. Further, the development of new fluorescent proteins coupling photo-activatable and photo-shiftable properties, such as mIrisFP, introduces the possibility of using a pulse-chase approach in conjunction with super-resolution imaging for single-particle tracking in dynamic processes, such as monomer turnover in macromolecules (69).



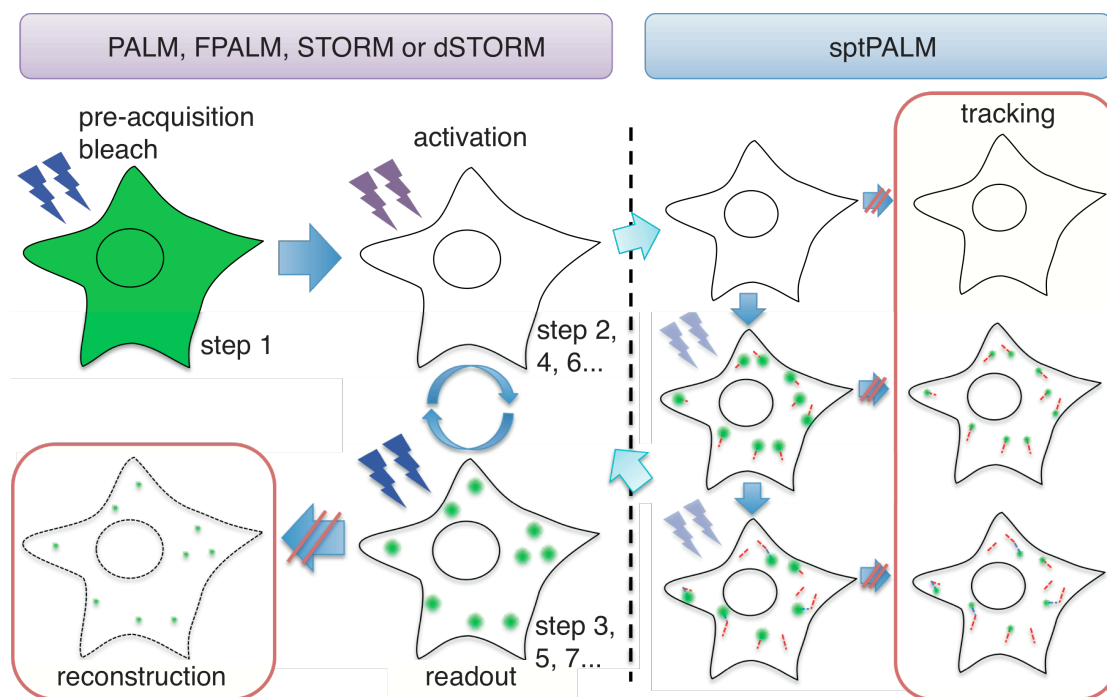


Figure 2.4. Acquisition steps for PALM, FPALM, STORM, dSTORM and sptPALM. The typical acquisition in SMLM for PALM, FPALM, STORM, dSTORM is divided in three independent steps: pre-activation bleach – where cells are illuminated by a strong excitation laser, forcing any unwanted active fluorophore to go into an OFF-state; activation – the light-induced activation of an extremely reduced number of fluorophores preventing excessive spatial-overlapping of the visualized particles; readout – excitation and imaging of the activated fluorophores followed by bleaching in order to minimize the presence of already visualized particles in posterior acquired images. These final two-steps can be cycled until a sufficient number of molecules has been identified. In parallel to the readout phase particles can be detected and assembled into a reconstruction. In sptPALM, the readout phase is divided into multiple images where particle movement is captioned and tracked in parallel until bleaching of most active fluorophores has occurred leading to a new imaging cycle started by the activation phase.

### 2.3.2.1 Synthetic fluorophores

The two most important photo-physical characteristics determining the spatial resolution are the brightness of the molecules in the fluorescent state used for localization, and the ratio between this state and the brightness of the molecules in the

inactivated state. The former determines the number of photons that can be detected, which in turn determines the localization precision. The latter factor – the contrast ratio - contributes to the background, which again directly affects the localization precision. It should also be noted that the contrast ratio affects the resolution in a slightly more subtle way: low contrast ratios limit the ability of the system to localize molecules at high molecular densities, which is crucial for achieving high Nyquist-limited resolution (63). Consequently, it is important to choose fluorescent labels that have both high brightness and high contrast ratios. Many of the most commonly used photo-modulatable fluorescent proteins present high contrast ratios -  $\sim 10^5$  for EosFP – but with a smaller photon output when compared with small-molecule fluorescent dyes (6000 photons per Cy5 molecule have been detected versus 490 photons per mEos molecule – reviewed in (67)). Therefore, small-molecule dyes may be attractive candidates as probes for live-cell SMLM. Yet, the impossibility of genetically encoding such labels leaves researchers with the difficult task of devising appropriate strategies for specific and sensitive targeting of fluorophores to biological molecules of interest, in a living cell. Cell membrane impermeability to many dyes and dye-conjugates, not least of all conventionally labelled antibodies, stands as the greatest barrier to labelling intracellular targets under live-cell conditions, where the membrane should stay intact.

Currently available strategies fit into two broad categories - those that target fluorophores to peptide sequences or proteins fused to the target protein, and those that use enzymes to label the target sequence with the fluorescent tag (see Table 2.2). The small labelling systems used by peptide-targeting labelling strategies, such as TetraCys (70), HexaHis (71) and PolyAsp (72), cause minimal protein or cell perturbation. Thus far, however, only the TetraCys system has been successfully used in live-cell or intra-cellular labelling (71). Protein-directed labelling, such as SNAP/CLIP tags (73), Halo Tags, and Dihydrofolate reductase (DHFR) targeting with trimethoprim (TMP)-conjugates (74), allows improved targeting specificity, but at the cost of an increase in the size of the recruiting system, increasing the risk of perturbing protein function. Despite this, the tag-dye conjugates in a number of these approaches are sufficiently cell permeable to allow intracellular labelling. Covalent labelling with the DHFR-based system has been successfully used in live-cell STORM imaging of Histone H2B dynamics (75). Enzyme mediated protein labelling makes use of a small peptide sequence fused to the target protein and an enzyme,

natural or engineered, which ligates the fluorescent probe to the recognition sequence. Some of these methods, such as those based on the use of sortase (76, 77), phosphopantetheine transferases (78), and biotin ligase (79), have been used to ligate fluorophore-conjugates to recognition sequences on target proteins in living cells or at the single-molecule level. These approaches combine the benefits of a small directing peptide sequence and those of specific and rapid covalent labelling, and thus provide an ideal system for SMLM. However, the primary disadvantage currently encountered with the above systems is a lack of cell-permeability of the tags themselves, such that only membrane-protein labelling is possible.

In contrast, a Lipioic acid ligase based system has been developed which makes labelling at both the cell membrane and intracellular fluorophore possible (80). Two engineered forms of the microbial lipoic acid ligase have been developed by the Ting lab. The first is able to ligate cyclo-octyne conjugated probes to a Lipioic Acid Ligase Peptide (LAP) sequence fused to both cell surface and intracellular targets using a two-step process (81, 82). Practical challenges with the two-step process when applied to intracellular labelling led to the development of a second engineered ligase, a highly specific “fluorophoreligase,” capable of specifically ligating hydroxycoumarin to intracellular LAP fusion proteins. This newly engineered enzyme may be most suitable for the direct and specific labelling of intracellular targets, however, the strict restriction to only one dye limits the applicability of the system for SMLM at this stage. Further engineered forms, able to make use of multiple dye-conjugates, would provide a valuable system for multi-color labelling in live-cells in the future.

Besides strategies for the specific labelling of intracellular proteins with a wide variety of fluorescent dyes for live cell imaging, the suitability of specific fluorescent dyes for SMLM, particularly their photo-switching abilities, as well as the necessary conditions for such blinking, are also an important consideration, especially for live-cell imaging. Developments in imaging buffers have allowed photo-switching properties to be attributed to the majority of synthetic fluorescent dyes.

Targeting peptide	Ligand	Enzyme	Bond	Cellular Targets	Comments
Peptide/Protein based targeting					
TetraCys	Biarsenical fluorophores	---	Covalent	Membrane/ intracellular proteins	Live imaging with FIAsh tags
HexaHis	NTA- conjugates	---	Noncovalent	Membrane proteins	N/A
PolyAsp	Dpa tyr conjugates	---	Noncovalent	Membrane proteins	N/A
SNAP/CLIP tags	Benzylguanine conjugates	AGT	Covalent	Membrane/ intracellular proteins	Greater specificity, larger label
Halo tags	Chloroalkane conjugates	Dehalogenase	Covalent	Membrane/ intracellular proteins	
DHFR	TMP	DHFR	Noncovalent or covalent	Membrane/ intracellular proteins	
Enzyme based targeting					
Sortag	Oligo-glycine dye conjugate	Sortase	Covalent	Membrane proteins, C- & N- terminals	N/A
Q-tag	Amine-modified probes	Transglutaminase	Covalent	Membrane proteins, N-terminal	Low substrate specificity
ACP/ PCP	Co-enzyme A- conjugates	Phosphopantetheine transferases (Sfp & AcpS)	Covalent	Membrane proteins	N/A
AP	Biotin conjugates	Biotin ligase, BirA	Covalent	Membrane proteins	N/A
LAP	cyclo-octyne conjugates/ hydroxycoumarin	Lipoic acid ligase	Covalent	Membrane/ intracellular proteins	One or two-step process

Table 2.2. Targeting strategies for synthetic dyes. DHFR: dihydrofolate reductase; ACP: acyl-carrier protein; PCP: peptidyl-carrier protein; AP: biotin ligase acceptor peptide; LAP: Lipoic acid ligase acceptor peptide; NTA: Nitrilotriacetic acid; TMP: trimethoprim; AGT: O<sup>6</sup>-alkylguanine-DNA alkyltransferase; N/A: not applicable.

### 2.3.2.2 Blinking-inducing buffers

Fluorescence excitation occurs by the absorption of a photon, which promotes a singlet, ground state molecule ( $S_0$ ), to the excited singlet state ( $S_1$ ). The subsequent return to  $S_0$  produces a fluorescence photon emission. Alternatively the competing process of inter-system conversion can occur maintaining the fluorophore in a long-lived triplet state ( $T_1$ ) formation (see Figure 2.5).

While in  $T_1$  the fluorophore is unable to undergo fluorescence emission until relaxation to  $S_0$  is re-achieved. During this period the fluorophore is sensitive to an irreversible photo-bleaching event if it reacts with molecular oxygen. This in turn results in the production of reactive oxygen species (ROS) – one of the major sources of photo-toxicity in cells. Notwithstanding, this process does not only create light-induced damage but the overall absorption of light by the cell can produce toxicity (83, 84).

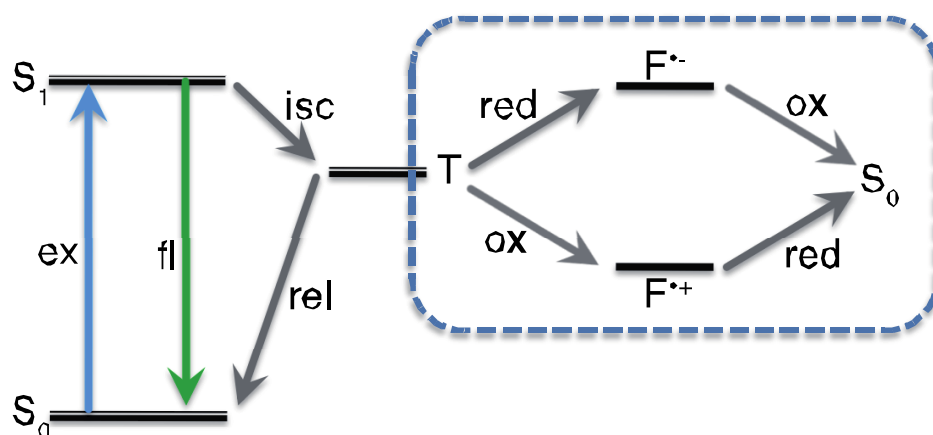


Figure 2.5. Scheme of the photo-switching process and redox triplet state depletion mechanism. A ground state fluorophore is excited to the  $S_1$  singlet state by the absorption of a photon. The fluorophore may then return to the ground state or transverse into a dark triplet state by intersystem crossing, followed by stochastic relaxation back to ground state. Boxed region: The addition of reducing and oxidizing agents depletes the triplet state by electron transfer reactions, producing either form of fluorophore radical and retrieving the reactive intermediates by the reciprocal reduction or oxidation. This returns the fluorophore to ground state, avoiding photo-bleaching and allowing cycling or switching of the fluorophore between excited, triplet and ground states.  $S_0$ : ground state;  $S_1$ : excited singlet state;  $T$ : triplet state; ex: excitation; fl: fluorescence; isc: inter-systen crossing; rel: relaxation; red: reduction; ox: oxidation; F: fluorophore

If reactions with oxygen can be avoided, then fluorophore photo-bleaching can be reversed. This process can be used to induce switching behaviour in fluorophores (56, 85) as the  $T_1$  transition is stochastic and can be employed as the transient OFF-state of a fluorophore. Under these conditions, fluorophore blinking compatible with single-molecule localization of a large population of fluorophores can be attained by imaging the cycling of short fluorophore photon bursts caused by  $S_0$ - $S_1$  transitions (the ON-state) followed by the temporary arrest of fluorescence in the  $S_1$ - $T_1$  shift (the OFF-state). Initially, a very limited selection of dyes known to be able to undergo such photo-switching processes was available. Cyanine dyes (86, 87) have been most commonly used for SMLM as they can be induced to switch by the presence of a second, activating fluorophore. Such a photo-switching mechanism requires oxygen

removal and the use of millimolar concentrations of a reducing agent, such as  $\beta$ -mercaptoethanol, in the imaging medium (88).

The demonstration of light-induced reversible photo-switching of single standard fluorophores for use in SMLM, termed dSTORM (6), initiated significant advances in establishing SMLM imaging systems in which a much larger range of standard fluorophores can now be used. Central to these developments is an understanding of this ‘blinking’ mechanism in fluorescent molecules, and concomitantly, the formulation of a system that modulates the switching rates (see Table 2.3).

Photo-bleaching can be limited by the depletion of oxygen in the sample, either by embedding with poly-(vinyl-alcohol) (PVA) or using enzymatic oxygen scavenging buffers. This removes singlet oxygen and thus lengthens the  $T_1$  lifetime, while addition of a reducing agent is often used to recover ionized fluorophores. The versatility of these approaches remains limited by their dependence on the specific fluorophores inherent single-state return rate for establishment of an appropriate rate of blinking, while oxygen depletion and toxic reducing agents make this setup incompatible with most live-cell experiments.

By approaching the photo-bleaching and triplet state recovery processes as a redox system, the Sauer and Tinnefeld groups have determined a simple, live-cell adaptable imaging setup to allow the fine-tuning of the rate of singlet-state return relative to triplet state formation. In this system, the reactive triplet state is rapidly depleted, either by oxidation to a radical cation, or by reduction to a radical anion. These ions can be recovered by the addition of a reducing or oxidizing agent, respectively, returning the fluorophore to the singlet state. Thus a buffering system with both reducing and oxidizing agents (termed ROXS) recovers reactive triplet state intermediates, repopulating the ground state and avoiding photo-bleaching. By adjusting the relative ROXS buffer concentrations as required, the rate of photo-switching can be directly controlled to ensure sufficient fluorophores are in a dark state at each time point and that fluorescent lifetimes are sufficient to yield photons for accurate localization.

<b>Redox Buffer</b>	<b>Action</b>	<b>Endogenous</b>	<b>Toxicity</b>
Trolox	Reductant	No	Low
$\beta$ -mercaptoethanol	Reductant	No	High
Propyl galate	Reductant	No	Low
Ascorbic acid	Reductant	Yes	Low
Glutathione	Reductant	Yes	Low
Dithiotriitol	Reductant	No	High
Tris(2-carboxyethyl)phosphine hydrochloride	Reductant	No	High
Methylviologen	Oxidant	No	High
Ambient oxygen	Oxidant	Yes	Low

Table 2.3. Redox buffer agents to modulate photo-switching.

The toxicity of ROXS reagents had to be addressed in order to adapt such systems for live-cell imaging (see Table 2.3). Typically, thiol-reagents such as  $\beta$ -mercaptoethanol or  $\beta$ -mercaptoethylamine have been used as reducing agents in SMLM buffers (56, 85). Recently, glutathione and ascorbic acid have proven to be appropriate live-cell compatible alternatives to these reducing agents (85, 89). Despite its toxicity methylviologen remains the primary oxidizing agent used (89). By taking advantage of the oxidizing potential of oxygen itself, and using the molecular oxygen present in the cellular environment to fulfil the role of the oxidant in ROXS (85) the challenge of oxidant toxicity, as well as the need for oxygen-depletion in SMLM, has been neatly side-stepped. Although the presence of oxygen slightly restricts the experimenter's capacity to modulate the dyes photo-physics, this nevertheless greatly simplifies the application of ROXS for use in live-cell SMLM.

Essentially any desired fluorophore labels with suitable photo-physical properties can be used in a biologically compatible ROXS imaging buffer, without the need for oxygen depletion. The ATTO dyes, such as ATTO520, ATTO565, ATTO655, ATTO680 and ATTO700, have proven particularly well suited for use in "blink microscopy" with ROXS (85). Investigations are broadening into the suitability of more water-soluble dyes, such as perylene dicarboximide fluorophores, specifically for use in live-cell imaging.

ROXS provides a dye and buffer system that provides a prime choice of multi-colour dyes to use in live-cell SMLM with minimal perturbation to the cell.

### **2.3.3 Single-molecule analysis and reconstruction**

Analysis and reconstruction are one of the major parts of PALM and STORM. Post-acquisition or in-acquisition processing infer the characteristics of each molecule present in the large amount of images that constitutes the dataset. In a typical experiment 10.000 to 100.000 images are generated where tens to hundreds of particles are present in each frame. Although the acquisition by itself takes few minutes, the data analysis can take up to several hours and is highly dependent on the processing power available to the user. Ironically this means that the super-resolved image cannot be “seen” until well after the end of the actual acquisition and imaging of the sample. Localization accuracy depends greatly on the capacity of the algorithms to deal with detection noise, PSF overlaps and particle motion. Fortunately biology can inherit a great deal of knowledge and solutions from astronomy, as astronomers have faced a similar problem when observing stars that are in essence also diffraction limited. For example, Egner and colleagues describe the usage of a modified version of the 1974 Hogbom’s CLEAN algorithm (90) in conjunction with a mask-fitting algorithm of the Airy spot to provide particle segmentation and positioning (8). These tasks become more difficult when particle tracking is needed as in the case of following molecular dynamics.

Single-particle tracking (SPT) algorithms need to relate the different particles being detected at different time-points. Such tasks face several challenges, such as particles disappearing due to blinking, moving into or outside of the region being imaged, particle splitting, particle merging and detection failure (91, 92). Recently, both groups of Jaqaman et al. (92) and Serge et al. (93) have provided the research community with freely available Matlab (Mathworks) based algorithms able to achieve localization accuracies near the theoretical limit and multi-particle tracking.

As PALM and STORM evolve to live cell imaging, the need for in-acquisition real-time analysis increases in order to optimize and adapt the microscope settings. This would be the case in data-driven excitation and activation optimization in order to reduce the needed imaging time and the high photo-toxicity of PALM and STORM experiments. Also, this would provide biologists with tools that allow experimental decisions based on the immediate observed super-resolution information. It is clear that as the technique becomes more generally used in the near future, so too will



algorithm optimization, multi-processor analysis and clustered computing evolve to provide these features.

## **2.4 Stepping into 3D super-resolution**

Although PALM and STORM have been generally used to improve 2D image resolution, achieving 3D intra-cellular information has been one of the major challenges for the techniques. Other nanoscopy methods like 4Pi or I<sup>5</sup>M have been able to surpass this problem and achieve an axial resolution below 100nm (20, 21, 94), STED microscopy in a 4Pi illumination geometry has been shown to reach resolutions as high as 30 to 50 nm however without super-resolution in the lateral dimensions (95). The recent work of Lemmer and colleagues on super-resolving cellular nanostructures through the combination of spectral precision distance microscopy (SPDM) with spatially modulated illumination (SMI) as achieved 20 nm lateral- and 50 nm axial-resolution (96). PALM and STORM have been mostly used under total-internal reflection fluorescence (TIRF) imaging due to the inherent high contrast optical sectioning achieved with such systems limiting the z-axis imaging depth generated by the evanescence field to around 150 nm. A similar technique called highly inclined and laminated optical sheet (HILO) microscopy makes use of a highly inclined light beam to generate a thin optical sheet that penetrates the sample at a shallow angle, HILO has effectively been used in single-molecule fluorescence nanoscopy of the cell nucleus with high signal/background ratios (97) and should prove to be compatible with PALM and STORM imaging but no such case has been reported to the date. Two-photon activation based optical sectioning with PALM has been achieved on photochromic rhodamine dyes (7). Recently two elegant solution to the PALM and STORM 3D problem have been demonstrated without optical-beam scanning: by inducing optical astigmatism on a wide-field setup where the PSF shape becomes ellipsoid dependent on the Z-position of the fluorophore - a trait that has been shown to allows 20-30 nm lateral and 50-60 nm axial resolution (45) - or the usage of a biplane (BP) detection scheme where a 3D stack of two slightly displaced Z-planes are acquired simultaneously allowing for accurate z-position determination leading to a experimentally measured 30 nm lateral and 75 nm axial resolution (46), one of the main problems of this last described technique comes out of the need to

split the incoming emitted light into two images leading to a decrease of the detected signal-to-noise ratio.

## **2.5 Imaging of molecular structures**

The super-resolution method PALM first distinguished itself in the labelling of lysosomal transmembrane protein CD63 fused to Kaede (see Table 2.1) (43). In this case cryosectioning, similar to transmission electron microscopy (TEM), was performed but with imaging under ambient conditions. As a control (to confirm localization), they performed comparative immuno-fluorescence staining in similar samples. *Betzig* and co-workers were able to visualize the intricate structures of the lysosome, including interacting membrane structures and possibly late endosomes. In the same work, *Betzig* and co-workers go on to label dimeric Eos (see Table 2.1) with a cytochrome-C oxidase localization sequence, thus targeting the mitochondria. In a comparison with TEM images of the same mitochondria they were able to achieve highly similar structural information and images. The power of this technique is clearly the nanometer resolution that is achieved in determining the distribution of a given protein within the cellular ultra-structure. Obviously the minimal preparation required by PALM as compared to TEM is a great advantage.

Early experiments using PALM to study cellular ultra-structures focused on fixed cells or cryosections. However being able to observe the assembly of such structures in real-time with super-resolution opens up several areas of scientific investigation under *in vivo* conditions. These include how other cellular factors contribute to the assembly and development of these processes with high spatio-temporal resolution. Important criteria that must be met for live cell super-resolution are: as acquisition cycles typically require high laser powers for fluorophore activation and bleaching, a significant amount of photo-toxicity is generated leading to abnormal cell behaviour or death – this becomes a greater problem when UV-lasers are used for fluorophore activation due to the high energy of the photons used. In order to compensate for molecular motility and maintain a fair number of molecules detected, a high frame rate needs to be used potentially leading to a decrease in the detected signal to noise ratio and thus compromising the localization accuracy and resolution. Another limitation arises from the limited number of detected photons. As the overall number

of molecules able to photo-switch is depleted due to irreversible photo-bleaching, the detected molecular density per frame will decrease over time. Notwithstanding these challenges, at least two groups have been able to successfully achieve super-resolution in live cells. To image the assembly of ultra-structures *Shroff et al* tagged the protein paxillin with a dimer of Eos (63). They were able to image the adhesion complexes or transmembrane cytoskeleton-substrate attachment points central to the process of cell migration. They overcome the inherent problems of live-cell imaging in PALM by using a fast imaging speed or image acquisition rates, which must be faster than the activity imaged. In addition they compensated for photon scarcity by using a dimer of Eos for each target protein thereby achieving a dense labelling of paxillin. Combining all these approaches enabled them to observe the formation of individual adhesion complexes for extended periods of time, measuring the number of individual paxillin molecules entering and leaving the complex in real time over 25 minutes. Furthermore, they were able to note that during cell migration adhesion complexes assume a wide diversity of morphologies.

### 2.6 Breaking through the technological limits

SMLM of a large population of fluorophores typically demands that hundreds to thousands of diffraction-limited images be acquired and processed in order to reconstruct a super-resolution dataset. There is a trade-off between reconstruction quality and temporal resolution. The number of localizations, i.e. the molecular density of localized molecules within each final reconstructed time-point, determines the reconstruction sparsity and thus the capacity to recognize the underlying labelled structures – the reconstruction quality. The acquisition time for a final reconstructed SMLM image, that is the sum of the exposure times of the raw data frames used to generate the final image, determines the temporal resolution of the processed super-resolution data. Additionally in order to obtain a reliable super-resolution reconstruction, algorithms have to analytically detect and localize each individual sub-diffraction particle present in each acquired frame. This is generally a major setback because visualization of the sample in parallel to the acquisition is crucial for making decisions on how to best adjust imaging conditions. Raw unprocessed images can be partially used to observe the sample but these are corrupted by the technique

itself – each raw-image is generally composed of few emitting molecules not permitting a complete understanding of underlying cellular structures.

Recently several algorithms have been published allowing for processing speeds concurrent with the acquisition itself (98-102). QuickPALM (100), an ImageJ based algorithm, in conjunction with  $\mu$ Manager (103), an open-source software for hardware control is able to both acquire and process 3D and 4D SMLM providing the super-resolution reconstruction in real-time as images are streamed from the camera (see Figure 2.3). This feature allows for data-driven algorithmic decisions on how to optimally adapt the acquisition and provides the user a reconstructed view of the sample being acquired.

### **3 Methods and Results**

Sections 3.1, 3.2 and 3.3 of this chapter present the original research work I have developed in my Ph.D.

#### **3.1 QuickPALM: 3D real-time photo-activation nanoscopy image processing in ImageJ**

This section follows the structure and information from the original paper: **Ricardo Henriques**, Mickael Lelek, Eugenio F Fornasiero, Flavia Valtorta, Christophe Zimmer & Musa M Mhlanga (2010). QuickPALM: 3D real-time photo-activation nanoscopy image processing in ImageJ. *Nature Methods* 7: 339–340.

Some of the results presented and discussed in this section are the product of collaborative work. R.H. planed the experiments, wrote all the software, did all the imaging experiments, assembled the samples into the final dSTORM compatible coverslips and wrote the article. M.L. was responsible by the assembly and optical setup of one of the super-resolution microscopes used in this work (at Pasteur Institut, Paris). E.F. Fornasiero prepared and provided the labeled neuron cells. F. Valtorta supervised Eugenio's work. C.Z. and M.M.M. edited and reviewed the article. Also, I would like to thank J. Enninga (Institut Pasteur, Paris) for assistance with experiments, T. Duong (Institut Pasteur, Paris) and R. Fesce (Insubria University, Varese and San Raffaele Scientific Institute, Milano) for helpful insight in the preparation of the manuscript.

### **3.1.1 Introduction**

Super-resolution microscopy using photo-switchable molecules requires fast and efficient software for single-molecule detection, localization, drift correction, and visualization. However, there is still a dearth of freely available, flexible and easy-to-use reconstruction software coupled with image acquisition. Here, we present QuickPALM, an ImageJ plugin enabling real-time reconstruction of 3D super-resolution images during acquisition and drift correction. We illustrate its application by reconstructing Cy5-labelled microtubules with a resolution of 40-50 nm.

Although conventional microscopes have a resolution limited by diffraction to about half the wavelength of light, several recent advances have led to microscopy methods that achieve roughly ten-fold improvements in resolution. Among them, Photo-Activated Light Microscopy (PALM) and Stochastic Optical Resolution Microscopy (STORM) have become particularly popular, as they only require relatively simple and affordable modifications to a standard Total-internal Reflection Fluorescence (TIRF) microscope (3-5) and have been extended to 3D super-resolution and multi-colour imaging (45, 104). PALM and STORM achieve super-resolution by sequentially imaging sparse subsets of photo-switchable molecules. Positions of individual molecules are computed from individual low-resolution images with sub-diffraction accuracy. These positions are then corrected for drifts and subsequently assembled into one or more super-resolution images. Unfortunately, in most current implementations, this reconstruction may take from several hours to days for a single dataset, thus forbidding visual inspection of super-resolution images in real-time. In addition, PALM and STORM software used to date is generally not freely available, strongly limiting the adoption of this otherwise relatively simple microscopy method. Two recent publications independently demonstrated 2D algorithms for real-time PALM and STORM reconstructions (98, 99). Here, we present a freely available and open-source algorithm under the form of a plugin for the widely used ImageJ (<http://rsb.info.nih.gov/ij/>) software that combines real-time processing capability with additional important features including 3D reconstruction, drift correction, and real-time acquisition control (<http://code.google.com/p/quickpalm/>).

### **3.1.2 Material and Methods**

#### **3.1.2.1 Slide treatment**

Coverslips were prepared as previously described (105). Briefly, round 25x0.17-mm coverslips (Fisher Scientific, Pittsburgh, PA) were cleaned in porcelain racks for 18h in concentrated nitric acid, washed several times in tissue-culture-grade water and sterilized with dry heat (225° C for 8h) in a clean oven.

#### **3.1.2.2 Hippocampal neuron cell culturing**

Primary neuronal cultures were prepared from the hippocampi of Sprague-Dawley E18 rat embryos (Charles River Italiana, Calco, Italy) as previously described (106). Briefly, after euthanization of the pregnant mother, E18 rat embryos were isolated, and hippocampi were dissected in cold calcium- and magnesium-free Hank's balanced salt solution (HBSS; Gibco, United Kingdom) supplemented with 5 mM HEPES pH 7.4. Hippocampi were washed several times in HBSS and dissociated in 0.25 % trypsin (Gibco, United Kingdom) for 15 minutes at 37°C. After trypsin removal, neurons were plated in minimum essential medium with Earle's salts (MEM; Gibco, United Kingdom) containing 10% Horse serum during the time necessary for adhesion, and subsequently co-cultured for 3 days with primary astrocytes in N2 supplemented MEM.

#### **3.1.2.3 Cell labelling**

Neurons were fixed for 15 minutes at RT with 4% paraformaldehyde, 4% sucrose in 120 mM sodium phosphate buffer (pH 7.4) supplemented with 2 mM EGTA. After fixation, cells were washed in phosphate buffered saline (PBS) for 0.5h and incubated with anti neuronal tubulin beta-III antibody (Covance, United Kingdom) diluted 1:100 in goat serum buffer (450 mM NaCl, 20 mM phosphate buffer, 15% goat serum, and 0.3% Triton X-100) for 2h at RT. Upon primary antibody incubation cells were washed in PBS for 0.5h and incubated with Cy5 conjugated donkey anti rabbit

antibody (Jackson ImmunoResearch, West Grove PA) for 1h at RT. Fluorescent beads (100nm diameter) of a similar emission wavelength, were mounted with the sample as fiduciary landmarks.

### **3.1.2.4 Slide preparation for imaging and acquisition**

Slides were sealed in a Parafilm® M gasket. Imaging was performed in a “reactive oxygen scavenger photo-switching buffer” as previously described(6). The buffer contains 0.5 mg/mL glucose oxidase (Sigma), 40 µg/ml catalase (Roche Applied Science), 10% w/v glucose and 50 mM of β-mercaptoethylamine in PBS (pH 7.4). 150,000 fluorescence images were acquired with a 50 ms exposure time in laser-excitation wide-field. The sample was excited with a 635 nm laser with the power adjusted for optimal and fast bleaching of activated Cy5 molecules while a 488 nm laser was pulsed at decreasing intervals to stochastically reactivate bleached Cy5 molecules and maintain an optimal visible number of emitting molecules in the field of view.

### **3.1.2.5 Microscope components and setup**

Laser light from the two lasers (EXLSR-635C-60mW and CYAN- 488-100mW, Spectra-Physics, Japan) is combined using the mirror M1 and the dichroic beam-splitter DM1 (LM01-503-25, Semrock, Rochester, NY, USA). The switching between the activation wavelength and the excitation wavelength and intensity control of each laser are performed via an acousto-optic tuneable filter (AOTFnc-400.650, A-A Opto-Electronic, Orsay Cedex, France). Before the injection of the laser beams inside the microscope, they are widened by a telescope consisting of the achromatic doublet lenses L1 and L2 and focused into the back focal plane of the objective (CFI Apochromat, 100x, NA 1.49, Nikon, Japan) by the achromatic doublet lens L3. The far red fluorescence emission is collected by the same objective, separated from the illumination light by a quad-band line dichroic mirror DM2 (FF416/500/582/657-DiO1, Lot # 709240-709242 Semrock, Rochester, NY, USA and latter filtered with a dual band pass Filter F (FF01-577/690-25, Lot # 307339-207360 Semrock, Rochester, NY, USA) being finally detected by an EM-CCD camera (Ixon



DV887ECS-BV, Andor, Belfast, Northern Ireland) via the mirror M4. An additional lens L4 is used to achieve a final imaging magnification of 100 to 150 times yielding a pixel size from 160 to 106 nm. 3D imaging is performed by adding a cylindrical lens CL (RCX cylindrical lens 10m focal length, CVI Melles Griot) before L4 in order to create an astigmatism, whereby the detected spot shape depends on the fluorophore depth (45) – most microscope bodies have a polarizer insertion slider immediately below the filter cube wheel that can be cleverly adapted as a cavity to insert the cylindrical lens (see Figure 3.1).

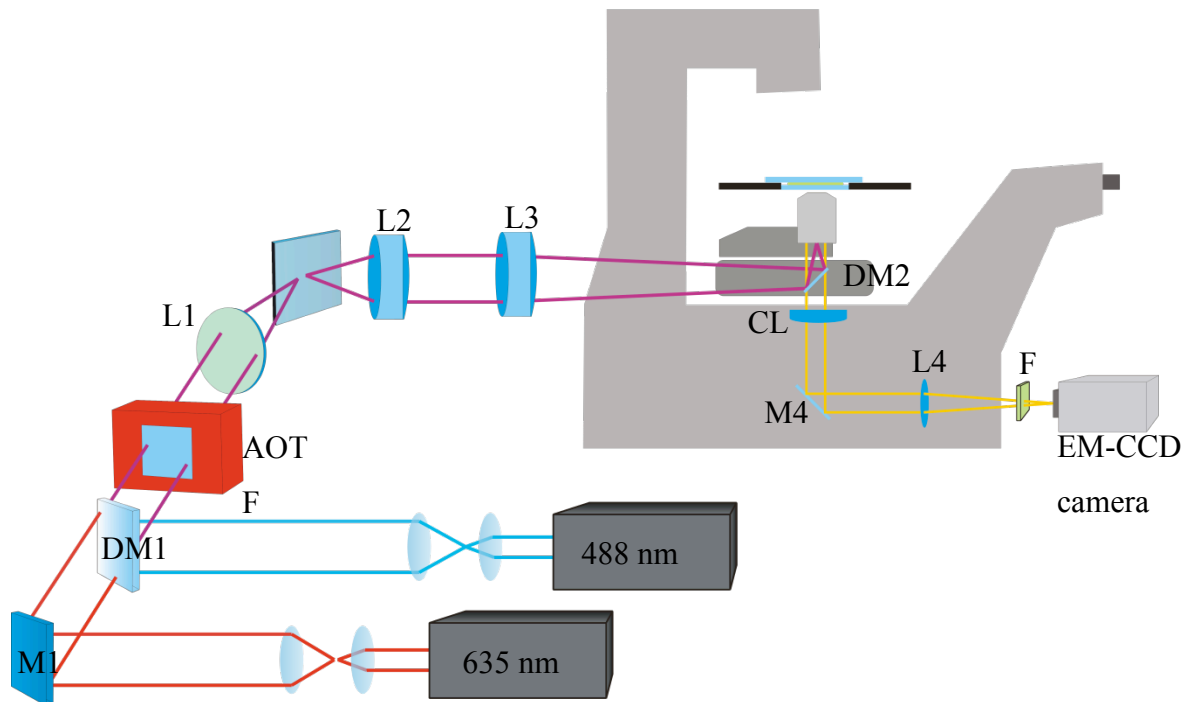


Figure 3.1. Microscope setup for 3D imaging. Laser light from two lasers is combined using the mirror (M1) and the dichroic beamsplitter (DM1). The two beams are switched using an acousto-optic tuneable filter (AOTF) and a series of lenses (L1-L3) directs the beams into the objective. Fluorescent light from the sample crosses the dichroic beam-splitter (DM2) and transverses a cylindrical lens (CL) that introduces an astigmatic aberration into the image allowing us to perform the 3D localization of sub-diffraction particles, the correspondent light is then redirected by a mirror (M4), magnified by a tube-lens (L4) and filtered by an emission filter (F) before reaching the camera.

### 3.1.2.1 Particle detection, localization and visualization

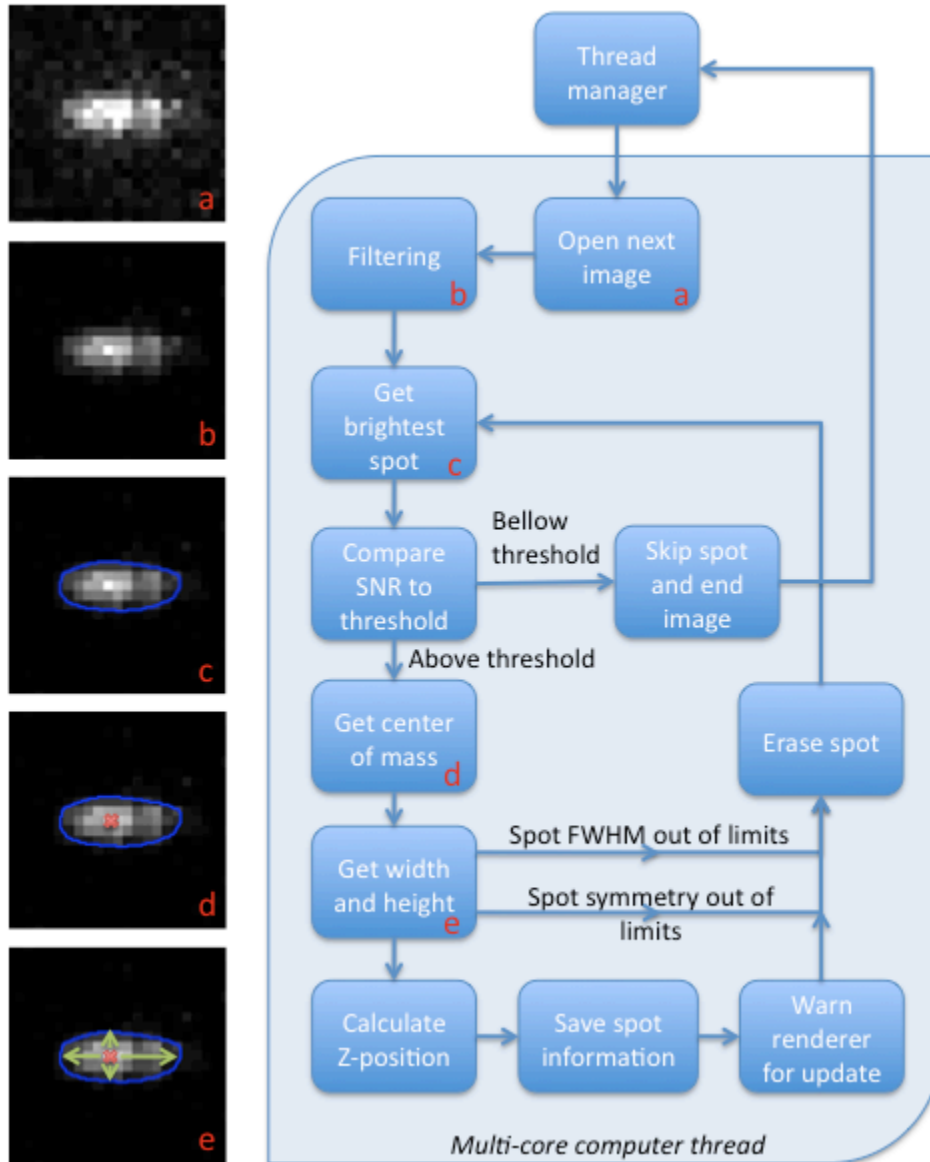


Figure 3.2. Flow-chart of particles detection, localization and visualization within QuickPALM. Images in left column schematically represent the corresponding steps on the flow-chart labelled with the same inset letter.

Particle detection and localization takes advantage of all available CPUs on the processing computer through the use of a thread manager (see “Thread Manager” in Figure 3.2) that distributes the processing jobs between available free CPUs or buffers the acquisition while waiting for these to become free.

Within each thread a new unprocessed image is collected (see “Open next image” in Figure 3.2) and the noise is characterized by calculating the standard deviation on a

small area of 13x13 pixels centred on the minimum intensity pixel of the image. It is assumed that due to the stochastic nature of a PALM or STORM image there is a low probability of having a blinking molecule in the immediate neighbourhood of this point. A band-pass filter is then applied to provide noise reduction and background correction on the overall image (see “Filtering” in Figure 3.2). Initially the image is convolved with a Gaussian kernel of sigma equal to 0.5 pixels and subtracted to a convolution of the original image with a Gaussian kernel of sigma with twice the maximum FWHM given by the user, thus both reducing the noise frequencies and background of the overall image without any visible decrease of the localization accuracy.

The image is then searched for the maximum intensity pixel, the surrounding pixels to this point are selected if within a square window of size twice the maximum *FWHM* whose values are above a relative threshold to the local peak intensity (see “Get brightest spot” in Figure 3.2). The local SNR is calculated as the division between the mean intensity of the selected pixels and the noise standard deviation. If this value is below the minimum SNR given by the user then the process for this image is halted (see “Compare against SNR” in Figure 3.2).

Before the spot is registered as a potentially valid particle it needs to pass the following tests: image edge – if a part of the intensity profile of the spot is obscured by the image edge; saturation/clamping – if the intensity of the local spot is not saturated; already analyzed region overlapping – if any of the pixels of the spot overlap with the region of an already previously analyzed spot on the same image. If these tests are correctly passed the algorithm proceeds to calculate the centre of the spot coordinates  $(c_x, c_y)$  as given by the centre of mass formulas:

$$c_x = \frac{\sum_{i,j} s_{i,j} x_{i,j}}{\sum_{i,j} s_{i,j}}$$

$$c_y = \frac{\sum_{i,j} s_{i,j} y_{i,j}}{\sum_{i,j} s_{i,j}}$$

where  $i, j$  are the  $x$ -axis and  $y$ -axis indices for each pixel within the spot,  $x_{i,j}$  and  $y_{i,j}$  are the coordinates of the pixel in nanometers and  $s_{i,j}$  the intensity of the pixel (see “Get center of mass” in Figure 3.2). The spot shape is then characterized by calculating the parameters:

$$\begin{aligned}\sigma_l &= \sum_{i,j} s_{i,j} (c_x - x_{i,j}) / \sum_{i,j} s_{i,j}, \text{ where } (i,j) \in \{(i,j) \mid x_{i,j} < c_x\} \\ \sigma_r &= \sum_{i,j} s_{i,j} (x_{i,j} - c_x) / \sum_{i,j} s_{i,j}, \text{ where } (i,j) \in \{(i,j) \mid x_{i,j} \geq c_x\} \\ \sigma_a &= \sum_{i,j} s_{i,j} (c_y - y_{i,j}) / \sum_{i,j} s_{i,j}, \text{ where } (i,j) \in \{(i,j) \mid y_{i,j} < c_y\} \\ \sigma_b &= \sum_{i,j} s_{i,j} (y_{i,j} - c_y) / \sum_{i,j} s_{i,j}, \text{ where } (i,j) \in \{(i,j) \mid y_{i,j} \geq c_y\}\end{aligned}$$

if the spot arises from a single diffraction limited particle and if the PSF is symmetric then the particles can approximate to a Gaussian PSF model where in the absence of astigmatism  $\sigma_l \approx \sigma_r \approx \sigma_a \approx \sigma_b$  or otherwise in its presence  $\sigma_l \approx \sigma_r$  and  $\sigma_a \approx \sigma_b$ . We can calculate the particle x-, y-axis symmetry as

$$S_x = 1 - \frac{|\sigma_l - \sigma_r|}{\sigma_l + \sigma_r}; \quad S_y = 1 - \frac{|\sigma_a - \sigma_b|}{\sigma_a + \sigma_b}$$

for a single diffraction limited particle, one expects  $S_x \approx 1$  and  $S_y \approx 1$  with or without astigmatism. The lateral *FWHM* along each axis (see “Get width and height” in Figure 3.2) can be defined as

$$\begin{aligned}FWHM_x &= 2.354(\sigma_l + \sigma_r)/2 \\ FWHM_y &= 2.354(\sigma_a + \sigma_b)/2\end{aligned}$$

in the absence of astigmatism one expects

$$\begin{aligned}FWHM_x &\approx FWHM_y \approx 2.354(\sigma_0/2) \\ \text{with } \sigma_0 &= 0.225(\lambda/NA); (107)\end{aligned}$$

it then becomes possible to test if the particle obeys a symmetry limit or if the *FWHM* values are within assigned margins given by the user in the graphical interface. The z-position of the particle is extracted by comparing the width minus height (*WmH*) of the particle calculated as  $WmH = FWHM_x - FWHM_y$  against the values on a z-calibration table (Figure 3.3) through linear interpolation of the closest *WmH* values on the table and associated Z-coordinates (see “Calculate Z-position” in Figure 3.2).

Finally if all tests are passed, the information for the spot is saved (“Save spot information” in Figure 3.2).

### 3.1.2.2 3D particle localization by comparison with an experimental calibration table

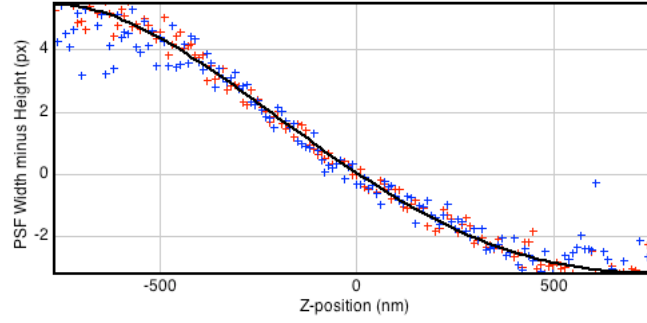


Figure 3.3. Example plot of the width minus height change for bead particles corrupted by astigmatism as a function of the z-position as calculated by QuickPALM. Crosses are measured values for each selected bead, the curve represents a 4<sup>th</sup> order polynomial fit to the data. The fitted values are saved as a calibration table and later used by the “Get Z-position” method previously described to estimate the z-position for each detected particle.

In order for QuickPALM to localize particles in the z-axis it needs to have prior-information on the astigmatic distortion, this is done by first acquiring a sequence of calibration images with the astigmatic lens (45) featuring sub-diffraction beads. Ideally these images are acquired at regular 10 nm Z intervals with the help of a piezo Z-motor. It should be possible to observe the width and height change of the PSF as a function of Z. QuickPALM is able to generate this calibration table, however, the user needs to first manually select which beads to use for calibration with the help of the “ROI Manager”. After this selection QuickPALM calculates the position, width and height of each selected bead through the “Get center of mass” and “Get width and height” methods discussed before and generates a plot of *Width-Height* vs. *Z* (see Figure 3.3).

### 3.1.2.3 Drift calculation and correction

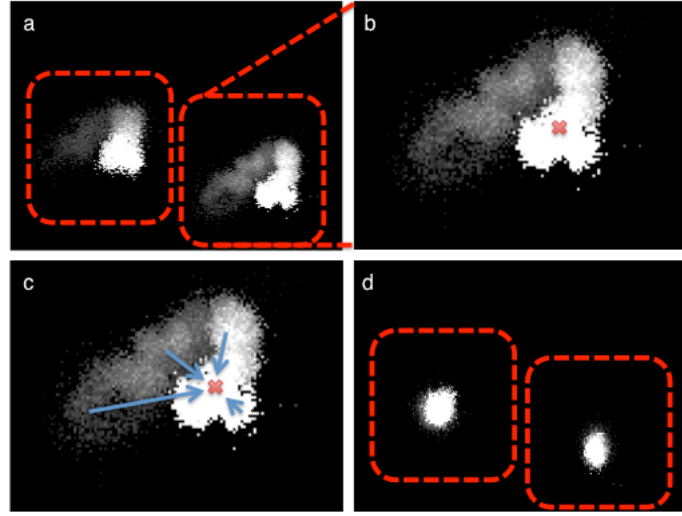


Figure 3.4. Drift correction with QuickPALM through the selection of individual spot clusters. **(a)** Identification and selection of individual spot clusters caused by the repetitive detection of beads or fluorophore clusters over time. **(b)** Calculation of the center of mass of the spot cluster. **(c)** Estimation of the displacement of each spot in regards to the cluster center. **(d)** Plot of the spot clusters after drift correction.

Drift correction is accomplished after the user has pre-defined one or more regions of interest around isolated spot clusters corresponding to either landmark beads added to the sample or individual molecules (Figure 3.4a). The algorithm then calculates the distribution center  $c_{r,w}$  in each axis (Figure 3.4b) for the selected clusters indexed by  $r$  ( $w$  represents either the  $x$ -,  $y$ - or  $z$ -axis):

$$c_{r,w} = \frac{\sum_t s_{r,t} w_{r,t}}{\sum_t s_{r,t}}$$

$$d_{w,t} = \sum_r s_{r,t} (c_{r,w} - w_{r,t}) / \sum_t s_{r,t}$$

where  $t$  is the time-point index for each detected spot within the cluster,  $s_{r,t}$  the intensity for that spot and  $w_{r,t}$  the localization of spot centre. The joint displacement between each element of the cluster and its centre is also calculated (Figure 3.4c) as  $d_{w,t}$ . Due to the possibility of missing detections, the displacement track  $d_{w,t}$  might not contain the displacement information for all time-points. In order to correct this, we

linearly interpolate the missing values and iteratively update both the cluster centers and displacements as follows:

$$\begin{aligned}\hat{c}_{r,w}^{i+1} &= \sum_t s_{r,t} (w_{r,t} + \hat{d}_{w,t}^i) / \sum_t s_{r,t} \\ \hat{d}_{w,t}^{i+1} &= \sum_r s_{r,t} (\hat{c}_{r,w}^{i+1} - w_{r,t} - \hat{d}_{w,t}^i) / \sum_r s_{r,t}\end{aligned}$$

where  $\hat{c}_{r,w}^{i+1}$  and  $\hat{d}_{w,t}^{i+1}$  are the corresponding cluster center and joint displacement estimations for the  $i$ -th iteration. The updates are performed until convergence is achieved. The particle position data is then corrected by subtracting the corresponding displacement value to each particle position (Figure 3.4d).

### 3.1.3 Results and discussion

PALM and STORM reconstruction algorithms usually rely on “fitting” Gaussian kernels to detected diffraction limited spots. Although permitting high accuracy localizations, these iterative methods can require up to several hours of processing time. We have developed a high-speed reconstruction algorithm that uses the classical Högbom CLEAN method (90) for spot finding, followed by a modified centre of mass algorithm to compute the spot position and parameters defining spot shape along the horizontal axes. These parameters allow not only precise 2D localization, but also extraction of the axial ( $Z$ ) coordinate for each spot when using an astigmatic lens (45) (see Figure 3.5).

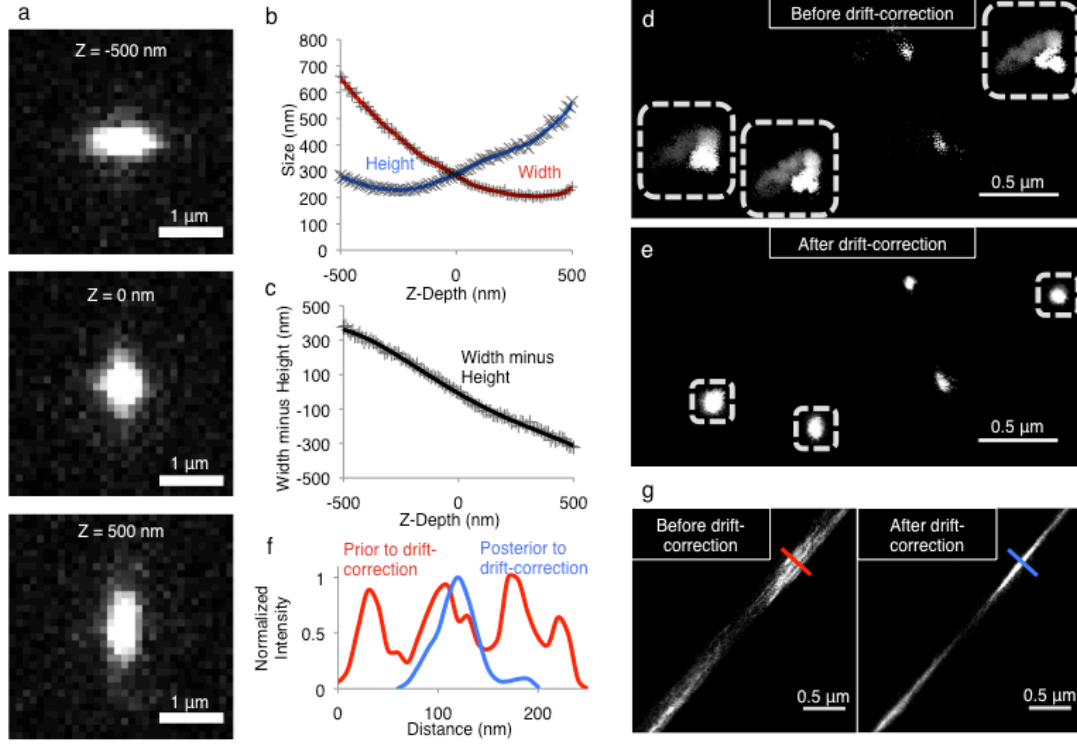


Figure 3.5. 3D localization and drift correction using QuickPALM. (a) Image sequence showing a single fiduciary sub-diffraction bead observed at different depths with an astigmatic configuration. Note the changes in the width to height ratio. (b) Measured width and height as a function of Z. Each data point represents the nine-point moving average from three beads. (c) Width minus height as a function of Z based on the values of (b); the black line shows a 4<sup>th</sup> order polynomial fit, which is used to extract the Z position of newly detected sub-diffraction spots. (d) Overlay of computed bead positions acquired during the image sequence showing lateral drift (dot brightness is proportional to the bead intensity, and decays over time due to photo-bleaching). (e) Same as (d) after drift-correction. (f,g) Drift effect on an image of microtubules creating the misleading appearance of multiple-filaments. (f) A line profile of the red and green cross-sections in (g) before (green) and after (red) drift-correction.



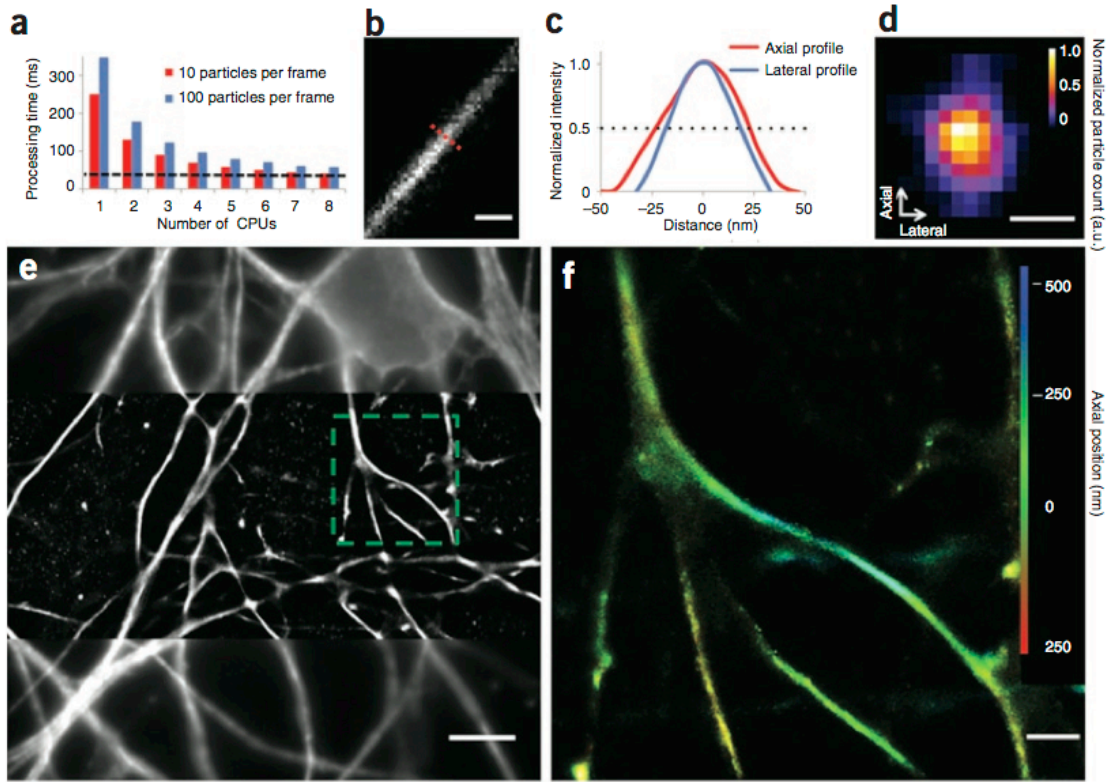


Figure 3.6. Three-dimensional dSTORM imaging of  $\beta$ -III-tubulin labelled microtubules in neuronal cells. **(a)** Performance of the complete algorithm analyzing a sequence of 512x512 images including image reading, peak search, localization and super-resolution image rendering in parallel - benchmarked on an Intel® Core 2 Quad 3.2 GHz personal computer. The segmented black line represents the 32 ms readout speed of the EMCCD camera (Andor® iXion-897). Note that this is the lower-bound frame-rate hard-limit imposed by the acquisition hardware itself. **(b)** Super-resolution reconstruction of a microtubule filament, scale bar equals 100 nm. **(c)** Intensity profile of the microtubule cross-section marked in red at **(b)** showing a 40 nm lateral and 50 nm axial full-width-half-maximum. **(d)** Particle distribution histogram of the marked cross-section in **(b)**, scale bar equals 50 nm. **(e)** The conventional wide-field epifluorescence image in the upper and lower horizontal bands. Middle band depicts the super-resolved reconstruction of the central portion of the same picture, scale bar equals 5  $\mu$ m. **(f)** 3D dSTORM image of the green inset in **(e)**, z-position is color-coded according to the color bar, scale bar equals 1  $\mu$ m.

A direct benefit of this method was our ability to achieve a typical processing time of 30-50ms per image with a very weak dependence on the number of spots per image (Figure 3.6), these values are of the same order as the common EM-CCD maximum

frame rates used in these techniques. Any drift on the microscope caused by vibrations or thermal dilation compromises resolution and can lead to artefacts in the reconstruction, such as the doubling of structures for sudden shifts (Figure 3.5f,g). To address this, QuickPALM can trace the movement of fiduciary landmarks such as beads imaged within the sample to estimate the drift in 2D or 3D and subtract it from particle positions (Figure 3.5d,e). Since fiduciary landmarks might not be detected throughout the entire image sequence because of blinking or photo-bleaching, we interpolated missing positions for each landmark (see section 2.1).

By combining QuickPALM with the  $\mu$ Manager (103) open source package for microscope hardware control and acquisition in tandem with a custom laser control system, we provide a full method for parallel acquisition and real-time visualization of PALM and STORM experiments.

To illustrate the potential of QuickPALM we observed microtubules in mouse neurons labelled with a primary anti-neuronal tubulin  $\beta$ -III antibody and a secondary Cy5 conjugated antibody (Figure 3.6b-f). dSTORM imaging (5, 6) was then used to collect 150,000 images, where the 635 nm laser was employed for excitation and the 488nm laser was pulsed at decreasing intervals for Cy5 fluorophore re-activation. A cylindrical lens was introduced at the position of the polarization slider (see Figure 3.1) to permit 3D probe localization (45). Using QuickPALM, we obtain real-time 3D reconstructions of microtubules with a resolution (as measured by the FWHM of an intensity profile across a microtubule) of 40 nm in X, Y and 50 nm in Z over a 1  $\mu$ m depth (see Figure 3.6b-f). With appropriate modifications to ensure precise alignment of differing colour channels, multi-colour PALM or STORM can be achieved by concurrently processing images from multiple colour channels.

### 3.1.4 Conclusions and outlook

During a typical image acquisition of 512x512 frames in a PALM/STORM experiment, the frame-rate hard-limit imposed by the readout speed of the camera, such as in the case of the EM-CCD technology, is on the order of 32ms. QuickPALM has a typical processing time of 30-50ms that may vary depending on the sample complexity and processing computer characteristics (Figure 3.6a). Notwithstanding, this standard processing speed allows real-time super-resolution image reconstruction,

albeit at a minor loss in localization accuracy compared to Gaussian fitting methods (45). In practice, our software automatically processes incoming low-resolution images streamed on the hard drive during image acquisition and accumulates the computed positions into a real-time super-resolution reconstruction. Without real-time reconstruction, imaging parameters such as activation/excitation intensities often need to be optimized by trial and error after multiple suboptimal experiments. Our method allows the dynamic inspection of sample behaviour and the adjustment of acquisition parameters “on the fly” for optimal imaging.

Real-time reconstruction and the integration of software for parallel processing and acquisition, in conjunction with an open source platform, allow super-resolution imaging modalities to be broadly adopted and extended. Since processing and reconstruction can occur in real-time and on a separate machines, data-driven decisions can be used in real-time to control actuators. For example, spatial light modulators could be used to locally optimize the activation laser power and ensure uniform blinking probabilities, thus minimizing acquisition time, as required for live super-resolution imaging (63, 68). In a further example, initial super-resolution images reconstructed from a limited number of frames may identify the presence of an event of interest and inform the decision to continue PALM/STORM imaging at this location with real-time visualization - or search for another region-of-interest. This would be an important feature to study events such as host-pathogen interactions in high-throughput screening approaches (67).

In summary, QuickPALM in conjunction with the acquisition control features mentioned above provides a complete solution for acquisition, reconstruction and visualization of 3D PALM/STORM images, achieving resolutions of ~40 nm in real-time. This software package should greatly facilitate the conversion of many laser excitation wide-field or TIRF microscopes into powerful super-resolution microscopes.



### **3.2 Blinkons: multi-colour tuneable photo-switchable fluorophores for super-resolution microscopy**

This section captions an unpublished original work and is under preparation to submission as an article in Nature Methods:

**Ricardo Henriques**, Mickael Lelek, Eugenio F Fornasiero, Flavia Valtorta, Christophe Zimmer & Musa M Mhlanga. Blinkons: multi-color tunable photo-switchable fluorophores for super-resolution microscopy, *in preparation*.

Similarly to section 3.1, results presented and discussed in this section are the product of collaborative work. R.H. planed the experiments, did all the experiments, wrote all the needed quantification software, analysed the data and wrote the full manuscript. M.L. was responsible by the assembly and optical setup used in this work (at Pasteur Institut, Paris). E.F.F. prepared and provided the labelled neuron cells. C.Z. has given invaluable insight and M.M.M. supervised the work.

#### **3.2.1 Introduction**

The recent emergence of the super-resolution fluorescence microscopy field has stimulated the birth of single-molecule localization microscopy (SMLM) techniques (67), such as Photo-Activated Light Microscopy (PALM) (43) and Stochastic Optical Resolution Microscopy (STORM) (5) that are able to detect a large population of individual fluorophores at the nanoscopic level. These techniques breach Rayleigh's classical resolution limit by cleverly circumventing the resolution barrier given by the diffraction limit of light. Traditionally, the maximum resolution of a microscope is calculated as the minimum distance at which two independent point sources of light can still be discriminated. This is approximately given by the emitted wavelength divided by twice the numerical aperture of the objective lens used (1). For most modern imaging microscopes this value is roughly in the order of 300 nm. The key to bypass this frontier lies in the principle of having only one active fluorophore within a diffraction-limited area in each instant of time. As such individual molecules at close

proximity but visible in independent moments can be discerned. However, this process can only be achieved if at least two conditions are met: the signal of an active fluorophore needs to be high enough to clearly allow the calculation of its centre with a high accuracy and fluorophores need to switch between a fluorescence emitting and non-emitting state to minimize the probability of two neighbouring particles being fluorescent in the same instant of time. These necessities have provoked a major effort to discover and develop bright and stable photo-switchable fluorophores as well as to coax the induction and modulation of photo-switchable properties of known fluorescent molecules. Synthetic dyes are a strong candidate for super-resolution probes due to their superior fluorescence in comparison to genetically encoded fluorescent proteins. Several methods have been discovered that improve their photo-switching characteristics, for example, by the use of photo-switching permissive buffers (56, 85, 89) and/or by creating probes featuring two fluorophores where one acts as a fluorescence activator and the counterpart as the photo-switchable fluorescent moiety (5). In this work we demonstrate that applying a hairpin oligonucleotide structure similar to that of molecular-beacons (108, 109) where a fluorophore and a high-efficiency (fluorescence) quencher are set on opposite ends of the oligo-nucleotide, can induce photo-switchable behaviour in classical synthetic dyes. We term this new class of probes “blinkons”. Furthermore, we show that the “blinking” dynamics of blinkons can be tuned by small changes in the hairpin design and can be modulated during imaging by either the light-excitation or the chemical environment. The blinkon conformation also improves the fluorescent dye resistance to permanent photo-bleaching, allowing their use for direct STORM (dSTORM) like experiments (6) without the need of special buffers such as the conventional oxygen-scavenger systems used in dSTORM. Overall, blinkons are invaluable tool to the super-resolution field as they provide a method to convert most synthetic dyes of any spectral colour into stable super-resolution probes.

### **3.2.1.1 Photodynamics of organic fluorophores**

Organic fluorophores may be described as planar highly delocalized  $\pi$ -electron systems with covalently coupled atoms which are conventionally carbon, oxygen and nitrogen. Electronic excitation is dependent on the number of associated delocalized

electrons and attached groups. The lowest energy transition is normally achieved by compatible photon stimulation in the UV or visible spectral range. The number of atoms in an individual fluorophore also induces the existence of extended degrees of freedom in the form of vibrational or rotational quantization of the single electronic state (*110*) (see Figure 3.7).

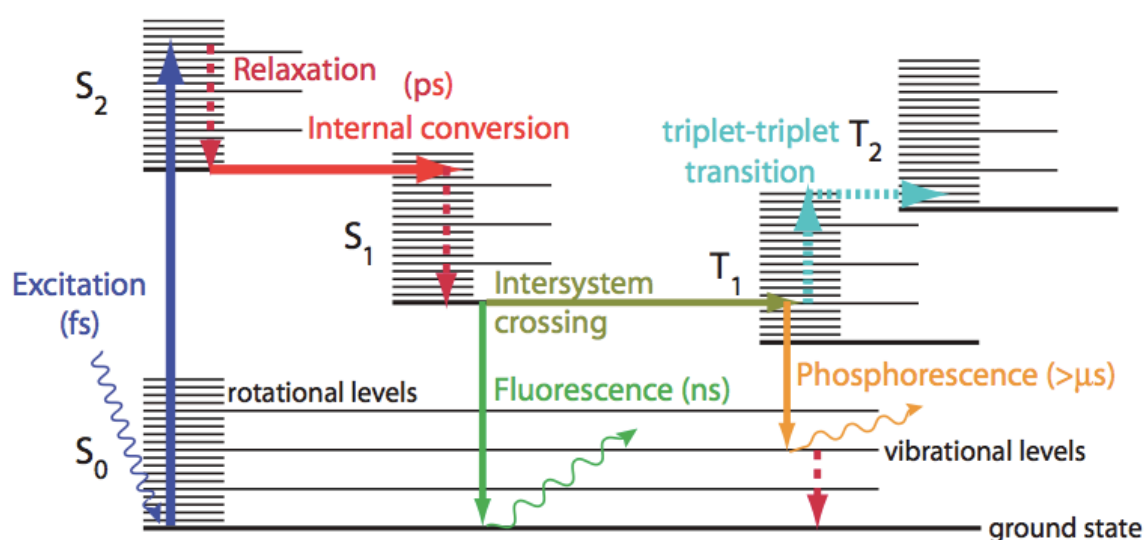


Figure 3.7. Excitation and emission of light by a fluorophore. The energy states of a fluorophore molecule are represented in this Jablonski diagram. The electronic levels are indicated by thick black horizontal lines whereas the vibration and rotational levels are represented by thinner horizontal lines. When a photon with the appropriate wavelength is absorbed by the molecule, it causes a transition to a high vibrational level of the excited electronic state  $S_2$  (dark blue arrows). The molecule then undergoes rotational and vibrational relaxations (dotted dark red arrows) and internal conversion (red arrow) before it reaches the lowest energy level of  $S_1$ . Transition to the ground state usually occurs via emission of a photon, by fluorescence (green arrows). Alternatively, the molecule might undergo intersystem crossing (brown arrow) and arrive at a triplet state, where it may cause phosphorescence emission (orange arrows) or triplet-triplet transitions (light blue arrows) that further delay the emission of light or prevent it altogether. Image from (*111*).

When a photon with a suited amount of energy is absorbed, an electron within the molecule is promoted into a higher excited state – the  $S_N$ -state – this energy is given

by the well known Planck's equation  $E = h \cdot c / \lambda$  where  $E$  is the photon energy,  $h$  the Planck's constant,  $c$  the speed of light in vacuum constant and  $\lambda$  the wavelength of the exciting photon. The energy exchanged between the photon and electron must be correspondent to the energetic difference between the  $S_N$ -state and  $S_0$ -state (ground state) and is typically in the range of 1-10 eV. The product of the absorption cross-section and the applied excitation intensity gives the excitation rate  $k_{exc}$ , for organic fluorophores it is typically in the order of  $10^7 \text{ s}^{-1}$  for a moderate excitation intensity ( $1 \text{ kW/cm}^2$ ). Once in an excited state, the molecule relaxes back to the first excited state  $S_I$  according to the Franck-Condon principle (112) with an internal conversion rate  $k_{Ic} < 10^{12} \text{ s}^{-1}$  (see Figure 3.7). A vibration relaxation follows pulling the electron into the vibrational ground state of  $S_I$  with a rate  $k_{Vib} < 10^{11} \text{ s}^{-1}$ . The electron can then return to the ground-state  $S_0$  by either: a non-radiative process with  $k_{Nr}$  between  $10^6 \text{ s}^{-1}$  and  $10^9 \text{ s}^{-1}$  (generally in an organic fluorophore); undergo a forbidden spin reversion into the triplet state  $T_I$  with  $k_{Isc}$  in the range of  $10^5$  to  $10^{11} \text{ s}^{-1}$  followed by a reverse intersystem crossing with  $K_T$  in the order of  $10^6$  to  $10^{-4} \text{ s}^{-1}$ ; emitting a fluorescence photon with  $k_{Fl}$  in the order of  $10^6$  to  $10^9 \text{ s}^{-1}$  (113). The quantum yield of a fluorophore describes the probability that upon the absorption of an exciting photon a fluorescent photon will be generated and is described as  $\phi_{Fl} = k_{Fl} / (k_{Fl} + k_{Nr} + k_{Isc})$ . Good fluorophores should present both a high quantum yield and absorption cross-section. Normally the emitted fluorescence photons obey the Stokes-shift by shifting to the less energetic higher wavelengths in comparisons to the exciting photon, as a portion of the excitation energy was lost in the vibration relaxation of the molecule. A single fluorophore can only emit a single photon per cycle, notwithstanding, an organic dye will generally be able to cycle millions of times generating a significant amount of photons until arrested by an irreversible reaction – also known as irreversible bleaching. The probability of irreversible bleaching is proportional to the amount of time a fluorophore spends in the highly reactive excited states. While the singlet state  $S_I$  has a small lifetime in the order of nanoseconds, the triplet state  $T_I$  on the other hand can last up to several milliseconds – see  $k_{Isc}$  above. On the event of a  $T_I$  promotion the fluorophore becomes dark until ground state relaxation is achieved, during this period the fluorophore is particularly sensitive to reactions, such as with oxygen – a natural triplet ground state molecule (114).



### **3.2.1.2 Fluorescence quenching**

Fluorescence quenching represents the realm of effects that can reduce the intensity of fluorescence emission by a given fluorophore. Quenching can be caused by solvents or quenching moieties directly attached to the molecular structure supporting the fluorophore, being highly dependent on the proximity between the quencher and fluorescent core. Several processes can lead to quenching, such as: excited state reactions, fluorescent resonant energy transfer, contact quenching and collisional quenching.

### **3.2.1.3 Fluorescent Resonance Energy Transfer**

One of the best understood and explored mechanism of quenching is fluorescent resonance energy transfer (FRET) or Förster energy transfer (*115*). In this process the energy of the excited state of a fluorophore (the “donor”) is transmitted into another molecule (the “acceptor”), relaxing the donor into the ground state without emission while the acceptor is promoted into a higher energy level of singlet state. For FRET to occur the fluorescence emission of the donor must overlap the absorption spectra of the acceptor, which in turn may or may-not be a fluorescent molecule. If the acceptor is fluorescent then the relaxation of the transferred energy can be done by emitting a fluorescence photon with the spectral emission characteristics of the acceptor – typically with a higher wavelength than that of the donor fluorescence emission. FRET efficiency is dependent on both the dipole orientation between the donor-acceptor pair and their spatial separation that should be in the 10 to 100 ångström range (*116, 117*) – roughly the distance between 3 and 30 nucleotides of a DNA oligomer (*118*).

### **3.2.1.4 Contact Quenching**

Also known as “static quenching” or “ground state complex formation” contact quenching is formed through the establishment of a non-radiative complex between two fluorophores or a fluorophore and a non-fluorescent molecule. The pair interacts by proton-coupled electron transfer via the formation of hydrogen bonds and when

absorption of light occurs then relaxation to the ground state immediately takes place and no fluorescent light is emitted. As a result of contact quenching, the complex absorption spectra is shifted, a feature that does not occur in FRET (118).

### **3.2.1.5 Collisional Quenching**

Also named “dynamic quenching” it occurs when an excited fluorophore is pushed into the ground state by contact with another molecule in the solution. Contact induces a return to the ground state with fluorescence photon emission. Oxygen, halogens and amines are known collision quenchers. For example, ethidium bromide becomes fluorescent when intercalated with double-stranded DNA (dsDNA) since it is protected from oxygen quenching, in comparison ethidium bromide is naturally quenched when in solution due to the direct access to oxygen (118).

### **3.2.1.6 Molecular-beacons**

Molecular beacons (MBs) are a class of oligo-nucleotide probes able to fluoresce in the presence of a specific RNA or DNA target. MBs work as fluorescent switches and by default are in a non-emitting (“OFF”) state. This non-emitting state is obtained due to their hairpin structure composed of a stem and a loop. The stem consists of a double-stranded region, often 5 to 6 nucleotides long, in which a fluorophore and a quencher are kept in close proximity preventing the fluorophore from emitting a signal due to resonant energy transfer and contact quenching. The loop section is generally 15-30 nucleotides long and is complementary to a target sequence of a desired nucleic acid. The hybridization of this single stranded region with the target sequence leads to the denaturation of the stem portion, locally separating the fluorophore and quencher moiety inducing a fluorescence permissive (“ON”) state (108, 109) (see Figure 3.8).

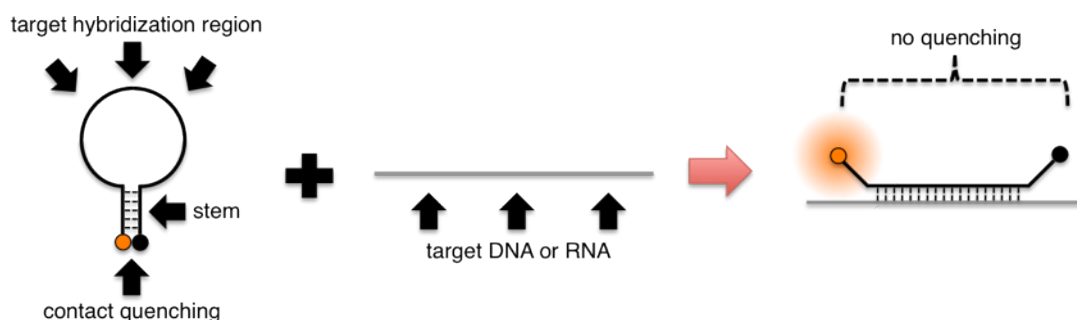


Figure 3.8. Schematic overview of molecular beacons conformational change upon hybridization.

### 3.2.1.7 Blinkons: photo-switchable molecular-beacons

In the absence of a hybridization target, several factors can still influence the stability of the stem hybrid. Temperature, light and reagent solutions can lead to a transient opening of the MB producing a fluorescence burst for the period up until the stem is able to re-establish a double-stranded structure. In the following section we will explore and characterize methods to take advantage of this feature in order to provide desirable stochastic photo-switchable properties to MB-like structures.

### **3.2.2 Material and Methods**

In this section we provide an overview of the experimental preparation procedures, imaging apparatus and analysis methods used to study the photodynamic behaviour of blinkons at the single-molecule level and its application to super-resolution imaging.

#### **3.2.2.1 Probe design and synthesis**

Blinkon design was based upon a molecular-beacon structure modified to hold a biotinylated thymine base in the centre of the hairpin loop. The introduction of this specific modification permits the attachment of the molecular structure to streptavidin coated coverslips for single-molecule imaging or streptavidin conjugated labelling agents (e.g. antibodies, phalloidin eg.) for cell imaging. Generally MBs are designed to hybridize and label a specific RNA or DNA target, in contrast, the blinkons are designed to explore the natural stochastic melting of the stem portion as a source of photo-switching behaviour. As such, blinkon oligo-nucleotide sequences are selected in a slightly different manner than conventional MBs sequences. To prevent unwanted secondary structures and to minimize any undesirable interactions with other oligo-nucleotides, the loop section is set to be a repeating thymine sequence.

Candidate blinkons for characterization were designed by incrementally changing the size of the loop and stem section and appending both a 5' Black Hole Quencher 2 (BHQ2) moiety and a 3' organic dye fluorophore - either Alexa488 or Cy3 (see Table 3.1 and Figure 3.9). 2'-O-methyl bases were used to render probes resistant to nuclease degradation. This permits their use in living cells and other applications where nucleases are present.

Oligo label	Sequence	Stem $T_m$ (°C)
B3S9L	<u>GCG</u> TTT TTT TTT <u>CGC</u>	44.8
B5S9L	<u>TAGCG</u> TTT TTT TTT <u>CGCTA</u>	54.5
B10S9L	<u>AGCTTAGCGA</u> TTT TTT TTT <u>TCGCTAAGCT</u>	71.9
B3S19L	<u>GCG</u> TTTTT TTT TTT TTT TTTTT <u>CGC</u>	36.4
B5S19L	<u>TAGCG</u> TTTTT TTT TTT TTT TTTTT <u>CGCTA</u>	53.5
B10S19L	<u>AGCTTAGCGA</u> TTTTT TTT TTT TTT TTTTT <u>TCGCTAAGCT</u>	70
B3S39L	<u>GCG</u> TTTTT TTTTT TTTTT TTT TTT TTT TTTTT TTTTT TTTTT <u>CGC</u>	20.1
B5S39L	<u>TAGCG</u> TTTTT TTTTT TTTTT TTT TTT TTT TTTTT TTTTT TTTTT <u>CGCTA</u>	41.1
B10S39L	<u>AGCTTAGCGA</u> TTTTT TTTTT TTTTT TTT TTT TTT TTTTT TTTTT TTTTT <u>TCGCTAAGCT</u>	61.3

Table 3.1. Synthesized blinkon sequences. Underlined portion demarkcates the stem sequence and the bold T represents a biotinylated thymine base. Blinkon structure and stem melting temperature (Stem  $T_m$ ) predicted using mFOLD (119).

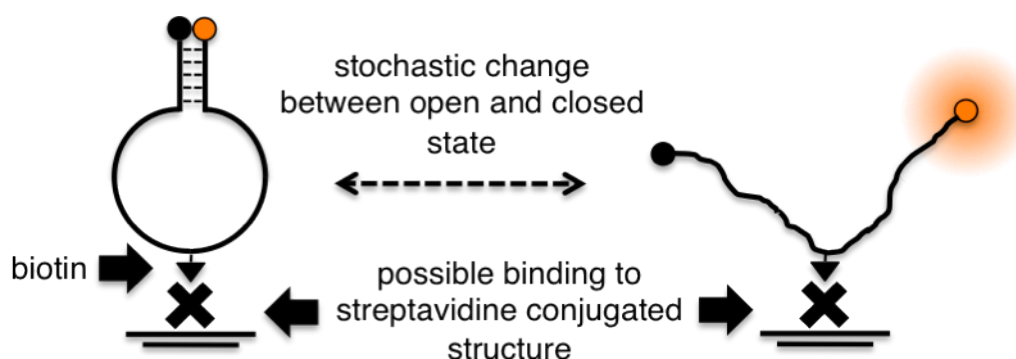


Figure 3.9. Blinkon structure and stochastic conformation change.

Blinkons synthesis was carried out by C. Gouyette at the Plate-forme Synthèse d'Oligonucléotides Longs à Haut Débit (Institut Pasteur, Paris). All oligo-nucleotides containing both a fluorophore and a quencher were purified by high-pressure liquid chromatography (HPLC). After synthesis and purification blinkons were dissolved at a concentration of  $\sim 100 \mu\text{M}$  in TE buffer (10 mM Tris-HCL, 1 mM EDTA, pH 7.5) and stored at  $-20^\circ\text{C}$ , shielded from light sources.

### 3.2.2.2 Coverslip cleaning

Coverslips were cleaned as thoroughly as possible. Debris present on the coverslips is often excited by the used lasers, and contributes either to elevated background counts in each frame or as sources of unwanted single-molecule fluorescence. Coverslips were cleaned with acetone (spectroscopic grade, *Sigma*) followed by methanol (spectroscopic grade, *Sigma*) and rinsed with distilled water milliQ. Coverslips were then sonicated in KOH 1 M for 45 minutes and then for 20 minutes in distilled water milliQ. Finally they are stored in a sterile container with distilled water milliQ, which was sealed with parafilm.

### 3.2.2.3 Single-molecule characterization within a flow-cell

The observation of a large molecular ensemble yields the average behaviour of its components. Yet, the capacity to resolve and discriminate individual molecules provides a deeper understanding of the heterogeneity in the population, thus revealing fine details in its elements such as fluctuations and stochasticity. Only then is it possible to truly understand that within the average behaviour exists a true distribution which can be of a Gaussian or even a power-law, in nature.. In pursuit of this goal we have decided to use flow-cells with streptavidin coated coverslips, acting as a controllable immobilization system, where a small number of probes could be deposited and analysed at the single-molecule level. This approach presents several advantages: the usage of a reduced amount of reagents, the possibility to locally pre-bleach any unwanted fluorescence source before the introduction of the blinkon probes and the tight control of the thermal and aqueous environment subjected to the probes.

Blinkons in contact with the streptavidin coating become highly-immobile as the receptor-ligand biotin-streptavidin coupling has one of the highest association constant known for biological molecules, with a  $K_A = 10^{15} \text{ M}^{-1}$ .

### 3.2.2.4 Creating the flow-cell system

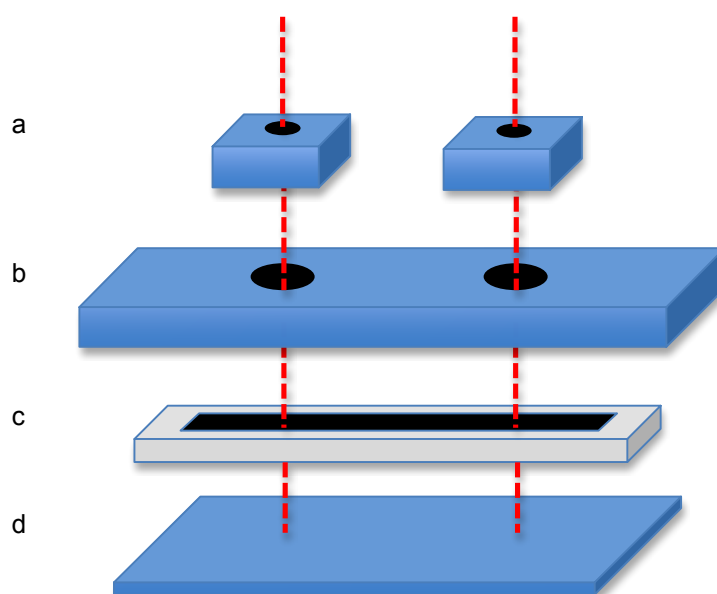


Figure 3.10. Schematic representation of the flow-cell assembly. The flow-cell is composed by: (a) PDMS blocks with a cylindrical perforation in the interior, (b) glass-slide with two perforations, (c) parafilm with a rectangular cut in the centre and (d) glass coverslip.

In order to immobilize the blinkon probes in space and to fully control their aqueous environment we have created a re-usable home-built flow-cell system. In essence, two perforations in a microscopy glass-slide are made 15 mm apart. In parallel two small polydimethylsiloxane (PDMS) blocks of  $1 \text{ cm}^3$  with a cylindrical cavity in their centre are prepared. By exposing both the PDMS blocks and glass-slide to an oxygen plasma for 15 min through a Plasma Cleaner system (Plasma Cleaner, *Harrick*) both the surface of the PDMS and glass become sticky to each other. This occurs due to the oxidation of the surfaces of the PDMS and production of Si-OH groups analogues to the ones present in the glass. The PDMS and slide become strongly attached due to the formation of hydrogen bounds. Next, we cut a small parafilm strip with

dimensions equal to the coverslip to be used and make an internal cut of 2x20 mm. The parafilm is deposited directly between the coverslip and glass-slide and heated to 50 °C just until becoming transparent (typically less than 30 seconds). The parafilm melting leads to its adherence to both the glass-slide and coverslip. The parafilm also acts as a spacer that will contain the aqueous medium surrounding the probes (see Figure 3.10).

To re-use the flow-cell the parafilm and coverslip are removed by heating to 50 °C. After cleaning with ethanol the upper part of the flow-cell can be reapplied to new parafilm and coverslips.

### 3.2.2.5 Generating a streptavidin coated coverslip

Glass coverslips were silanized with 0.1% v/v aminopropyl-triethoxysilane (*Sigma Chemical*) in acidic ethanol and then assembled into the flow-cell, as described above. To generate a streptavidin coated coverslip we introduced a biotinylated blocking reagent (1 mg/ml) in the flow cell for 10 minutes. The biotinylated blocking reagent was prepared through reaction of 2 µl of Sulfo-NHS-LC-LC-Biotin (*Pierce*) at 100 mg/ml in DMSO with 200 µl of 2 mg/ml Blocking Reagent (*Roche Diagnostics*) in PIPES 20mM, NaCl 100 mM, pH 6.8. A second incubation with 0.1 mg/ml streptavidin in PIPES 20 mM, pH 6.8 was performed for 10 minutes (*120*).

### 3.2.2.6 Probe fixation within the flow-cell

In order to correctly analyse our probes at the single-molecule level it is necessary to immobilize a small enough concentration within the imaging area that covers a 54 µm<sup>2</sup> portion of the coverslip surface. We randomly targeted 100-500 probes to this field – a low enough number that minimalizes the probability of probes overlapping within a sub-diffraction area and thus prevents a complexity increase in the single-molecule identification. We have observed that for such a low number of probes the coverslip cleaning protocol is not robust enough to remove all unwanted fluorescent debris. Therefore, after conjugating streptavidin to the coverslip and assembling the flow cell we perform a light-induced bleaching. With the flow-cell set on the microscope we choose and register 6 positions in x-y space (correspond to the



same positions to be used later for the probe imaging) using the microscope stage. We then irradiated each position for 20 minutes with either the 561 nm laser ( $2.4 \text{ kW/cm}^2$ ) or 488 nm laser ( $2.7 \text{ kW/cm}^2$ ) at full power depending on whether we would visualize a Cy3-BHQ2 or Alexa488-BHQ2 blinkon. After this process, residual fluorescence with emission between 590-625 nm or 500-550 nm (corresponding to our emission filters) is at a minimum while the biotin-streptavidin binding efficiency appears unaffected. We then added fiduciary sub-diffraction beads (TetraSpeck™ microspheres,  $0.1 \text{ }\mu\text{m}$ , fluorescent blue/green/orange/dark red, *Invitrogen*) diluted  $10^6$  in PBS to the flow cell that serve as landmarks for drift calculation and correction during image acquisition. When in PBS these beads will become hydrophobic and stably attach to the coverslip. We allowed the beads to settle for 5 minutes and then flowed PBS within the flow-cell to clean any unattached beads and to prepare the blinkon probes for insertion. Finally,  $3 \text{ pg}/\mu\text{l}$  of blinkon probes in beacon-buffer are injected into the flow-cell and allowed to incubate for 5 minutes. The interior of the flow-cell is then rinsed with PBS to remove probes not bound to the coverslip surface.

### 3.2.2.7 Total-internal Reflection Microscopy

In order to characterize the photodynamics of the designed blinkons at the single-molecule level we have chosen to use a total-internal reflection fluorescence microscopy (TIRFM) system. This method is similar to wide-field epifluorescence in the sense that the full field of view is illuminated simultaneously and data can be acquired by the use of a sensitive camera. The main difference comes from the formation of an evanescent field that constrains the fluorescence excitation to a depth range of around 200 nm directly over the coverslip surface. . Moreover, the evanescent field decays exponentially with increasing distance from this surface. This feature is of great advantage in contrast to normal epifluorescence due to the low background and increased signal.

### Principles of TIRFM

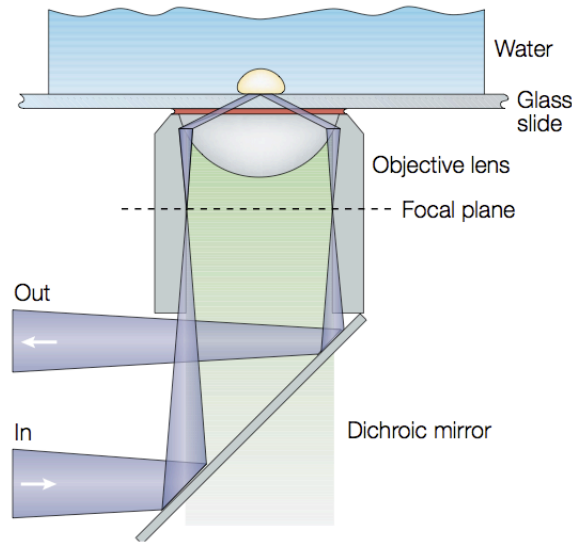


Figure 3.11. Schematic drawing of the TIRFM illumination and optics. Image adapted from Steyer *et al.* (121).

The evanescent wave is produced when light rays are totally reflected by the surface of the coverslide (*ergo* the name “total-internal reflection”) due to a high incident angle. This angle, also known as the critical angle, is achieved by focusing the excitation illumination in the edges of the back focal plane of the objective (see Figure 3.11) and can be described by  $\theta_c = \arcsin(n_2/n_1)$  where  $n_2$  is the refractive index of the sample medium and  $n_1$  the refractive index of the coverslip. Current microscopy setups can only achieve total-internal reflection if  $n_2$  is similar to water and for objectives whose numerical aperture is higher than 1.4. The resulting evanescent field has an intensity that can be described by  $I(z) = I_0 \exp(-z/\delta)$  where  $\delta$  is given by  $\delta = \lambda / [4\pi (n_1^2 \sin^2(\theta) - n_2^2)^{0.5}]$  (see Figure 3.12) (121).

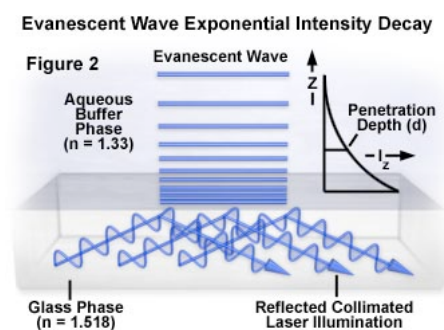


Figure 3.12. Schematic of an evanescence wave as generated over a glass surface. Figure from <http://www.olympusmicro.com/primer>.

### 3.2.2.8 Experimental setup

Fluorescent imaging was performed on a Nikon Ti-E eclipse working in TIRF configuration for the single-molecule flow-cell studies or wide-field configuration for cell imaging. An oil-immersion objective (CFI Apochromat, 100x, NA 1.49, Nikon) was used. Five continuous-wave laser beams: 405nm and 635nm diode laser (Spectra physics) and a 488nm, 532 nm, 561nm solid-state laser (Spectra Physics) were selected by an acousto-optic tunable filter (AOTF-AA optoelectronic). The laser beams were coupled into the microscope objective by 3 dichroic filters. Fluorescent light was spectrally filtered using filters and imaged on an EM-CCD camera (Andor Ixon DU-897E-CS0-BV). Additional lenses were used to achieve a final imaging magnification of 100 to 150x (i.e. a pixel size from 160 to 106nm). The laser powers were chosen to ensure that the fraction of activated fluorophores at any given time was sufficiently low to allow the detection and localization of individual fluorophores. For TIRFM microscopy the laser position was set to focus on the edges of the back focal plane of the imaging objective generating the needed evanescent wave. For more information refer to the optical setup described in section 2.1.

### 3.2.2.9 Photo-switching analysis

After the establishment of the evanescence field and the addition of fiduciary fluorescence beads, the image acquisition was performed over the full field of view

(512x512 pixels) of an EM-CCD camera running at 30 Hz for 10-minutes, generating around 18.000 images per dataset. As a post-processing step, a maximum intensity projection (MIP) of the dataset is created allowing for the identification of the probes that have undergone a fluorescent emitting state throughout the acquisition and also giving an assessment of the sample drift that has occurred. Regions-of-interest (ROI) of 9x9 pixels within the dataset were then selected where individual probes are observed. We considered individual probes spots that present gaussian-shape and full-width-half-maximum (FWHM) within the range of that predicted for a single-fluorophore observed within our imaging apparatus ( $\sim 380$  nm). The concentration of probes bound to the coverslip is low enough (generally less than 100 spots visible on the MIP) such that the majority of the observed population presents single-molecule characteristics (see figure Figure 3.13).

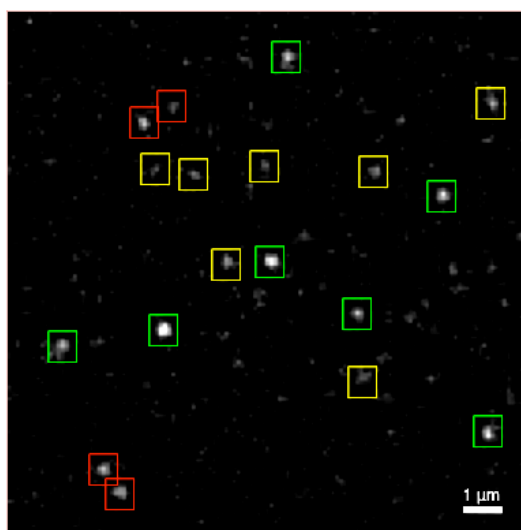


Figure 3.13. Particle detection and region-of-interest (ROI) selection in the maximum intensity projection. Red ROIs are discarded due to particle proximity and possible overlapping. Yellow ROIs represent particles whose full-width-half-maximum or shape is not within that expected for a sub-diffraction spot. Green ROIs represent regions accepted for analysis.

Intensity time-tracks are then generated for each ROI by integrating the 9x9 pixel signal for each frame over time. The photo-switching is identified by considering transitions that are 5-fold above the background noise standard deviation. The distribution of the ON-times and OFF-times can then be calculated for a large

population of probes as well as the number of switching cycles occurred within the acquisition time-range.

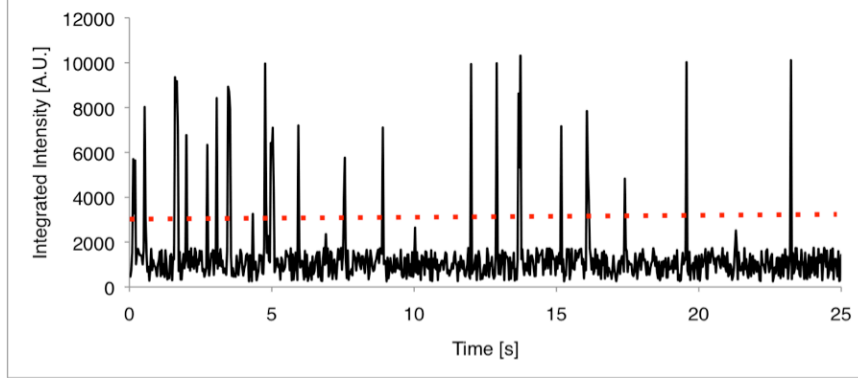


Figure 3.14. Example transient photo-switching for a single-blinkon probe (B5S9L). Red line represents the state-switch threshold.

### 3.2.2.10 Photon-count estimation

To estimate the photon count for a given dataset we have first studied the transfer function responsible for converting incoming photons on the detector into gray levels obtained with our EM-CCD camera. Assuming that the camera noise follows Poisson distribution, as such the number of photons measured during a time interval should follow:

$$P(N_p; N) = \frac{e^{-N} \times N^{N_p}}{N_p!}$$

where  $N$  is the real expected photon number. We can then write  $N = \overline{N_p}$  where  $\overline{N_p}$  is the average photons corrupted by Poisson noise. In a Poisson distribution the expected value is equal to the variance:

$$\overline{N_p} = \text{var } N_p = \sigma_{N_p}^2$$

For a detector following a linear gain such as an EM-CCD camera, the transfer function that yields the gray levels  $b$  can be described as:

$$b = G \times N_p + B$$

where  $G$  is the gain and  $B$  the offset – note that these values are dependent on the set camera properties (such as EM-gain and pre-amplifier gain). From here we can infer:

$$\text{var } b = \sigma_b^2 = \frac{1}{n} \sum (b - \bar{b})^2 = \frac{G^2}{n} \times \sum (N_p - \bar{N}_p)^2 = G^2 \times \text{var } N_p = G^2 \times \bar{N}_p$$

$$\text{var } b = G \times (\bar{b} - B)$$

where  $n$  is the sample size used to compute the variance and average photon value. As we have a linear relationship between the variance of the gray values and their mean value, we can fit this relationship and extract both  $G$  and  $B$  from it. We then acquired a set of images featuring fluorescent beads, the camera was set with the same conditions used for single-molecule detection and datasets of 100 frames were acquired with 10 ms to 150 ms exposure time with increments of 10 ms. We then selected pixels within the visual beads outline and calculated both the mean intensity for each individual pixel and corresponding variance (see Figure 3.15).

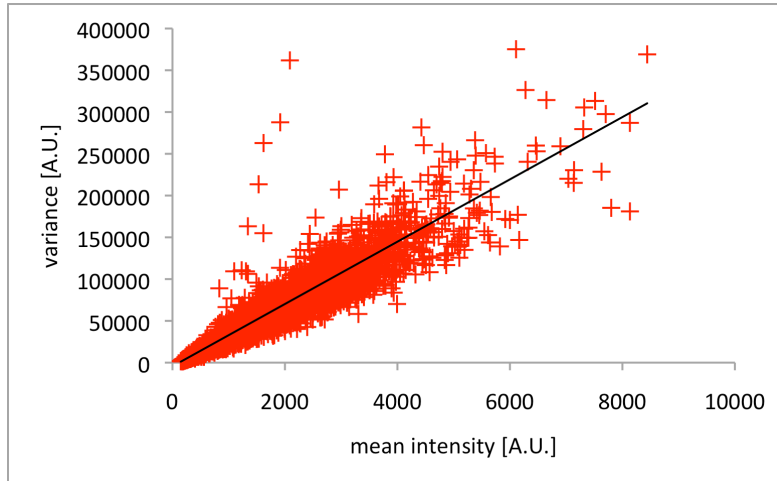


Figure 3.15. Mean pixel intensity vs. variance. The black line corresponds to a linear fit of the data and allows retrieving the camera gain and bias.

Fitting yields a camera gain and offset of 37 and 118. We henceforth used these values to estimate the conversion of image gray levels into photon count.

### **3.2.2.11 Super-resolution microscopy**

For a demonstration of blinkon efficiency in cell labelling we decided to use a similar strategy as described in section 3.1.2 by labelling tubulin with a neuronal beta-III antibody. The protocol diverges at the point where to demonstrate blinkon labelling we use a streptavidin conjugation kit (Lightning-Link Streptavidin Antibody Labelling Kit, Novus Biologicals) with a primary antibody and skipped the use of a secondary antibody. The detailed conjugation protocol used can be viewed in <http://www.novusbio.com/support/protocols/lightning-link-streptavidin-conjugation-kit-protocol.html>. After preparation of the streptavidin conjugated primary antibody, the biotinylated oligo-nucleotides were mixed at a concentration of ~100 units per antibody and incubated overnight.

Neurons were fixed for 15 minutes at room temperature (RT) with 4% paraformaldehyde, 4% sucrose in 120 mM sodium phosphate buffer (pH 7.4) supplemented with 2 mM EGTA. After fixation, cells were washed in PBS for 30 min and incubated with a anti-neuronal tubulin beta-III antibody (Covance, United Kingdom) diluted 1:100 in goat serum buffer (450 mM NaCl, 20 mM phosphate buffer, 15% goat serum, and 0.3% Triton X-100) for 2h at RT. Upon primary antibody incubation, cells were washed in PBS for 30 min. As a control step we also incubated cells with a primary antibody that has not been conjugated to streptavidin plus blinkons and consequently used a Cy3 conjugated donkey anti-rabbit antibody (Jackson ImmunoResearch, West Grove PA), this secondary antibody was incubated for 1h at RT. Fluorescent beads (100nm diameter) of a similar emission wavelength, were mounted with the sample as fiduciary landmarks.

dSTORM imaging (5, 6) was used to collect 150,000 images. The 561 nm laser was employed to observe the Cy3 labelling from blinkons, control oligonucleotides or a secondary antibody.

### **3.2.3 Results and discussion**

SMLM techniques intended for the detection of large population of molecules such as PALM and STORM require a firm control over the photo-switchable properties of fluorophores. In each acquired image, the visible spatial overlap of individual fluorophores needs to be minimized while keeping a sufficiently high number of fluorophores detectable in each frame in order to prevent the need to accumulate an excessively large amount of images to have a sufficient population of detected molecules. Each individual active fluorophore needs to yield a high amount of photons while in the ON-state to allow its precise localization, and when in the OFF-state photon-emission needs to be kept at a minimum or be non-existing. Optimally fluorophores should have ON-state periods smaller than the exposure time of individual frames to prevent the appearance of the same particle for more than two consecutive frames. The desired OFF-state is dependent on the population density of fluorophores to be detected. Short OFF-states will lead to undesirable particle overlaps in tightly packed regions. Fluorophores able to cycle multiple times between fluorescent switching states have both advantages and disadvantages. The advantages are the ability to detect the same fluorophore multiple times therefore both increasing image contrast and the possibility that each fluorophore will be detected at least once. However, the disadvantages are that it prevents one from inferring the number of detected molecules as it is not possible to identify from which fluorophore a “blink” originates (unless the labelling is extremely sparse) and also extends the chance of overlaps.

In this section we will explore how the photo-switching behaviour of blinkons can be characterized and modulated. We will also show its application by demonstrating super-resolution imaging with blinkons and the main advantages regarding other photo-switching probes or processes.



### **3.2.3.1 The molecular-beacons photo-switching discovery**

Our initial aim was to study the possibility of modifying MBs to infer photo-activatable properties similar to the ones described by Bates et al. (53) for the STORM technique. For this purpose, we initially designed MBs containing a Cy3-Cy5 pair (see Figure 3.16a, first generation MBs).

By quenching the Cy3 moiety with a BHQ2 we expected to disable the Cy5-activator effect of Cy3 while the MB was closed and allow it to fluoresce when the MB would open due to hybridization with a target oligo-nucleotide sequence.

A biotinylated thymine was inserted on the stem of the MB in order to fix it on a coverslip containing streptavidine for single-molecule imaging and characterization (see Table 3.2). During our test studies we looked at the quenching efficiency of Cy3 and observed sporadic transient photon bursts of the probes (putatively in a “closed” non-emitting state) in the absence of a hybridization oligo-nucleotide target (that otherwise would “open” the MBs).

This led us to believe that the insertion of the biotin attached to a single oligo-nucleotide on the stem could result in its unstable hybridization and therefore inefficient quenching. This steered us to design a second generation of probes (see Figure 3.16b and Table 3.2) where the biotin was moved to the centre of the loop section of the molecule but again the Cy3 moiety showed transient blinking.

This motivated us to explore this transient blinking effect due to its potential also for super-resolution imaging. After testing several probe configurations we have designed the final candidates shown in Table 3.1. In the final blinkon configurations we kept the biotin on the loop centre and designed the loop portion as a repetitive thymine sequence, which has minimal disruptive interference with the stem hybridization.

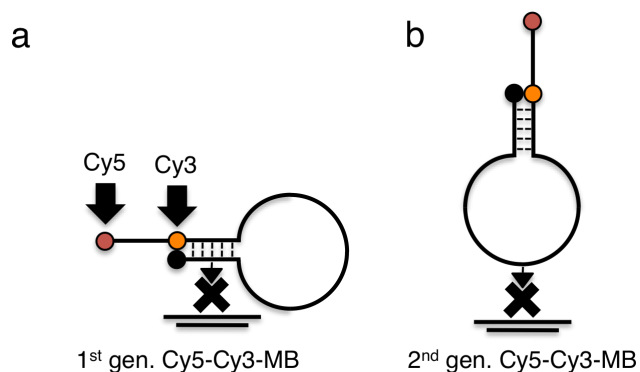


Figure 3.16. Schematic structure of the initially designed Cy5-Cy3-MB probes (1<sup>st</sup> and 2<sup>nd</sup> generations) for STORM imaging.

Oligo label	Sequence
1 <sup>st</sup> gen. Cy5- Cy3-MB	Cy5-TTT TTT TTT-Cy3- <u>CGACG</u> ACT TGC AGC TTT TGG GCT TTG ACA CCT CGC <u>CGTCG</u> -BHQ2
2 <sup>nd</sup> gen. Cy5- Cy3-MB	Cy5-TTT TTT TTT-Cy3- <u>GCTGC</u> CGC TCC ACA GTT TCG GGT TTT CGA CGT TCA <u>GCAGC</u> -BHQ2

Table 3.2. Sequence for the initial designed Cy5-Cy3-MB probes (1<sup>st</sup> and 2<sup>nd</sup> generations) for STORM imaging. Underline portion demarks the stem sequence, bold T represents a biotinylated thymine base.

### 3.2.3.2 Single-molecule characterization of the Blinkon probes

Most imaging applications taking advantage of the photo-switching of (conventional) synthetic fluorophores such as dSTORM, ground state depletion microscopy followed by individual molecule return (GSDIM) (56), and blinking microscopy (122) rely on the transient “switch-OFF” of the fluorophores by depleting their ground state and transiently pushing them to a dark triplet state. Although, the great majority of the fluorophores are in an actively fluorescent state at the beginning of the imaging procedure, the continuous excitation subsequently inactivates this population. However, this generally entails the use of an embedding medium with low oxygen

concentration, mobility or the presence of reducing and/or oxidizing reagents (6, 56, 122, 123). The latter requirement comes from the need to lessen the probability of irreversible bleaching caused by the high reactivity of the relatively long-lived triplet state. Therefore, the use of enzymatic oxygen-scavenging mediums has become highly popular in these applications but at the cost of a high toxicity, which renders the field of super-resolution using organic dyes largely unavailable to live-cell imaging.

Taking this into consideration, we decided to exploit a secondary method to induce an OFF-state non-dependent on transit to the triple-state of the blinkons fluorophores. By benefiting from the transient interactions of the quencher and fluorophore we could exploit this photo-switching behaviour thereby reducing sensitivity to permanent bleaching. Several buffers have been described for molecular-beacon usage (124) including the use of phosphate-buffered saline (PBS) based mediums (125). In our studies we observed the blinkon behaviour both under normal PBS at room temperature and sequentially at two different excitation powers. Each blinkon was imaged in a newly prepared flow cell twice. Six imaging areas were selected per flow cell and pre-bleached before blinkon binding to the coverslip. As result we obtained intensity time-tracks for the blinkons immobilized in the flow-cell. The analysis of 350 to 600 intensity-over-time tracks for each blinkon type allowed us to register the ON-state and OFF-state durations for each individual particle as well as the number of cycles (number of observed ON-state switches), the photon output per ON-state and the integrated photon output for the duration of the imaging procedure for each field (approximately 10 minutes). Figure 3.17, Figure 3.18, Figure 3.19 and Figure 3.20 demonstrate the averaged values in relation to the designed blinkon structure. We first observed that both altering the number of base pairs on the stem portion or nucleotides in the loop severely changes the photodynamic behaviour of the probes. In contrast, the behaviour of the same beacon structure with different fluorophores (Alexa488 and Cy3 in this case) shows little divergence. The Alexa488 based blinkons present roughly a 25% increase in the ON-state interval, 4% in the OFF-state interval and 40% on the number of cycles when compared to the Cy3 equivalent.

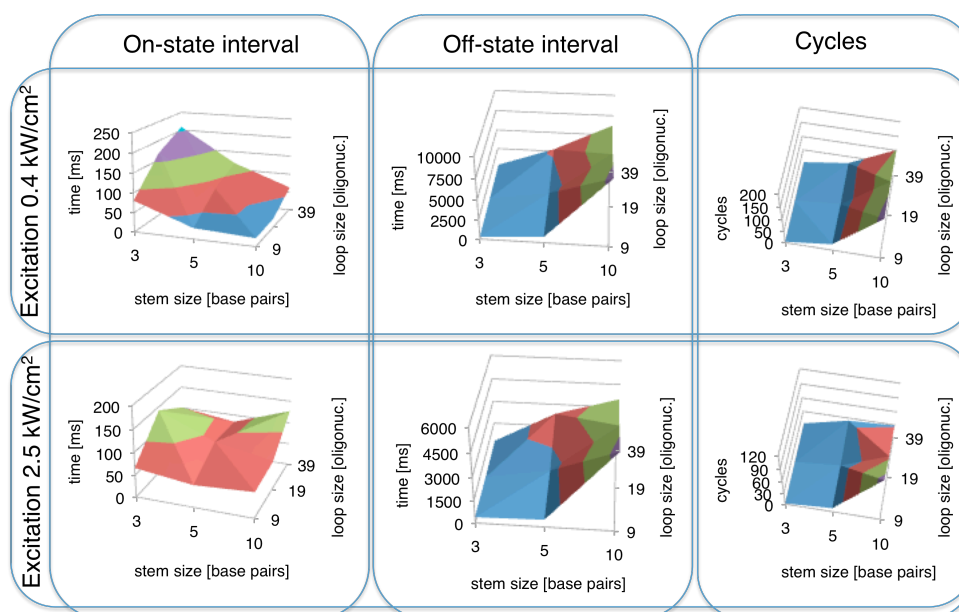


Figure 3.17. ON-state, OFF-state and cycles for Cy3-BHQ2 based blinkons in PBS at room temperature.

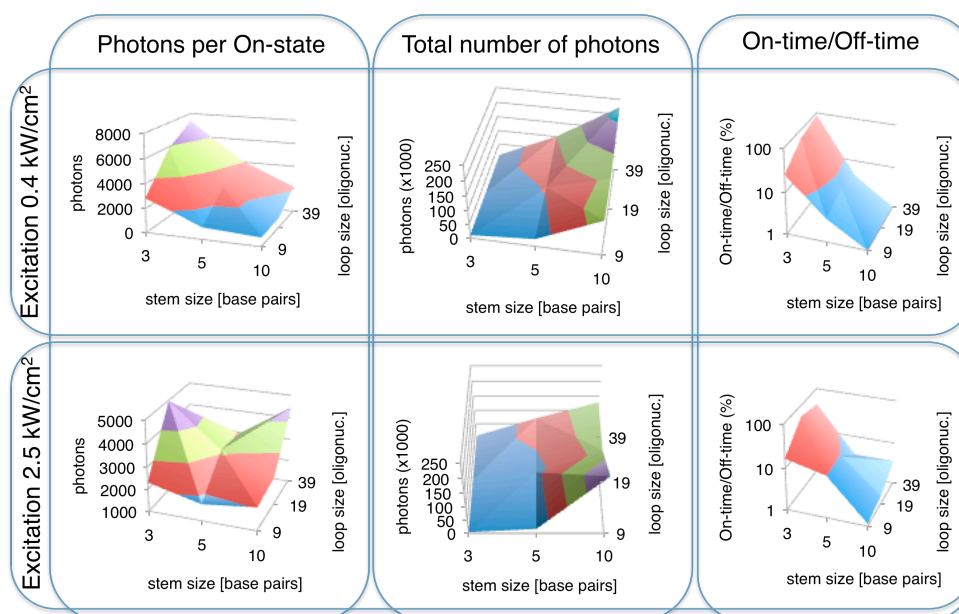


Figure 3.18. Photon output and on/off interval ratio for Cy3-BHQ2 based blinkons in PBS at room temperature.

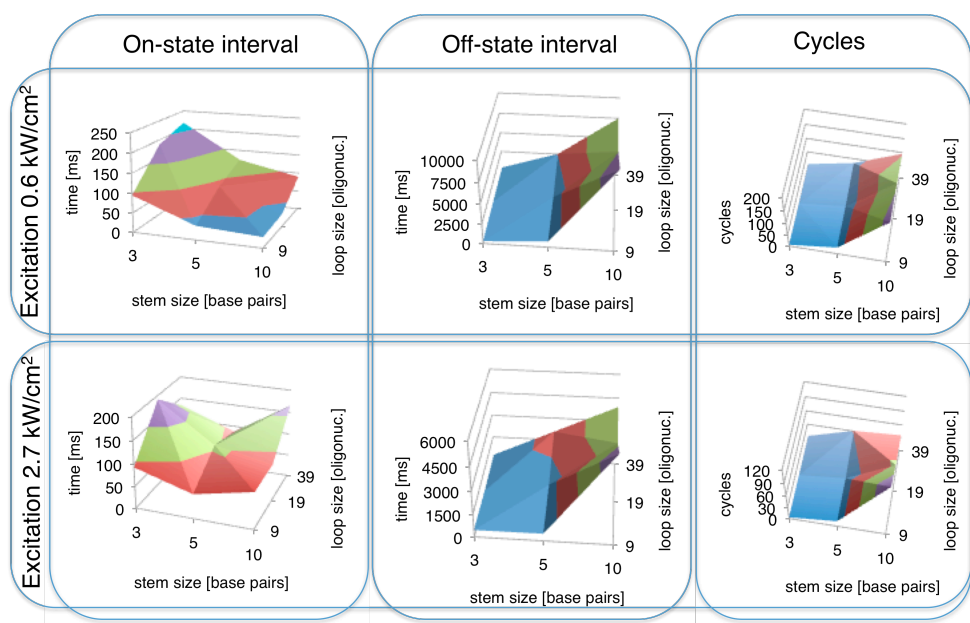


Figure 3.19. ON-state, OFF-state and cycles for Alexa488-BHQ2 based blinkons in PBS at room temperature.

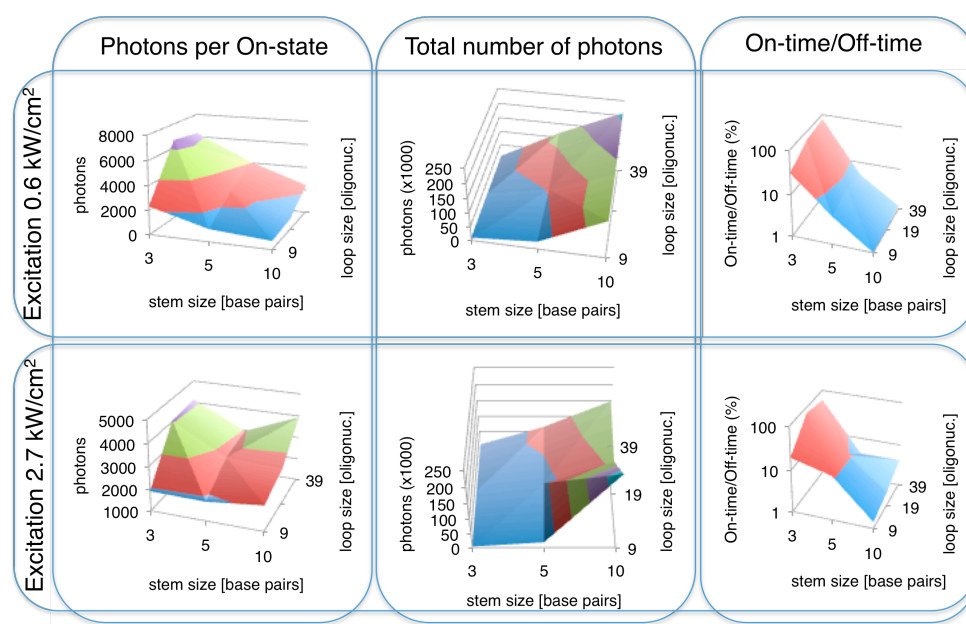


Figure 3.20. Photon output and on/off interval ratio for Alexa488-BHQ2 based blinkons in PBS at room temperature.

A special case is observed when exciting blinkons with stems of 3 or 10 base pair at  $\sim 2.6 \text{ kW/cm}^2$ . Although these present high ON-state times, there are considerable fluctuations in their signal while in an emitting state (effect exemplified on Figure 3.21). We believe that these oscillations correspond to extremely fast switches not accurately time-resolvable. For the typical frame rates used in PALM and STORM these oscillations will be integrated into single long-lived ON-states. This behaviour is less evident for stems with 5 base pairs and also more prominent in the Alexa488 blinkons in comparison to Cy3.

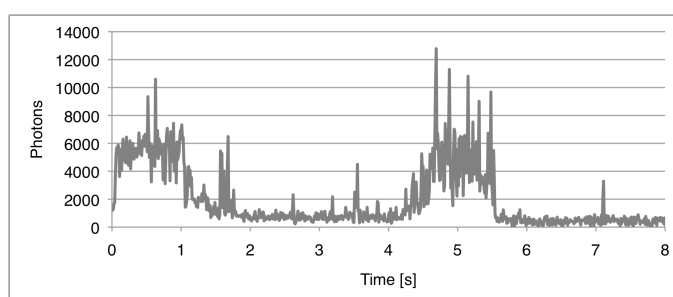


Figure 3.21. Intensity track for an individual Cy3-B3S39L particle at 100 frames-per-second.

We also tested if any endogenous switching behaviour of the fluorophores could be observed without the help of a quencher in the same conditions. To do so, we created an oligo with the sequence CGC TCC ACA GTT TCG GGT TTT CGA CGT TCA with either a 5' Cy3 or Alexa488 and a biotin conjugated to the 3' end. We observed that for this probe, the majority of particles emit continuously until permanently bleached. For an excitation of  $\sim 0.5 \text{ kW/cm}^2$ , blinking was observed in less than 4% of the particles with an average of  $1.42 \pm 0.19$  and  $1.24 \pm 0.16$  cycles for the Cy3 and Alexa488 based oligo-nucleotides, blinking under  $\sim 2.6 \text{ kW/cm}^2$  was negligible.

Overall, we observe that blinkons with 3 base-pairs on the stem cannot efficiently close and, therefore, spend most of their time in an emitting state (see On-time/Off-time ratio in Figure 3.18 and Figure 3.20). This feature also leads to the quick irreversible bleaching of these probes. These are attributes that render this class of blinkons ineffective for most super-resolution dSTORM applications. This is consistent with data that blinkons with 5 to 10 base-pairs provide excellent potential as super-resolution probes due to their short on-time and long off-time.

### **3.2.3.3 Quenching efficiency**

The quenching efficiency of BHQ2 with either Cy3 or Alexa488 has been previously characterized in full populations of oligo-nucleotides (126). Here we followed a similar procedure but at the single-molecule level. For this, we integrated the signal of blinkon particles while on the OFF-state using the Cy3-B5S39L blinkon and removed the contribution of the background fluorescence by also integrating the signal of a region where no particles are evident and subtracting it. By doing it so, a photon leak of  $899 \pm 92$  photon/s was observed. In contrast when on the ON-state we observed an average photon emission of  $35061 \pm 1819$  photon/s leading to a quenching efficiency of 97% and a 39-fold contrast ratio between the two states. Similarly, for the Alexa488-B5S39L blinkon we observed  $1358 \pm 282$  photon/s for the OFF-state and  $27094 \pm 510$  photon/s for the ON-state, yielding a 95% quenching efficiency and a 20-fold contrast ratio.

### **3.2.3.4 Chemically modulating blinkon behaviour**

The most straightforward way to chemically modulate the photo-dynamics of blinkons is to directly interfere with the stem hybridization. Formamide is a common reagent in fluorescence in situ hybridization (FiSH) used to prevent RNA degradation and decrease the hybridization temperature (127). In addition it is also known to induce molecular-beacon opening (124). To study formamide's effect on blinkon switching, intensity time-tracks for Cy3 based blinkon probes in the flow-cells were collected at incremental concentrations of formamide mixed in PBS at room temperature. For this study, we decided to use the blinkon probes with 3 base-pairs (instead of the 5 or 10 base-pairs blinkons) as the 3-base variant already presents a highly unstable stem. Figure 3.22 depicts the analysed results. We observed that modulation of formamide concentration could lead to approximately a 10-fold increase of the ON-state time and 15-fold decrease of the OFF-state time. With higher concentrations of formamide the number of cycles per probe is reduced due to the added probability of irreversible bleaching caused by increased ON-state intervals.

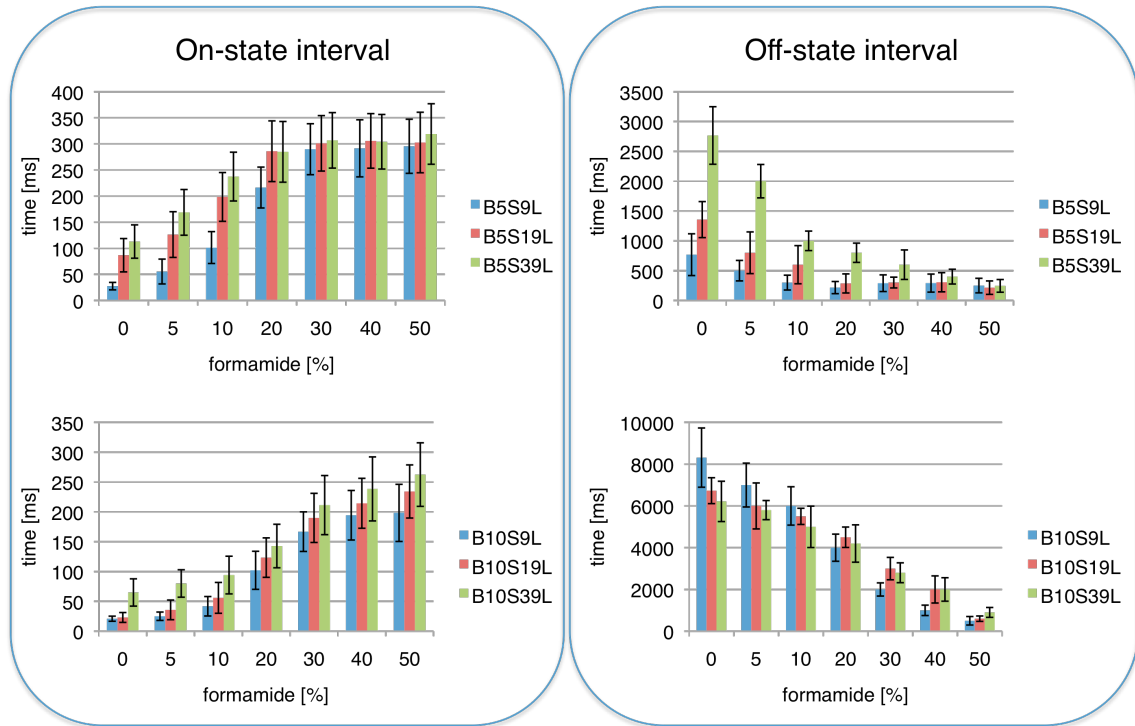


Figure 3.22. Effect of formamide on blinkon photo-switching.

### 3.2.3.5 Super-resolution microscopy

To demonstrate the blinkons capacity as cellular super-resolution probes, the Cy3-B5S39L probe attached to an anti-tubulin antibody was used to stain fixed neuron cells and sub-diffraction images were acquired (Figure 3.23). Around 150.000 images were captured in a TIRF configuration illuminated at 2.6 kW/cm<sup>2</sup> with a 561 nm laser to generate the super-resolution dataset. The first acquired frames provide a normal wide-field fluorescence image, in which a higher portion of probes is in the ON-state when compared to later time points in the acquisition. In fact, it is difficult to generate a good “classical” resolution image as the great majority of the blinkons probes are in the OFF-state even in the beginning of the acquisition. This makes it problematic to observe, without super-resolution, finer details on structures with a low concentration of fluorophores such as at the edges of the dendrites.



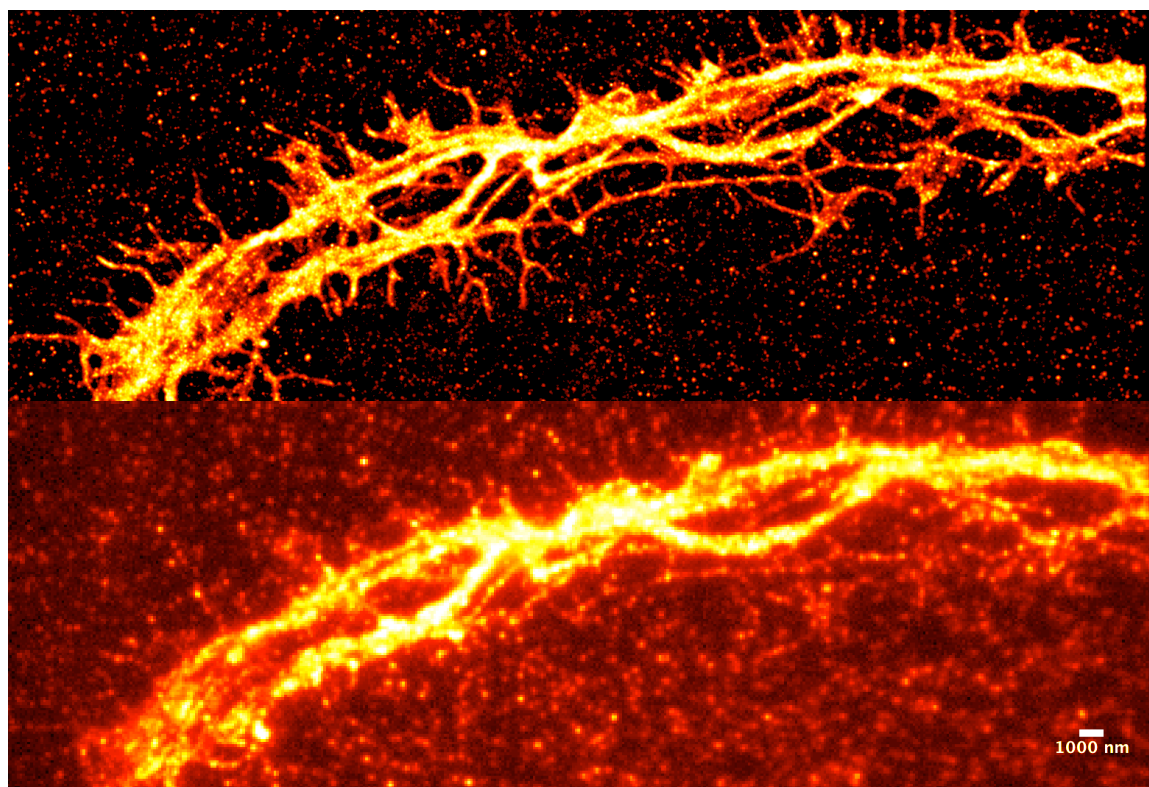


Figure 3.23. Super-resolution (above) and total-internal reflection microscopy (below) images of bundled microtubules in dendrites of neuron cells.

Nevertheless, this property also brings a major advantage as a smaller pre-acquisition bleaching period is required on dSTORM like imaging with “classical dyes”, in which the majority of fluorophores needs to be pushed into the OFF-state before single-molecule detection is possible (a process that can take up to several minutes). In comparison blinkons have most of their population with a closed secondary structure at the beginning of the imaging procedure and are, therefore, on a non-emitting state (see next paragraph for benchmark tests).

We then tested the same imaging procedure using a control oligo - CGC TCC ACA GTT TCG GGT TTT CGA CGT TCA – with a 5' Cy3 and 3' biotin. To be able to super-resolve structures and to induce blinking with this probe we embedded the sample in an oxygen scavenger buffer (as described on section 2.1) to avoid the sample bleaching out rapidly without yielding a considerable number of detectable individual particles. Figure 3.24 compares the pre-acquisition bleaching time for both the control oligo and the Cy3-B5S39L blinkon. We observed a short pre-acquisition bleaching period for the blinkon, meaning the number of detectable particles rapidly

stabilizes in less than 5 seconds while in the control oligo the number of detectable particles takes up to 30 seconds to stabilize.

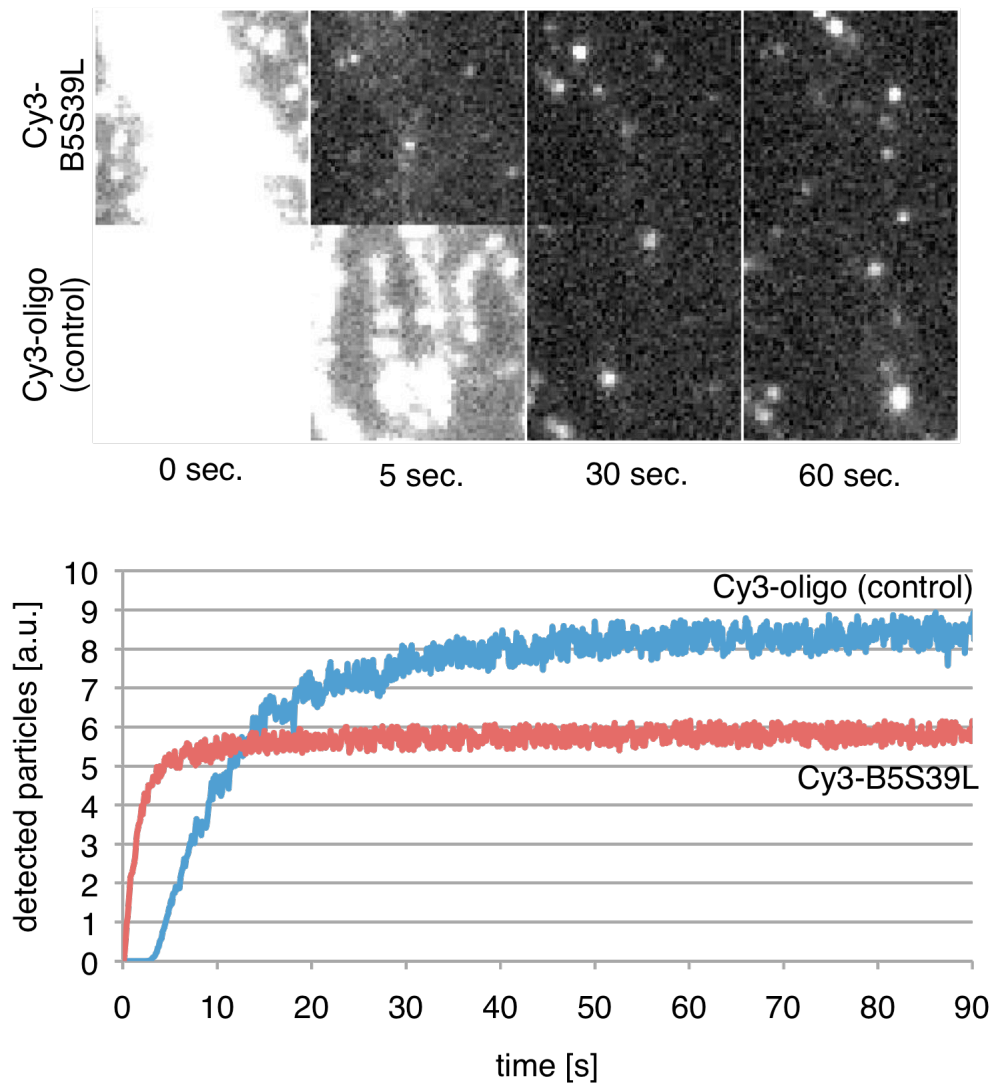


Figure 3.24. (Above) Raw-images of a small-subsection of dSTORM imaging of neuron dendrites labelled with either the Cy3-B5S39L probes or a control biotinylated Cy3-oligo. (Below) Individual particles detectable per time-unit for the same raw-image sequence.

### **3.2.4 Conclusions and Outlook**

In this work we have shown the potential of inducing photo-switchable properties in “standard” organic dyes by conjugation with an oligo-nucleotide structure that explores the transient interaction of fluorophores with high-efficiency quenchers. This feature provides a secondary stochastic activation method that does not depend on fluorophore triplet-state recruitment as currently used in most STORM based super-resolution techniques where stochastic “blinking” is induced through chemical buffers (5, 6, 53, 56, 85, 89). In contrast, our new method allows the sample to be embedded in standard cell non-toxic phosphate buffered saline buffer and to be imaged using fairly low excitation powers. These conditions are a key factor for live-cell super-resolution imaging, in which both the management of chemical- and photo-toxicity is crucial.

The novel blinkon structure seems to generate stable photo-switching characteristics even for different fluorophores, as demonstrated here with the use of Cy3 and Alexa488. This feature is important as it allows selecting the optimal properties for a determined experimental setup. For example, to label a structure with a high-molecular density where the probability of fluorophores spatially overlapping is high, we can choose a blinkon with a small on-time/off-time ratio therefore minimizing this challenge. Additionally, this feature is also crucial to multi-color or multiplex imaging in systems using parallel dual-channel acquisition (52, 128). In the latter systems a dual-view apparatus splits the camera image in half, where each half corresponds to different spectral components. Therefore, as in these systems both channels have an equal exposure time, it is important to use probes with controllable photo-switching spectral characteristics that can be selected for an optimal imposed frame-rate and labelling density.

We have also shown that further “tweaking” of the probe photo-dynamics can be achieved by altering the embedding medium, such as with the help of formamide. This opens up the potential to locally change the probe properties either before or during imaging as needed. Notwithstanding, doing so alters the buffer from physiological conditions and can limit its potential for live-cell imaging. Finally, blinkons also present a reduction in the pre-acquisition bleaching period, allowing a

short waiting period until single-molecules can be detected which overall accelerates the imaging procedure.

In conclusion, blinkons have an enormous potential as super-resolution probes. In the future we will try to explore their prospects in live-cell imaging. We already know that blinkons can be transfected into cells with standard methods. However, it is necessary to bind the probes to the target proteins and for this it is necessary to explore new methods, such as the SNAP-, CLIP-, ACP- and MCP-tags techniques (for more details refer to section 2.3.2.1).

### **3.3 A sub-cellular super-resolution view on NEMO and NF- $\kappa$ B activation.**

This section details unpublished original work. It contains preliminary data currently still being acquired.

Results presented and discussed in this section are the product of collaborative work. Experimental plan and design was carried by R. Henriques, E. Laplantine (Institut Pasteur), F. Agou (Institut Pasteur), M. Veron (Institut Pasteur) and M. Mhlanga. Cell culture was initially carried by R. Henriques and then taken over by E. Laplantine and J. Chiaravalli (Institut Pasteur). Sample preparation was carried by R. Henriques and E. Laplantine. Imaging and analysis done by R. Henriques. M. Lelek was responsible by the assembly of the optical setup used in this work (Institut Pasteur).

#### **3.3.1 Introduction**

We have seen over the last decade the development of microscopy approaches that break the diffraction barrier. Techniques such as Stochastic Optical Reconstruction Microscopy (STORM) (5), have become particularly attractive to researchers due to their easy adaptation to Total-Internal Reflection Fluorescence (TIRF) based optical setups, yielding resolutions of few tens of nanometres. Direct STORM (dSTORM) (6) simplifies both the imaging and labelling process by enabling the use of standard antibodies for immuno-fluorescence staining, facilitating even further multi-colour imaging. In this work, we apply dSTORM to study NF- $\kappa$ B pathway, more particularly the NEMO (NF- $\kappa$ B Essential **MO**dulator) protein, which is a key regulatory subunit of the IKK complex, needed for the translocation of NF- $\kappa$ B into the cell nucleus and at poly-ubiquitin chains involved with the IKK activation.

##### **3.3.1.1 The NF- $\kappa$ B activation pathway**

NF- $\kappa$ B represents a family of transcription factors with a key role in immune, inflammatory and anti-apoptotic responses. It stimulates immune cell function and

acts in a pro-inflammatory manner by inducing the expression of cytokines, chemokines and their receptors (129). Furthermore, NF- $\kappa$ B is capable of inhibiting programmed cell death through transcriptional stimulation of anti-apoptotic genes and as such, can be also a main driver in cancer growth and survival (see Figure 3.25).

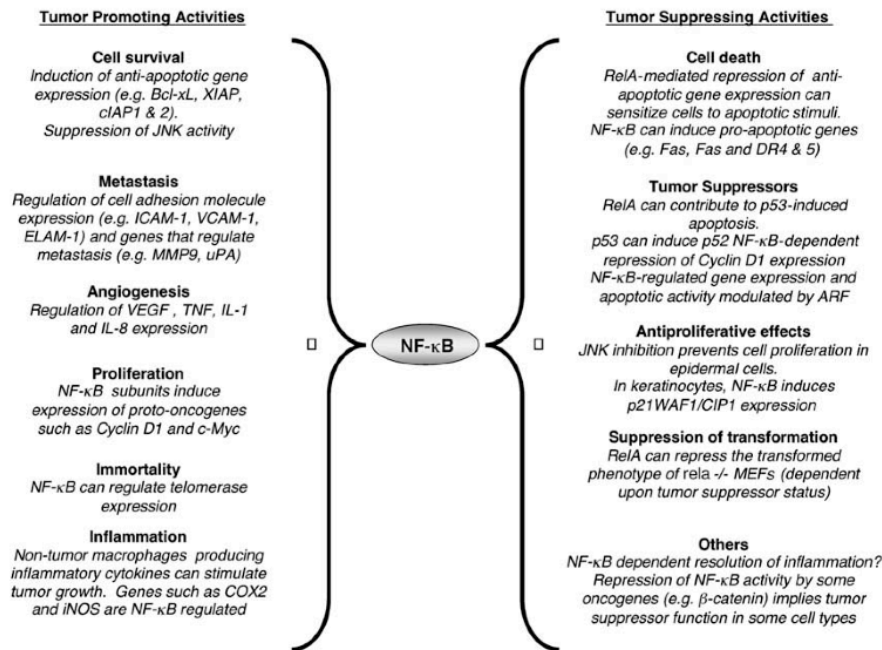


Figure 3.25. Different functions of NF- $\kappa$ B can have either tumor-promoting or tumor suppressing effects. On the left is a summary of the different tumorigenic processes to which aberrantly active NF- $\kappa$ B has been shown to contribute. In contrast, on the right is evidence indicating that under other circumstances active NF- $\kappa$ B can act to inhibit tumor growth and survival. Adapted from *N.D. Perkins et al. (130)*.

NF- $\kappa$ B is naturally sequestered in the cytosol of unstimulated cells. The I $\kappa$ Bs are inhibitor proteins that prevent the NF- $\kappa$ B translocation to the nucleus (131). The activation of the NF- $\kappa$ B pathway can be induced by several factors such as viral or bacterial infections, mitogen phorbol esters (PMA), antigens and pro-inflammatory cytokines like the tumor necrosis factor- $\alpha$  (TNF- $\alpha$ ) and interleukin 1 (IL-1). These activation processes initiate pathways eventually converging on the IKK (also known as I $\kappa$ B-kinase) complex (132). The activation of the IKK complex leads to the phosphorylation of the I $\kappa$ Bs. These in turn are ubiquitinated and degraded through the proteasome-mediated pathway (133-135), allowing the release of NF- $\kappa$ B into the nucleus, leading to the expression of its target genes (see Figure 3.26).

The IKK complex is mainly constituted by two catalytic subunits - IKK $\alpha$  and IKK $\beta$  – and a key regulatory subunit – NEMO (also known as IKK $\gamma$ ). The latter is our main protein of interest in this study. There are alternative NF- $\kappa$ B activation pathways that only rely on IKK $\alpha$  dimers and are independent of IKK $\beta$  or NEMO. Notwithstanding, NEMO is required for the formation of the IKK complex and for the canonical NF- $\kappa$ B activation pathway (136).

Poly-ubiquitin binding activity of NEMO through Lys63 (K63)-linked or linear chains prompts the IKK activation (137-141). Kinases then phosphorylate the inhibitory I $\kappa$ B proteins, which are rapidly modified by Lys48 (K48) poly-ubiquitin chains and degraded by the 26S proteasome. K63-linked poly-ubiquitine chains represent protein-protein interaction motifs that allow inducible recruitment of proteins or their interacting partners to specific sub-cellular localization. A large number of proteins are known to contain ubiquitin-binding domains (UBDs) recognizable by these chains (142, 143).

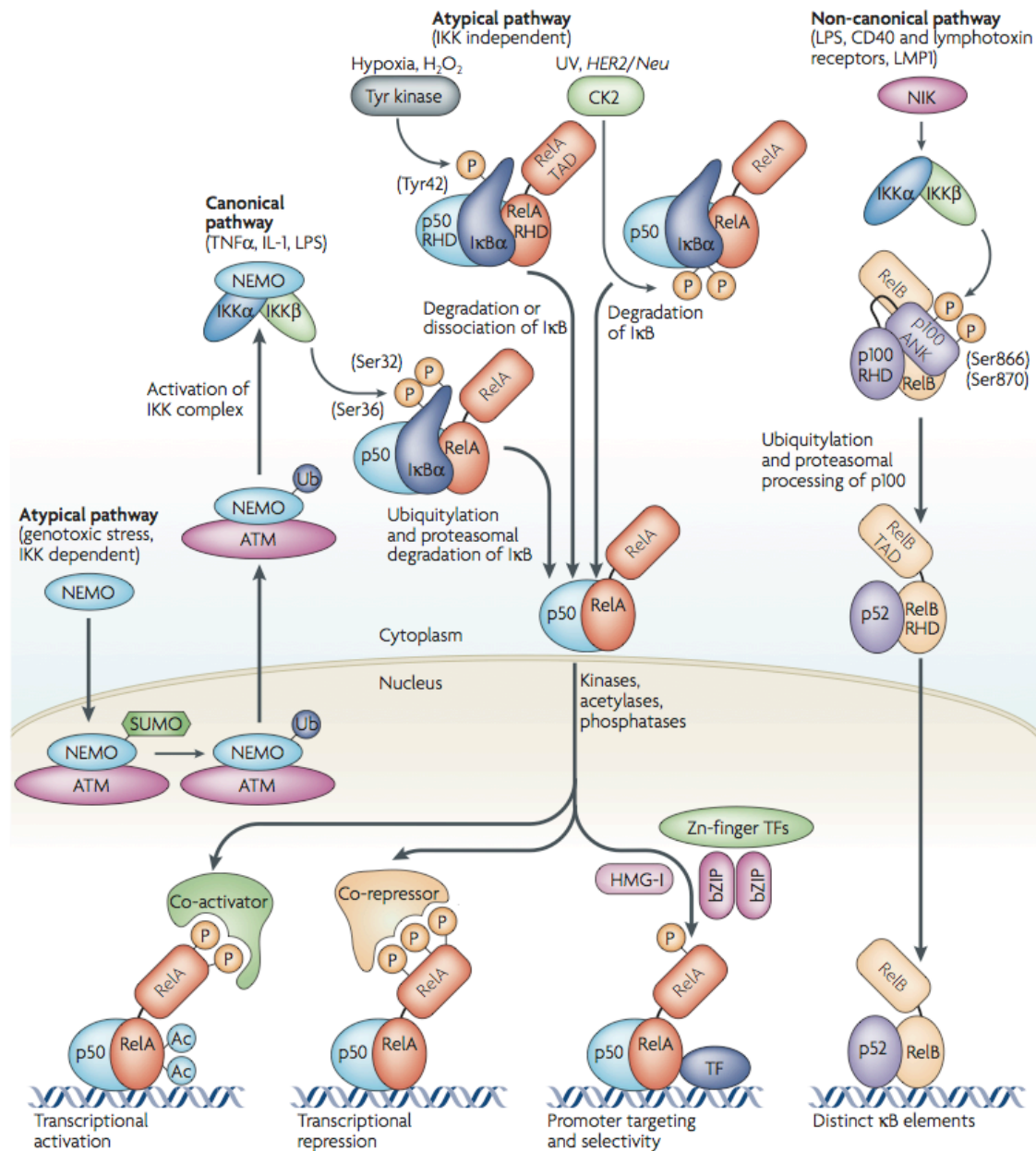


Figure 3.26. Pathways leading to the activation of NF- $\kappa$ B. The canonical pathway is induced by tumour necrosis factor- $\alpha$  (TNF $\alpha$ ), interleukin-1 (IL-1) and many other stimuli, and is dependent on activation of IKK $\beta$ . This activation results in the phosphorylation (P) of I $\kappa$ B $\alpha$  at Ser32 and Ser36, leading to its ubiquitylation (Ub) and subsequent degradation by the 26S proteasome. Release of the NF- $\kappa$ B complex allows it to relocate to the nucleus. Under some circumstances, the NF- $\kappa$ B-I $\kappa$ B $\alpha$  complex shuttles between the cytoplasm and the nucleus (not shown). IKK-dependent activation of NF- $\kappa$ B can occur following genotoxic stress. Here, NEMO localizes to the nucleus, where it is sumoylated and then ubiquitylated, in a process that is dependent on the ataxia telangiectasia mutated (ATM) checkpoint kinase. NEMO



relocates back to the cytoplasm together with ATM, where activation of IKK $\beta$  occurs. IKK-independent atypical pathways of NF- $\kappa$ B activation have also been described, which include casein kinase-II (CK2) and tyrosine-kinase-dependent pathways. The non-canonical pathway results in the activation of IKK $\alpha$  by the NF- $\kappa$ B-inducing kinase (NIK), followed by phosphorylation of the p100 NF- $\kappa$ B subunit by IKK $\alpha$ . This results in proteasome dependent processing of p100 to p52, which can lead to the activation of p52–RelB heterodimers that target distinct  $\kappa$ B elements. Phosphorylation of NF- $\kappa$ B subunits by nuclear kinases, and modification of these subunits by acetylases and phosphatases, can result in transcriptional activation and repression as well as promoter-specific effects. Moreover, cooperative interactions with heterologous transcription factors can target NF- $\kappa$ B complexes to specific promoters, resulting in the selective activation of gene expression following cellular exposure to distinct stimuli. Ac, acetylation; bZIP, leucine-zipper-containing transcription factor; HMG-I, high-mobility-group protein-I; I $\kappa$ B, inhibitor of  $\kappa$ B; IKK, I $\kappa$ B kinase; LMP1, latent membrane protein-1; LPS, lipopolysaccharide; NF- $\kappa$ B, nuclear factor- $\kappa$ B; RHD, Rel-homology domain; TAD, transcriptional activation domain; TF, transcription factor; UV, ultraviolet; Zn-finger TF, zinc-finger-containing transcription factor. Adapted from *N. Perkins et al. (144)*.

### 3.3.1.2 NEMO's structure

The N-terminus half of NEMO contains a long coiled-coiled domain (CC1) and is responsible for its interaction with IKK kinases. The C-terminal half is involved in signal recognition from upstream molecules (145) and is comprised by coiled-coil domain (CC2), a leucine zipper (LZ) motif and a CCHC-type zinc finger (ZF) domain (see Figure 3.27) (146).

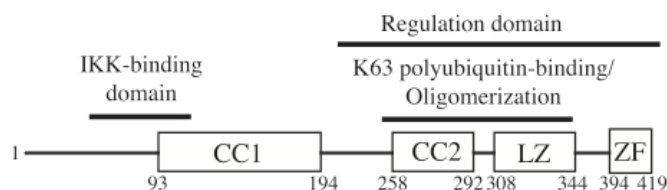


Figure 3.27. Structural and functional domains of the NEMO protein. These include the coiled-coil (CC1 and CC2), LZ and ZF motifs. The functional NEMO domains are indicated on top. Sequence numbering is given for human NEMO protein. Adapted from Cordier *et al.* (146).

The CC2-LZ domain is required for NEMO oligomerization (147, 148) and contains an ubiquitin-binding domain (UBD) preferentially interacting with K63-linked chains (149, 150). K63-linked chains binding through the CC2-LZ domain of NEMO is required for NF- $\kappa$ B signalling from different receptors. NEMO's middle region, residues 194 to 248 (HLX2), constitutes a binding site for proteins, such as the viral proteins vFLIP, TANK or RIP (see Figure 3.28).

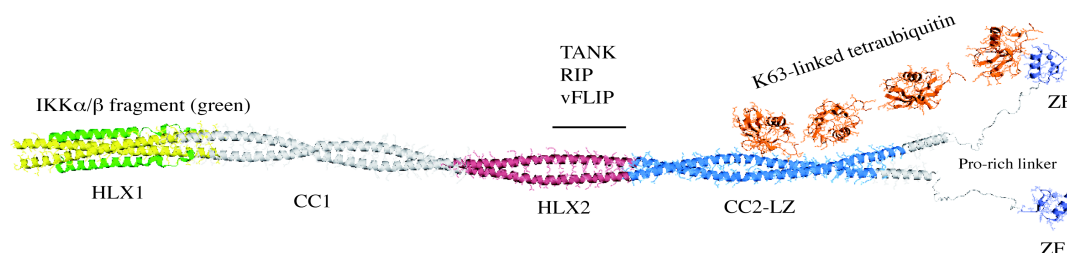


Figure 3.28. Structural model of NEMO with associated K63 ubiquitin chains. The model is constituted by the different domains determined by X-ray crystallography and nuclear magnetic resonance (NMR), modelled domains are set in gray. A fragment of the kinase IKK $\alpha$ / $\beta$  which binds to NEMO at its N-terminus is shown in green. Image courtesy of the F. Agou group at Institut Pasteur.

### 3.3.1.3 Super-resolution imaging of NEMO and poly-ubiquitin

The mechanism behind the IKK control by NEMO is at the core of NF- $\kappa$ B regulation. Although its role has been well described by biochemical and structural studies, the sub-cellular mechanisms behind NEMO involvement in the NF- $\kappa$ B pathway are still

fairly unknown. The aim of the present work is to characterize NEMO's territories within the sub-cellular environment, more specifically in the vicinity of the cell membrane and therefore near the NF- $\kappa$ B associated receptors. In addition, we also address the modulation of these territories in cells in which NF- $\kappa$ B activation was induced by cell treatment with TNF- $\alpha$  and IL-1.

### **3.3.2 Material and Methods**

Here we provide an overview of the experimental preparation procedures, imaging apparatus and analysis tools used.

#### **3.3.2.1 Cell culture**

U2OS (human osteosarcoma) cells were cultured in D-MEM/F-12 without Phenol Red (a source of medium auto-fluorescence) supplemented with 10% fetal calf serum and antibiotics.

#### **3.3.2.2 Cell fixation**

##### **Paraformaldehyde fixation**

Cells to be processed for immuno-fluorescence were fixed for 5 minutes with 4% paraformaldehyde (PFA) at 4°C, washed and followed by a 5 minute incubation in 50 mM NH<sub>4</sub>Cl. Cells were then permeabilized through treatment with 0.2% Triton X 100 for 5 minutes.

##### **Methanol fixation**

Methanol fixation was also used as a control for comparison against the PFA fixation. For this, 0.5 ml of 100% methanol at -20 °C was applied to the cell plates on ice for 5 minutes. After, cells were washed and rehydrated by a sequence of cold ethanol washes at 95%, 80% and 50%. Cells were then washed with PBS .

#### **3.3.2.3 Cell labelling**

After permeabilization, cells were incubated with 1% bovine serum albumin (BSA) for 20 minutes and, then incubated with a primary antibody (see Results and Discussion for the antibody references) in 1% BSA for 60 minutes. After washing with PBS, cells were incubated with a secondary antibody in 1% BSA also for 60 minutes.

#### **3.3.2.4 siRNA treatment**

Cells to be treated with siRNA anti-NEMO were incubated with a mix of 100  $\mu$ L of DMEM, 25nM of siRNA and 6  $\mu$ L of the HiPerFect transfection reagent (Qiagen) for two days and then fixed. As a control to ensure that the siRNA treatment does not produce any artefacts, additional cells were treated with a nonspecific siRNA that does not target any mRNA.

#### **3.3.2.5 CYLD transfection**

Cells to be transfected with the CYLD plasmid were treated with a mix of 1  $\mu$ g of the plasmid DNA, 2 $\mu$ L of FuGENE HD (Roche) in 50  $\mu$ L of Opti-MEM (Invitrogen) for two days and then fixed. Additionally, cells were also transfected with a control CYLD plasmid for which its deubiquinating function has been disabled (*151*). The CYLD plasmids also presented a FLAG epitope that was used to report the expression by immuno-fluorescence staining against FLAG.

#### **3.3.2.6 TNF- $\alpha$ or IL1 treatment**

Cells for NF- $\kappa$ B pathway activation were treated either with TNF- $\alpha$  or IL1. For this cells are incubated with 20 ng/mL of either TNF- $\alpha$  or IL1 for 15 minutes and then washed and fixed.

#### **3.3.2.7 Total-internal reflection fluorescence microscopy**

TIRF/dSTORM imaging of cells was performed with a Nikon Ti-E eclipse in TIRF configuration. An oil-immersion objective (CFI Apochromat, 100x, NA 1.49, Nikon) was used. Either a 488nm (solid state), 561nm (solid state) or 635nm (diode laser) from Spectra Physics was selected by an acousto-optic tunable filter (AOTF-AA optoelectronic) depending on the fluorophore used. Fluorescence light was spectrally filtered using filters and imaged on an EM-CCD camera (Andor Ixon DU-897E-CS0-BV). The laser powers were chosen to ensure that the fraction of activated

fluorophores at any given time was sufficiently low to allow the detection and localization of individual fluorophores. After setting the evanescent field with the help of the fiduciary fluorescence beads, the image acquisition was performed over the full field of view (512x512 pixels) of the EM-CCD camera running at 10 Hz generating around 20.000 images per channel for each dataset. For additional information refer to the optical setup described on section 2.1 and 3.2.

### **3.3.2.8 Super-resolution image analysis and reconstruction**

dSTORM data was analyzed with QuickPALM (see section 3.1) and ImageJ (W. Rasband, National Institute of Health, Bethesda, USA). Super-resolution single-particle detection was carried out with optimal settings previously evaluated also in section 2.1. Super-resolution datasets were reconstructed as 2D histograms of particle-counts with a 10nm bin-size.

### **3.3.3 Results and discussion**

We first observed NEMO labelling in U2OS cells by TIRF-dSTORM super-resolution. Labelling was provided by immuno-fluorescence where we used a monoclonal antibody (Anti-NEMO, 611306, BD Biosciences) as a primary labelling source, and a secondary antibody with the Cy5 dye – one of the best performing fluorophores in super-resolution microscopy.

Our first collected images immediately revealed that NEMO forms nanostructures in the immediate vicinity of the cytoplasm membrane (see Figure 3.29 and Figure 3.30). These structures seem to be composed by small round clusters of NEMO with an average of 50-100 nm width that can be connected to each other by elongated bridges also composed by NEMO with an average length of 300 nm. The remarkably small size of the structures observed is in the order of the sub-diffraction limit making it impossible their observation on standard fluorescence imaging methods.

As a second step it was important to observe if the NF-  $\kappa$ B pathway activation could induce in anyway a change in the formation of the NEMO structures on the cell. For this, cells were stimulated by TNF- $\alpha$  for 15 minutes before imaging. Previous western blot experiments have indicated that the maximum IKK phosphorylation occurs within this period of incubation, which is an indicative of the pathway activation (data not shown).

In parallel experiments we also used P65 immuno-fluorescence staining prior and post TNF- $\alpha$  treatment, P65 is known to translocate to the nucleus upon NF-  $\kappa$ B activation. Acquired images revealed that cells treated with TNF- $\alpha$  for 15 minutes showed the expected translocation by a remarkable increase by fluorescence in the nucleus, while untreated cells kept the P65 signal on the cytoplasm. Therefore giving us confidence that the TNF- $\alpha$  treatment did activate the NF-  $\kappa$ B pathway (data not shown).

Despite of these controls, to our best attempts it was not possible to observe any significant changes in the characteristics of the NEMO territories in the cells activated (see Figure 3.30).

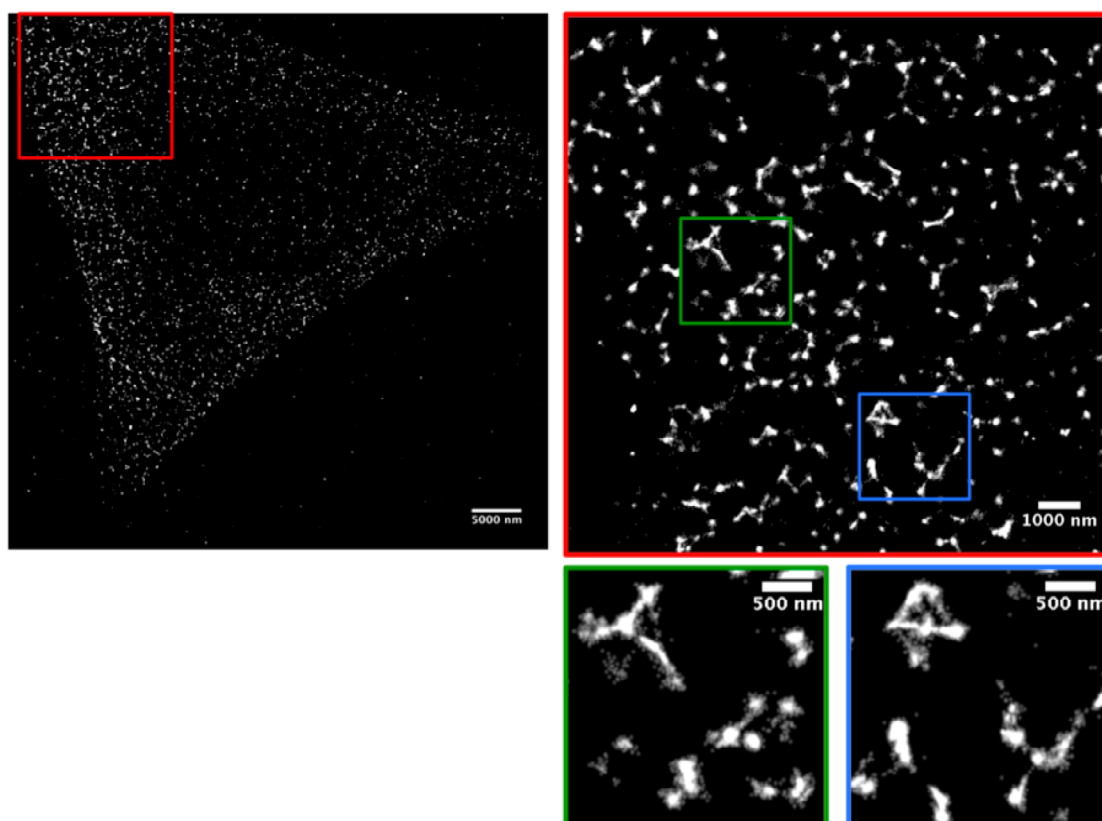


Figure 3.29. NEMO immuno-fluorescence in U2OS unstimulated cells. Super-resolution imaging by TIRF-dSTORM of the Cy5 dye. Colour squares outlines correspond to zoomed areas shown in the proceeding images.



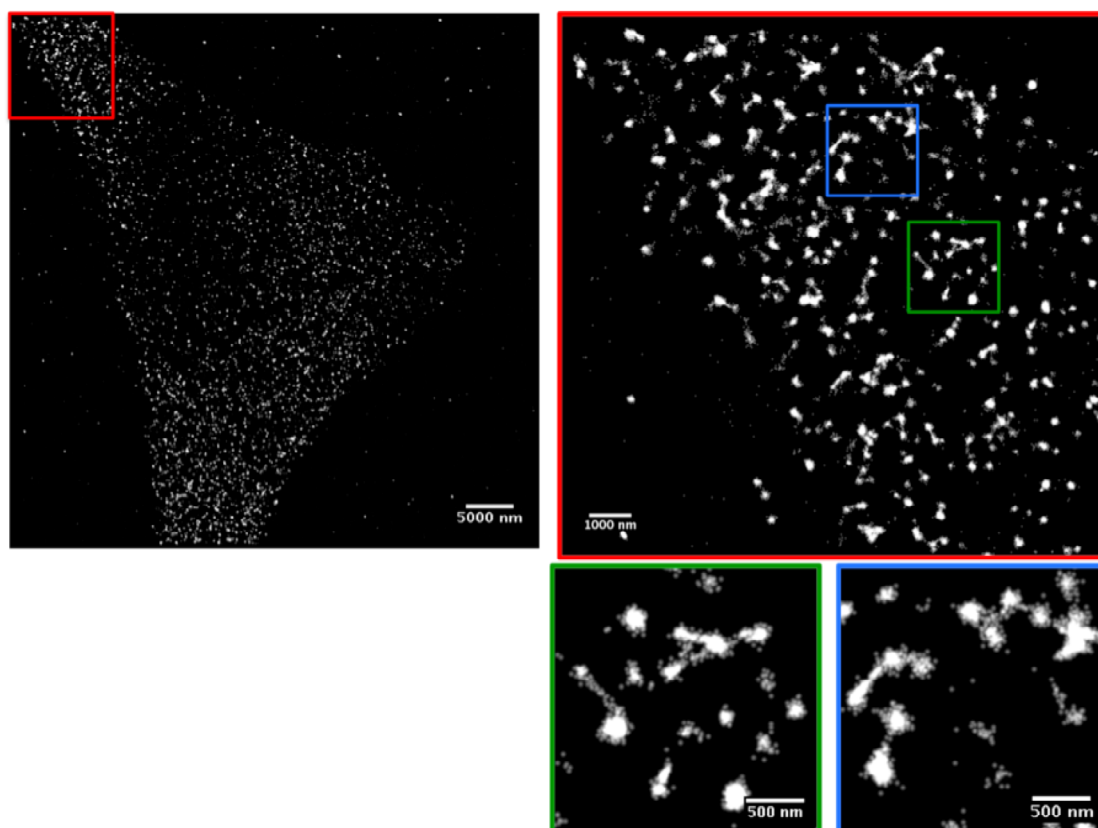


Figure 3.30. Super-resolution dSTORM imaging of NEMO immuno-fluorescence staining in U2OS TNF- $\alpha$  stimulated cells. Colour squares outlines correspond to zoomed areas shown in the proceeding images.

Since these structures formed by NEMO were being observed for the first time, it was important to clarify if they could be in anyway the result of a technical artifact. As such, two controls were performed. For the first control, both paraformaldehyde and methanol based fixations were performed in independent samples to observe if the structures would be kept and if they could be in anyway related to a fixation artifact. The resulting acquired images were similar for both methods suggesting the inexistence of disruptive fixation effects (data not shown). On the second control, cells were treated and transfected with a siRNA down-regulating NEMO. The aim of this control was to establish if the primary antibody could be unspecifically labeling alternative proteins. The resulting images of cells in which NEMO was knocked-down showed a decrease in NEMO signal and the absence of the structures previously observed (see Figure 3.31). Therefore this data indicates that the primary antibody used is highly specific.

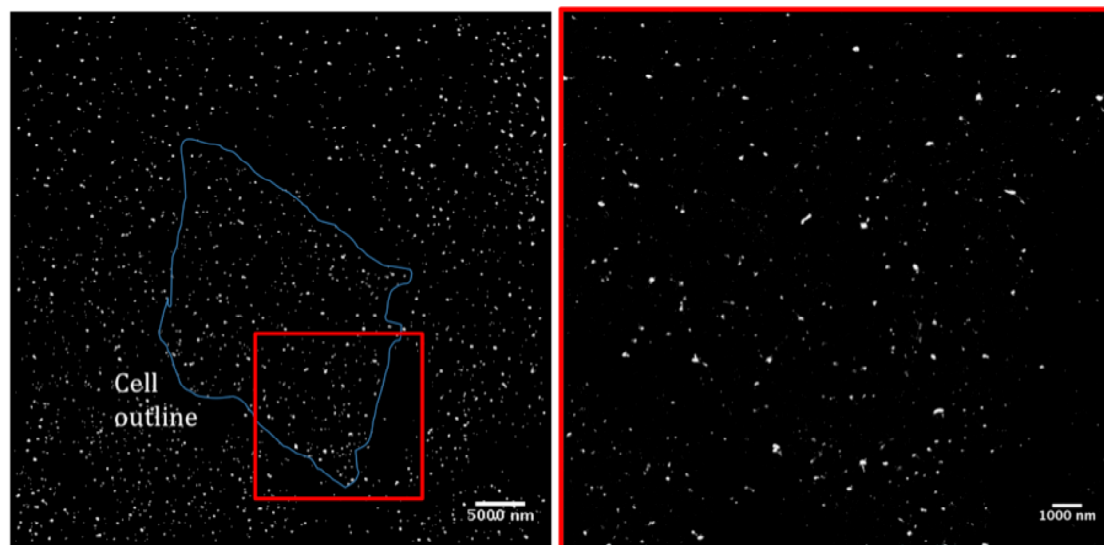


Figure 3.31. Cell transfected with a siRNA against NEMO. Super-resolution dSTORM imaging of NEMO immuno-fluorescence staining in U2OS TNF- $\alpha$  stimulated cells. Colour square outlines correspond to zoomed areas shown in the proceeding images. The blue line outlines the cell cytoplasm.

Next, we transfected cells with a cylindromatosis (CYLD) expression plasmid. CYLD is a de-ubiquitinase, which exhibits very little activity toward Lys48-linked poly-ubiquitin chains (138, 147). On the other hand, the enzyme hydrolyses K63-linked chains with high-efficiency, as well as linear ubiquitin chains that are structurally

equivalent to K63-chains. Our premise was that it would be possible for NEMO to be interacting with K63-chains in the cytoplasm and that these could be partly responsible for the NEMO structure we were observing. Imaging of the CYLD transfected cells did reveal a severe reduction on the NEMO structures (see Figure 3.32). As a control, we also transfected cells on same conditions with a mutant form of CYLD that is unable to degrade any poly-ubiquitin chains. The mutated CYLD transfected cells rescued the original phenotype, suggesting then that the NEMO network-like territories are dependent of K63- and/or linear poly-ubiquitin chains, these experiments also demonstrate that the CYLD transfection and expression mechanisms themselves do not cause an artifact on the NEMO territories (see Figure 3.33).

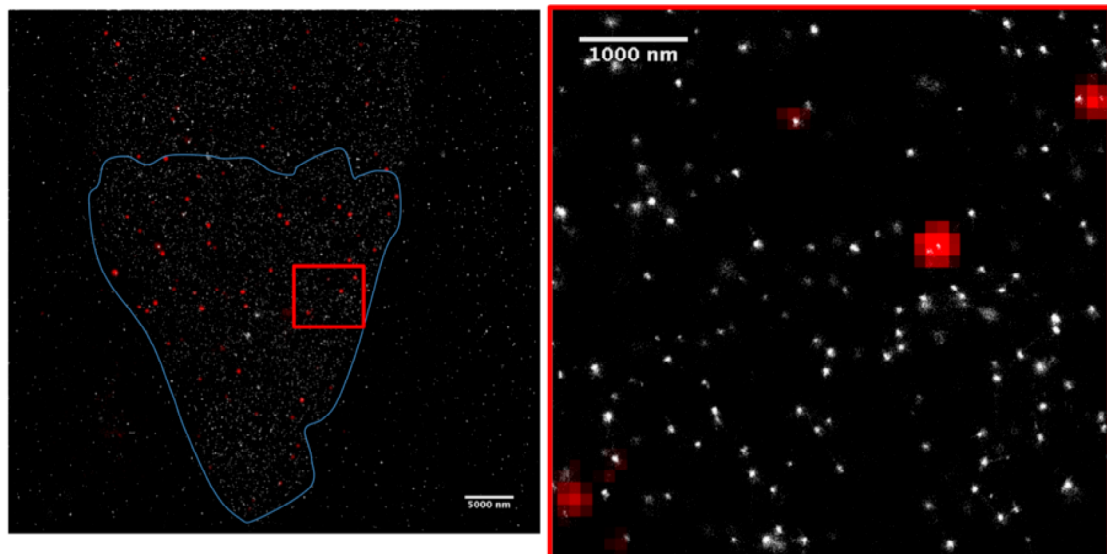


Figure 3.32. Cell transfected with CYLD. Super-resolution dSTORM imaging of NEMO immuno-fluorescence staining in U2OS unstimulated cells. Color square outlines correspond to zoomed areas shown in the proceeding images. Red spots correspond to the TNF-R1 receptor labelling captioned on wide-field non-super-resolution imaging. The blue line outlines the cell cytoplasm.

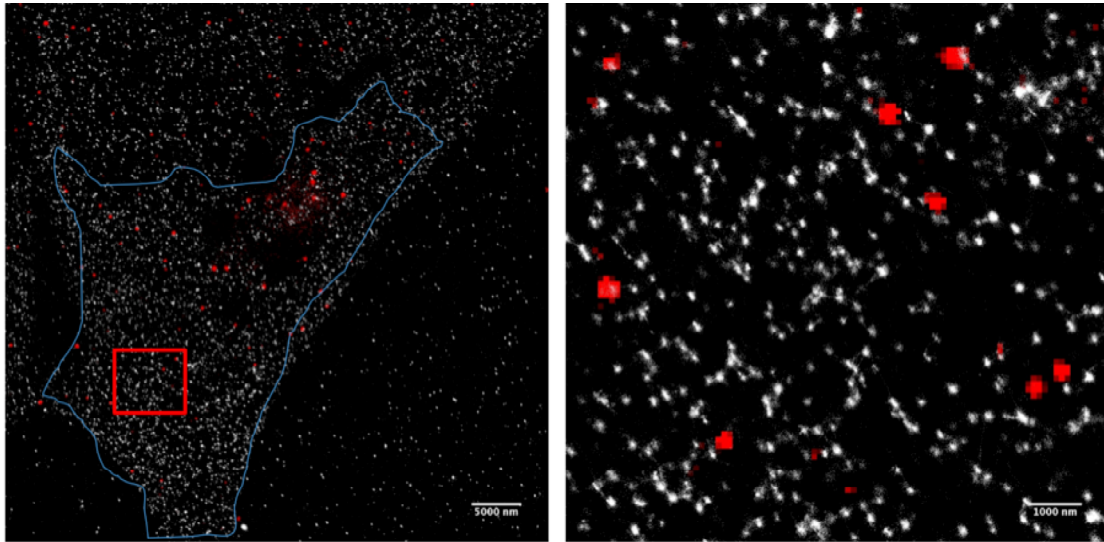


Figure 3.33. Cell transfected with a mutated CYLD preventing its deubiquitinating function. Super-resolution dSTORM imaging of NEMO immuno-fluorescence staining in U2OS unstimulated cells. Color square outlines correspond to zoomed areas shown in the proceeding images. Red spots correspond to the TNF-R1 receptor labelling captioned on wide-field non-super-resolution imaging. The blue line outlines the cell cytoplasm.

Still it was unclear why there was no noticeable difference in the NEMO images of activated NF- $\kappa$ B cells. We then recognized a major flaw with our labeling protocol. Our primary antibody was specifically binding to the LZ region of the NEMO molecule, the region also used for K63 binding. As such, our antibody had a preference for labeling non-ubiquitinated NEMO. We then tested a different primary antibody against NEMO (sc-8330, Santa Cruz) and also tried activation not only by TNF- $\alpha$  but also by IL-1.

First, the imaging of untreated cells revealed similar structures to that observed with the previous antibody, but at a much higher density. Possibly suggesting that the new antibody had a higher labeling efficiency. This feature also introduced the notion that NEMO seems to form a linked network on the cell cytoplasm (see Figure 3.35).

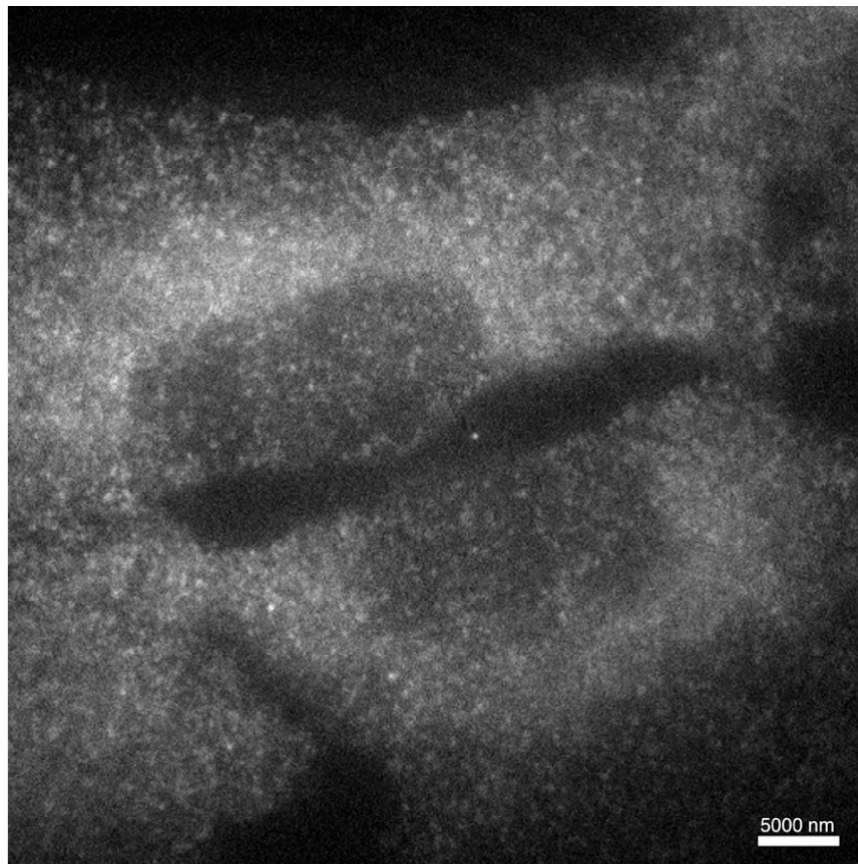


Figure 3.34. Wide-field imaging of NEMO immuno-fluorescence staining in U2OS unstimulated cells.



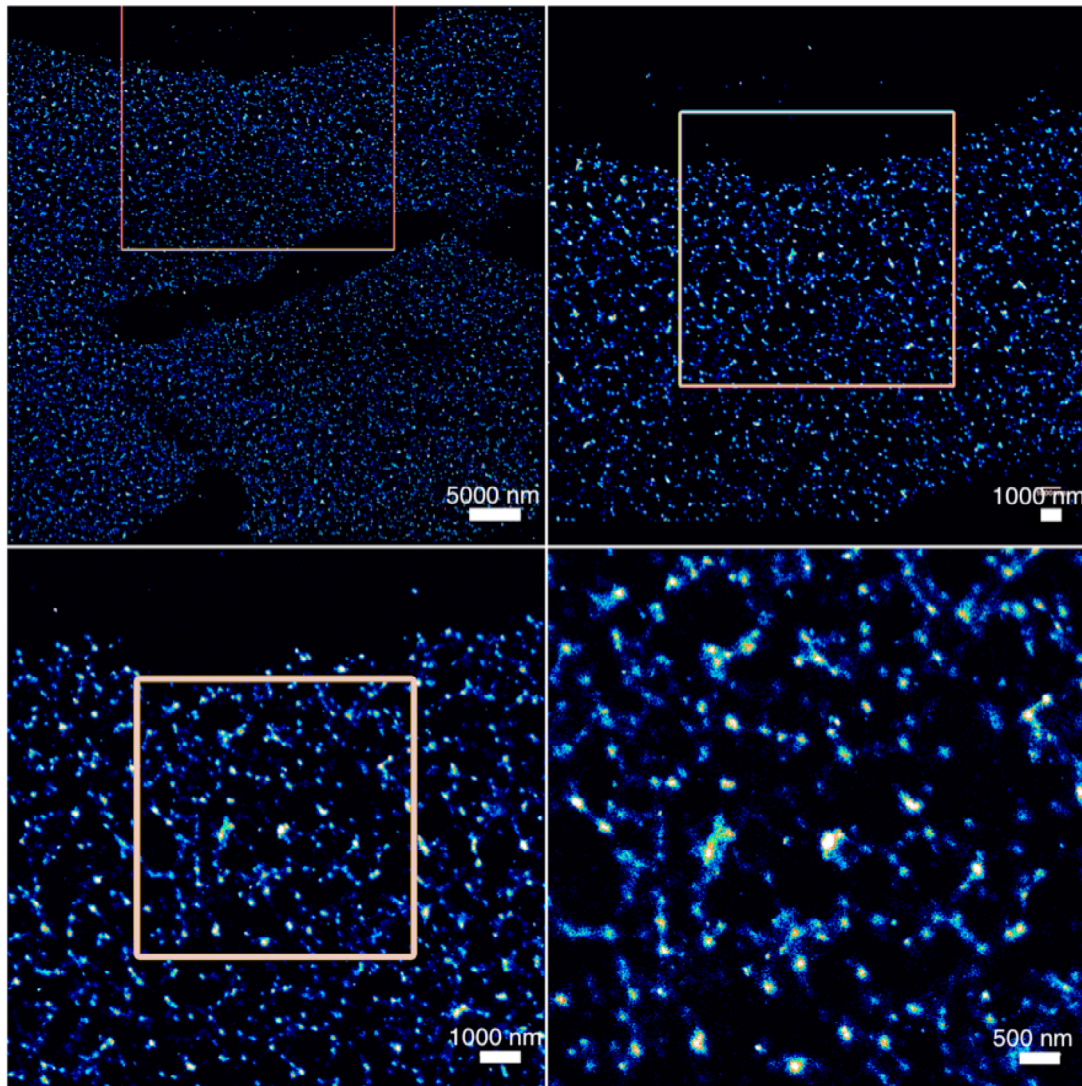


Figure 3.35. Super-resolution dSTORM imaging of NEMO immuno-fluorescence staining in U2OS cells in unstimulated cells. Pink square outlines correspond to zoom areas shown in the proceeding image. Image is colour coded where blue colours corresponds to low-molecular density and white colours high-molecular density.

NEMO activation by IL-1 treatment revealed a strong phenotype that is even evidently observed by simple wide-field fluorescence (see Figure 3.36). It was possible to observe the appearance of speckles characterized by a high-concentration of NEMO. Super-resolution TIRF-dSTORM imaging of these samples further revealed the depletion of NEMO in the immediate surrounding region of these spots of highly concentrated NEMO (see Figure 3.38). This data suggests a possible recruitment of NEMO to these spot regions at the cost of NEMO depletion in the immediate surrounding regions or, the presence of a structure confining NEMO to the spot region.

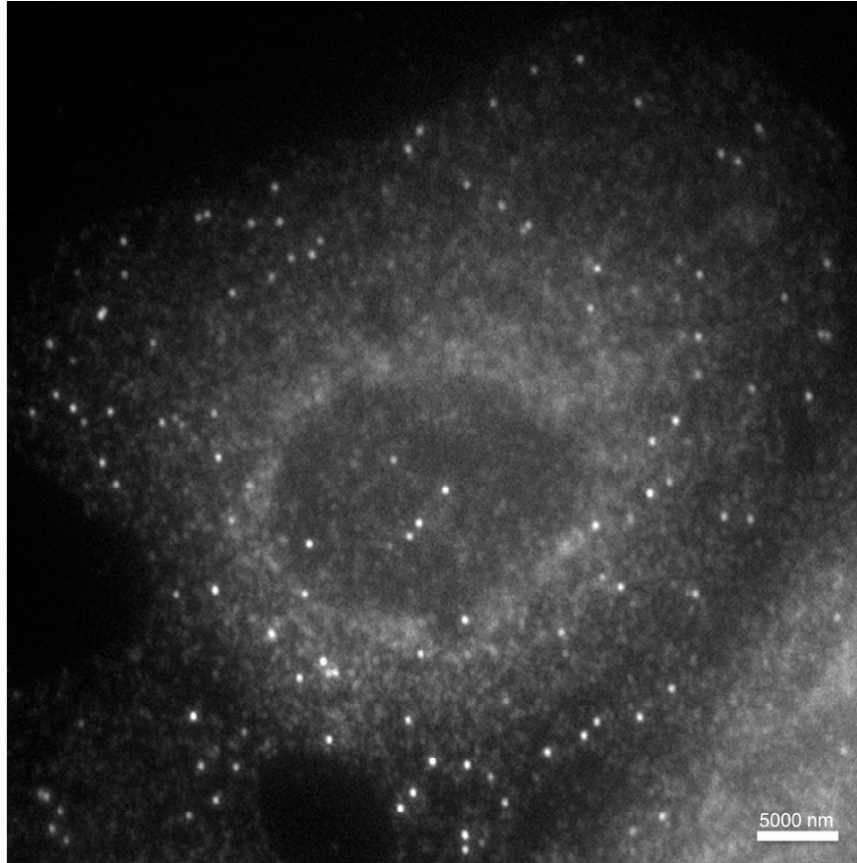


Figure 3.36. IL-1 stimulated cell. Wide-field fluorescence imaging of NEMO immuno-fluorescence staining in U2OS cells.

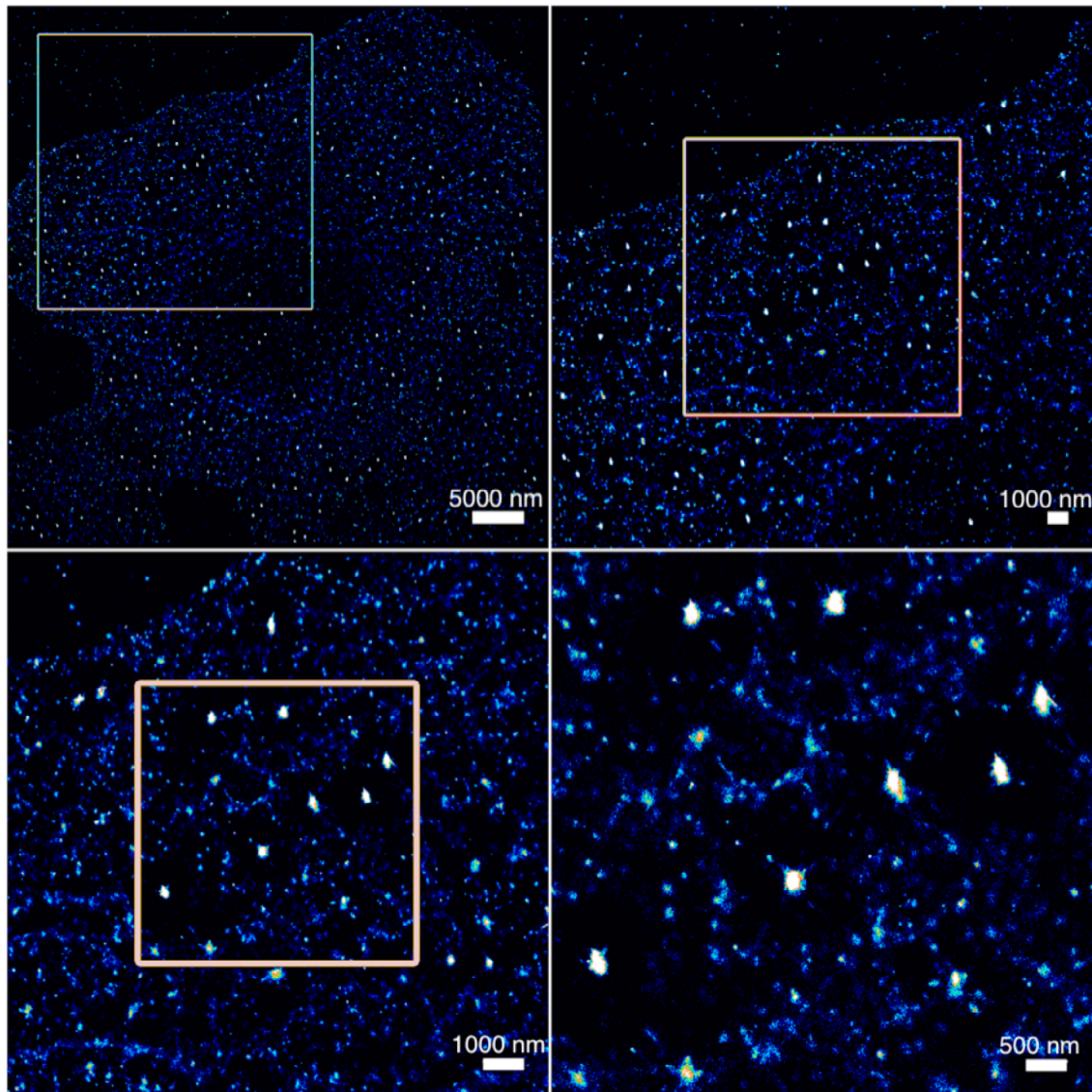


Figure 3.37. IL-1 stimulated cell. Super-resolution dSTORM imaging of NEMO immuno-fluorescence staining in U2OS cells. Pink square outlines correspond to zoom areas shown in the proceeding image. Image is colour coded, where blue and white colours correspond respectively to low-molecular and high-molecular density.

In  $\text{TNF-}\alpha$  treated cells the phenotype described is not as evident in wide-field fluorescence as the same high-intensity spots cannot be discerned anymore (see Figure 3.38). Still these can be observed with super-resolution imaging, in which we observe that the spot formation has a lower concentration of NEMO when compared to the IL-1 activation. Nevertheless, there is still a several-fold increase when compared with any of the similar spot-like structures in untreated cells. In  $\text{TNF-}\alpha$  treated cells it is also possible to observe a NEMO depletion surrounding the high-intensity spots (see Figure 3.39).



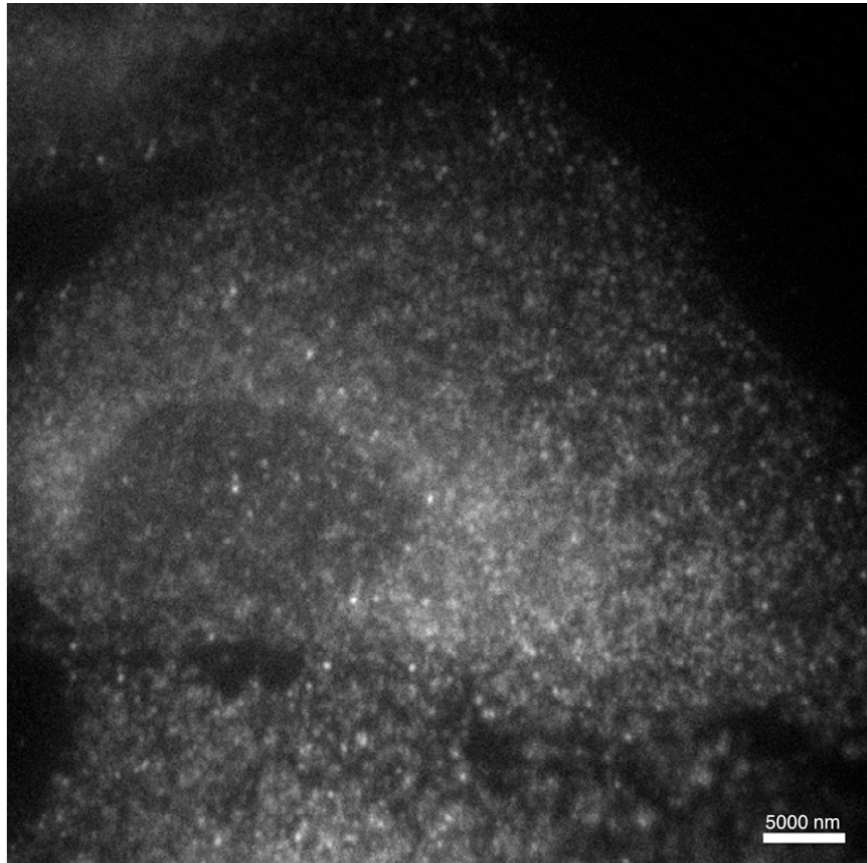


Figure 3.38. Wide-field imaging of NEMO immuno-fluorescence staining in U2OS cells in TNF- $\alpha$  stimulated cells.

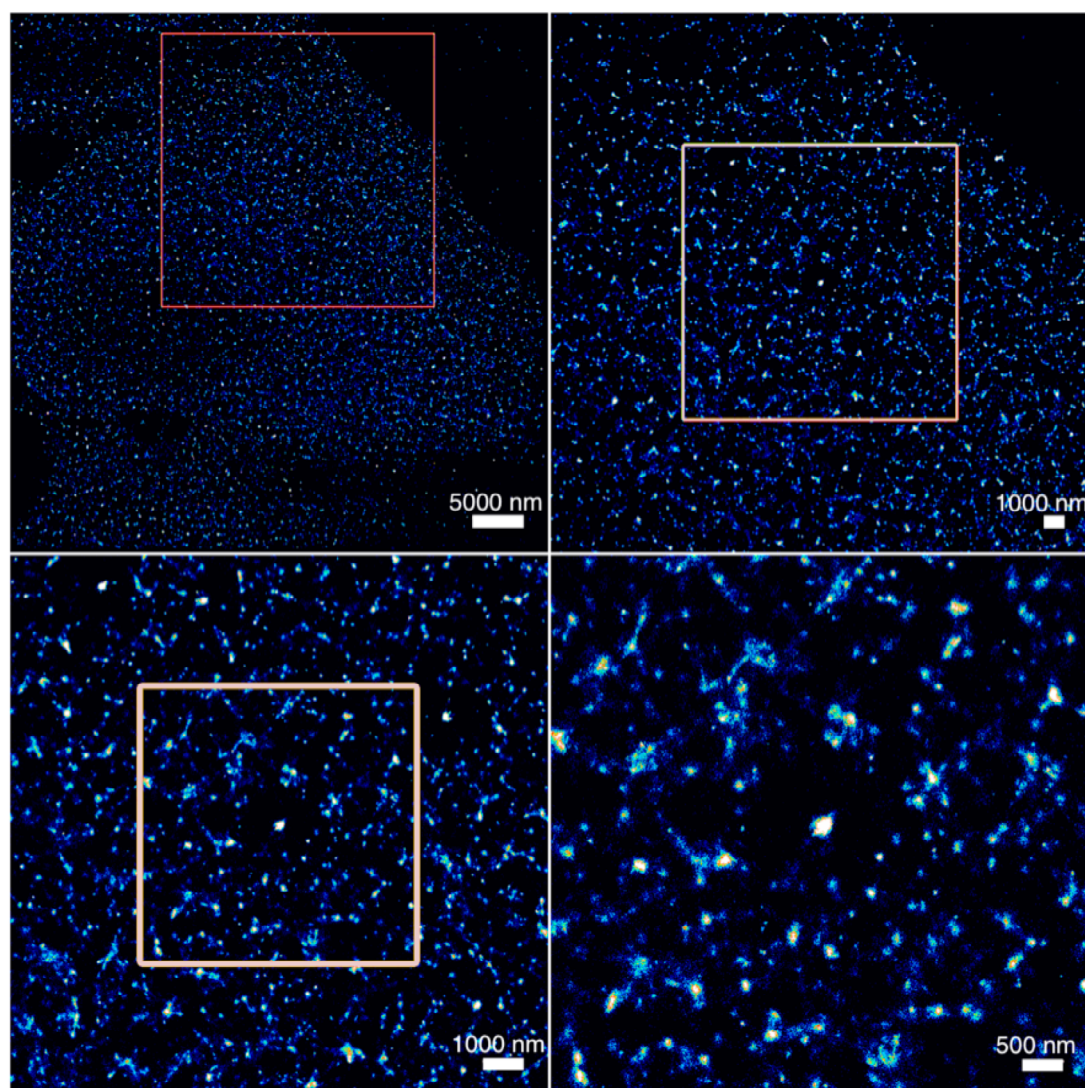


Figure 3.39. Super-resolution dSTORM imaging of NEMO immuno-fluorescence staining in U2OS cells in TNF- $\alpha$  stimulated cells. Pink square outlines correspond to zoom areas shown in the preceding image. Image is colour coded where blue colours corresponds to low-molecular density and white colours high-molecular density.

The analysis of the NEMO clusters in each of these conditions further differentiates phenotypes derived from NF- $\kappa$ B, as shown in Figure 3.40. The number of detected particles cannot be directly converted into a number of detected NEMO molecules, as the Cy5 fluorophores are able to switch multiple times yielding several particle detections per molecule. Notwithstanding, the number of detected particles is proportional to the number of NEMO molecules and the high-variation of detected particles in cluster with sizes of 150 nm or greater suggests a larger accumulation of NEMO in these clusters within stimulated cells with IL-1 or TNF- $\alpha$ .

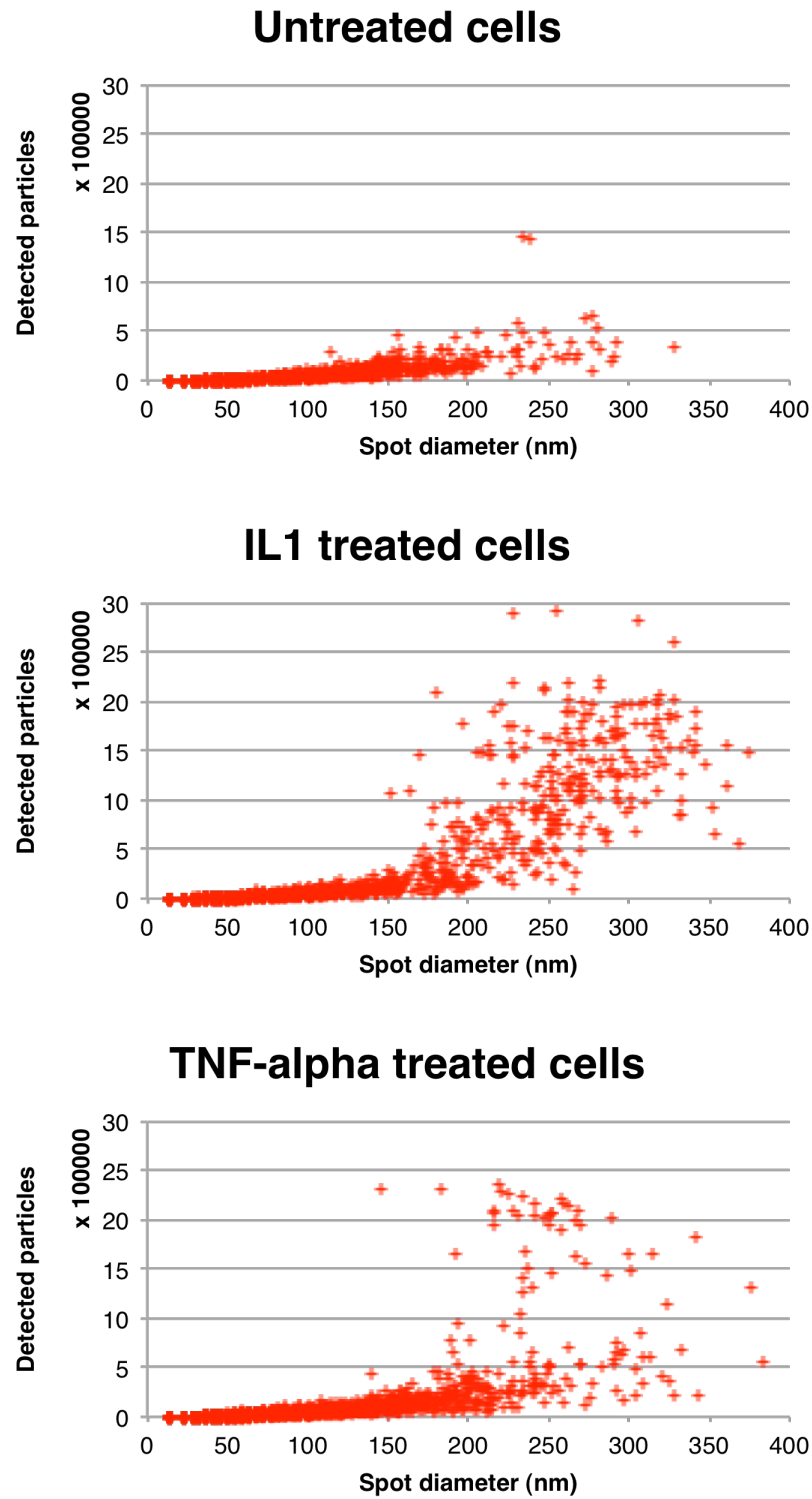


Figure 3.40. Particle detected within NEMO clusters (spots) on the untreated, IL-1 or TNF- $\alpha$  treated cells. Data was collected in 3 arbitrary cells within each condition.

### **3.3.4 Conclusions and outlook**

Super-resolution imaging of NEMO provides a novel view into its territories in the cell membrane vicinity. A new network-like structure for NEMO at the sub-diffraction level is here presented for the first time. Furthermore, super-resolution dSTORM imaging provides a quantitative view of the NEMO molecular accumulations at a scale of few nanometers. Remarkably these features are beyond the resolvable power of classical light microscopy methods as shown in the comparative wide-field fluorescence images. This clearly shows the potential of super-resolution techniques applied to the study of the NF- $\kappa$ B pathway.

NEMO labeling shows a clear distinguishable phenotype in NF- $\kappa$ B activated cells through IL-1 or TNF- $\alpha$  treatment, namely NEMO accumulation within clusters and subsequently NEMO depletion in the surrounding regions of the clusters. These observations lead us to question the spatial relationship between some of the other NF- $\kappa$ B pathway components. Preliminary data already suggests the need of K63 or linear poly-ubiquitin chains for the formation of the NEMO network-like structure.

Future experiments will focus on the discovery of the mechanisms involved in the formation of the NEMO network and cluster formation. Multi-color super-resolution will be used to address the co-localization between NEMO and other proteins in order to study their possible interaction.

## **4 General Discussion and Perspectives**

This work aimed to improve the PALM and STORM techniques and through them bring new insights into biological structures within cells at the super-resolution level.

Within the research presented in this thesis, four scientific fields are tackled: (i) applied optical microscopy – by creating a home-built setup able to achieve 3D super-resolution; (ii) computer vision – by developing QuickPALM, an algorithm able to achieve real-time processing and control of super-resolution imaging systems; (iii) biochemistry – through the development of a new class of fluorescent photo-switchable probes for super-resolution microscopy and (iv) structural cell biology – by characterizing the ultra-structures formed by the NEMO protein at the sub-cellular level and its relation with the NF- $\kappa$ B pathway.

The first step of my work consisted of the design and assembly of a super-resolution microscope. This was achieved initially by exploiting and adapting a commercial TIRF microscope supplied by Andor Technology (see section 5.1.1 for full details) and then through the creation of two home-built super-resolution systems, one in Institut Pasteur (M. Lelek was the main researcher behind the construction of this setup) and then by single-handedly assembling another system in South Africa (see section 5.1). Through the exploitation of the application of a cylindrical lens to the optical path of the microscope, I was able to use astigmatism as a source to achieve 3D super-resolution as detailed by the X. Zhuang group (45). With the help of M. Lelek, we further simplified this setup and I was able to develop the software needed to fully control of the microscope. This software also lead to the development of QuickPALM.

Currently SMLM hardware has unfolded into many different configurations, most aim to tackle 3D super-resolution through different methods. In a biplane (BP) detection scheme, a 3D stack of two slightly displaced Z-planes is acquired over time, the position of detectable molecules can then be extracted in Z-space. Biplane has been found to provide a better z-range than 3D SMLM by astigmatism, but on the other side, astigmatism provides a better resolution in the immediate vicinity of the

objective focal plane (46). Another set of approaches tries to constrain the illumination in the Z-axis in order to avoid the activation of fluorophores outside of the resolvable Z-space therefore reducing unwanted sample background, increasing localization accuracy and reducing the depletion of fluorophores outside of the resolvable volume. This is achieved by iPALM (i = interferometric), taking advantage of the interference field created by two-opposing objectives (similar to 4Pi), the technique can yield higher resolutions than the biplane or astigmatism 3D methods but is more sensitive to the sample thickness or complexity as the interference field can be highly modulated by the sample morphology (152). Two-photon temporal focusing in conjunction with water immersion objectives has also been used recently by the H. Shroff group to achieve high-penetration depths in PALM microscopy (153). Recently E. Betzig and co-workers developed the Bessel beam plane illumination technique (154), that has not been demonstrated in tandem with PALM or STORM yet, but has the potential to achieve high-depth super-resolution imaging by using two opposing objectives creating a light-sheet similar to that used in selective plane illumination microscopy (SPIM) (155). 3D astigmatism is still the easiest means to implement of this method, achieving high-resolutions in both XY and Z-space but at the cost of a high-sensitivity to the active fluorophore density that needs to be kept low.

Only in 2011 did commercial PALM and STORM systems become partially available to researchers. Still, currently these are in a beta-testing phase, therefore, not being completely accessible to all the scientific community. By describing our super-resolution systems in detail on the QuickPALM publication and also on its website, we allowed multiple researchers to clone my microscope systems for 3D PALM and STORM with astigmatism. The group of Dr. Jan Schmoranz (Freie Universität Berlin) represents one of the groups that has profited from our developments.

The development of QuickPALM in conjunction with the real-time acquisition control features allowed me to provide a complete solution for acquisition, reconstruction and visualization of 3D PALM and STORM images to the research community. This feature is still not achieved by the competing methods. Without the high-speed processing of QuickPALM, which allows the visualization of the data in parallel to the acquisition, users would be forced to adjust imaging parameters such as activation and excitation by trial and error after multiple suboptimal experiments. The

QuickPALM method allows the dynamic inspection of the sample behaviour and the adjustment of the acquisition parameters “on the fly” for optimal imaging.

Today, several competing algorithms exist providing similar processing speeds with higher-localization and detection accuracy (101, 156). These are able to do so with the help of the high-speed graphical processing units (GPUs) found in common personal computers. Notwithstanding, this process makes these kinds of algorithms bound to a specific operative system or computer hardware architecture. Furthermore, the closed-source nature of their release does not allow researchers to adapt them to their own needs.

QuickPALM has the major advantage of being built in a language agnostic from the computer hardware architecture itself (Java) and being open-source. As such, it is remarkably easy to install, to be modified and it can be run on any computer supporting Java. Furthermore, QuickPALM is a complete package producing all the needed features for super-resolution imaging, providing an easy-to-use user interface able to go through all the steps needed in PALM and STORM, namely, single-particle detection, super-resolution image reconstruction and drift-correction.

A dominant challenge in SMLM is minimizing light induced cell damage (83, 84) as super-resolution techniques tend to dramatically increase the photo-damage caused to the cell by either increasing or prolonging the amount of light needed for imaging when compared to classical fluorescence microscopy. Conventionally in fluorescence imaging the entire field of view is illuminated uniformly, both light-excitation and acquisition time are adjusted so as to obtain a high enough signal-to-noise ratio (SNR) to resolve cellular structures of interest. Yet, fluorophore concentrations within cells vary, leaving researchers with the decision of how to best set the illumination characteristics at the cost of either under-exposing or over-exposing sub-regions of the image.

Controlled light-exposure microscopy (CLEM) introduces the concept of applying a non-uniform illumination to the imaging area in laser scanning systems where on a pixel-by-pixel basis the light-exposure is interrupted if a sufficient SNR has been achieved (157). As a combination of “hardware” and “software” approaches, this method improves image-quality and severely reduces photo-toxicity (158). Problematically, SMLM uses cameras that only permit the parallel acquisition of all the pixels composing an image theoretically preventing the implementation of CLEM. Non-uniform illumination in time has been previously applied to SMLM in the work

of Betzig *et al.* (3) where the sample activation is incrementally increased over time to compensate for fluorophore depletion. This concept can be further adapted by modulating the illumination both in the spatial and temporal domain with the help of a spatial-light-modulator (SLM). In SMLM two light beams are used: a low-intensity activation beam to induce fluorophores into an ON-state and a high-intensity readout beam to excite and bleach the fluorophore. By definition, the images acquired in SMLM have a sparse concentration of fluorophores. This means that most of the area subjected to illumination is not occupied by active fluorophores. By concentrating the readout illumination to the areas where only actively emitting fluorophores are present, a drastic reduction in the amount of light used for imaging is achieved therefore minimizing cell damage. A major focus of the QuickPALM (100) development will be to bring this feature forward by combining the power of real-time processing with the capacity for both SLM and acquisition hardware control brought by  $\mu$ Manager (103).

In STORM-like experiments a single fluorophore can photo-switch multiple times. A well-known concept in the super-resolution field is that this feature could be used to further increase by several-fold the resolution of the technique. The localization error of a single-fluorophore could be severely reduced by its multiple detection over the various switching cycles, through for example, averaging its multiple localizations. Unfortunately, this feature is somewhat difficult to achieve, as it is almost impossible to attribute a single-switch to a particular fluorophore when the fluorophores are densely packed together. Notwithstanding, by taking advantage of fluorophores with stable and known photo-dynamics it is possible to estimate and statistically determine the probability maps of localization to specific fluorophores and, as such, heighten the resolution of super-resolution imaging. The new fluorophores developed within the scope of the present thesis, called “blinkons”, support some of these features by providing well-defined and characterized photodynamics. Blinkons are a new kind of photo-switchable probes based on molecular-beacons, their hairpin structure is designed to stochastically open and therefore to transiently enable a fluorescence emitting state on the molecule.

The properties of blinkons seem to be stable across the different fluorophore moieties used in their structure, which is extremely advantageous since it allows their application to perform multi-colour super-resolution. By optimizing QuickPALM to



support the described resolution increase provided by multiple photo-switching aggregation and merging it with the stable photo-switching dynamics of blinkons, we might see the birth of a new super-resolution modality further breaking the resolution barrier.

One of the key aspects of blinkons is their capacity to photo-switch in physiological buffers (for example PBS), which allows their use in live-cell imaging. Still for this the labelling challenges discussed in section 3.2.4 have to be first addressed. One of the features that we are actively working on is the incorporation of blinkons into aptamers, therefore generating a system to label target proteins in live-cells. With this new feature blinkons will present themselves as strong alternatives to photo-activatable genetically encoded fluorophores, as they do not require activation pulses and yield a larger amount of photons, therefore, possessing a greater potential for increased resolution. Once again, merging QuickPALM's data-driven light modulation aspects will further increase the potential for live-cell imaging by reducing photo-damage in the sample.

My technical developments within the super-resolution field, implementation of the microscope set-up and development of QuickPALM have also been exploited to address the biological question of ultra-structures formed by the NEMO protein at the sub-cellular level and its relation with the NF- $\kappa$ B pathway. Although preliminary, the already generated data shows that only through imaging with super-resolution it is possible to resolve the sub-cellular territories of NEMO. This is due to the fact that the NEMO scaffold structure revealed by super-resolution exists at a sub-diffraction level impossible to be resolved with standard microscopy methods.

Within this project, our future aims will be to further correlate the spatial location of NEMO with other key proteins in the NF- $\kappa$ B pathway and their relationship with receptor activation. One of the difficulties we foresee is related to the low-throughput of the super-resolution process itself, which is caused by the required time to image a single dataset (typically 30 minutes). Within this time, the pre-acquisition bleaching needed to push most fluorophores to a dark state is a considerable bottleneck. Therefore, blinkons may in the future constitute the key tool to further speed-up this process due to their rapid pre-acquisition bleaching periods.

The work in super-resolving the NEMO territories has shown the great potential of PALM and STORM when used in parallel with total-internal reflection fluorescent microscopy (TIRF). By constricting the illumination to the immediate vicinity of the plasma membrane, TIRF can greatly increase the signal-to-noise ratio of observed fluorophores, this feature is extremely powerful not only in the study of membrane receptors and associated proteins as demonstrated on this work, but also for example in the study of host-pathogen interactions. Recently *Hess* and co-workers have used FPALM to examine a clustered membrane protein - influenza hemagglutinin (HA) (49). Influenza viral entry and membrane fusion is mediated by hemagglutinin (HA) and its visualization until recently was limited to classical resolution limits. To enter its host, the influenza virus uses HA to open a fusion pore in the endosomal membrane and then inserts its viral RNA into the host cytoplasm. Lipid rafts are believed to play an important role in the distribution of HA at the cell surface, though several theories exist on the nature and dynamics of these rafts. *Hess* and co-workers went on to use FPALM to discriminate between the various raft theories, which all propose for lipid rafts to exist at resolutions well below the diffraction limit of light. As in the earlier mentioned work of *Shroff* and co-workers, they were able to perform these experiments in live-cells principally because the diffusion coefficient of HA was low and thus a single-molecule of HA tagged with PA-GFP could be localized. Essentially, for such experiments in live cells, to successfully localize a single-molecule, the mean-squared displacement attributable to two dimensional diffusion (during acquisition) must be smaller than  $r_0^2$ , where  $r_0$  is the  $1/e^2$  radius of the point-spread-function.

One area, which has an intense interest in advances in the dissolving of the resolution limits of light microscopy, is the study of nuclear biology. The spatial organization of the nucleus, the apparently non-random organization of the genome within the nucleus and several of the processes surrounding transcription and gene expression are all questions ripe for the use of super-resolution techniques. Current microscopy approaches, in live cells, have focused on using statistical mapping to understand genome organization (159) and fluorescent microscopy techniques to visualize chromosome repositioning within the nucleus (160). These approaches have fallen short when it has come to the study of gene expression and transcription resorting to

fluorescent in situ hybridization (FISH) to take snap-shots of these events in fixed cells, albeit at times with single-molecule resolution (*161*).

Gene expression is a fundamentally stochastic process, and in some instances appears purposefully so [reviewed in (*162*)]. This makes the construction and modelling of gene networks especially difficult. Transcription is thought to occur in bursts with little known as to their source (*163*). One may be the existence of pre-initiation complexes formed on the promoter that may permit multiple rounds of RNA Polymerase II transcription (*164, 165*). Such complexes could form in so-called “transcription factories” where active genes would be recruited. Some evidence for transcription factories does exist though at best 3 differing transcripts have been imaged in putative factories (*166*). Where super-resolution could be most informative in this field is the ability to image all the species transcripts within these factories and to understand the contents of the transcriptional machinery in real time. This would give key insights into the fundamental process of transcription whose “molecular players” have only been observed as snapshots. Since there is great heterogeneity in transcription in even otherwise identical cell types, observing the minutiae of this process over several cells is perhaps the only way stochasticity can be understood.

## 5 Appendix

### 5.1 The Ph.D. research time-line and additional results

I started my PhD work with Dr. Musa M. Mhlanga at Instituto de Medicina Molecular (IMM, Lisbon, Portugal) in 2008. From the beginning it was clear that the technology we needed to employ in our research goals was not fully established, and as such, there was a great call for the implementation and development of the new quantitative microscopy methods we required. There were three different aspects we needed to tackle: (i) to set up the super-resolution microscope hardware, (ii) to develop the software infrastructure to generate the super-resolution data and (iii) to generate labelling tools for our specific goals. Into a certain extent, only after the establishment of these would be possible to obtain relevant biological data.

Stochastic optical reconstruction microscopy (STORM) (5), a method first described in 2006, was our tool of choice. The super-resolution STORM technique is based on the stochastic photo-switching of synthetic fluorophore pairs in TIRF based microscopes. One of the most interesting aspects of it was the potential to develop new probes by applying STORM compatible synthetic fluorophore pairs into molecular-beacons, allowing us to study the presence single-stranded oligonucleotides at the super-resolution level, such as transcribed mRNA.

To simplify the hardware implementation, we initially acquired a commercial Andor TIRF system tailored with some of the features required. While we overtook preparations to acquire the system, I started a small traineeship for 4 months with the group of Dr. Jean-Christophe Olivo-Marin at Institut Pasteur (IP, Paris, France) (see Table 5.1).

While performing my traineeship at Olivo-Marin's group, I was able to learn from the expertise of his group in quantitative microscopy data analysis and started developing the initial tools for single-molecule localization and tracking required for STORM. It rapidly became evident that one of the major bottlenecks to be tackled was the large computation time needed to identify and pinpoint sub-diffraction particles (single-molecules) in super-resolution data. This would typically require iterative maximum

likelihood estimators fitting Gaussian models to each individual particle. In STORM, we would need to apply this process to millions of fluorophore molecules.

A possible solution to this problem could be achieved by parallelizing the analysis of the large amount of data composed by a single STORM experiment into multiple computers. To implement it, I tried to take advantage of the C4 cluster (more details in section 5.1.2) at the Council for Scientific and Industrial Research (CSIR, Pretoria, South Africa).

At the end of my stay in Olivo-Marin's group, I started working for the first time on the ThunderSTORM software (see section 5.1.2), a set of high-performance algorithms for STORM data analysis able to work seamlessly in multiple computer processing units (CPUs) both on the same machine or remote.

### **5.1.1 Microscopy challenges**

The next step taken was to oversee the setup of the new Andor TIRF microscope in the CSIR (South Africa) and to set up the software framework required for experiments (see Table 5.1). Our system was “experimental” in the sense that it was the first system with that specific configuration ever assembled and sold by Andor. This actually generated major setbacks as we rapidly discovered unforeseen problems and challenges with the hardware, such as the TIRF adaptor not being able to function properly. Although, Andor provided us technical support to fix the problem, this led to a troubleshooting period and, therefore, to some delays. One lesson was learned, “experimental” may imply having a system in the forefront of technology, but does not necessarily convey stability.

Meanwhile, drift became apparent to be a respectable challenge. The single-particle imaging procedure we needed typically required extended acquisition times (minutes to hours) during which it is natural for the sample to present an unwanted movement over space in regards to the objective. Are several the sources that can generate drift, the most preeminent are: airflow over the sample, temperature variations and human interaction. Drift correction can be done partially analytically through the use and tracking of fiduciary landmarks on the sample such as fluorescent beads. Unfortunately, this method is not efficient for extended drifts (generally more than one micron) as different aberration territories on the microscope objective start having

their toll on the particle localization. Another aspect is that the analytical drift correction is more efficient in the XY-axis of the microscope than in the Z-axis. Currently, there are commercial auto-focus feedback systems implemented in the hardware that minimize the Z-axis drift. Our initial Andor system did not feature this hardware, and as such, we had severe difficulties with the Z-drift.

The final hardware challenge was the light excitation power required for STORM. In this technique, multiple fluorophores need to be turned-off (“bleached”) in few milliseconds, a time interval directly related with the light intensity projected over the sample. The Andor system injected laser light over the sample via a fibber optics system, which implied loss of  $\sim 40\%$  over the total laser power caused by the fibber coupling. This loss in tandem together with the low power of the diode and solid-state lasers supplied (40-60mW) prevented us from rapidly switching-off the fluorophores. The referred obstacles did not hamper us from achieving our goals. In fact these have allowed us to gather enough knowledge leading to the latter development and assembly of our own home-built super-resolution microscope system in South Africa (see Table 5.1).

### **5.1.2 The rise and fall of ThunderSTORM**

ThunderSTORM is the codename of our first analytical approach for single-particle detection and super-resolution image reconstruction, in which I have tried to implement state-of-the-art software methods for high-performance analysis of the data. The challenge was clear, as a single super-resolution dataset was typically constituted by hundreds of thousands of images (a single image corresponds to around 0,5 MB), we required a software framework able to deal with multiple datasets and process them in a short amount of time, preferably in real-time.

At the core of ThunderSTORM was an HDF5 data management system. HDF5 is a file format designed for efficient high-speed data storage and exchange. It is specially developed to cache multi-dimensional matrix data and is one of the preferred formats for most physicists collecting massive amounts of information, such as in particle-accelerators or research nuclear reactors (my first contact with HDF5 was through collaborations with an accelerator in the European Organization for Nuclear Research, CERN). Our home-built HDF5 database was able to store the massive raw

unprocessed data acquired from our camera, and supply it as hyper-dimensional packages on demand to requesting “workers”.

To be noted, a “worker” in this context corresponds to an independent instance of an analysis algorithm working within a single CPU. In comparison, a “job-server” is an algorithm specialized in dispatching workloads (data packages to be analysed) to volunteer “workers”.

The ThunderSTORM HDF5 database acted as an independent software instance able to communicate with other algorithms over the network (via socket). It seated over a Redundant Array of Independent Disks (RAID) server with a large amount of free space available for data storage and consultation (see Figure 5.1). It observed the acquisition by monitoring a selected folder where new incoming images were streamed to and pulled each image for storage, in parallel it communicated to any “worker” that a new image was available for treatment.

On a different level, an algorithm on a workstation within our lab would work as a first layer of data-analysis. It would pull new available images from the HDF5 database, denoise each and find particles within the image without engaging high-precision localization (in essence, this algorithm was a simplified version of the latter developed and published QuickPALM – see section 2.1). The particles were then classified by a k-means clustering algorithm in order to remove misshaped objects such as particle packs too dense to be resolved. The clustering procedure also allowed extracting the most common shape of the particle in order to estimate a parametric description latter given to the more precise (and slower) particle localization estimators. The particles were then fed to available “workers” in the cluster (see Figure 5.1).

Finally, available nodes (workers) in the cluster would receive the segmented particles and localize each through a maximum likelihood estimator and return the particle position back to HDF5 database. I had other features for this level, such as particle tracking and movement correction, but these never got to be implemented.

## Analysis Framework

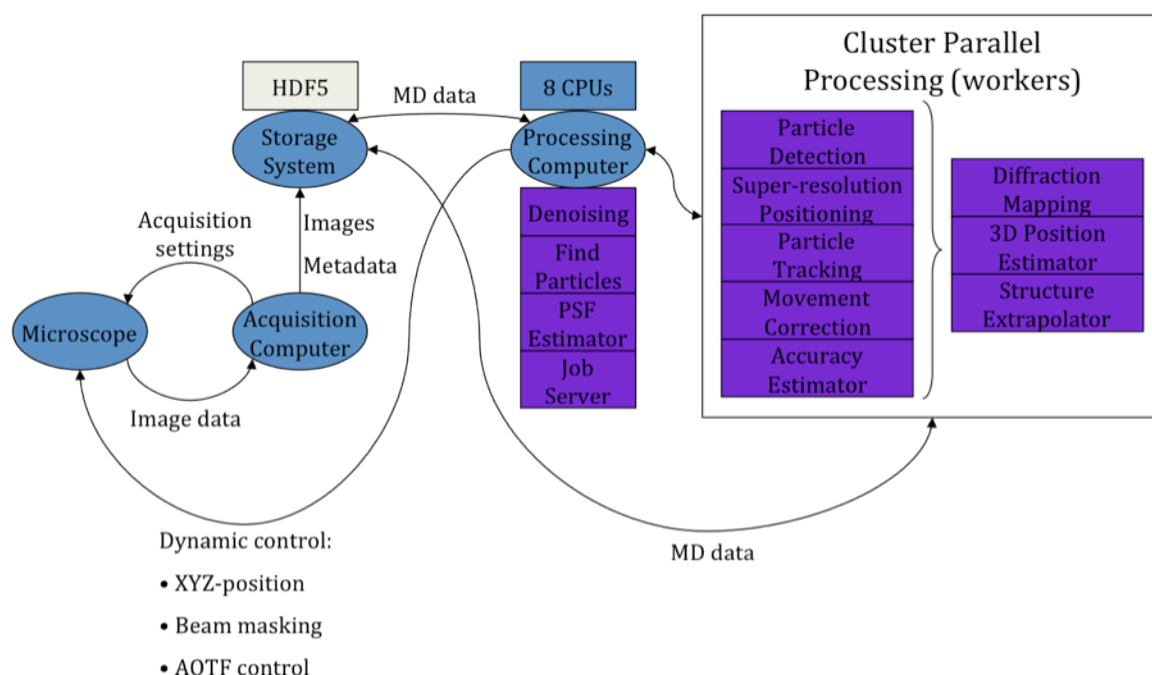


Figure 5.1. ThunderSTORM data analysis framework. ThunderSTORM was composed of 4 levels, each corresponding to an independent program: (i) on the first level an observer program detected new incoming image data streamed from the camera, typically controlled by the  $\mu$ Manager software (103), and passed it to the HDF5 database; (ii) the HDF5 database stores data, generates events informing any listeners that new data is available for processing; (iii) a first processing computer denoises each image and segments any found particles, they are then passed to available workers on the cluster and in parallel clustered together to generate a parametric estimation of the PSF; (iv) the workers on the cluster super-resolve the position of each particle and retrieve all additional possible data.

At this point we got into one vital pitfall, namely the way the cluster was set and managed.

The C4 cluster is a system shared by all the research teams at the CSIR. It corresponds to a 3-in-1 cluster (a 184 Opeteron-CPU cluster, a 64 Xeon-CPU cluster and a 64-Itanium2 CPU cluster). The cluster was designed with the goal of having a large number of queued or scheduled programs processing a relatively small amount



of data for large periods of time. For this reason it had a dedicated storage system shared by all the worker nodes and the worker nodes could not be accessed directly by users or programs neither could communicate between each other. All communication was managed through a central node that then passed instructions to the worker nodes (see Figure 5.2).

Oppositely, we required a large number of inter-communicating programs (one per node) to process a high amount of data supplied by our own external database. This on-demand basis directly conflicted with the queuing/scheduling procedure and the required nodes to interchange information dynamically.

I solved these setbacks in a non-trivial way, by hacking the cluster. Normally, users would need to login to the central node to then push a job to the worker nodes. In addition, the worker nodes could also simulate a user login to the central node and this would be the trick I used. When we needed to use the cluster on-demand, we would load a certain share of worker nodes with a sleeper program. The program would then login to the central node and set a port-forward between both nodes (via ssh). Once this connection was established, the sleeper program would then extend the port-forwarding between the central node and our own workstation where the analysis program sit (creating a connection that otherwise would not exist). This way, we actually reversed the connections, instead of being our workstation connecting to the cluster nodes (a procedure not possible), it were the cluster nodes that connected to us. In parallel, once our workstation was made aware of the nodes through their initial connection, they were then also made aware of each other, allowing their needed inter-communication (see Figure 5.2).

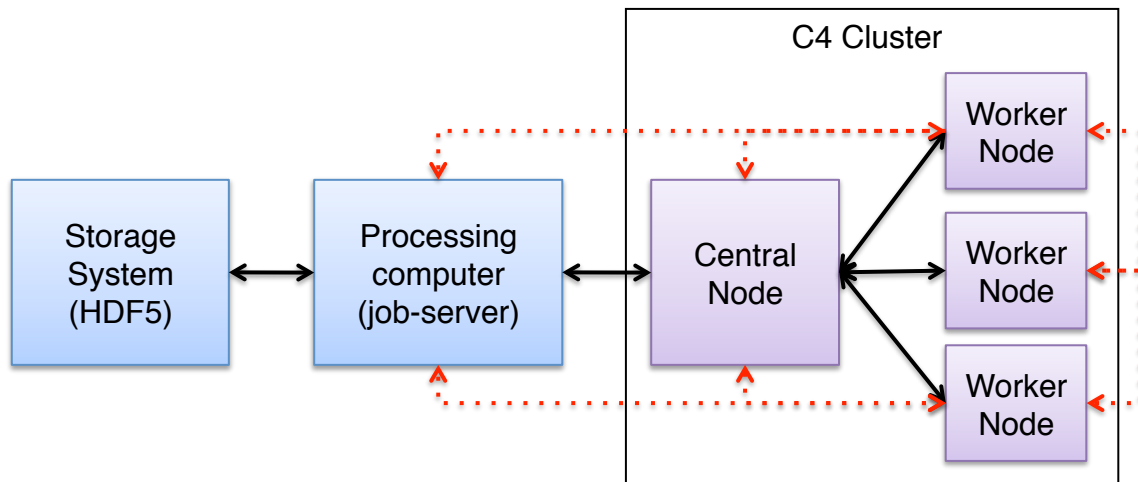


Figure 5.2. ThunderSTORM connection scheme to the cluster. Black lines corresponds to the “canonical” communication method. Red lines correspond to the “non-standard” connections created on-demand by our algorithms.

This process was not optimal for several reasons. The main one was that the cluster was not designed to be run this way, and although we had the blessing of the cluster manager, we were exploiting security flaws in the cluster management software that allowed us to be in advantage in comparison with other users. On the other side, the port-forwarding system forced us to encrypt our connections, generating severe data transmission latency and lag in parallel to a CPU overhead.

At this time, I joined as a visitor scientist the group of Christophe Zimmer at Institut Pasteur (Paris, France). Zimmer’s group was at that time starting projects within the field of super-resolution.

The downfall of ThunderSTORM came about when we discovered a final fatal problem, the very slow Internet bandwidth speed in South Africa. My plan was to continue the development of ThunderSTORM in Paris by connecting remotely to the CSIR and pushing the results between the two institutes. Unfortunately, up to until recently, the Internet speed in South Africa was forbiddingly slow making the full remote analysis effort a fruitless effort. In fact, the Internet bandwidth speed was such a problem that latter we became aware of research groups in astrophysics using carrier pigeons to transport memory sticks with critical data between remote institutes, an alternative faster than the direct network data transfer itself (see <http://news.bbc.co.uk/2/hi/8248056.stm> for a news report).

I publically released a critical component out of the core of ThunderSTORM that made all the system possible, the Simple Remote Python (SRPy) package (see <http://code.google.com/p/srpy/>), which corresponds to the engine that enabled ThunderSTORM to seamlessly communicate with multiple computers and divide tasks over several CPUs.

My own description of SRPy can be found on its site and is as follows: *“Simple Remote Python (SRPy) intends to harness the power of the Python language by allowing multiple python programs (instances) to seamlessly communicate and share information between each other. As such, each CPU (or core) in each computer can be considered as an individual that can request for other individuals to store information or run processing tasks. In this context, SRPy abstracts itself from the physical boundaries between processors and computers by looking at them simply as volunteer workers that are able to deal with workloads - this workers can even work in a social manner by communicating with each other on a non-centralized way, sharing information and processing requests.”*

The SRPy package has gained increasing popularity over time. Today it has over 500 known users and is part of several software packages, such as the Andor iQ acquisition software developed by Andor Technology.

### 5.1.3 From ThunderSTORM to QuickPALM

Zimmer’s group started assembling a home-built super-resolution microscope few months after my arrival (see Table 5.1). I had the chance to participate on the system design, still most of it was an implementation of my colleague Mickael Lelek. The referred system was based on a previous built super-resolution microscope at Maxim Dahan’s lab at the École Normale Supérieure (ENS, Paris, France).

Zimmer’s microscope system had several advantages in comparison to our own commercial South African version. It was built with high-powered lasers (100 mW) injected to the objective without the use of fiber-optics, allowing us to have the required fast bleaching of the activated state of fluorophores. Additionally, the system featured an active hardware based Z-drift compensation system, which facilitates imaging over long periods.

By this time, the majority of my data was being acquired using the microscope from Zimmer's group. This together with the difficulties encountered, led us to stop the development of the ThunderSTORM framework implemented in South Africa.

One challenge we had to face with the new microscope system was the absence of acquisition software able to deal with the complexity of the PALM/STORM data acquisition. We needed software both able to provide laser pulsing for photo-activation and streaming of hundreds of thousands of images.

To tackle this aspect, I started to implement an acquisition software based on  $\mu$ Manager (103) for my experiments. This software started initially as an interface between ImageJ,  $\mu$ Manager and parts of ThunderSTORM developed to control hardware. Latter this converged to two independent software packages. One was  $\mu$ Manager itself, a software not developed by me, which was responsible for the camera streaming. A second software, developed by me, enabled the laser pulsing control required for the photo-switching in PALM and STORM. The latter was renamed as "Laser control for QuickPALM" and became an integrated part of the tools released in my Nature Methods paper.

Core parts of this software development were also publically released as the "Python for ImageJ" (Py4IJ) project (see <http://code.google.com/p/py4ij/>).

At this moment, we started collaborating with the Shawn Lewenza's group, an expert in bacteriology. Our goal was to study the distribution of the pCHAP protein family within pseudomonas bacteria (Table 5.1). We believed these proteins should be associated with an internal helix-like structure (167). Jost Enninga's at Institut Pasteur graciously allowed me to use his lab for bacteria culture and perform the experiments. Our initial strains of the pseudomonas bacteria expressed pCHAP-mCherry fusions. We intended to super-resolve the mCherry fluorophore by photo-switching induced through ground state depletion. The first datasets acquired represented our first super-resolution data of biological samples.

To analyse this data through single-particle detection and super-resolution reconstruction, I started working on a set of ImageJ tools. Once again, these were based on the initial code developed for ThunderSTORM. I had a notion that some of the "find particle" routines previously implemented were able to yield super-resolution localization of particles at high-speed, without the need of iterative fitting algorithms making the whole data processing step extremely slow.

By exploiting this aspect and through several optimizations I arrived to QuickPALM – my own ImageJ plugin for real-time processing of PALM and STORM data (Table 5.1). The whole concept behind QuickPALM was the idea that a simple center-of-mass method adapted to the CLEAN algorithm could provide a robust method for super-resolution analysis. QuickPALM was able to perform over a thousand-fold faster than my previous implementation of a maximum likelihood algorithm, with a minor loss in resolution (in the range of 10-30nm loss for Cy5 stained cells). My goal was not to achieve the best localization-accuracy algorithm but the most useful one (see section 2.1 for our publication on QuickPALM). QuickPALM currently has over 600 known users.

Unfortunately, mCherry was not efficient as a super-resolution fluorophore. This fluorophore provided very few re-activation cycles causing a high-sparsity on the reconstructed images (see Figure 5.3). Posterior attempts were made to fuse pCHAP with mEos2, a more efficient photo-activatable fluorophore, but these had to be left in stand-by in favour of other projects.

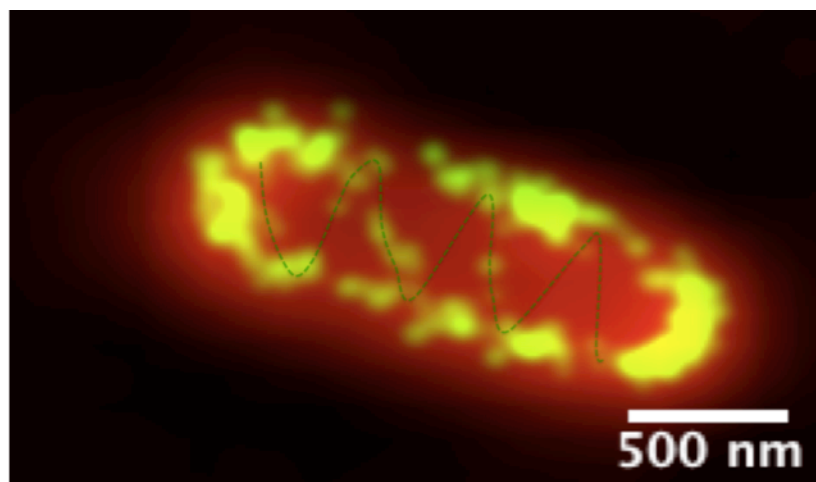


Figure 5.3. Super-resolution image of pCHAP6672-mCherry in the pseudomonas bacteria. Red corresponds to a wide-field image of the bacteria, yellow dots are the super-resolution localization of the pCHAP6672-mCherry fluorophores, and the green line intends to demark the helix pattern of the protein.

### 5.1.4 Blinking molecular-beacons

Since the beginning of my PhD we had focused on the possibility of using molecular-beacons as super-resolution probes. This feature would allow us to super-resolve mRNA territories within the cell nucleus and cytoplasm. Our original idea was to try to couple Cy3-Cy5 fluorophore pairs to molecular-beacons (see Figure 5.4). Cy3 is a known fluorescence activator for bleached Cy5, first described by the work of the Zhuang group (5).

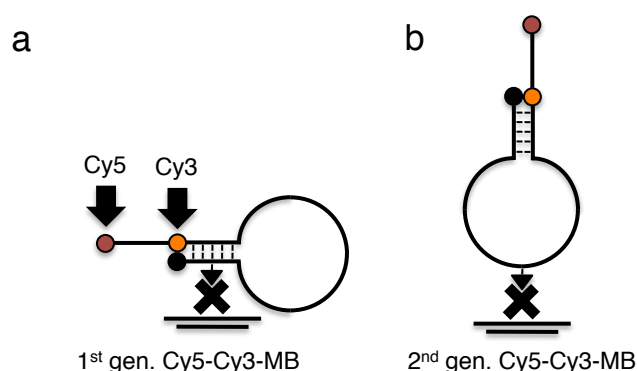


Figure 5.4. Schematic structure of the initially designed Cy5-Cy3-MB probes (1<sup>st</sup> and 2<sup>nd</sup> generations) for STORM imaging.

Conceptually, if we could disable the fluorescence of the Cy3 moiety when the beacon was on a closed state, then the Cy5 fluorophore would only reactivate by going through a slow triplet-state to ground-state regression. This would allow us to differentiate between the two states of the beacon: when these would be opened and the Cy3 not quenched or when these would be closed and the Cy3 quenched.

One of the controls I performed was to observe the fluorescence of the Cy3 moiety of these beacons at the single-molecule level through a flow cell system. We wanted to certify that the Cy3 would be correctly quenched when the beacons were on the closed-state and emitting on the open-state.

To our surprise, I could never efficiently quench the Cy3. Instead, the moiety would transiently transition between emitting and non-emitting states. This was against our goals and as such, something we wanted to avoid. For several months I tried to determine if we were observing non-specific blinking caused by auto-fluorescence of

contaminant molecules inserted into the flow cell by our reagents. In addition, I tested several oligo-nucleotide structures to try to discover a method to stabilize the quenching of Cy3.

Throughout the experiments performed, it became apparent that this transient blinking effect could actually be explored as a means to create super-resolution stochastic probes. This exploitation led to the development of Blinkons, a molecular-beacon like structure that generates multi-colour tuneable photo-switchable probes (described in section 3.2).

### **5.1.5 Super-resolving neuron vesicles**

In 2009 during a EMBO workshop in Lisbon, I met Eugenio Fornasiero, a researcher in the field of neurosciences. A collaboration was initiated with the aim of studying the role of synapsins as a regulator of synapse development and function. Synapsins are the first identified vesicle-specific proteins present in all organisms endowed with a nervous system. Generation of a knock-out mice for the multiple synapsin isoforms had shown a decreased total amount of synaptic vesicles (SVs) in parallel to the fewer presence of SVs at presynaptic sites (168).

Eugenio's model proposed that synapsins were implied in the recruitment and immobilization of SVs at synapses, possibly through the physical tethering of vesicles.

To test this hypothesis Eugenio produced a triple knock-out (TKO) mouse model of the three distinct genes (synI, synII and synIII) responsible for the synapsins expression. We could then compare the phenotype of the knock-out model against a wild-type. Eugenio used immuno-fluorescence staining against vesicular glutamate transporters (VGlut) to decorate SVs and against bassoon (a presynaptic protein) to decorate the presynaptic region (see Figure 5.5).

3D direct-STORM (dSTORM) imaging (6, 100) of both wild-type and TKO neurons cells showed evidence of the expected phenotypes (see Figure 5.6). Latter, electron microscopy also confirmed the phenotypes observed.

## Neuron

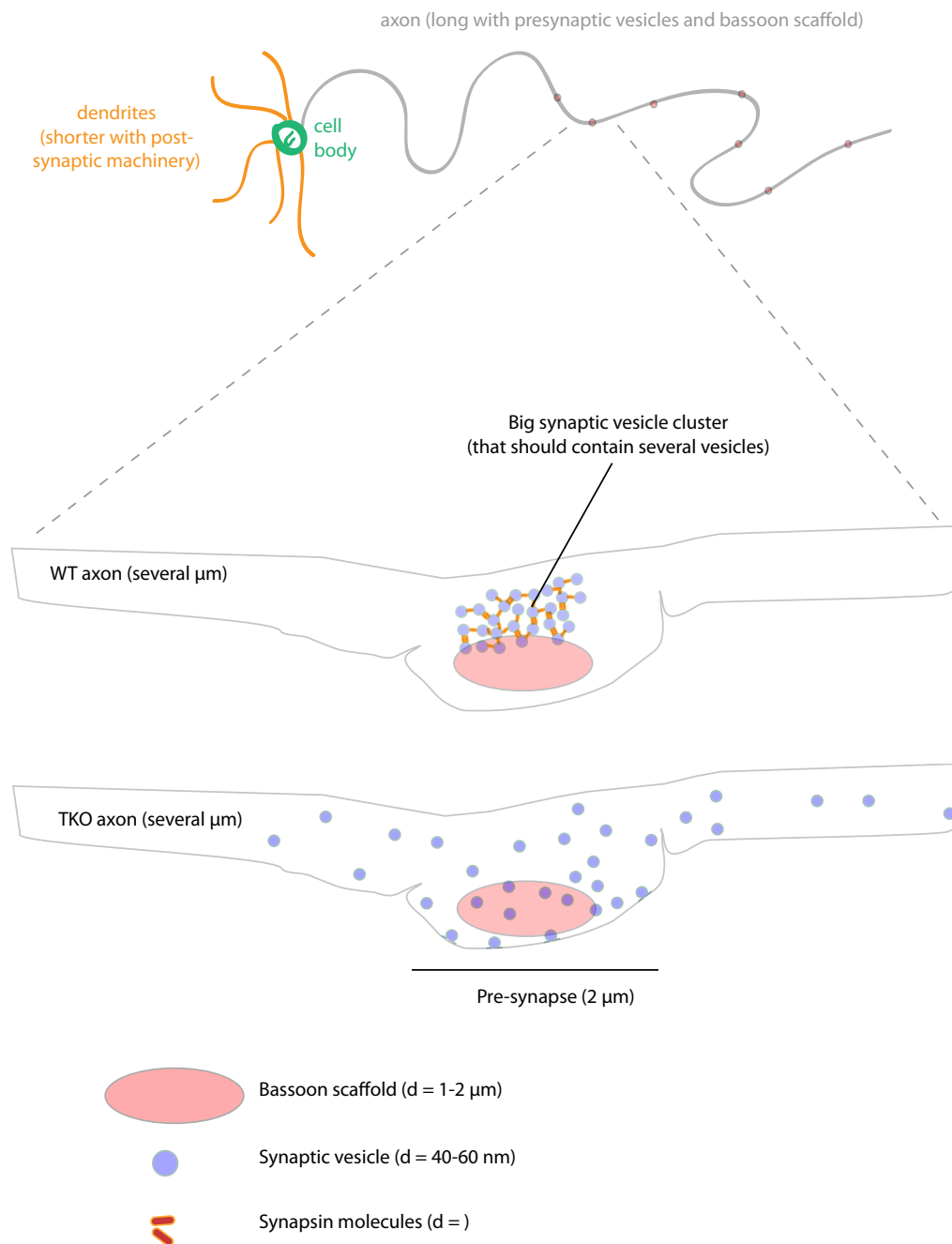


Figure 5.5. Model for synapsin regulated synaptic vesicles clustering in presynaptic regions. Comparison of expected wild-type and synapsin (synI, synII, synIII) knock-out phenotypes. Image courtesy of Eugenio Fornasiero.



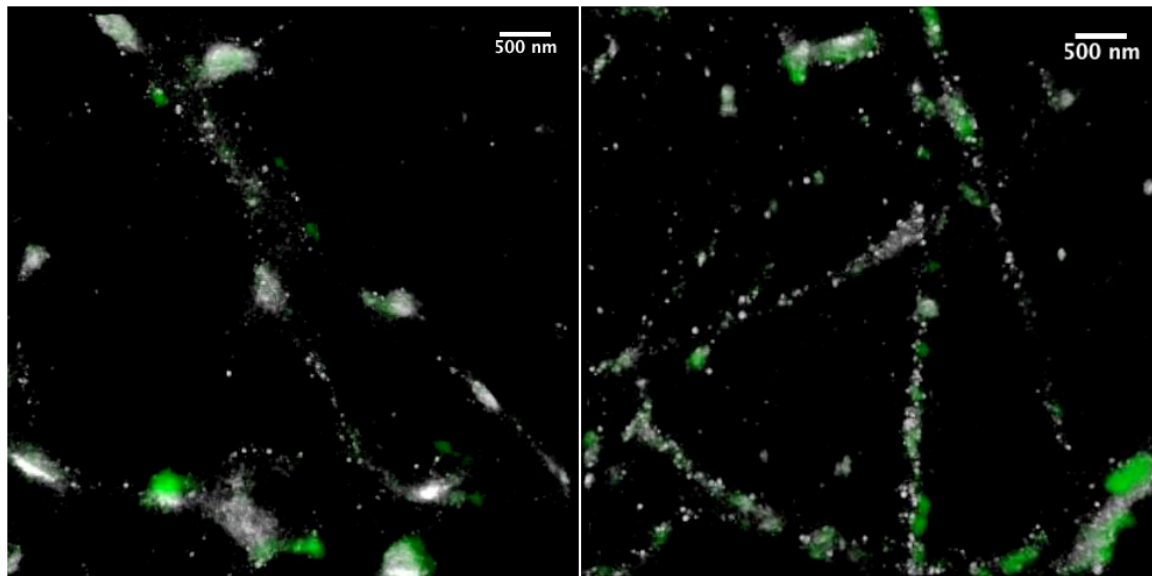


Figure 5.6. 3D dSTORM image of axonal tracks in neurons. Green represents the bassoon labelled presynaptic region, white the VGlut decorated synaptic vesicles. Left image is from wild-type cells and right from the synapsins TKO cells. On wild-type, SVs concentrate mostly on presynaptic regions; on synapsins TKO, SVs can be seen dispersed all through the axonal tracks.

The collaboration with Eugenio extended itself beyond the study of the role of synapsins as neurons revealed themselves to be ideal cells for super-resolution imaging. Their high flatness implied a low contribution of unwanted background fluorescence from active fluorophores and provided an excellent environment for 3D super-resolution with astigmatism. Eugenio provided me the cells used on the QuickPALM publication and Blinkon section of this dissertation.

Some of the best super-resolution images I have been able to acquire have been from neuron cells, such as the example of Figure 5.7, where a single synaptic vesicle is super-resolved at an estimated resolution of 20 nm.

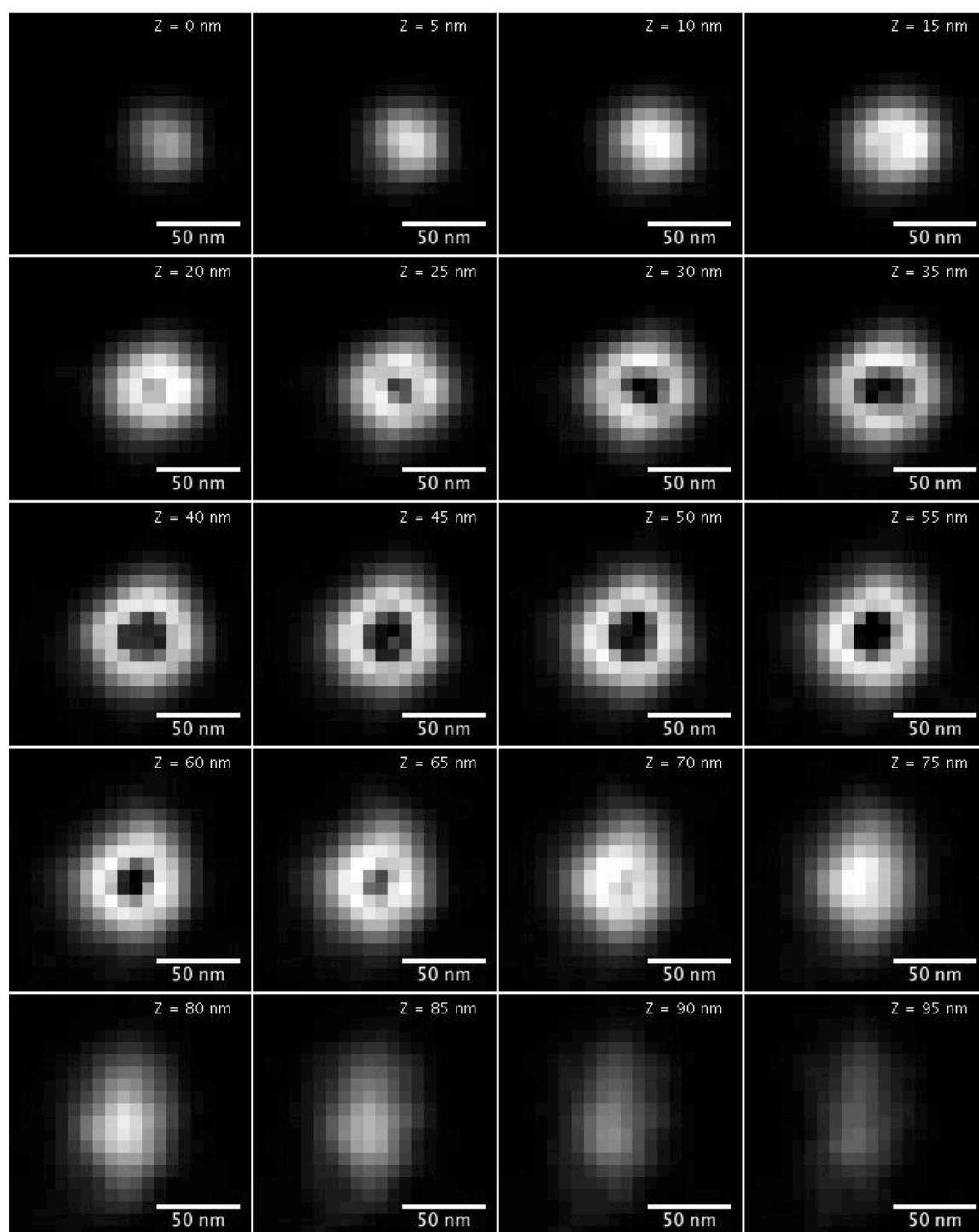


Figure 5.7. Individual synaptic vesicle super-resolved by 3D dSTORM. Labelling by immuno-fluorescence against VGlut labelled with Alexa488.

### 5.1.6 Looking at NEMO with super-resolution glasses

In October of 2010, a collaboration was established with Dr. Fabrice Agou's group in Dr. Michel Veron's unit at Institut Pasteur. The goal set was to study the sub-cellular territories of the NF- $\kappa$ B Essential **MO**dulator (NEMO) protein and its modulation upon the NF- $\kappa$ B pathway activation, which is approached in depth in section 3.3.

### 5.1.7 One PhD, two continents, five different groups

All the work I developed during my PhD was not possible without the help of the multiple researchers, namely, my supervisor Dr. M. Mhlanga, Dr. C. Zimmer, Dr. JC. Olivo-Marin and Dr. F. Agou. Their five groups (Mhlanga's at IMM and CSIR; Zimmer's, Olivo-Marin's and Agou's at IP) fostered my research. The interaction with all my colleagues was essential for the development of the present Ph.D. Another key group involved was Dr. J. Enninga's group (also at IP), where the majority of my "wet lab" experiments were performed. The physical location over time where my research has been performed is depicted on Table 5.1.

Institute	CSIR - Pretoria	Institut Pasteur - Paris		
Group	M. Mhlanga's	JC. Olivo-Marin's	C. Zimmer's	F. Agou's
2008 - 1st half		A		
2008 - 2nd half	A, B, G			
2009 - 1st half			C, G, H	
2009 - 2nd half	D, G		E, H, I	
2010 - 1st half			E, G, I	
2010 - 2nd half	E, F, G		E, F, G, I, J	J
2011 - 1st half			G, J	J
2011 - 2nd half			G, J	J

Table 5.1. Contributing groups and locations where my PhD was performed. Capital letters represent the following events: (A) development of ThunderSTORM; (B) assembly and set up of the Andor TIRF microscope; (C) assembly and set up of the super-resolution microscope at Zimmer's lab; (D) assembly and set up of the super-resolution microscope at Mhlanga's lab; (E) development of QuickPALM; (F) release of QuickPALM; (G) single-molecule analysis of molecular-beacons; (H) super-resolution imaging of pCHAP in pseudomonas bacteria; (I) super-resolution imaging

of synaptic vesicles in neurons and (J) super-resolution imaging of NEMO in U2OS cells.

## Review

# PALM and STORM: What hides beyond the Rayleigh limit?

*Ricardo Henriques<sup>1</sup> and Musa M. Mhlanga<sup>1,2</sup>*<sup>1</sup> Gene Expression and Biophysics Unit, Instituto de Medicina Molecular, Faculdade de Medicina Universidade de Lisboa, Lisbon, Portugal<sup>2</sup> Gene Expression and Biophysics Group, CSIR Synthetic Biology, Pretoria, South Africa

Super-resolution imaging allows the imaging of fluorescently labeled probes at a resolution of just tens of nanometers, surpassing classic light microscopy by at least one order of magnitude. Recent advances such as the development of photo-switchable fluorophores, high-sensitivity microscopes and single particle localization algorithms make super-resolution imaging rapidly accessible to the wider life sciences research community. As we take our first steps in deciphering the roles and behaviors of individual molecules inside their living cellular environment, a new world of research opportunities beckons. Here we discuss some of the latest developments achieved with these techniques and emerging areas where super-resolution will give fundamental new “eye” sight to cell biology.

Received 1 February 2009  
Revised 15 May 2009  
Accepted 15 May 2009

**Keywords:** Fluorescent proteins · Microscopy · Nanoscopy · Single molecule · Super-resolution

## 1 Introduction

Light microscopy was hampered until recently by a resolution limit that in principle did not allow the localization of single molecules within a cell, despite the myriad claims to the contrary. This resolution limit of about 200 nm, based on the work of Abbe and Rayleigh [1] was recently overcome with the development of a series of new microscopy techniques that allow the localization of molecules down to about 10-nm precision. What are the most tractable biological questions that can be addressed with this new set of techniques in the coming years? Given the limitations of existing fluorescent proteins, fluorescent dyes and probes for “super-resolution,” is it possible for the common life scientist to deploy and profit from the available

technologies? Recently, a number of super-resolution techniques have emerged that are within reach of laboratories possessing a total internal reflection fluorescence (TIRF) or laser-based wide-field microscopy setup and experience in quantitative image analysis. Breaching Rayleigh’s limit vastly enhances our capabilities to image single molecules since all the molecular “players” in biology, DNA, RNA and protein, exist at a scale at least an order of magnitude below the diffraction limit. Recent work offers tantalizing views of where far-field nanoscopy can take us.

### 1.1 The optical microscopy diffraction limit

When observing a single fluorophore on a microscope, the emitted light must traverse several different physical mediums until it reaches the detector. As a result, light scatters throughout the different environments leading to an artificial spatial broadening of the discrete point. In the 19<sup>th</sup> century Abbe described analytically this hard limit on optical microscopy by which any point source of light smaller than the diffraction limit of the imaging system would have a fixed observable size [1]. Thus, the minimum distance where two different points are regarded as resolvable, the Rayleigh limit

**Correspondence:** Dr. Musa Mhlanga, CSIR-Synthetic Biology, Gene Expression and Biophysics, Box 395, Pretoria 0001, South Africa  
**E-mail:** mhlanga@gmail.com  
**Fax:** +27-12-841-3651

**Abbreviations:** FPALM, fluorescence PALM; PALM, photoactivation localization microscopy; PSF, point spread function; STED, stimulated emission depletion; STORM, stochastic optical reconstruction microscopy; TIRF, total internal reflection fluorescence

it, equals the space where the diffraction maximum of one point image coincides with the first minimum of the other. The points become indistinguishable if this distance is smaller while they remain resolvable if the distance between the two objects is greater. The observable spatial profile of such spots defines the point spread function (PSF) of the microscope, also known by the Airy diffraction pattern.

Any two fluorescent molecules whose overlapping PSFs are separated by a distance smaller than the PSF width become difficult or impossible to resolve as separate objects. This distance known as the Rayleigh Criterion is given approximately by  $\lambda/(2NA)$  laterally ( $x$ - $y$ ) and  $2\lambda\eta/(2NA)^2$  axially ( $z$ ), where  $\lambda$  is the wavelength of the emitted light,  $\eta$  is the index of refraction of the medium and  $NA$  the numerical aperture of the objective lens [2]. In a conventional fluorescence microscope using visible light ( $\lambda$  between 450 and 700 nm) and a high numerical aperture objective ( $NA=1.4$ ) the resolution limit given by the Rayleigh Criterion is approximately ~200 nm in the focal plane ( $x,y$ ) and 500–800 nm along the optic axis ( $z$ ).

## 1.2 From micro-to-nano

For several years electron microscopy (EM) has been the predominant technique for high-resolution nanoscopy of biological samples [3], and has had an immense significance on our understanding of biology. Nonetheless, this technique has several limitations such as low labeling efficiency and laborious sample preparation methods that are incompatible with live-cell imaging. As a result the vast majority of microscopy research in the life sciences is still carried out with optical light microscopy [4].

By default, fluorescence microscopes are able to detect and position single molecules with a high accuracy if they present distinct spectral emissions or if their associated PSFs do not spatially overlap extensively [5, 6]. Problem arise when neighboring markers are excited simultaneously stimulating a

coincident emission, making the separation of their overlapping PSFs virtually impossible (Fig. 1).

One of the earliest techniques that attempted to tackle this problem was near-field scanning optical microscopy (NSOM) where the detection of evanescent light waves emanating from a very restricted number of molecules was achieved through scanning with a nanosized tip [7]. However, this technique is restricted to the imaging of the sample surface and not able to give information about the interior and contents of cells.

Far-field fluorescence nanoscopy arose by cleverly making use of Abbe's formulas; one such way was to reduce the PSF size, *e.g.*, by increasing the angular aperture of the imaging optics. These concepts have been appraised since the late 1970s, such as in the case of the first 4Pi illumination ideas from the Cremer brothers in Heidelberg [8], leading to the development of the 4Pi confocal microscope [9–11] or the wide-field approach I<sup>5</sup>M [12]. Both techniques take advantage of opposing objective lenses leading to up to a sevenfold increase in the  $z$ -axis resolution. However, using two objectives creates a wave front that is still non-spherical giving rise to the appearance of unwanted side lobes on the focal spot that need to be reduced mathematically in post-processing steps [13]. Another approach has been achieved by structured illumination microscopy (SIM) [14–16], where a wide-field periodically patterned illumination allows for the expansion of the frequency space detectable by the microscopy reducing the size of the PSF and allowing a resolution increase of up to a factor of two [17]. The combination of this method with I<sup>5</sup>M allows for a 3-D image resolution of around 100 nm [18]. By implementing saturated intensities, saturated SIM (SSIM) is able to use arbitrarily high spatial frequencies to generate an excitation pattern [19]. This enables SSIM to achieve an experimentally measured 50-nm lateral resolution [20]. Stimulated emission depletion (STED) fluorescence microscopy makes use of two lasers; while a focused excitation laser beam pushes fluorophores to their excited state, a second laser with

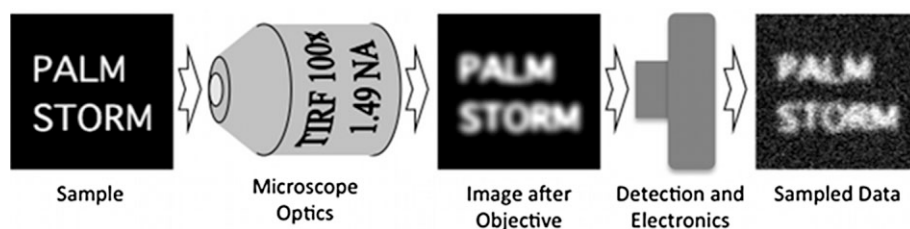


**Figure 1.** Scheme of the distortion created by a fluorescence microscope. Using the words PALM and STORM as an example, as light travels from the emitting molecules through the optics of the imaging system, diffraction occurs and the spatial information of the fluorophores becomes blurred. When a light detector acquires this information, noise is introduced into the resulting produced image.

a doughnut-shaped intensity profile prompts a stimulated emission of the excited fluorophores surrounding the excitation spot impelling them to the ground state [10, 21]. This feature confines the fluorescence emission to the non-stimulated region inside the doughnut reducing the size of the PSF and thus achieving measured resolutions as high as 20 nm laterally and 30–40 nm axially. Resolutions of 40–45 nm can be achieved in any of the three dimensions if STED is combined with a 4Pi setup [22, 23]. Recently, STED has been shown to be able to produce video-rate images of synaptic vesicles with a resolution of 60 nm in live neuronal cells [24]. Thus, Abbe's basic insight remains true and is only overcome by "PSF engineering".

A concept observed since the 1980s comes out of the fact that, although the size of observable particles is limited by the resolution of the microscope, the center of the particle can be determined precisely if a sufficient number of photons are detected, [25, 26]. Thus, unlimited resolution could even be achieved if this number tends to infinity [27]. Notwithstanding, two main constraining factors in achieving accurate particle localization exist: firstly, the PSFs of neighboring particle cannot overlap and, secondly, the localization accuracy depends heavily on the signal to noise ratio of the sampled image. Despite these limitation it has still been possible to conduct far-field microscopy single-particle tracking studies with an astonishing precision as high as 1 nm, as is the case of the work of Gelles *et al.* [28] in the movement of kinesin-coated beads, or Yildiz *et al.* [29] on the movement of myosin V over actin filaments. However, in most instances, biological-imaging experiments will encounter the visualization of densely labeled samples. In such cases the overlapping PSFs due to the emission of the densely packed fluorophores prevent their accurate localization (Fig. 1).

Researchers have been able to find clever methods to circumvent these constraints. In 1995, Eric Betzig [30] suggested that one might be able to identify individual molecules with differing spectra whose separation is smaller than the PSF width. Several groups then later showed the application of these ideas in single molecule spectral selection sub-diffraction imaging [31–33]. Other ingenious approaches have also been developed such as single-molecule localization through sequential photobleaching [34, 35] or through the analysis of the stochastic blinking of quantum dots [36].

One of the solutions to these problems that has become popular in the research community emerges through the sequential and stochastic switching on and off of fluorophores, therefore minimizing the probability that at any given time two or more fluorophore light emissions (and thus PSFs) spatially overlap. In each imaging cycle most molecules remain dark but a small number are randomly switched on, imaged and localized. This process can then be repeated for numerous iterations until the majority of molecules have been accurately detected and positioned (Fig. 2). A side effect of using this method means that thousands of images may need to be acquired to generate one super-resolution dataset. This feature has become the backbone of techniques such as photoactivation localization microscopy (PALM) [37], fluorescence photoactivation localization microscopy (FPALM) [38], stochastic optical reconstruction microscopy (STORM) [39] and PALM with independently running acquisition (PALMIRA) [40–42]. For the remainder of this review we focus on this method and how it has emerged as one of the most tractable approaches for any laboratory wishing to generate super-resolved data.

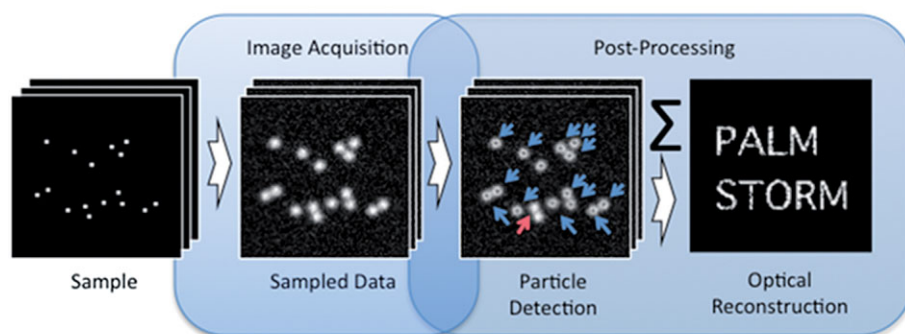


**Figure 2.** PALM and STORM imaging scheme. Several images are acquired where very few emitting molecules are observed in each. Although ultimately images become blurred and noisy during acquisition, the low probability of overlapping fluorophores (and PSFs) allows for the detection and localization of the majority of emitting particles inside each image. As this information is integrated in time, the localization of all detected molecules can be matched and a final super-resolution dataset or image is generated.



## 2 Super-resolution localization by stochastic activation of single molecules

Three key components are required to achieve super resolution with stochastic activation. They are firstly the microscope optics and the detector that must be able to detect very few photons. Secondly, the fluorescent dyes and proteins that enable photoswitching, permitting stochastic activation. Thirdly, and perhaps not fully appreciated, analysis of thousands of images and their reconstruction into a super-resolved image.

### 2.1 Detection and microscope optics

As isolated emitting diffraction-limited spots are imaged, their centroid can be localized with an approximate precision of  $\sigma/\sqrt{N}$ , where  $\sigma$  is the standard deviation of the PSF and  $N$  is the number of detected photons [5]. This relationship reveals the importance of the imaging system and fluorophores used. To achieve high localization accuracy, one would want to achieve a small PSF by using a high NA objective and optical components that minimize the unwanted diffraction. Yet one of the main problems is the low photon-detection efficiency in microscopes, leading to the need for high-sensitivity and low-noise detectors as is the case with electron-multiplying charge-coupled devices (EM-CCD) cameras and low absorption optics. Labeled biological samples, however, can present a large number of fluorophores in a diffraction-limited region preventing precise single-molecule localization. A solution based on photo-switchable fluorescent molecules – molecules that can be reversibly switched from non-fluorescent (off-state) to fluorescent (on-state) by stimulation of light with specific wavelengths – can be created through the use of activation-deactivation imaging cycles. Importantly the density of activated molecules in each single image must be kept very low, such that the images (in this case PSFs) of individual fluorophores do not overlap, permitting non-overlapping single-particle detection. In each step of this imaging process a small number of molecules are activated, imaged and deactivated; repeating this cycle creates a sequence of images in which most of the photo-switchable population will appear sequentially distributed over a large number of temporal slices, allowing for individual spot detection and localization.

Imaging by itself can be easily implemented on a TIRF or wide-field based system that features a high magnification and numerical aperture objective ( $100\times$  1.45 NA or better), high-efficiency optics and detector, and an excitation system that is com-

patible with the photoswitching activation and excitation of the chosen fluorophore (see Table 1) – minor modifications to the setup might be needed to achieve 3-D information such as the introduction of astigmatic lenses or a simultaneous double-plane detection [43, 44].

### 2.2 Fluorescent proteins and dyes

For PALM and STORM, the choice of the right photoswitchable fluorophores is vital as they are critical factors that modulate the speed of acquisition and localization accuracy of the techniques. Desirable fluorescent molecules should be extremely bright to allow for the detection of the maximum possible amount of photons per molecule ( $N$ ); this can be achieved by selecting dyes/fluorescent proteins that have both a large extinction coefficient ( $\epsilon$ ) and quantum yield ( $QY$ ). It is important to have a good ratio between the amounts of photons emitted in the fluorescent activated state and the residual photons emitted in the non-activated state. Acquisition speed is highly dependent on the activation and deactivation rates of the fluorophores and experimental settings need to be optimized to prevent unwanted PSFs overlapping (this issue comes to the forefront in specific biological examples described later). Thus, single-molecule super-resolution can be achieved by maintaining a good balance between the small number of fluorescent molecules that are activated in each acquired frame and the amount that do not immediately deactivate between consecutive frames. Several different classes of photoswitchable fluorophores compatible with super-resolution localization have been described (see Table 1).

Irreversible photoactivatable fluorescent proteins can only make a single transition from a dark to an emitting state. Deactivation is done by irreversibly bleaching the molecule. One of the earliest developed and most successful fluorophores of this class is PA-GFP [45], leading to the early work of the Diaspro group on restricting the activation of PA-GFP in 3-D space through 2-photon activation [46] or the recent work of Hess and colleagues [47] with live-cell FPALM. Due to its low contrast ratio the spatial resolution is severely limited.

Irreversible photoshiftable fluorescent proteins are able to make an irreversible shift between two fluorescent colors. These proteins are some of the most commonly used proteins for super-resolution imaging. mKiKGR has been recently engineered based on the KiKGR tetramer, making it a more suitable alternative for cellular protein imaging [48]. Of this class, PS-CFP2 is the only green-emit-



Table 1. Photoswitchable fluorophores for super-resolution imaging<sup>a)</sup>
























Fluorophore	Switch	$\lambda(\text{act})$	$\lambda(\text{ex})$	$\lambda(\text{em})$	$\epsilon$	QY	N	Fluorescence Increase	Oligom. State	Reference (s)
Irreversible photoactivation fluorescent proteins										
PPA-GFP (Pre)		413	400	515	20.700	0.13	~70	5	Monomer	[53, 58]
PPA-GFP (Post)			504	517	17.400	0.79	~300			
PAmCherry (Pre)		405	ND	ND	ND	ND	ND	5000	Monomer	[59]
PAmCherry (Post)			570	596	24.000	0.53	ND			
Irreversible photoswitchable fluorescent proteins										
PS-CFP2 (Pre)		405	400	468	43.000	0.20	ND	>2000	Monomer	[53, 58, 60]
PS-CFP2 (Post)			490	511	47.000	0.23	~260			
Kaede (Pre)		350–410	508	518	98.800	0.88	ND	2000	Tetramer	[53, 58]
Kaede (Post)			572	580	60.400	0.33	~460			
mKikGR (Pre)		405	505	519	49.000	0.69	ND	>2000	Monomer	[48]
mKikGR (Post)			580	591	28.000	0.63	~970			
mEosFP (Pre)		400	505	516	67.200	0.64	ND	ND	Monomer	[53, 58]
mEosFP (Post)			569	581	37.000	0.62	~490			
tdEos (Pre)		405	506	516	84.000	0.91	ND	200	Tandem dimer	[59, 61, 62]
tdEos (Post)			569	581	33.000	0.62	~750			
mEos2 (Pre)		405	506	519	56.000	0.84	ND	ND	Monomer	[61]
mEos2 (Post)			573	584	46.000	0.66	ND			
Dendra-2 (Pre)		405 or 488	490	507	45.000	0.50	ND	300	Monomer	[53, 59, 60]
Dendra-2 (Post)			553	573	35.000	0.55	ND			
Reversible photoactivatable fluorescent proteins										
Photoswitchable EYFP		405	514	527	137.000	0.61	ND	ND	Monomer	[63, 64]
Dronpa		405	503	522	125.000	0.68	120	ND	Monomer	[50, 53, 58]
bsDronpa		405	460	504	45.000	0.50	ND	ND	Monomer	[50]
Padron		496	503	522	43.000	0.64	ND	ND	Monomer	[50, 53]
rsFastlime		405	496	518	46.000	0.60	>2000	ND	Monomer	[41, 50]

Table 1. Continued

Fluorophore	Switch	$\lambda(\text{act})$	$\lambda(\text{ex})$	$\lambda(\text{em})$	$\epsilon$	QY	N	Fluorescence Increase	Oligom. State	Reference (s)
<i>Reversible photoactivatable fluorescent dyes</i>										
Photochromic Rhodamine	●●●●	375	530	620	105 000	0.65	~750	ND	NA	[40, 53]
Alexa Fluor 647*	●●●●	532*	650	665	240 000	0.33	~6000	ND	NA	[51, 53]
Cy5*	●●●●	405 or 457 or 532*	649	664	250 000	0.28	~6000	ND	NA	[51, 53]
Cy5.5*	●●●●	532*	675	694	190 000	0.23	~6000	ND	NA	[51, 53]
Cy7*	●●●●	532*	747	767	200 000	0.28	~1000	ND	NA	[51, 53]
<i>Photocaged fluorophores</i>										
Caged Q-rhodamine	●●●●	405	545	575	90 000	0.90	ND	ND	NA	[53]
Caged carboxyfluorescein	●●●●	405	494	518	29 000	0.93	ND	ND	NA	[53]

a)  $\lambda(\text{act})$ , photoactivation wavelength in nm;  $\lambda(\text{ex})$ , excitation wavelength in nm;  $\lambda(\text{em})$ , emission wavelength in nm;  $\epsilon$ , extinction coefficient in  $\text{M}^{-1}\text{cm}^{-1}$ ; QY, fluorescence quantum yield; N, emitted number of photons per molecule; Oligom. State, oligomeric state.

\* Pairing this fluorophores with a second activator chromophore greatly increases the photoswitching characteristics, literature described pairs: Cy3-Alexa Fluor 647, Alexa Fluor 405-Cy5, Cy2-Cy5, Cy3-Cy5, Cy3-Cy5.5, Cy3-Cy7 [51].

ting protein and has successfully been used in multicolor super-resolution imaging [49].

Reversible photoactivatable fluorescent proteins are capable of shifting between active and non-active states multiple times, even though the wavelength of the emission peaks of bsDronpa, rs-FastLime and Padron are near each other. Andresen *et al.* [50] have shown that taking advantage of the time-spectral photoswitching characteristics of these fluorophores can be differentiated in multicolor imaging.

Reversible photoactivatable fluorescent dyes are not genetically encoded and are unable to undergo several shifts between a fluorescent and non-fluorescent state. In comparison to their analog photoswitchable proteins, the photon output ( $N$ ) of some of these probes is extremely high leading to lateral resolutions in the order of 20 nm, as achieved in STORM [51]. Although some of these dyes are able to photoswitch alone, *e.g.*, Cy5 [52], when paired with a secondary chromophore switching might be improved. This feature greatly increases the color range of STORM probes [51].

In the case of caged fluorophores, irradiation with UV light causes the release of a protective group leading to a fluorescence increase of the dye. Caging brings a novel way to create new photoswitchable probes based on pre-existing fluorophores with desirable photophysical properties [53].

Fluorophores with reversible photobleaching have been recently developed. It was shown that embedding samples in oxygen-depleted mediums such as polyvinyl alcohol, glucose oxidase or even standard media such as glycerol, allows conventional fluorophores (such as EGFP, EYFP, ECFP, Alexa 488, Alexa 568, fluorescein among many others) to switch into dark states after strong illumination. This allows them to stochastically switch back to an emitting state after a relaxation time [54–56]. This resulted in a 30-nm resolution by imaging Alexa 488 [57].

## 2.3 Single molecule analysis and reconstruction

Analysis and reconstruction are one of the major parts of PALM and STORM. Post-acquisition or in-acquisition processing infer the characteristics of each molecule present in the large amount of images that constitute the dataset. In a typical experiment 1000–10 000 images are generated in which tens to hundreds of particles are present in each frame. Although the acquisition by itself takes few minutes, the data analysis can take up to several hours and is highly dependent on the processing power available to the user. Ironically, this means

that the super-resolved image cannot be “seen” until well after the end of the actual acquisition and imaging of the sample. Localization accuracy depends greatly on the capacity of the algorithms to deal with detection noise, PSF overlapping and particle motion. Fortunately, biology can inherit a great deal of knowledge and solutions from astronomy, as astronomers have faced a similar problem when observing stars that are in essence also diffraction limited. For example, Egner and colleagues [41] describe the usage of a modified version of the 1974 Hogbom’s CLEAN algorithm [65] in conjunction with a mask-fitting algorithm of the Airy diffraction pattern to provide particle segmentation and positioning. These tasks become more difficult when particle tracking is needed as in the case of following molecular dynamics.

The single-particle tracking (SPT) algorithm needs to relate the different particles being detected at different time points. Such tasks face several challenges, such as particles disappearing due to blinking, moving into or outside of the region being imaged, particle splitting, particle merging and detection failure [66, 67]. Recently, both groups of Jaqaman *et al.* [67] and Serge *et al.* [68] have provided the research community with freely available Matlab (Mathworks)-based algorithms able to achieve localization accuracies near the theoretical limit and multi-particle tracking.

As PALM and STORM evolve to live-cell imaging, the need for in-acquisition real-time analysis increases in order to optimize and adapt the microscope settings. This would be the case in data-driven excitation and activation optimization to reduce the needed imaging time and the high phototoxicity of PALM and STORM experiments. Also, this would provide biologists with tools that allow experimental decisions based on the observed super-resolution information immediately. It is clear that as the technique becomes more generally used in the near future, so too will algorithm optimization, multi-processor analysis and clustered computing evolve to provide these features.

### 3 Stepping into 3-D super-resolution

Although PALM and STORM have been generally used to improve 2-D image resolution, achieving 3-D intracellular information has been one of the major challenges for the techniques. Other nanoscopy techniques like 4Pi or I<sup>3</sup>M have been able to surpass this problem and achieve an axial resolution below 100 nm [12, 13, 69]. STED microscopy in a 4Pi illumination geometry has been shown to reach resolutions as high as 30–50 nm, although without

super resolution in the lateral dimensions [70]. The recent work of Lemmer and colleagues on super-resolving cellular nanostructures through the combination of spectral precision distance microscopy (SPDM) with spatially modulated illumination (SMI) has achieved 20-nm lateral and 50-nm axial resolution [71]. PALM and STORM have been mostly used under TIRF imaging due to the inherent high-contrast optical sectioning achieved with such systems limiting the z axis imaging depth generated by the evanescent field to around 150 nm. A similar technique called highly inclined and laminated optical sheet (HILO) microscopy makes use of a highly inclined light beam to generate a thin optical sheet that penetrates the sample at a shallow angle, HILO has effectively been used in single-molecule fluorescence nanoscopy of the cell nucleus with high signal/background ratios [72] and should prove to be compatible with PALM and STORM imaging, but no association has been reported to the date. Two-photon activation-based optical sectioning with PALM has been achieved with photochromic rhodamine dyes [40]. Recently, two elegant solutions circumventing optical-beam scanning have been demonstrated that allow 3-D PALM and STORM imaging. Firstly, by inducing optical astigmatism on a wide-field setup where the PSF shape becomes ellipsoid and dependent on the Z-position of the fluorophore – a trait that has been shown to allow 20–30-nm lateral and 50–60-nm axial resolution [43]. Secondly, the use of a biplane (BP) detection scheme where a 3-D stack of two slightly displaced Z-planes are acquired simultaneously allowing for accurate z-position determination, leading to a experimentally measured 30-nm lateral and 75-nm axial resolution [44]. One of the main problems of this latter technique comes from the need to split the incoming emitted light into two images, leading to a decrease of the detected signal to noise ratio.

### 4 Imaging of molecular structures

The super-resolution method PALM first distinguished itself in the labeling of lysosomal transmembrane protein CD63 fused to Kaede (see Table 1) [37]. The resolution improvements offered by PALM were adeptly illustrated when a transmission EM and a PALM image of the same thin cryosection were overlaid, resulting in a near perfect fit. In the same work, Betzig and coworkers went on to label dimeric Eos (Table 1) with a cytochrome C oxidase localization sequence, thus targeting the mitochondria. In a comparison with transmission EM images of the same mitochondria

they were able to achieve highly similar structural information and images. The power of this technique is clearly the nanometer resolution that is achieved in determining the distribution of a given protein within the cellular ultrastructure in a live sample.

Early experiments using PALM to study cellular ultrastructure focused on fixed cells or cryosections. However, being able to observe the assembly of such structures in real time with super-resolution opens up several areas of scientific investigation under *in vivo* conditions. These include visualising how other cellular factors contribute to the assembly and development of these processes with high spatio-temporal resolution. To achieve this level of resolution the sampling interval must be half the desired resolution (i.e., the Nyquist criterion must be met). Other important criteria must be met for live-cell super-resolution. As acquisition cycles typically require high laser powers for fluorophore activation and bleaching, a significant amount of phototoxicity is generated, leading to abnormal cell behavior or death – this becomes a greater problem when UV-lasers are used for fluorophore activation due to the high energy of the photons used. To compensate for molecular motility and ensure that a fair number of molecules remain detected, a high frame rate needs to be used, potentially leading to a decrease in the detected signal to noise ratio and thus compromising the localization accuracy and resolution. Another limitation arises from the limited number of detected photons. As the overall number of molecules able to photoswitch is depleted due to irreversible photobleaching, the detected molecular density per frame will decrease over time. Notwithstanding these challenges, at least two groups have been able to successfully achieve super resolution in live cells. To image the assembly of ultrastructures, Schroff *et al.* [62] tagged the protein paxillin with a dimer of Eos. They were able to image the adhesion complexes or transmembrane cytoskeleton-substrate attachment points central to the process of cell migration. They overcome the inherent problems of live-cell imaging in PALM using a fast imaging speed or image acquisition rate, which must be faster than the activity imaged. In addition, they compensated for photon scarcity by using a dimer of Eos for each target protein, thereby achieving a dense labeling of paxillin. Combining all these approaches enabled them to observe the formation of individual adhesion complexes for extended periods of time, measuring the number of individual paxillin molecules entering and leaving the complex in real time over 25 min. Further, they were able to note that, during cell migration, adhesion

complexes assume a wide diversity of morphologies.

#### 4.1 Host-pathogen interactions

Because of the use of TIRF microscopy, the study of plasma membrane-associated proteins with PALM is particularly suited to imaging viral entry. Hess and coworkers [47] have used FPALM, (essentially identical to PALM) to examine a clustered viral membrane protein, influenza hemagglutinin (HA). Influenza viral entry and membrane fusion is mediated by HA and its visualization until recently was limited to classical resolution limits. To enter its host, the influenza virus uses HA to open a fusion pore in the endosomal membrane and then inserts its viral RNA into the host cytoplasm. Lipid rafts are believed to play an important role in the distribution of HA at the cell surface, although several theories exist on the nature and dynamics of these rafts. Hess and coworkers [47] went on to use FPALM to discriminate between the various raft theories, which all propose that lipid rafts exist at resolutions well below the diffraction limit of light. As in the earlier work of Shroff and coworkers, they were able to perform these experiments in live cells principally because the diffusion coefficient of HA was low, and thus a single molecule of HA tagged with PA-GFP (Table 1) could be localized. Essentially, for such experiments in live cells, to successfully localize a single molecule, the mean-squared displacement attributable to two dimensional diffusion (during acquisition) must be smaller than  $r_0^2$ , where  $r_0$  is the  $1/e^2$  radius of the PSF. Most recently STED microscopy has been used to address at least one of these theories.

#### 4.2 Super-resolution particle tracking

Advances in the use of photoactivatable markers have enabled the dynamics of individual molecules to be determined and thus tracked with super-resolution at the single-molecule level. Manley and coworkers [73] were able to track the dynamics of thousands of vesicular stomatitis virus G (VSVG) and Gag (HIV-1 structural protein) proteins (tagged with Eos) in the plasma membrane using PALM. To do so, the data acquisition rate and cell viability had to be optimized and a very high numerical aperture lens (1.65 NA) was utilized. Using what they termed sptPALM (single-particle tracking PALM), they were able to observe a relatively homogenous localization of VSVG and the multimerization of the Gag particles into virus-like particles. They also could track single particles for path lengths of up to  $\sim 1\ \mu\text{m}$  determining the mean



square displacement within given molecular environments. Using this information they created a spatially resolved map of single molecule diffusion coefficients for VSVG and Gag. The potential for the use of sptPALM in the exploration of the behavior of different subsets of individual molecules based on their spatial organization and subcellular dynamics is enormous. Indeed, such information could be correlated with different viral strains or mutations as well as different cell types. Many existing imaging tools and reagents exist that permit the use of sptPALM in the study of host-pathogen interactions.

### 4.3 STORMing onto the scene

While PALM has been used by several groups to image structural features in fixed and living cells, STORM has been used similarly to image cellular organelles and microtubules. Zhuang and coworkers [51] were able to achieve dramatic improvements in the resolution of the microtubule network in fixed cells. Microtubules [labeled with antibodies conjugated to Cy3 and Cy5 (Table 1)] separated by 80 nm were clearly visible after 20 s of STORM acquisition, and a theoretical resolution limit of 24 nm was possible within cells. Further, Zhuang and coworkers were able to achieve multicolor super-resolution in the fixed cells labeling clathrin-coated pits, structures implicated in receptor-mediated endocytosis, simultaneously with microtubules (Fig. 3). This was achieved using combinations of Cy2 and Alexa 647 to label microtubules and Cy3 and Alexa 647 to label clathrin-coated pits. Extending these techniques to three dimensions, they have recently used STORM to study the spatial relationship between the cellular structures of the mitochondria and microtubules, also in fixed cells [43]. Their super-resolved 3-D images of the mitochondria reveal it to have a hollow shape in the outer membrane and identified two distinct mito-

chondrial morphologies, tubular and globular. When co-imaged with microtubules, frequent contacts between globular mitochondria and microtubules were observed. The interactions of tubular mitochondria and microtubules were found to be more complex with noncontiguous interaction between the two.

STORM, at present, has the distinct disadvantage of not permitting live-cell imaging due to the buffer conditions that are necessary for photo-switching of fluorescent dyes. It has, however, the advantage of using dyes that have high contrast ratios and are far brighter than fluorescent proteins. STORM also does not require the construction of fusion proteins, unlike PALM, although it does require the availability of antibodies to label the protein of interest. These advantages make it likely that the ability to perform live-cell imaging with STORM imaging will represent a significant advance in super resolution.

### 4.4 Stochasticity and the study of gene expression

Another area, which has an intense interest in advances in the dissolving of the resolution limits of light microscopy, is the study of nuclear biology. The spatial organization of the nucleus, the apparently non-random organization of the genome within the nucleus and several of the processes surrounding transcription and gene expression are all questions ripe for the use of super-resolution techniques [74]. Current microscopy approaches, in live cells, have focused on using statistical mapping to understand genome organization [75], and fluorescent microscopy techniques to visualize chromosome repositioning within the nucleus [76]. These approaches have fallen short when it has come to the study of gene expression and transcription, resorting to fluorescent *in situ* hybridization (FISH) to take snap shots of these events in fixed cells, albeit at times with single-molecule resolution [77].

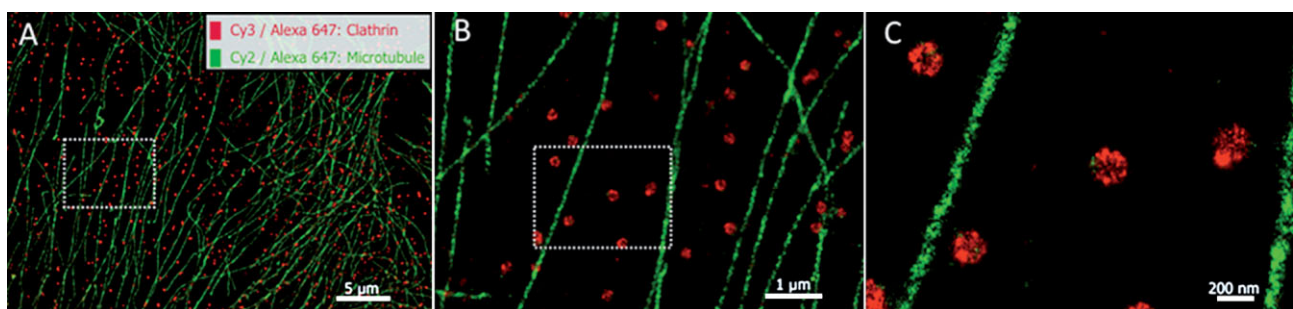


**Figure 3.** STORM imaging of microtubules and clathrin-coated pits. (A–C) BS-C-1 cells: secondary antibodies in microtubule staining are labeled with Cy2 and Alexa 647 (false color green), those for clathrin are labeled with Cy3 and Alexa 647 (false color red). These images demonstrate the level of magnification the STORM technique and others such as PALM. (B) Magnification of the boxed section in (A), (C) further magnification of boxed region in (B). Images modified, with permission from [51] © (2007) American Association for the Advancement of Science.

Gene expression is a fundamentally stochastic process, and in some instances appears purposefully so (reviewed in [78]). This makes the construction and modeling of gene networks especially difficult. Transcription is thought to occur in bursts with little known as to their source [79]. One may be the existence of pre-initiation complexes formed on the promoter that may permit multiple rounds of RNA polymerase II transcription [80, 81]. Such complexes could form in so-called “transcription factories” where active genes would be recruited. Some evidence for transcription factories does exist though at best three differing transcripts have been imaged in putative factories [82]. Where super-resolution could be most informative in this field is in the ability to image all the species transcripts within these factories and to understand the contents of the transcriptional machinery in real time. This would give key insights into the fundamental process of transcription whose “molecular players” have only been observed as snapshots. Since there is great heterogeneity in transcription in even otherwise identical cell types, observing the minutiae of this process over several cells is perhaps the only way stochasticity can be understood.

*We thank Christophe Zimmer, Mickael Lelek for valuable comments and help in preparation of Table 1. We also thank Xiaowei Zhuang for informal advice and interactions.*

*The authors have declared no conflict of interest.*

## References

- [1] Abbe, E., Beiträge zur Theorie des Mikroskops und der mikroskopischen Wahrnehmung. *Arch. Mikroskop. Anat.* 1873, 9, 413–420.
- [2] Pawley, J., *Handbook of Biological Confocal Microscopy*, Springer, New York 2006.
- [3] Koster, A., Klumperman, J., Electron microscopy in cell biology: Integrating structure and function. *Nat. Rev. Mol. Cell Biol.* 2003, Supp. S56–10.
- [4] Hell, S., Far-field optical nanoscopy. *Science* 2007, 316, 1153.
- [5] Thompson, R. E., Larson, D. R., Webb, W. W., Precise nanometer localization analysis for individual fluorescent probes. *Biophys. J.* 2002, 82, 2775–2783.
- [6] Basché, T., *Single-Molecule Optical Detection, Imaging and Spectroscopy*, John Wiley & Sons, New York 1997.
- [7] Novotny, L., Hecht, B., *Principles of Nano-Optics*, Cambridge University Press, Cambridge 2006.
- [8] Cremer, C., Cremer, T., Considerations on a laser-scanning-microscope with high resolution and depth of field. *Microsc. Acta* 1978, 81, 31–44.
- [9] Hell, S., Stelzer, E. K., Fundamental improvement of resolution with a 4Pi-confocal fluorescence microscope using two-photon excitation. *Opt. Commun.* 1992, 93, 277–282.
- [10] Hell, S., Wichmann, J., Breaking the diffraction resolution limit by stimulated emission: Stimulated-emission-depletion fluorescence microscopy. *Opt. Lett.* 1994, 19, 780–782.
- [11] Hanninen, P. E., Hell, S. W., Salo, J., Soini, E., Cremer, C., Two-photon excitation 4Pi confocal microscope: Enhanced axial resolution microscope for biological research. *Appl. Phys. Lett.* 1995, 66, 1698–1700.
- [12] Gustafsson, M. G. L., Agard, D. A., Sedat, J. W., Sevenfold improvement of axial resolution in 3D widefield microscopy using two objective lenses. *Proc. SPIE Int. Soc. Opt. Eng.* 1995, 2412, 147–158.
- [13] Egner, A., Hell, S., Fluorescence microscopy with super-resolved optical sections. *Trends Cell Biol.* 2005, 15, 207–215.
- [14] Bailey, B., Farkas, D., Taylor, D., Lanni, F., Enhancement of axial resolution in fluorescence microscopy by standing-wave excitation. *Nature* 1993, 366, 44–48.
- [15] Gustafsson, M., Surpassing the lateral resolution limit by a factor of two using structured illumination microscopy. *J. Microsc.* 2000, 198, 82–87.



**Ricardo Henriques** received his Physics Engineering degree in 2005 from the Faculty of Sciences University of Lisbon, Portugal and trained further in microscopy at the cell imaging facility of the Instituto Gulbenkian de Ciências, Oeiras. In 2006 he took a position as manager of the Biolmaging facility in the Institute of Molecular Medicine, Lisbon, Portugal, researching new data-

driven adaptive microscopy methods through the use of artificial vision and robotics. He has been a PhD student in the laboratory of Dr. Musa Mhlanga since 2008. His research interest is focused on creating technological tools for sub-diffraction visualization of the nuclear architecture and its re-organization driven by gene expression activation.



**Musa Mhlanga** received his PhD in Cell Biology & Molecular Genetics from New York University, School of Medicine, in 2003 where he focused on the visualization of mRNA in living cells. He went on to do his postdoc at the Institut Pasteur in Paris, France where he worked on imaging gene expression in the nucleus and RNA transport. Since 2008 he has been a Research Group Leader at the CSIR in Pretoria, South Africa and holds an ad-

junct position at the Institute of Molecular Medicine in Lisbon, Portugal. Research in his group spans the disciplines of “super” resolution imaging and image analysis/signal processing, the study and imaging of gene expression, and the development of cell-based bioassays for screening.

- [16] Schermelleh, L., Carlton, P., Haase, S., Shao, L. *et al.*, Subdiffraction multicolor imaging of the nuclear periphery with 3D structured illumination microscopy. *Science* 2008, **320**, 1332.
- [17] Langhorst, M. F., Schaffer, J., Goetze, B., Structure brings clarity: Structured illumination microscopy in cell biology. *Biotechnol. J.* 2009, **4**, this issue DOI: 10.1002/biot.200900025.
- [18] Shao, L., Isaac, B., Uzawa, S., Agard, D. *et al.*, I5S: Wide-field light microscopy with 100-nm-scale resolution in three dimensions. *Biophys. J.* 2008, **94**, 4971–4983.
- [19] Heintzmann, R., Jovin, T., Cremer, C., Saturated patterned excitation microscopy—S concept for optical resolution improvement. *J. Opt. Soc. Am. A* 2002, **19**, 1599–1609.
- [20] Gustafsson, M., Nonlinear structured-illumination microscopy: Wide-field fluorescence imaging with theoretically unlimited resolution. *Proc. Natl. Acad. Sci. USA* 2005, **102**, 13081–13086.
- [21] Schrader, M., Meinecke, F., Bahlmann, K., Kroug, M. *et al.*, Monitoring the excited state of a fluorophore in a microscope by stimulated emission. *Bioimaging* 1995, **3**, 147–153.
- [22] Klar, T. A., Jakobs, S., Dyba, M., Egner, A., Hell, S. W., Fluorescence microscopy with diffraction resolution barrier broken by stimulated emission. *Proc. Natl. Acad. Sci. USA* 2000, **97**, 8206–8210.
- [23] Schmidt, R., Wurm, C., Jakobs, S., Engelhardt, J. *et al.*, Spherical nanosized focal spot unravels the interior of cells. *Nat. Methods* 2008, **5**, 539–544.
- [24] Nan, X., Sims, P., Xie, X., Organelle tracking in a living cell with microsecond time resolution and nanometer spatial precision. *ChemPhysChem* 2008, **9**, 707–712.
- [25] Burns, D. H., Callis, J. B., Christian, G. D., Davidson, E. R., Strategies for attaining superresolution using spectroscopic data as constraints. *Appl. Opt.* 1985, **24**, 154–161.
- [26] Bobroff, N., Position measurement with a resolution and noise-limited instrument. *Rev. Sci. Instrum.* 1986, **57**, 1152–1157.
- [27] Hell, S., Soukka, J., Hanninen, P., Two- and multiphoton detection as an imaging mode and means of increasing the resolution in far-field light microscopy: A study based on photon-optics. *Bioimaging* 1995, **3**, 64–69.
- [28] Gelles, J., Schnapp, B., Sheetz, M., Tracking kinesin-driven movements with nanometre-scale precision. *Nature* 1988, **331**, 450–453.
- [29] Yildiz, A., Forkey, J., McKinney, S., Ha, T. *et al.*, Myosin V walks hand-over-hand: Single fluorophore imaging with 1.5-nm localization. *Science* 2003, **300**, 2061–2065.
- [30] Betzig, E., Proposed method for molecular optical imaging. *Opt. Lett.* 1995, **20**, 237–239.
- [31] Van Oijen, A., Köhler, J., Schmidt, J., Müller, M., Brakenhoff, G., 3-Dimensional super-resolution by spectrally selective imaging. *Chem. Phys. Lett.* 1998, **292**, 183–187.
- [32] van Oijen, A. M., Kohler, J., Schmidt, J., Müller, M., Brakenhoff, G. J., Far-field fluorescence microscopy beyond the diffraction limit. *J. Opt. Soc. Am. A* 1999, **16**, 909–915.
- [33] Lacoste, T. D., Michalet, X., Pinaud, F., Chemla, D. S. *et al.*, Ultrahigh-resolution multicolor colocalization of single fluorescent probes. *Proc. Natl. Acad. Sci. USA* 2000, **97**, 9461–9466.
- [34] Gordon, M. P., Ha, T., Selvin, P. R., Single-molecule high-resolution imaging with photobleaching. *Proc. Natl. Acad. Sci. USA* 2004, **101**, 6462–6465.
- [35] Qu, X. H., Wu, D., Mets, L., Scherer, N. F., Nanometer-localized multiple single-molecule fluorescence microscopy. *Proc. Natl. Acad. Sci. USA* 2004, **101**, 11298–11303.
- [36] Lidke, K. A., Rieger, B., Jovin, T. M., Heintzmann, R., Super-resolution by localization of quantum dots using blinking statistics. *Opt. Express* 2005, **13**, 7052–7062.
- [37] Betzig, E., Patterson, G., Sougrat, R., Lindwasser, O. *et al.*, Imaging intracellular fluorescent proteins at nanometer resolution. *Science* 2006, **313**, 1642–1645.
- [38] Hess, S., Girirajan, T., Mason, M., Ultra-high resolution imaging by fluorescence photoactivation localization microscopy. *Biophys. J.* 2006, **91**, 4258.
- [39] Rust, M., Bates, M., Zhuang, X., Sub-diffraction-limit imaging by stochastic optical reconstruction microscopy (STORM). *Nat. Methods* 2006, **3**, 793–796.
- [40] Fölling, J., Belov, V., Kunetsky, R., Medda, R. *et al.*, Photochromic rhodamines provide nanoscopy with optical sectioning. *Angew. Chem. Int. Ed* 2007, **46**, 6266–6270.
- [41] Egner, A., Geisler, C., von Middendorff, C., Bock, H. *et al.*, Fluorescence nanoscopy in whole cells by asynchronous localization of photoswitching emitters. *Biophys. J.* 2007, **93**, 3285.
- [42] Bock, H., Geisler, C., Wurm, C., von Middendorff, C. *et al.*, Two-color far-field fluorescence nanoscopy based on photoswitchable emitters. *Appl. Phys. B Lasers Opt.* 2007, **88**, 161–165.
- [43] Huang, B., Wang, W., Bates, M., Zhuang, X., Three-dimensional super-resolution imaging by stochastic optical reconstruction microscopy. *Science* 2008, **319**, 810–813.
- [44] Jüette, M., Gould, T., Lessard, M., Mlodzianowski, M. *et al.*, Three-dimensional sub-100 nm resolution fluorescence microscopy of thick samples. *Nat. Methods* 2008, **5**, 527–529.
- [45] Patterson, G., Lippincott-Schwartz, J., A photoactivatable GFP for selective photolabeling of proteins and cells. *Science* 2002, **297**, 1873–1877.
- [46] Schneider, M., Barozzi, S., Testa, I., Faretta, M., Diaspro, A., Two-photon activation and excitation properties of PA-GFP in the 720–920-nm region. *Biophys. J.* 2005, **89**, 1346–1352.
- [47] Hess, S. T., Gould, T. J., Gudheti, M. V., Maas, S. A. *et al.*, Dynamic clustered distribution of hemagglutinin resolved at 40 nm in living cell membranes discriminates between raft theories. *Proc. Natl. Acad. Sci. USA* 2007, **104**, 17370–17375.
- [48] Habuchi, S., Tsutsui, H., Kochaniak, A. B., Miyawaki, A., van Oijen, A. M., mKikGR, a monomeric photoswitchable fluorescent protein. *PLoS ONE* 2008, **3**, e3944.
- [49] Shroff, H., Galbraith, C. G., Galbraith, J. A., White, H. *et al.*, Dual-color superresolution imaging of genetically expressed probes within individual adhesion complexes. *Proc. Natl. Acad. Sci. USA* 2007, **104**, 20308–20313.
- [50] Andresen, M., Stiel, A. C., Fölling, J., Wenzel, D. *et al.*, Photoswitchable fluorescent proteins enable monochromatic multilabel imaging and dual color fluorescence nanoscopy. *Nat. Biotechnol.* 2008, **26**, 1035–1040.
- [51] Bates, M., Huang, B., Dempsey, G. T., Zhuang, X., Multicolor super-resolution imaging with photo-switchable fluorescent probes. *Science* 2007, **317**, 1749–1753.
- [52] Heilemann, M., van de Linde, S., Schüttelpelz, M., Kasper, R. *et al.*, Subdiffraction-resolution fluorescence imaging with conventional fluorescent probes. *Angew. Chem. Int. Ed. Engl.* 2008, **47**, 6172–6176.
- [53] Fernandez-Suarez, M., Ting, A. Y., Fluorescent probes for super-resolution imaging in living cells. *Nat. Rev. Mol. Cell Biol.* 2008, **9**, 929–943.
- [54] Sinnecker, D., Voigt, P., Hellwig, N., Schaefer, M., Reversible photobleaching of enhanced green fluorescent proteins. *Biochemistry* 2005, **44**, 7085–7094.



- [55] Fölling, J., Bossi, M., Bock, H., Medda, R. *et al.*, Fluorescence nanoscopy by ground-state depletion and single-molecule return. *Nat. Methods* 2008, 5, 943–945.
- [56] Reymann, J., Baddeley, D., Gunkel, M., Lemmer, P. *et al.*, High-precision structural analysis of subnuclear complexes in fixed and live cells via spatially modulated illumination (SMI) microscopy. *Chromosome Res.* 2008, 16, 367–382.
- [57] Baddeley, D., Jayasinghe, I. D., Cremer, C., Cannell, M. B., Soeller, C., Light-induced dark states of organic fluorochromes enable 30 nm resolution imaging in standard media. *Biophys. J.* 2009, 96, L22–24.
- [58] Lukyanov, K. A., Chudakov, D. M., Lukyanov, S., Verkhusha, V. V., Innovation: Photoactivatable fluorescent proteins. *Nat. Rev. Mol. Cell Biol.* 2005, 6, 885–891.
- [59] Subach, F. V., Patterson, G. H., Manley, S., Gillette, J. M. *et al.*, Photoactivatable mCherry for high-resolution two-color fluorescence microscopy. *Nat. Methods* 2009, 6, 153–159.
- [60] Chudakov, D. M., Lukyanov, S., Lukyanov, K. A., Tracking intracellular protein movements using photoswitchable fluorescent proteins PS-CFP2 and Dendra2. *Nat. Protoc.* 2007, 2, 2024–2032.
- [61] McKinney, S. A., Murphy, C. S., Hazelwood, K. L., Davidson, M. W., Looger, L. L., A bright and photostable photoconvertible fluorescent protein. *Nat. Methods* 2009, 6, 131–133.
- [62] Shroff, H., Galbraith, C. G., Galbraith, J. A., Betzig, E., Live-cell photoactivated localization microscopy of nanoscale adhesion dynamics. *Nat. Methods* 2008, 5, 417–423.
- [63] McAnaney, T. B., Zeng, W., Doe, C. F., Bhanji, N. *et al.*, Protomation, photobleaching, and photoactivation of yellow fluorescent protein (YFP 10C): A unifying mechanism. *Biochemistry* 2005, 44, 5510–5524.
- [64] Biteen, J., Thompson, M., Tselentis, N., Bowman, G. *et al.*, Super-resolution imaging in live *Caulobacter crescentus* cells using photoswitchable EYFP. *Nat. Methods* 2008.
- [65] Högbom, J., Aperture synthesis with a non-regular distribution of interferometer baselines. *Astron. Astrophys. Suppl.* 1974, 15, 417.
- [66] Kalaidzidis, Y., Intracellular objects tracking. *Eur. J. Cell Biol.* 2007, 86, 569–578.
- [67] Jaqaman, K., Loerke, D., Mettlen, M., Kuwata, H. *et al.*, Robust single-particle tracking in live-cell time-lapse sequences. *Nat. Methods* 2008, 5, 695–702.
- [68] Serge, A., Bertaux, N., Rigneault, H., Marguet, D., Dynamic multiple-target tracing to probe spatiotemporal cartography of cell membranes. *Nat. Methods* 2008, 5, 687–694.
- [69] Nagorni, M., Hell, S., 4Pi-confocal microscopy provides three-dimensional images of the microtubule network with 100-to 150-nm resolution. *J. Struct. Biol.* 1998, 123, 236–247.
- [70] Hell, S., Toward fluorescence nanoscopy. *Nat. Biotechnol.* 2003, 21, 1347–1355.
- [71] Lemmer, P., Gunkel, M., Baddeley, D., Kaufmann, R. *et al.*, SPDM: Light microscopy with single-molecule resolution at the nanoscale. *Appl. Phys. B Lasers Opt.* 2008, 93, 1–12.
- [72] Tokunaga, M., Imamoto, N., Sakata-Sogawa, K., Highly inclined thin illumination enables clear single-molecule imaging in cells. *Nat. Methods* 2008, 5, 159–161.
- [73] Manley, S., Gillette, J. M., Patterson, G. H., Shroff, H. *et al.*, High-density mapping of single-molecule trajectories with photoactivated localization microscopy. *Nat. Methods* 2008, 5, 155–157.
- [74] Gunkel, M., Erdel, F., Rippe, K., Lemmer, P. *et al.*, Dual color localization microscopy of cellular nanostructures. *Biotechnol. J.* 2009, 4, this issue DOI: 10.1002/biot.200900005.
- [75] Berger, A. B., Cabal, G. G., Fabre, E., Duong, T. *et al.*, High-resolution statistical mapping reveals gene territories in live yeast. *Nat. Methods* 2008, 5, 1031–1037.
- [76] Cabal, G. G., Genovesio, A., Rodriguez-Navarro, S., Zimmer, C. *et al.*, SAGA interacting factors confine sub-diffusion of transcribed genes to the nuclear envelope. *Nature* 2006, 441, 770–773.
- [77] Raj, A., van den Bogaard, P., Rifkin, S. A., van Oudenaarden, A., Tyagi, S., Imaging individual mRNA molecules using multiple singly labeled probes. *Nat. Methods* 2008, 5, 877–879.
- [78] Raj, A., van Oudenaarden, A., Nature, nurture, or chance: Stochastic gene expression and its consequences. *Cell* 2008, 135, 216–226.
- [79] Raj, A., Peskin, C. S., Tranchina, D., Vargas, D. Y., Tyagi, S., Stochastic mRNA synthesis in mammalian cells. *PLoS Biol.* 2006, 4, e309.
- [80] Blake, W. J., Balazsi, G., Kohanski, M. A., Isaacs, F. J. *et al.*, Phenotypic consequences of promoter-mediated transcriptional noise. *Mol. Cell* 2006, 24, 853–865.
- [81] Blake, W. J., M. K. A., Cantor, C. R., Collins, J. J., Noise in eukaryotic gene expression. *Nature* 2003, 422, 633–637.
- [82] Osborne, C. S., Chakalova, L., Brown, K. E., Carter, D. *et al.*, Active genes dynamically colocalize to shared sites of ongoing transcription. *Nat. Genet.* 2004, 36, 1065–1071.



## Review

# PALM and STORM: Unlocking Live-Cell Super-Resolution

Ricardo Henriques,<sup>1,2</sup> Caron Griffiths,<sup>3,4</sup> E. Hesper Rego,<sup>5,6</sup> Musa M. Mhlanga<sup>1,3</sup>

<sup>1</sup> *Unidade de Biofísica e Expressão Genética, Instituto de Medicina Molecular, Faculdade de Medicina Universidade de Lisboa, Lisboa, Portugal*

<sup>2</sup> *Institut Pasteur, Groupe Imagerie et Modélisation, Centre National de la Recherche Scientifique, Unité de Recherche Associée 2582, Paris, France*

<sup>3</sup> *Gene Expression and Biophysics Group, Synthetic Biology Emerging Research Area, Council for Scientific and Industrial Research, Pretoria, South Africa*

<sup>4</sup> *Department of Biochemistry, Faculty of Natural and Agricultural Sciences, University of Pretoria, Pretoria, 0002, South Africa*

<sup>5</sup> *Graduate Group in Biophysics, University of California, San Francisco, CA 94158*

<sup>6</sup> *Howard Hughes Medical Institute, Janelia Farm Research Center, Ashburn, VA 20147*

Received 16 November 2010; revised 6 January 2011; accepted 6 January 2011

Published online 19 January 2011 in Wiley Online Library (wileyonlinelibrary.com). DOI 10.1002/bip.21586

### ABSTRACT:

*Live-cell fluorescence light microscopy has emerged as an important tool in the study of cellular biology. The development of fluorescent markers in parallel with super-resolution imaging systems has pushed light microscopy into the realm of molecular visualization at the nanometer scale. Resolutions previously only attained with electron microscopes are now within the grasp of light microscopes. However, until recently, live-cell imaging approaches have eluded super-resolution microscopy, hampering it from reaching its full potential for revealing the dynamic interactions in biology occurring at the single molecule level. Here we examine recent advances in the super-resolution imaging of living cells by reviewing recent breakthroughs in single molecule*

*localization microscopy methods such as PALM and STORM to achieve this important goal. © 2011 Wiley Periodicals, Inc. Biopolymers 95: 322–331, 2011.*

*Keywords:* super-resolution; microscopy; single molecule

*This article was originally published online as an accepted preprint. The “Published Online” date corresponds to the preprint version. You can request a copy of the preprint by emailing the Biopolymers editorial office at biopolymers@wiley.com*

### INTRODUCTION

Modern cell biology depends extensively on fluorescence light microscopy to provide key insights into cellular structure and molecular behavior. Inherent advantages, such as its non-invasive nature and the ability to use highly specific labeling tools, have made fluorescence light microscopy the preferred strategy for imaging fixed and living cells. The maximum optical resolution of this method is typically restricted to 200-nm laterally and 500-nm axially. This limitation constrains its ability to provide high-resolution structural information on molecules that are central to the dogma of biology, namely DNA, RNA, and protein, which exist as single molecules at scales of few nanometers. The physics-based

Correspondence to: Ricardo Henriques; e-mail: rhenriques@fm.ul.pt and Musa M. Mhlanga; e-mail: musa@mhlangelab.org  
Ricardo Henriques and Caron Griffiths contributed equally to this work.  
© 2011 Wiley Periodicals, Inc.

resolution limit of light microscopes imposed by their optical architecture and the wave nature of light was mathematically described in the 19th century by Abbe.<sup>1</sup>

Electron microscopy (EM) has been able to surpass the resolution limit of optical microscopy and for several years was the routine approach to resolve cellular architecture at the ultra-structural or atomic level. However, EM lacks the basic advantages of fluorescence microscopy such as highly specific multi-color labeling, and live-cell imaging, both of which remain altogether impossible with EM.

In response to this dilemma, recent developments in microscopy have aimed to create techniques able to retain the advantages of fluorescence microscopy while approaching the resolving power of EM. Indeed recent advances in single-molecule localization microscopy (SMLM) have shown resolution below the nanometer.<sup>2</sup> Variants such as photo-activated localization microscopy (PALM),<sup>3</sup> fluorescence PALM (FPALM),<sup>4</sup> stochastic optical reconstruction microscopy (STORM),<sup>5</sup> direct STORM (dSTORM),<sup>6</sup> and PALM with independent running acquisition (PALMIRA)<sup>7–9</sup> have emerged at the forefront of the new “super-resolution” methods retaining the labeling advantages of fluorescence imaging. However, these approaches are also hampered by their inability to be robustly used for live-cell imaging.

Ideally to achieve “EM-like” resolution while preserving the inherent advantages of live-cell fluorescence microscopy, the imaging needs to be carried out with minimal perturbation of the sample while acquiring multi-wavelength 2D or 3D data rapidly enough to correctly reconstruct a time-lapse movie of the cell behavior, with nanoscopic resolution.<sup>10</sup> Achieving this remains elusive in live-cell SMLM and is currently a major focus in the field necessitating innovations in imaging, microscopy, and sample preparation (termed “the hardware”) and in computational techniques (termed “the software”) that permit its routine implementation. For the remainder of this review we will discuss a number of novel strategies to address these goals.

### Achieving Single-Molecule Localization

In optical microscopy, any point source of light smaller than the diffraction limit appears with a fixed size and shape represented by an airy disk pattern or otherwise known as the point-spread function (PSF). This spatial broadening effect is dependent on the emission wavelength of the fluorophore and optical characteristics of the imaging apparatus such as the numerical aperture of the objective used. Classically the resolution limit is then calculated by applying Rayleigh’s criterion—where the resolution is equal to the minimum distance between observed points that can still be resolved as

discrete objects. Since individual elements of molecular assemblies such as DNA, RNA, and proteins exist at scales beyond this limit they cannot be easily distinguished or precisely localized as individual molecules. Thus an important element in achieving single molecule localization is the “hardware” challenge.

SMLM represents a suite of approaches able to achieve single molecule detection and localization in fluorescence microscopy. Extremely high nanoscopy resolutions can be achieved either at the sub-nanometer level for few molecules<sup>2</sup> or, more commonly, in the range of tens of nanometers for structural reconstructions involving thousands to millions of fluorescently-labeled objects. Such resolutions are typical of the techniques PALM, FPALM, STORM, dSTORM, and PALMIRA.

Vital to these approaches is the knowledge that the center of the detected emission light from the fluorophores can be localized analytically and computationally with sub-pixel accuracies beyond the classical resolution limit of optical microscopes.<sup>11,12</sup> To make this possible, three important criteria must be satisfied: (a) the number of photons detected for each fluorophore needs to be high enough so as to clearly distinguish individual PSFs from the surrounding background; (b) fluorophore mobility needs to be slow enough, as compared to the image acquisition time, so as to present well-defined PSFs without considerable blur effects from motion; (c) particle PSFs cannot overlap extensively or they will lead to an increase in the complexity of analytical segmentation and localization of neighboring fluorophores.

Meeting these criteria in live-cell imaging has proven to be a difficult challenge. Several factors can negatively influence the ability to satisfy the above criteria. These include motion of cellular and sub-cellular components and light-induced damage caused by laser illumination. The toxicity of aqueous solutions needed to manage the photo-dynamic behavior of fluorophores further hinders live-cell imaging. Finally variable levels of density and detection of the objects due to biological stochasticity complicate the localization of individual molecules. Thus the “hardware” challenges for live-cell SMLM span from the optical setup and architecture of the microscope to the sample preparation and buffer conditions under which image acquisition is achieved.

### Super-Resolving Large Populations of Fluorophores

PALM, FPALM, STORM, and dSTORM present a solution for some of these dilemmas by combining the sequential acquisition of images with the stochastic switching-on and -off of fluorophores. By regulating the number of active fluorophores in each time-instance through a light-induced envi-

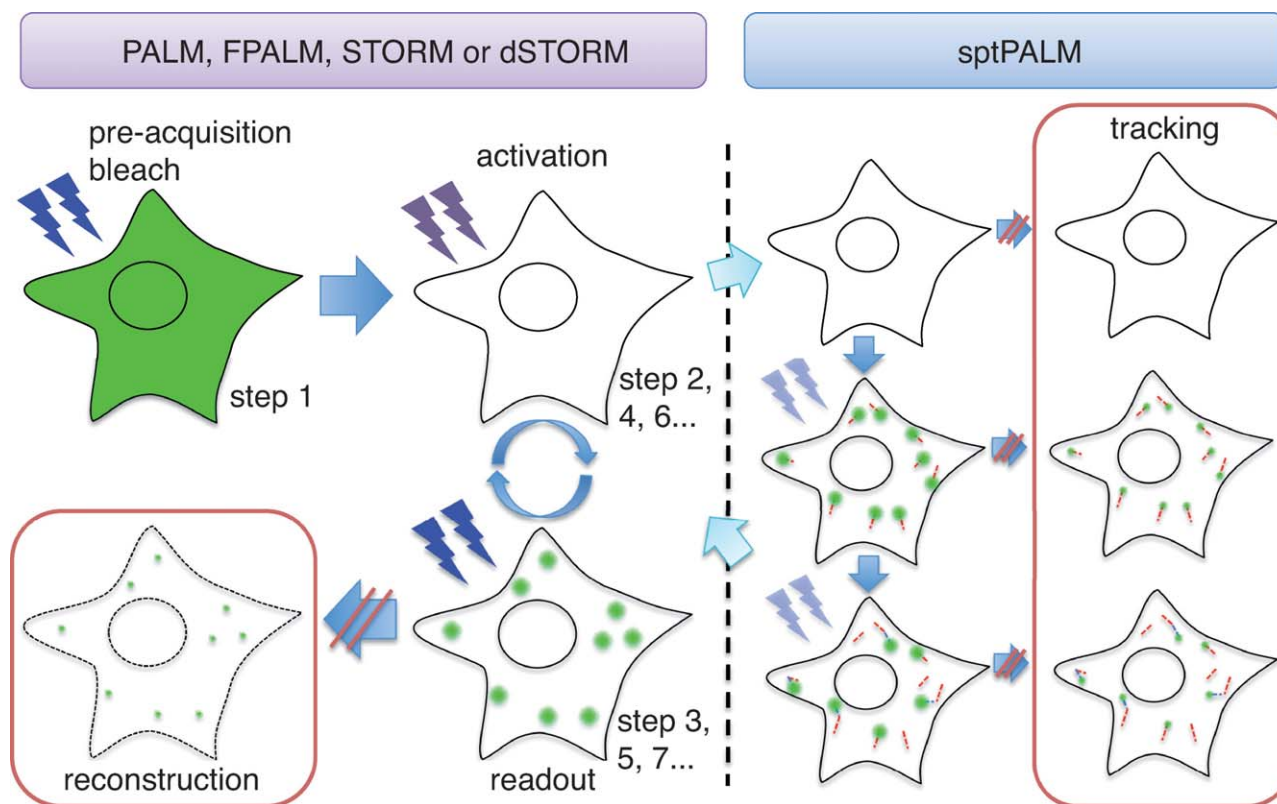


**FIGURE 1** Acquisition steps for PALM, FPALM, STORM, dSTORM, and sptPALM. The typical acquisition in SMLM for PALM, FPALM, STORM, and dSTORM is divided in three independent steps: pre-activation bleach—where cells are illuminated by a strong excitation laser, forcing any unwanted active fluorophore to go into an off-state; activation—the light-induced activation of an extremely reduced number of fluorophores preventing excessive spatial-overlapping of the visualized particles; readout—excitation and imaging of the activated fluorophores followed by bleaching to minimize the presence of already visualized particles in posterior acquired images. These final two-steps can be cycled until a sufficient number of molecules have been identified. In parallel to the readout phase particles can be detected and assembled into a reconstruction. On sptPALM, the readout phase is divided into multiple images where particle movement is captioned and tracked in parallel until bleaching of most active fluorophores has occurred leading to a new imaging cycle started by the activation phase.

ronment it is possible to minimize the probability that in any given image two or more particles spatially overlap, thus satisfying condition (c). A super-resolution dataset can then be reconstructed by plotting the accumulation of the localized particles from a sequence of images. The final resolution of the reconstruction depends only on the localization precision for each fluorophore, which in turn depends upon the particle's observable signal-to-noise ratio. Effectively, several hundred to thousands of images can be collected until enough detected molecules are accumulated to accurately generate a super-resolution dataset where cellular ultra-structure can be highly resolved. The speed of raw-data acquisition is thus dependent on the rate at which sufficient particles can be detected with enough photons to be precisely localized (see Figure 1).

The concept of image and time-point becomes complex when dealing with these methods. Generally a single acquired image does not fully illustrate a time-point as it contains too few detected molecules to resolve a biological structure, such as a cytoskeletal framework, for example. As a solution, multiple images may need to be gathered (typically hundreds) in a sufficiently short time, to represent the state of a structure for the duration of the time-point acquisition while preventing unwanted cell motion artifacts. In these methods, fluorophore mobility has to be slow enough in order to retain the ability to detect and localize moving objects so as not to violate aforementioned condition (b). As a result, published live-cell SMLM experiments to date have only been able to study complexes that are slow in nature. Hess et al. used FPALM to study slow moving membrane proteins

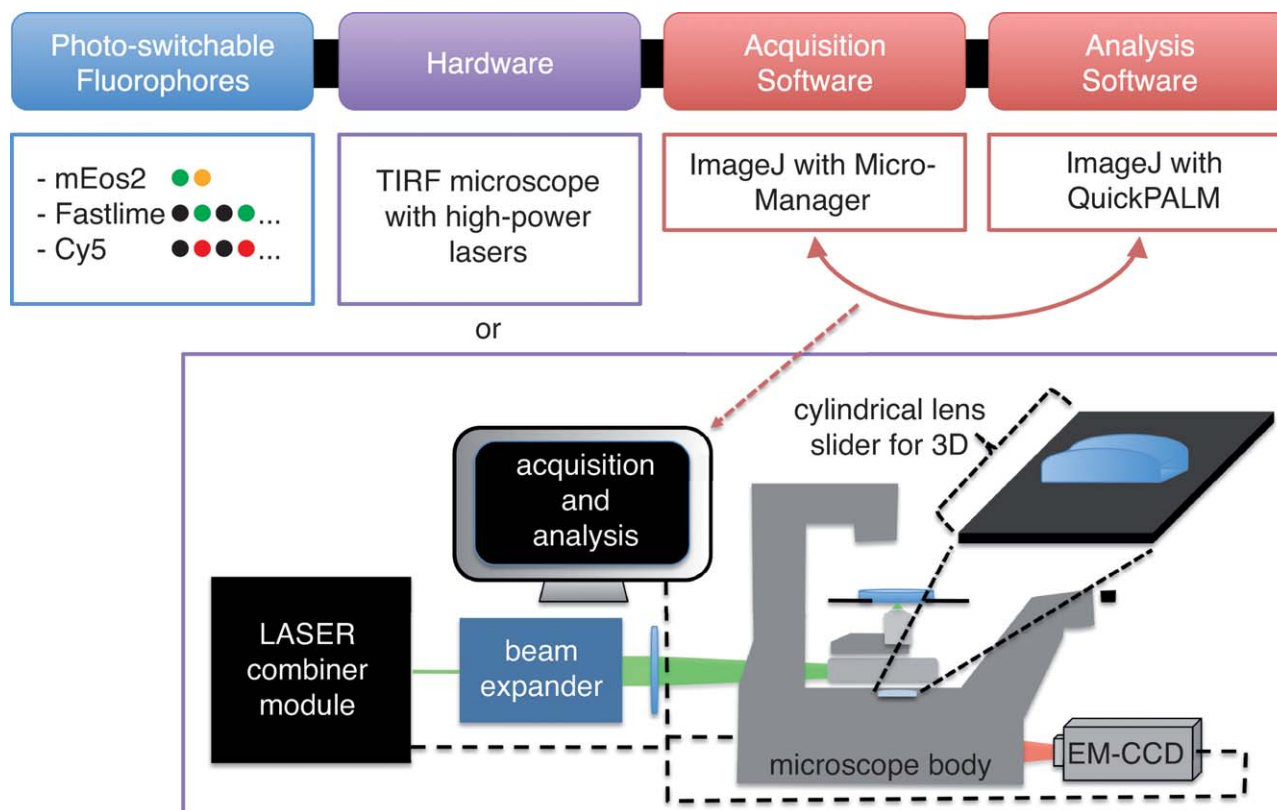


**FIGURE 2** Setting your own SMLM. Aside from the complexities involving fluorophore selection discussed extensively in this review, assembling a SMLM compatible microscope is both cost-effective and straightforward. TIRF microscopes can easily be adapted for SMLM or a custom system can be set up by combining a commercial microscope body with a high-sensitivity camera and a custom laser excitation system. A cylindrical lens inserted into a slider below the objective revolver can provide astigmatism characteristics enabling 3D imaging with the system—an extensive list of tutorials on the subject can be found in <http://code.google.com/p/quickpalm>.  $\mu$ Manager constitutes a free, open-source software for hardware control and acquisition compatible with SMLM experiments and can be used in tandem with QuickPALM—a dedicated ImageJ plugin to process SMLM data.

in fibroblasts at 40-nm resolution,<sup>13</sup> while Shroff et al. used PALM to study adhesion-complex dynamics using 25–60 s per frame, at 60-nm resolution.<sup>14</sup>

### Switching on the Lights

A cornerstone of SMLM is its use and control of the photo-activatable, photo-convertible, or photo-switchable (termed photo-modulatable in this article) properties of certain organic fluorophores/dyes and fluorescent proteins. This feature is so crucial to the functioning of the approach that it has become the principal reason behind the large suite of techniques surrounding SMLM such as PALM, FPALM, STORM, dSTORM, and PALMIRA. These techniques all share the same principle of stochastically switching-on fluorescent molecules to minimize their visual overlap in a

sequence of images thus permitting the precise localization of individual molecules. The imaging hardware and analysis algorithms vary only slightly for each approach and are fairly simple to establish<sup>15</sup> (see Figure 2). Where the methods diverge is in the various classes of fluorophores used and the underlying protocol to either induce or control their photo-modulatable properties.

While PALM and FPALM have chosen genetically encoded fluorophores as their label of choice, STORM on the other hand, exploits the photo-switching properties of fluorescent dyes (such as Cy5 or Alexa647) when in close proximity to a secondary fluorescent dye label (such as Cy3) that functions as a fluorescence re-activator after bleaching. dSTORM<sup>16</sup> has further simplified the sample labeling (making it similar to that of classical immuno-fluorescence) by showing that similar photo-switching properties can be induced in several



fluorescent dyes without the necessity of a secondary reactor fluorescent dye label. This is accomplished by using a compatible high-intensity laser that sufficiently stimulates bleached fluorophores to return to a fluorescent state.

Both PALM, FPALM, STORM, and dSTORM experiments are typically divided into three distinct steps (see Figure 1). PALMIRA demonstrated that both the activation and readout steps can be taken simultaneously while independently acquiring a sequence of images.<sup>8</sup> Given the correct illumination conditions of both the activation and excitation light-sources, it is possible to obtain a time-lapse dataset, in which only a few fluorophores in a fluorescent on-state are captured per raw frame before they are immediately pushed into a non-detectable off-state. This procedure permits the acceleration of the acquisition by merging the two previously distinct activation and readout steps, and removes the need for the pulsing of the activation laser, which is incompatible with most acquisition software available.

Live cell SMLM is thus far almost only compatible with PALM or its sister techniques, which use genetically-encoded fluorophores. STORM and dSTORM use synthetic fluorescent dyes and special buffers able to maintain photo-switching. These buffers are, in general, highly toxic to cells. Later in this review we will examine emerging approaches that seek to overcome these limitations.

### Switching on the Lights: Genetically Encoded Fluorophores

Perhaps the greatest advantage of genetically-encoded fluorescent proteins is the capacity to specifically label molecules in a non-invasive and live-cell compatible manner when compared to other methods such as immuno-fluorescence staining. Furthermore, cell-friendly mediums can be applied as opposed to the photo-switching buffers commonly used in STORM and dSTORM.

Interestingly, it has been known for many years that GFP itself switches between a fluorescent state and a dark state in response to light.<sup>17</sup> However, it was the engineering of proteins to change their spectral properties upon illumination with light of specific wavelengths that allowed for the possibility of SMLM to become a widely used tool in cell biology. There are now numerous examples of these proteins, each with slightly different photo-physical characteristics. Photo-activatable proteins, such as PA-GFP, undergo a single transition from a non-fluorescent to a fluorescent state upon light-induced activation; reversible photo-switchable fluorophores are capable of multiple cycles of activation from a dark to a fluorescent state and return to a dark state, as in the case of Dronpa; photo-shiftable proteins, exemplified by mEos2, can be stimulated to convert between two spectrally distinct fluo-

rescent forms (colors) by activating irradiation. These switching processes are manipulated by careful control of the imaging environment in tandem to the activation and excitation light intensities. This procedure permits for small subsets of fluorophores to be activated and rapidly bleach while captured in a sequence of images.

Most of the published literature on live-cell SMLM has utilized genetically-encoded fluorophores. Yet care needs to be taken when approaching these methods. Most photo-modulatable fluorophores require activation by near-UV light, which is toxic to the majority of cells. The Dendra2 fluorophore is a minor exception, since it can be activated at wavelengths close to a 488 nm wavelength (reviewed in Ref. 18). In most experiments it is also desirable that fluorophores immediately bleach following activation in order to eliminate their presence from multiple acquired images where they would augment the probability of particle spatial-overlap. A strong excitation light is then applied to bleach the fluorophores but the penalty is increased photo-toxicity.

For live-cell imaging in SMLM the “hardware” challenge can be partially overcome by using lower excitation intensities. This can be used to analyze the motility of the activated portion of fluorophores over a small sequence of images until the population is bleached, a process that can be repeated several times. If the fluorophores are confined to a specific cellular structure or location and motility is sufficiently slow so as not to cause blur artifacts (which degrade particle localization), then it becomes possible to reconstruct the domains where the fluorophores have been captured. This process uses each fluorophore multiple times to landmark their enclosing territory and causes less cell damage due to the reduction in the illumination intensity. Similarly, this strategy can also be used to study and map single-molecule motion as demonstrated by the single particle tracking PALM (sptPALM) technique that combines single-particle tracking with PALM microscopy<sup>19</sup> (see Figure 1).

The emergence of proteins with different emission spectra, such as rsCherry, a monomeric red photo-switchable fluorescent protein,<sup>20</sup> has made multi-color time-lapse SMLM imaging possible. Further, the development of new fluorescent proteins coupling photo-activatable and photo-shiftable properties, such as mIrisFP, introduces the possibility of using a pulse-chase approach in conjunction with super-resolution imaging for single particle tracking in dynamic processes, such as monomer turnover in macromolecules.<sup>21</sup>

### Switching on the Lights: Synthetic Fluorophores

The two most important photophysical factors determining the spatial resolution are the brightness of the molecules in the fluorescent state used for localization, and the ratio

between this state and the brightness of the molecules in the inactivated state. The former determines the number of photons that can be detected, which in turn determines the localization precision. The latter factor—the contrast ratio—contribute to the background, which again directly affects the localization precision. It should also be noted that the contrast ratio affects the resolution in a slightly more subtle way: low contrast ratios limit the ability of the system to localize molecules at high molecular densities, which is crucial for achieving high Nyquist-limited resolution.<sup>14</sup> Consequently, it is important to choose fluorescent labels that have both high brightness and high contrast ratios. Many of the most commonly used photo-modulatable fluorescent proteins have high contrast ratios but with a smaller photon output than many small-molecule fluorescent dyes (6000 photons per Cy5 molecule have been detected versus 490 photons per mEos molecule).<sup>18</sup> Therefore, small-molecule dyes may be attractive candidates as probes for live-cell SMLM. Yet, the impossibility of genetically encoding such labels leaves researchers with the difficult task of devising appropriate strategies for specific and sensitive targeting of fluorophores to biological molecules of interest, in a living cell. Cell membrane impermeability to many dyes and dye-conjugates, not least of all conventionally-labeled antibodies, stands as the greatest barrier to labeling intracellular targets under live-cell conditions, where the membrane should stay intact.

Currently available strategies fit into two broad categories—those that target fluorophores to peptide sequences or proteins fused to the target protein, and those that use enzymes to label the target sequence with the fluorescent tag (see Table I). The small labeling systems used by peptide-targeting labeling strategies, such as TetraCys,<sup>22</sup> HexaHis,<sup>24</sup> and PolyAsp,<sup>23</sup> cause minimal protein or cell perturbation. Thus far, however, only the TetraCys system has been successfully used in live-cell or intra-cellular labeling.<sup>24</sup> Protein-directed labeling, such as SNAP/CLIP tags,<sup>26</sup> Halo Tags,<sup>27</sup> and Dihydrofolate reductase (DHFR) targeting with trimethoprim (TMP)-conjugates,<sup>28,39</sup> allows improved targeting specificity, but at the cost of an increase in the size of the recruiting system, increasing the risk of perturbing protein function. Despite this, the tag-dye conjugates in a number of these approaches are sufficiently cell permeable to allow intracellular labeling. Covalent labeling with the DHFR-based system has been successfully used in live-cell STORM imaging of Histone H2B dynamics.<sup>39</sup> Enzyme mediated protein labeling makes use of a small peptide sequence fused to the target protein and an enzyme, natural or engineered, which ligates the fluorescent probe to the recognition sequence. Some of these methods, such as those based on the use of

Table I Targeting Strategies for Synthetic Dyes

Targeting Peptide	Ligand	Enzyme	Bond	Cellular Targets	Comments	Reference
<b>Peptide/protein-based targeting</b>						
TetraCys	Biarsenical fluorophores	—	Covalent	Membrane/intracellular proteins	Live imaging with FAsH tags	22,23
HexaHis	NTA-conjugates	—	Noncovalent	Membrane proteins	N/A	24
PolyAsp	Dpa tyr conjugates	—	Noncovalent	Membrane proteins	N/A	25
SNAP/CLIP tags	Benzylguanine conjugates	AGT	Covalent	Membrane/intracellular proteins	Greater specificity, larger label	26
Halo tags	Chloroalkane conjugates	Dehalogenase	Covalent	Membrane/intracellular proteins	Greater specificity, larger label	27
DHFR	TMP	DHFR	Noncovalent or covalent	Membrane/intracellular proteins	Greater specificity, larger label	25,28
<b>Enzyme-based targeting</b>						
Sortag	Oligo-glycine dye conjugate	Sortase	Covalent	Membrane proteins, C- and N-terminals	N/A	29,30
Q-tag	Amine-modified probes	Transglutaminase	Covalent	Membrane proteins, N-terminal	Low substrate specificity	31,32
ACP/PCP	Co-enzyme A-conjugates	Phosphopantetheine transferases (Sfp and AcpS)	Covalent	Membrane proteins	N/A	33,34
AP	Biotin conjugates	Biotin ligase, BirA	Covalent	Membrane proteins	N/A	35
LAP	cyclo-octyne conjugates/hydroxycoumarin	Lipoic acid ligase	Covalent	Membrane/intracellular proteins	One or two-step process	36–38

DHFR: dihydrofolate reductase; ACP: acyl-carrier protein; PCP: peptidyl-carrier protein; AP: biotin ligase acceptor peptide; NTA: nitrilotriacetic acid; TMP: trimethoprim; AGT: O<sup>6</sup>-alkylguanine-DNA alkyltransferase; N/A: not applicable

sortase,<sup>29,30</sup> phosphopantetheine transferases,<sup>33</sup> and biotin ligase,<sup>35</sup> have been used to ligate fluorophore-conjugates to recognition sequences on target proteins in living cells or at the single molecule level. These approaches combine the benefits of a small directing peptide sequence and those of specific and rapid covalent labeling, and thus provide an ideal system for SMLM. However, the primary disadvantage currently encountered with the above systems is a lack of cell-permeability of the tags themselves, such that only membrane-protein labeling is possible.

In contrast, a Lipoic acid ligase-based system has been developed which makes labeling at both the cell membrane and intracellular targets possible.<sup>36,37</sup> Two engineered forms of the microbial lipoic acid ligase have been developed by the Ting lab. The first is able to ligate cyclo-octyne conjugated probes to a Lipoic Acid Ligase Peptide (LAP) sequence fused to both cell surface and intracellular targets using a two-step process.<sup>36–39</sup> Practical challenges with the two-step process when applied to intracellular labeling led to the development of a second engineered ligase, a highly specific “fluorophoreligase,” capable of specifically ligating hydroxycoumarin to intracellular LAP fusion proteins.<sup>37</sup> This newly engineered enzyme may be most suitable for the direct and specific labeling of intracellular targets, however, the strict restriction to only one dye limits the applicability of the system for SMLM at this stage. Further engineered forms, able to make use of multiple dye-conjugates, would provide a valuable system for multi-color labeling in live-cells in the future.

Besides strategies for the specific labeling of intracellular proteins with a wide variety of fluorescent dyes for live cell imaging, the suitability of specific fluorescent dyes for SMLM, particularly their photoswitching abilities, as well as the necessary conditions for such blinking, are also an important consideration, especially for live-cell imaging. Developments in imaging buffers have allowed photo-switching properties to be attributed to the majority of synthetic fluorescent dyes.

### Switching on the Lights: Blinking-Inducing Buffers

Fluorescence excitation occurs by the absorption of a photon, which promotes a singlet, ground state molecule ( $S_0$ ), to the excited singlet state ( $S_1$ ). The subsequent return to  $S_0$  produces a fluorescence photon emission. Alternatively the competing process of inter-system conversion can occur maintaining the fluorophore in a long-lived triplet state ( $T_1$ ) formation (see Figure 3).

While in  $T_1$  the fluorophore is unable to undergo fluorescence emission until relaxation to  $S_0$  is re-achieved. During

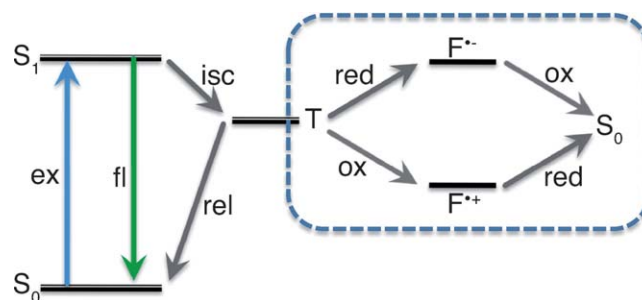


**FIGURE 3** Scheme of the photoswitching process and redox triplet state depletion mechanism. A ground state fluorophore is excited to the  $S_1$  singlet state by the absorption of a photon. The fluorophore may then return to the ground state or transverse into a dark triplet state by intersystem crossing, followed by stochastic relaxation back to ground state. Boxed region: The addition of reducing and oxidizing agents depletes the triplet state by electron transfer reactions, producing either form of fluorophore radical and retrieving the reactive intermediates by the reciprocal reduction or oxidation. This returns the fluorophore to ground state, avoiding photobleaching and allowing cycling or switching of the fluorophore between excited, triplet, and ground states.  $S_0$ : ground state;  $S_1$ : excited singlet state;  $T$ : triplet state; ex: excitation; fl: fluorescence; isc: inter-system crossing; rel: relaxation; red: reduction; ox: oxidation; F: fluorophore.

this period the fluorophore is sensitive to an irreversible photobleaching event if it reacts with molecular oxygen. This in turn results in the production of reactive oxygen species (ROS)—one of the major sources of photo-toxicity in cells. Notwithstanding, light-induced damage is not only created by this process but the overall absorption of light by the cell can produce toxicity.<sup>38,40</sup>

If reactions with oxygen can be avoided, then fluorophore photobleaching can be reversed. This process can be used to induce switching behavior in fluorophores<sup>16,41</sup> as the  $T_1$  transition is stochastic and can be employed as the transient off-state of a fluorophore. Under these conditions, fluorophore blinking compatible with single molecule localization of a large population of fluorophores can be attained by imaging the cycling of short fluorophore photon bursts caused by  $S_0$ – $S_1$  transitions (the on-state) followed by the temporary arrest of fluorescence in the  $S_1$ – $T_1$  shift (the off-state). Initially, a very limited selection of dyes known to be able to undergo such photoswitching processes was available. Cyanine dyes<sup>42,43</sup> have been most commonly used for SMLM as they can be induced to switch by the presence of a second, activating fluorophore. Such a photoswitching mechanism requires oxygen removal and the use of millimolar concentrations of a reducing agent, such as  $\beta$ -mercaptoethanol, in the imaging medium.<sup>42,44</sup>

The demonstration of light-induced reversible photo-switching of single standard fluorophores for use in SMLM,

**Table II** Redox Buffer Agents to Modulate Photo-Switching

Redox Buffer	Action	Endogenous	Toxicity	Reference
Trolox	Reductant	No	Low	46
$\beta$ -mercaptoethanol	Reductant	No	High	44,46,47
Propyl galate	Reductant	No	Low	46
Ascorbic acid	Reductant	Yes	Low	46,48
Glutathione	Reductant	Yes	Low	44,46,48
Dithiotriitol	Reductant	No	High	47
Tris(2-carboxyethyl)phosphine hydrochloride	Reductant	No	High	47
Methylviologen	Oxidant	No	High	16,45,48
Ambient oxygen	Oxidant	Yes	Low	16,48

termed dSTORM,<sup>6</sup> initiated significant advances in establishing SMLM imaging systems in which a much larger range of standard fluorophores can now be used. Central to these developments is an understanding of this “blinking” mechanism in fluorescent molecules, and concomitantly, the formulation of a system which modulates the switching rates (see Figure 3).

Photobleaching can be limited by the depletion of oxygen in the sample, either by embedding with poly-(vinyl-alcohol) (PVA) or using enzymatic oxygen scavenging buffers. This removes singlet oxygen and thus lengthens the  $T_1$  lifetime, while addition of a reducing agent is often used to recover ionized fluorophores. The versatility of these approaches remains limited by their dependence on the specific fluorophore's inherent single-state return rate for establishment of an appropriate rate of blinking, while oxygen depletion and toxic reducing agents make this setup incompatible with most live-cell experiments.

By approaching the photobleaching and triplet state recovery processes as a redox system, the Sauer and Tinnefeld groups have determined a simple, live-cell adaptable imaging setup to allow the fine-tuning of the rate of singlet-state return relative to triplet state formation. In this system, the reactive triplet state is rapidly depleted, either by oxidation to a radical cation, or by reduction to a radical anion. These ions can be recovered by the addition of a reducing or oxidizing agent, respectively, returning the fluorophore to the singlet state. Thus a buffering system with both reducing and oxidizing agents (termed ROXS) recovers reactive triplet state intermediates, repopulating the ground state and avoiding photobleaching.<sup>45</sup> By adjusting the relative ROXS buffer concentrations as required, the rate of photoswitching can be directly controlled to ensure sufficient fluorophores are in a dark state at each time point and that fluorescent lifetimes are sufficient to yield photons for accurate localization.<sup>16,45</sup>

The toxicity of ROXS reagents has had to be addressed in order to adapt the system for live-cell imaging (see Table II). Typically, thiol-reagents such as  $\beta$ -mercaptoethanol or  $\beta$ -

mercaptoethylamine have been used as reducing agents in SMLM buffers.<sup>16,41,44</sup> Recently, glutathione and ascorbic acid have proven to be appropriate live-cell compatible alternatives to these reducing agents.<sup>16,44,45</sup> Despite its toxicity methylviologen remains the primary oxidizing agent used.<sup>45,48</sup> By taking advantage of the oxidizing potential of oxygen itself, and using the molecular oxygen present in the cellular environment to fulfill the role of the oxidant in ROXS<sup>16,48</sup> the challenge of oxidant toxicity, as well as the need for oxygen-depletion in SMLM, has been neatly side-stepped. Although the presence of oxygen slightly restricts the experimenter's capacity to modulate the dyes' photophysics, this nevertheless greatly simplifies the application of ROXS for use in live-cell SMLM.

Essentially any desired fluorophore labeled with suitable photo-physical properties can be used in a biologically compatible ROXS imaging buffer, without the need for oxygen depletion. The ATTO dyes, such as ATTO520, ATTO565, ATTO655, ATTO680, and ATTO700, have proven particularly well suited for use in “blink microscopy” with ROXS.<sup>16,48</sup> Investigations are extending into the suitability of more water-soluble dyes, such as perylene dicarboximide fluorophores,<sup>49</sup> specifically for use in live-cell imaging.

ROXS provides a dye and buffer system that gives us prime choice of multi-color dyes to use in live-cell SMLM with minimal perturbation to the cell.

### Breaking Through the Technological Limits

SMLM of a large population of fluorophores typically demands that hundreds to thousands of diffraction-limited images be acquired and processed in order to reconstruct a super-resolution dataset, the central “software” challenge. What is the relationship between localization precision and resolution? It is clear that the resolution of an SMLM image cannot be higher than the precision to which the molecules are localized. However, the Nyquist theorem, as applied here, requires that a structural-dynamics be sampled at twice the finest spatio-temporal resolution one wants to detect. This is



especially relevant in live-cell SMLM. In this case, a series of raw data frames are taken and subsequently parsed into SMLM time-points. For instance, if 1000 raw data frames are taken, one might parse these into 10 time-points of 100 raw data-frames or 100 time-points of 10 raw data frames. While the precision at which the molecules are localized does not change in either of these examples, the sparseness of detected particles will be far greater in the latter case than in the former case, and the underlying sample structure may be unrecognizable. Consequently, there is a fundamental trade-off between spatial and temporal resolution.

Additionally in order to obtain a reliable super-resolution reconstruction, algorithms have to analytically detect and localize each individual sub-diffraction particle present in each acquired frame. This is generally a major setback because visualization of the sample in parallel to the acquisition is crucial for making decisions on how to best adjust imaging conditions. Raw unprocessed images can be partially used to observe the sample but these are corrupted by the technique itself—each raw-image is generally composed of few emitting molecules not permitting a complete understanding of underlying cellular structures.

Recently several algorithms have been published allowing for processing speeds concurrent with the acquisition itself.<sup>15,50–53</sup> QuickPALM,<sup>15</sup> an ImageJ-based algorithm, in conjunction with  $\mu$ Manager,<sup>54</sup> an open-source software for hardware control is able to both acquire and process 3D and 4D SMLM providing the super-resolution reconstruction in real-time as images are streamed from the camera (see Figure 2). This feature allows for data-driven algorithmic decisions on how to optimally adapt the acquisition and provides the user a reconstructed view of the sample being acquired.

A dominant challenge in SMLM is minimizing light-induced cell damage<sup>55,56</sup> as super-resolution techniques tend to dramatically increase the photo-damage caused to the cell by either increasing or prolonging the amount of light needed for imaging when compared to classical fluorescence microscopy. Conventionally in fluorescence imaging the entire field of view is illuminated uniformly, both light-excitation and acquisition time are adjusted so as to obtain a high enough signal-to-noise ratio (SNR) to resolve cellular structures of interest. Yet, fluorophore concentrations within cells vary, leaving researchers with the decision of how to best set the illumination characteristics at the cost of either under-exposing or over-exposing sub-regions of the image.

Controlled light-exposure microscopy (CLEM) introduces the concept of applying a non-uniform illumination to the imaging area in laser scanning systems where on a pixel-by-pixel basis the light-exposure is interrupted if a sufficient SNR has been achieved.<sup>55</sup> As a combination of “hardware” and “software” approaches, this method improves image-quality

and severely reduces photo-toxicity.<sup>55</sup> Problematically, SMLM uses cameras that only permit the parallel acquisition of all the pixels composing an image theoretically preventing the implementation of CLEM. Non-uniform illumination in time has been previously applied to SMLM in the work of Betzig et al.<sup>3</sup> where the sample activation is incrementally increased over time to compensate for fluorophore depletion. This concept can be further adapted by modulating the illumination both in the spatial and temporal domain with the help of a spatial-light-modulator (SLM). In SMLM two light beams are used: a low-intensity activation beam to induce fluorophores into an on-state and a high-intensity readout beam to excite and bleach the fluorophore. By definition, the images acquired in SMLM have a sparse concentration of fluorophores. This means that most of the area subjected to illumination is not occupied by active fluorophores. By concentrating the readout illumination to the areas where only actively emitting fluorophores are present, a drastic reduction in the amount of light used for imaging is achieved therefore minimizing cell damage. A major focus of the QuickPALM<sup>16</sup> development team is to bring this feature forward by combining the power of real-time processing with the capacity for both SLM and acquisition hardware control brought by  $\mu$ Manager.<sup>54</sup>

The authors thank members of the Mhlanga and Zimmer Lab for comments. They especially thank C. von Middendorff, C. Zimmer, and T. Duong for valuable comments and advice.

## REFERENCES

1. Abbe, E. *Arch Mikroskop Anat* 1873, 9, 413–420.
2. Pertsinidis, A.; Zhang, Y.; Chu, S. *Nature* 2010, 466, 647–651.
3. Betzig, E.; Patterson, G. H.; Sougrat, R.; Lindwasser, O. W.; Olenych, S.; Bonifacino, J. S.; Davidson, M. W.; Lippincott-Schwartz, J.; Hess, H. F. *Science* 2006, 313, 1642–1645.
4. Hess, S. T.; Girirajan, T. P.; Mason, M. D. *Biophys J* 2006, 91, 4258–4272.
5. Rust, M.; Bates, M.; Zhuang, X. *Nat Methods* 2006, 3, 793–796.
6. Heilemann, M.; van de Linde, S.; Schuttpelz, M.; Kasper, R.; Seefeldt, B.; Mukherjee, A.; Tinnefeld, P.; Sauer, M. *Angew Chem Int Ed Engl* 2008, 47, 6172–6176.
7. Fölling, J.; Belov, V.; Kunetsky, R.; Medda, R.; Schönle, A.; Egner, A.; Eggeling, C.; Bossi, M.; Hell, S. *Angew Chem Int Ed* 2007, 46, 6266–6270.
8. Egner, A.; Geisler, C.; von Middendorff, C.; Bock, H.; Wenzel, D.; Medda, R.; Andresen, M.; Stiel, A.; Jakobs, S.; Eggeling, C. *Biophys J* 2007, 93, 3285.
9. Bock, H.; Geisler, C.; Wurm, C.; von Middendorff, C.; Jakobs, S.; Schönle, A.; Egner, A.; Hell, S.; Eggeling, C. *Appl Phys B Lasers Opt* 2007, 88, 161–165.
10. Carlton, P. M.; Boulanger, J.; Kervrann, C.; Sibarita, J. B.; Salamer, J.; Gordon-Messer, S.; Bressan, D.; Haber, J. E.; Haase, S.; Shao, L.; Winoto, L.; Matsuda, A.; Kner, P.; Uzawa, S.; Gustafsson, M.; Kam, Z.; Agard, D. A.; Sedat, J. W. *Proc Natl Acad Sci USA* 2010, 107, 16016–16022.

11. Burns, D. H.; Callis, J. B.; Christian, G. D.; Davidson, E. R. *Appl Opt* 1985, 24, 154–161.
12. Bobroff, N. *Rev Sci Instrum* 1986, 57, 1152–1157.
13. Hess, S.; Gould, T.; Gudheti, M.; Maas, S.; Mills, K.; Zimmerberg, J. *Proc Natl Acad Sci USA* 2006, 104, 17370–17375.
14. Shroff, H.; Galbraith, C. G.; Galbraith, J. A.; Betzig, E. *Nat Methods* 2008, 5, 417–423.
15. Henriques, R.; Lelek, M.; Fornasiero, E. F.; Valtorta, F.; Zimmer, C.; Mhlanga, M. M. *Nat Methods* 2010, 7, 339–340.
16. van de Linde, S.; Endesfelder, U.; Mukherjee, A.; Schuttpelz, M.; Wiebusch, G.; Wolter, S.; Heilemann, M.; Sauer, M. *Photochem Photobiol Sci* 2009, 8, 465–469.
17. Dickson, R.; Cubitt, A.; Tsien, R. Moerner, W. *Nature* 1997, 388, 355–358.
18. Henriques, R.; Mhlanga, M. M. *Biotechnol J* 2009, 4, 846–857.
19. Manley, S.; Gillette, J. M.; Patterson, G. H.; Shroff, H.; Hess, H. F.; Betzig, E.; Lippincott-Schwartz, J. *Nat Methods* 2008, 5, 155–157.
20. Subach, F. V.; Patterson, G. H.; Manley, S.; Gillette, J. M.; Lippincott-Schwartz, J.; Verkhusha, V. V. *Nat Methods* 2009, 6, 153–159.
21. Fuchs, J.; Bohme, S.; Oswald, F.; Hedde, P. N.; Krause, M.; Wiedenmann, J.; Nienhaus, G. U. *Nat Methods* 2010, 7, 627–630.
22. Adams, S. R.; Campbell, R. E.; Gross, L. A.; Martin, B. R.; Walkup, G. K.; Yao, Y.; Llopis, J.; Tsien, R. Y. *J Am Chem Soc* 2002, 124, 6063–6076.
23. Martin, B. R.; Giepmans, B. N.; Adams, S. R.; Tsien, R. Y. *Nat Biotechnol* 2005, 23, 1308–1314.
24. Guignet, E. G.; Segura, J. M.; Hovius, R.; Vogel, H. *ChemPhys Chem* 2007, 8, 1221–1227.
25. Ojida, A.; Honda, K.; Shinmi, D.; Kiyonaka, S.; Mori, Y.; Hamachi, I. *J Am Chem Soc* 2006, 128, 10452–10459.
26. Gautier, A.; Juillerat, A.; Heinis, C.; Corrêa I. R., Jr.; Kindermann, M.; Beaufils, F.; Johnsson, K. *Chem Biol* 2008, 15, 128–136.
27. Los, G. V.; Encell, L. P.; McDougall, M. G.; Hartzell, D. D.; Karassina, N.; Zimprich, C.; Wood, M. G.; Learish, R.; Ohana, R. F.; Urh, M.; Simpson, D.; Mendez, J.; Zimmerman, K.; Otto, P.; Vidugiris, G.; Zhu, J.; Darzins, A.; Klaubert, D. H.; Bulleit, R. F.; Wood, K. V. *ACS Chem Biol* 2008, 3, 373–382.
28. Miller, L. W.; Cai, Y.; Sheetz, M. P.; Cornish, V. W. *Nat Methods* 2005, 2, 255–257.
29. Popp, M. W.; Antos, J. M.; Grotenbreg, G. M.; Spooner, E.; Ploegh, H. L. *Nat Chem Biol* 2007, 3, 707–708.
30. Yamamoto, T.; Nagamune, T. *Chem Commun (Camb)* 2009, 1022–1024.
31. Lin, C. W.; Ting, A. Y. *J Am Chem Soc* 2006, 128, 4542–4543.
32. Sunbul, M.; Yin, J. *Org Biomol Chem* 2009, 7, 3361.
33. Zhou, Z.; Cironi, P.; Lin, A. J.; Xu, Y.; Hrvatin, S.; Golan, D. E.; Silver, P. A.; Walsh, C. T.; Yin, J. *ACS Chem Biol* 2007, 2, 337–346.
34. Jacquier, V.; Prummer, M.; Segura, J. M.; Pick, H.; Vogel, H. *Proc Natl Acad Sci USA* 2006, 103, 14325–14330.
35. Howarth, M.; Chinnapen, D. J.; Gerrow, K.; Dorrestein, P. C.; Grandy, M. R.; Kelleher, N. L.; El-Husseini, A.; Ting, A. Y. *Nat Methods* 2006, 3, 267–273.
36. Fernandez-Suarez, M.; Baruah, H.; Martinez-Hernandez, L.; Xie, K. T.; Baskin, J. M.; Bertozzi, C. R.; Ting, A. Y. *Nat Biotechnol* 2007, 25, 1483–1487.
37. Uttamapinant, C.; White, K. A.; Baruah, H.; Thompson, S.; Fernandez-Suarez, M.; Puthenveetil, S.; Ting, A. Y. *Proc Natl Acad Sci USA* 2010, 107, 10914–10919.
38. Baruah, H.; Puthenveetil, S.; Choi, Y. A.; Shah, S.; Ting, A. Y. *Angew Chem Int Ed Engl* 2008, 47, 7018–7021.
39. Wombacher, R.; Heidebreder, M.; van de Linde, S.; Sheetz, M. P.; Heilemann, M.; Cornish, V. W.; Sauer, M. *Nat Methods* 2010, 7, 717–719.
40. Stephens, D. J.; Allan, V. J. *Science* 2003, 300, 82–86.
41. Fölling, J.; Bossi, M.; Bock, H.; Medda, R.; Wurm, C. A.; Hein, B.; Jakobs, S.; Eggeling, C.; Hell, S. W. *Nat Methods* 2008, 5, 943–945.
42. Bates, M.; Huang, B.; Dempsey, G. T.; Zhuang, X. *Science* 2007, 317, 1749–1753.
43. Bates, M.; Blosser, T. R.; Zhuang, X. *Phys Rev Lett* 2005, 94, 108101.
44. van de Linde, S.; Kasper, R.; Heilemann, M.; Sauer, M. *Appl Phys B Lasers Opt* 2008, 93, 725–731.
45. Vogelsang, J.; Kasper, R.; Steinhauer, C.; Person, B.; Heilemann, M.; Sauer, M.; Tinnefeld, P. *Angew Chem Int Ed* 2008, 47, 5465–5469.
46. Rasnik, I.; McKinney, S. A.; Ha, T. *Nat Methods* 2006, 3, 891–893.
47. Aitken, C. E.; Marshall, R. A.; Puglisi, J. D. *Biophys J* 2008, 94, 1826–1835.
48. Vogelsang, J.; Cordes, T.; Forthmann, C.; Steinhauer, C.; Tinnefeld, P. *Proc Natl Acad Sci USA* 2009, 106, 8107–8112.
49. Cordes, T.; Vogelsang, J.; Anaya, M.; Spagnuolo, C.; Gietl, A.; Summerer, W.; Herrmann, A.; Mullen, K.; Tinnefeld, P. *J Am Chem Soc* 2010, 132, 2404–2409.
50. Wolter, S.; Schuttpelz, M.; Tscherepanow, M.; van de Linde, S.; Heilemann, M.; Sauer, M. *J Microsc* 2010, 237, 12–22.
51. Hedde, P. N.; Fuchs, J.; Oswald, F.; Wiedenmann, J.; Nienhaus, G. U. *Nat Methods* 2009, 6, 689–690.
52. Smith, C. S.; Joseph, N.; Rieger, B.; Lidke, K. A. *Nat Methods* 2010, 7, 373–375.
53. Quan, T.; Li, P.; Long, F.; Zeng, S.; Luo, Q.; Hedde, P. N.; Nienhaus, G. U.; Huang, Z. L. *Opt Express* 2010, 18, 11867–11876.
54. Stuurman, N.; Amodaj, N.; Vale, R. D. *Microsc Today* 2007, 15, 42–43.
55. Hoebe, R. A.; Van Oven, C. H.; Gadella, T. W., Jr.; Dhonukshe, P. B.; Van Noorden, C. J.; Manders, E. M. *Nat Biotechnol* 2007, 25, 249–253.
56. Hoebe, R. A.; Van der Voort, H. T.; Stap, J.; Van Noorden, C. J.; Manders, E. M. *J Microsc* 2008, 231, 9–20.

*Reviewing Editor: Julie Biteen*

We hope that the code and suggestions provided here will inspire other researchers to take advantage of the benefits of using MLE for analyzing Poisson-distributed data, reducing biases and errors in parametric results from histogram-based analysis.

*Note: Supplementary information is available on the Nature Methods website.*

#### ACKNOWLEDGMENTS

This work was performed under the auspices of the US Department of Energy by Lawrence Livermore National Laboratory under contract DE-AC52-07NA27344.

#### COMPETING FINANCIAL INTERESTS

The authors declare no competing financial interests.

#### Ted A Laurence & Brett A Chromy

Physical and Life Sciences Directorate, Lawrence Livermore National Laboratory, Livermore, California, USA.  
e-mail: laurence2@llnl.gov

1. Ross, S.M. *Introduction to Probability and Statistics for Engineers and Scientists* (Wiley, New York, New York, 1987).
2. Turton, D.A., Reid, G.D. & Beddard, G.S. *Anal. Chem.* **75**, 4182–4187 (2003).
3. Marquardt, D.W. *J. Soc. Indust. Appl. Math.* **11**, 431–441 (1963).
4. Bunch, D.S., Gay, D.M. & Welsch, R.E. *ACM T. Math. Software* **19**, 109–130 (1993).
5. Gay, D.M. & Welsch, R.E. *J. Am. Stat. Assoc.* **83**, 990–998 (1988).
6. Nishimura, G. & Tamura, M. *Phys. Med. Biol.* **50**, 1327–1342 (2005).

## QuickPALM: 3D real-time photoactivation nanoscopy image processing in ImageJ

**To the Editor:** Although conventional microscopes have a resolution limited by diffraction to about half the wavelength of light, several recent advances have led to microscopy methods that achieve roughly tenfold improvements in resolution. Among

them, photoactivated light microscopy (PALM) and stochastic optical resolution microscopy (STORM) have become particularly popular, as they only require relatively simple and affordable modifications to a standard total internal reflection fluorescence (TIRF) microscope<sup>1–3</sup> and have been extended to three-dimensional (3D) super-resolution and multicolor imaging<sup>4,5</sup>. PALM and STORM achieve super-resolution by sequentially imaging sparse subsets of photoswitchable molecules. Positions of individual molecules are computed from individual low-resolution images with subdiffraction accuracy. These positions are then corrected for drifts and subsequently assembled into one or more super-resolution images. Unfortunately, in most current implementations, this reconstruction may take from several hours to days for a single dataset, thus forbidding visual inspection of super-resolution images in real time. Additionally, PALM and STORM software used to date is generally not freely available, strongly limiting the adoption of this otherwise relatively simple microscopy method. Two recent publications independently demonstrated two-dimensional (2D) algorithms for real-time PALM and STORM reconstructions<sup>6,7</sup>. Here we present QuickPALM (Supplementary Software 1), a freely available and open-source algorithm as a plugin for the widely used ImageJ (<http://rsb.info.nih.gov/ij/>) software that combines real-time processing capability with additional important features including 3D reconstruction, drift correction and real-time acquisition control (<http://code.google.com/p/quickpalm/>).

PALM and STORM reconstruction algorithms usually rely on ‘fitting’ Gaussian kernels to detected diffraction-limited spots. Although they permit high-accuracy localizations, these iterative methods can require up to several hours of processing time. We have developed a high-speed reconstruction algorithm that uses the classical Högbom ‘CLEAN’ method<sup>8</sup> for spot finding, followed by a modified center of mass algorithm to compute the spot position and parameters defining spot shape along the hori-

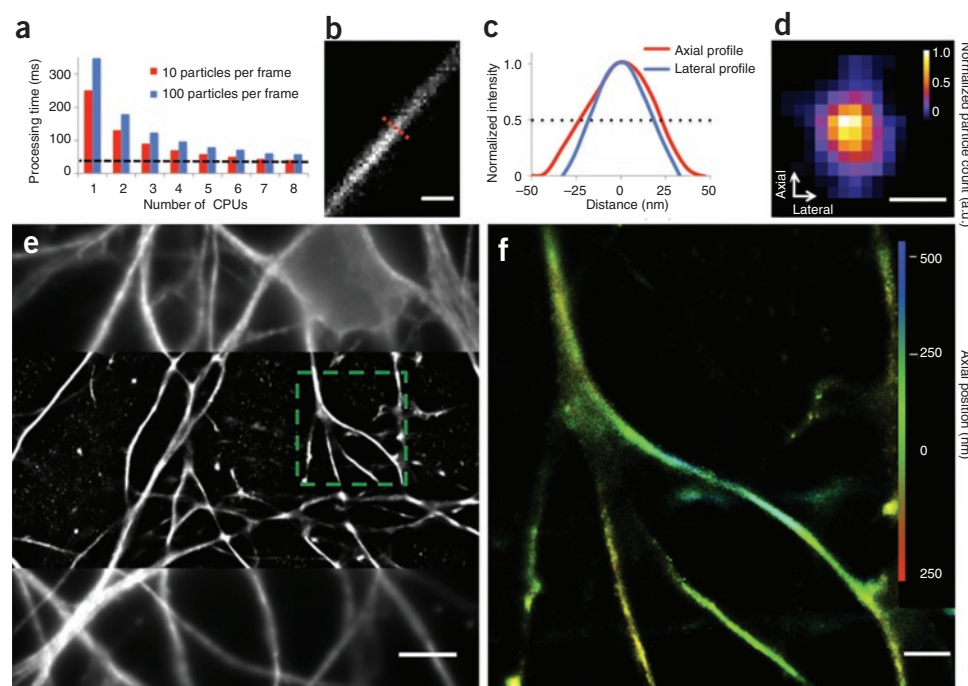


**Figure 1** | Three-dimensional dSTORM imaging of  $\beta$ -III-tubulin-labeled microtubules in neuronal cells. **(a)** Performance of the complete algorithm analyzing a sequence of  $512 \times 512$  pixel images including image reading, peak search, localization and super-resolution image rendering in parallel, benchmarked on an Intel Core 2 Quad 3.2 GHz personal computer. The dashed line represents the 32 ms readout speed of the EMCCD camera (Andor iXion-897). Note that this is the lower-bound frame-rate hard limit imposed by the acquisition hardware itself. **(b)** Super-resolution reconstruction of a microtubule filament. **(c)** Intensity profile of the microtubule cross-section (dotted line in **b**) showing a 40 nm lateral and 50 nm axial full-width half maximum. **(d)** Particle distribution histogram of the marked cross-section in **b**. **(e)** The conventional widefield epifluorescence image, with the middle section showing the super-resolved reconstruction of the central portion of the image. **(f)** A 3D dSTORM image of the boxed area in **e**. Scale bars, 100 nm (**b**), 50 nm (**d**), 5  $\mu$ m (**e**) and 1  $\mu$ m (**f**).



zontal axes. These parameters allow not only precise 2D localization but also extraction of the axial ( $z$ ) coordinate for each spot when using an astigmatic lens<sup>5</sup> (Supplementary Fig. 1 and Supplementary Note 1). A direct benefit of this method was our ability to achieve a typical processing time of 30–50 ms per image with a very weak dependence on the number of spots per image (Fig. 1a); these values are of the same order as the common electron-multiplying charge-coupled device (EMCCD) maximum frame rates used in these techniques. Any drift on the microscope caused by vibrations or thermal dilation compromises resolution and can lead to artifacts in the reconstruction, such as the doubling of structures for sudden shifts (Supplementary Fig. 1f,g). To address this, QuickPALM can trace the movement of fiduciary landmarks such as beads imaged in the sample to estimate the drift in two or three dimensions and subtract it from particle positions (Supplementary Fig. 1d,e). As fiduciary landmarks might not be detected throughout the entire image sequence because of blinking or photobleaching, we interpolated missing positions for each landmark (Supplementary Note 1).

By combining QuickPALM with the  $\mu$ Manager<sup>9</sup> open source package for microscope hardware control and acquisition (Supplementary Software 1) in tandem with a custom laser control system (Supplementary Software 2), we provide a full method for parallel acquisition and real-time visualization of PALM and STORM experiments.

To test the potential of QuickPALM, we observed microtubules in mouse neurons labeled with a primary antibody to neuronal  $\beta$ -III-tubulin and a secondary Cy5-conjugated antibody (Fig. 1b–f and Supplementary Movie 1). Using direct STORM (dSTORM) imaging<sup>1,10</sup> we collected 150,000 images, using the 635 nm laser for excitation and pulsing the 488 nm laser at decreasing intervals for Cy5 fluorophore reactivation. We introduced a cylindrical lens at the position of the polarization slider (Supplementary Methods and Supplementary Fig. 2) to permit 3D probe localization<sup>5</sup>. Using QuickPALM, we obtained real-time 3D reconstructions of microtubules with a resolution (as measured by the full-width half maximum of an intensity profile across a microtubule) of 40 nm in  $x$  and  $y$  dimensions and 50 nm in the  $z$  dimension over a 1  $\mu$ m depth (Fig. 1b–f). With appropri-

ate modifications to ensure precise alignment of differing color channels, multicolor PALM or STORM can be achieved by concurrently processing images from multiple color channels.

In summary, QuickPALM in conjunction with the acquisition control features mentioned above (Supplementary Discussion) provides a complete solution for acquisition, reconstruction and visualization of 3D PALM or STORM images, achieving resolutions of  $\sim$ 40 nm in real time. This software package should greatly facilitate the conversion of many laser-excitation widefield or TIRF microscopes into powerful super-resolution microscopes.

*Note: Supplementary information is available on the Nature Methods website.*

#### ACKNOWLEDGMENTS

We thank J. Enninga for assistance with experiments, and T. Duong and R. Fesce for helpful insight in the preparation of the manuscript.

#### COMPETING FINANCIAL INTERESTS

The authors declare no competing financial interests.

**Ricardo Henriques<sup>1,2</sup>, Mickael Lelek<sup>2</sup>, Eugenio F Fornasiero<sup>3,4</sup>, Flavia Valtorta<sup>3,4</sup>, Christophe Zimmer<sup>2</sup> & Musa M Mhlanga<sup>1,5</sup>**

<sup>1</sup>Unidade de Biofísica e Expressão Genética, Instituto de Medicina Molecular, Faculdade de Medicina Universidade de Lisboa, Lisboa, Portugal. <sup>2</sup>Institut Pasteur, Groupe Imagerie et Modélisation, Institut Pasteur, Groupe Imagerie et Modélisation; Centre National de la Recherche Scientifique, Unité de Recherche Associée 2582, Paris, France. <sup>3</sup>Istituto Scientifico San Raffaele, Università Vita-Salute, Milano, Italia. <sup>4</sup>Unità di Neuroscienze Molecolari, Istituto Italiano di Tecnologia, Milano, Italia. <sup>5</sup>Gene Expression and Biophysics Group, Synthetic Biology Emerging Research Area, Council for Scientific and Industrial Research, Pretoria, South Africa.  
e-mail: rhenriques@fm.ul.pt

1. Rust, M.J., Bates, M. & Zhuang, X. *Nat. Methods* **3**, 793–795 (2006).
2. Hess, S.T., Girirajan, T.P. & Mason, M.D. *Biophys. J.* **91**, 4258–4272 (2006).
3. Betzig, E. *et al. Science* **313**, 1642–1645 (2006).
4. Huang, B., Jones, S.A., Brandenburg, B. & Zhuang, X. *Nat. Methods* **5**, 1047–1052 (2008).
5. Huang, B., Wang, W., Bates, M. & Zhuang, X. *Science* **319**, 810–813 (2008).
6. Wolter, S. *et al. J. Microsc.* **237**, 12–22 (2010).
7. Hedde, P.N., Fuchs, J., Oswald, F., Wiedenmann, J. & Nienhaus, G.U. *Nat. Methods* **6**, 689–690 (2009).
8. Högbom, J.A. *Astron. Astrophys.* **15** (Suppl.), 417–426 (1974).
9. Stuurman, N., Amodaj, N. & Vale, R.D. *Microscopy Today* **15**, 42–43 (2007).
10. Heilemann, M. *et al. Angew. Chem. Int. Edn Engl.* **47**, 617–6176 (2008).

## QuickPALM: 3D real-time photoactivation nanoscopy image processing in ImageJ

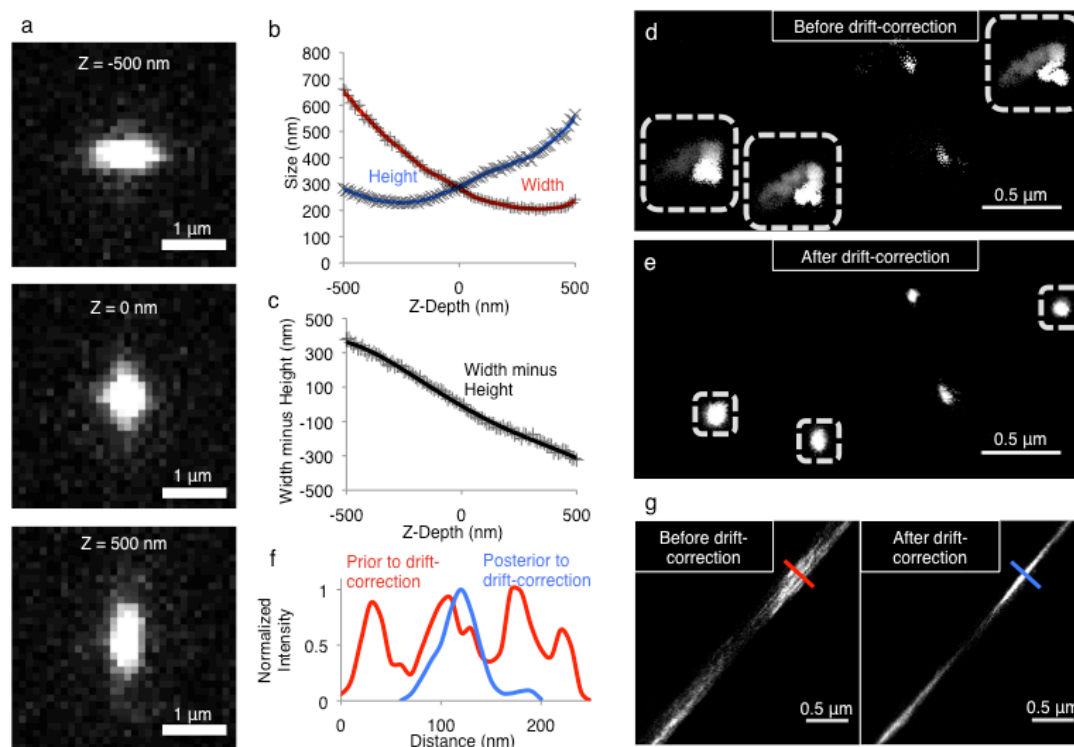
Ricardo Henriques, Mickael Lelek, Eugenio F Fornasiero, Flavia Valtorta, Christophe Zimmer & Musa M Mhlanga

Supplementary figures and text:

<b>Supplementary Figure 1</b>	3D localization and drift correction using QuickPALM.
<b>Supplementary Figure 2</b>	Microscope setup for 3D imaging.
<b>Supplementary Methods</b>	
<b>Supplementary Note 1</b>	Design and operation of QuickPALM
<b>Supplementary Discussion</b>	Overview of QuickPALM performance

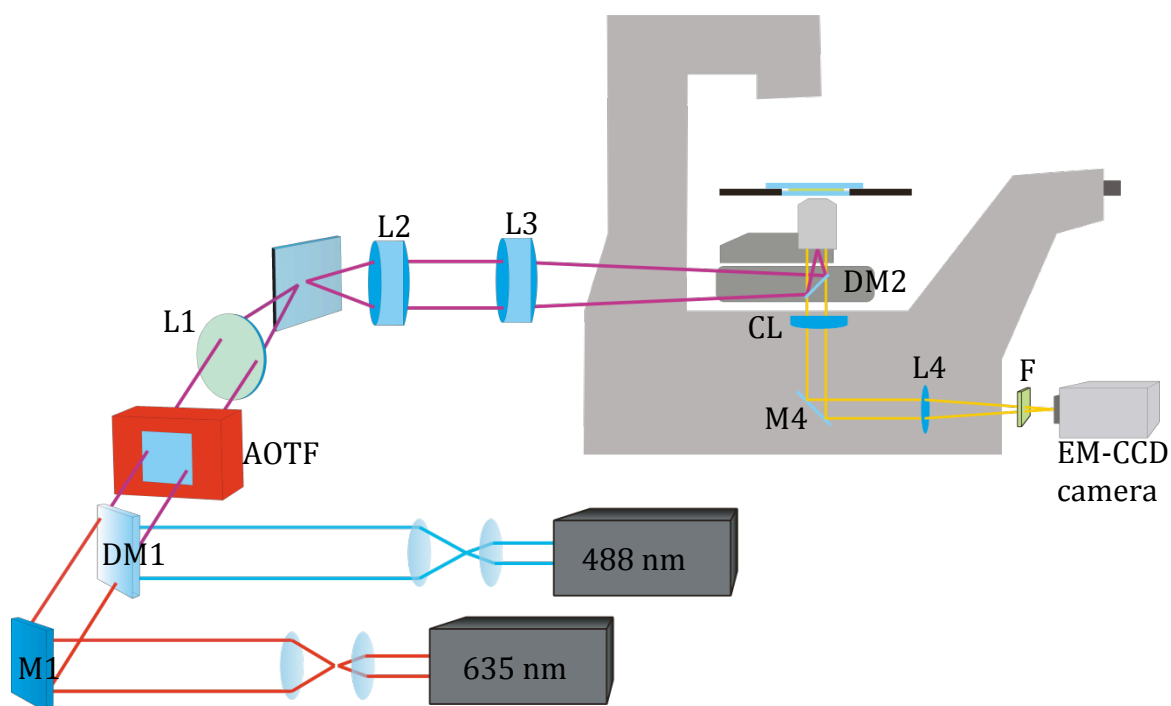
*Note: Supplementary Software 1–2 and Supplementary Video 1 are available on the Nature Methods website.*

## Supplementary Figure 1: 3D localization and drift correction using QuickPALM



**(a)** Image sequence showing a single fiduciary sub-diffraction bead observed at different depths with an astigmatic configuration. Note the changes in the width to height ratio. **(b)** Measured width and height as a function of  $Z$ . Each data point represents the nine-point moving average from three beads. **(c)** Width minus height as a function of  $Z$  based on the values of **(b)**; the black line shows a 4<sup>th</sup> order polynomial fit, which is used to extract the  $Z$  position of newly detected sub-diffraction spots. **(d)** Overlay of computed bead positions acquired during the image sequence showing lateral drift (dot brightness is proportional to the bead intensity, and decays over time due to photobleaching). **(e)** Same as **(d)** after drift-correction. **(f,g)** Drift effect on an image of microtubules creating the misleading appearance of multiple-filaments. **(f)** A line profile of the red and green cross-sections in **(g)** before (green) and after (red) drift-correction.

## Supplementary Figure 2: Microscope setup for 3D imaging



Schematic of the microscope used in this work. Laser light from two lasers is combined using the mirror (M1) and the dichroic beamsplitter (DM1). The two beams are switched using an acousto-optic tunable filter (AOTF) and a series of lenses (L1-L3) directs the beams into the objective. Fluorescent light from the sample crosses the dichroic beamsplitter (DM2) and transverses a cylindrical lens (CL) that introduces an astigmatic aberration into the image allowing us to perform the 3D localization of sub-diffraction particles, the correspondent light is then redirected by a mirror (M4), magnified by a tube-lens (L4) and filtered by an emission filter (F) before reaching the camera.

## Supplementary Methods

### *Slide treatment*

Coverslips were prepared as previously described<sup>1</sup>. Briefly, round 25x0.17-mm coverslips (Fisher Scientific, Pittsburgh, PA) were cleaned in porcelain racks for 18h in concentrated nitric acid, washed several times in tissue-culture-grade water and sterilized with dry heat (225° C for 8h) in a clean oven.

### *Hippocampal neuron cell culturing*

Primary neuronal cultures were prepared from the hippocampi of Sprague-Dawley E18 rat embryos (Charles River Italica, Calco, Italy) as previously described<sup>2</sup>. Briefly, after euthanization of the pregnant mother, E18 rat embryos were isolated, and hippocampi were dissected in cold calcium- and magnesium-free Hank's balanced salt solution (HBSS; Gibco, United Kingdom) supplemented with 5 mM HEPES pH 7.4. Hippocampi were washed several times in HBSS and dissociated in 0.25 % trypsin (Gibco, United Kingdom) for 15 minutes at 37°C. After trypsin removal, neurons were plated in minimum essential medium with Earle's salts (MEM; Gibco, United Kingdom) containing 10% Horse serum during the time necessary for adhesion, and subsequently co-cultured for 3 days with primary astrocytes in N2 supplemented MEM.

### *Cell labeling*

Neurons were fixed for 15 minutes at RT with 4% paraformaldehyde, 4% sucrose in 120 mM sodium phosphate buffer (pH 7.4) supplemented with 2 mM EGTA. After fixation, cells were washed in phosphate buffered saline (PBS) for 0.5h and incubated with anti neuronal tubulin beta-III antibody (Covance, United Kingdom) diluted 1:100 in goat serum buffer (450 mM NaCl, 20 mM phosphate buffer, 15% goat serum, and 0.3% Triton X-100) for 2h at RT. Upon primary antibody incubation cells were washed in PBS for 0.5h and incubated with Cy5 conjugated donkey anti rabbit antibody (Jackson ImmunoResearch, West Grove PA) for 1h at RT. Fluorescent beads (100nm diameter) of a similar emission wavelength, were mounted with the sample as fiduciary landmarks.

### *Slide preparation for imaging and acquisition.*

Slides were sealed in a Parafilm® M gasket. Imaging was performed in a "reactive oxygen scavenger photo-switching buffer" as previously described<sup>3</sup>. The buffer contains 0.5 mg/mL glucose oxidase (Sigma), 40 µg/ml catalase (Roche Applied Science), 10% w/v glucose and 50 mM of β-mercaptoethylamine in PBS (pH 7.4). 150,000 fluorescence images were acquired with a 50 ms exposure time in laser-excitation widefield. The sample was excited with a 635 nm laser with the power adjusted for optimal and fast bleaching of activated Cy5 molecules while a 488 nm laser was pulsed at decreasing intervals to stochastically reactivate bleached Cy5 molecules and maintain an optimal visible number of emitting molecules in the field of view.



## Microscope components and setup

Laser light from the two lasers (EXLSR-635C-60mW and CYAN- 488-100mW, Spectra-Physics, Japan) is combined using the mirror M1 and the dichroic beamsplitter DM1 (LM01-503-25, Semrock, Rochester, NY, USA). The switching between the activation wavelength and the excitation wavelength and intensity control of each laser are performed via an acousto-optic tunable filter (AOTFnC-400.650, A-A Opto-Electronic, Orsay Cedex, France). Before the injection of the laser beams inside the microscope, they are widened by a telescope consisting of the achromatic doublet lenses L1 and L2 and focused into the back focal plane of the objective (CFI Apochromat, 100x, NA 1.49, Nikon, Japan) by the achromatic doublet lens L3. The far red fluorescence emission is collected by the same objective, separated from the illumination light by a quad-band line dichroic mirror DM2 (FF416/500/582/657-DiO1, Lot # 709240-709242 Semrock, Rochester, NY, USA and latter filtered with a dual band pass Filter F (FF01-577/690-25, Lot # 307339-207360 Semrock, Rochester, NY, USA) being finally detected by an EM-CCD camera (Ixon DV887ECS-BV, Andor, Belfast, Northern Ireland) via the mirror M4. An additional lens L4 is used to achieve a final imaging magnification of 100 to 150 times yielding a pixel size from 160 to 106 nm. 3D imaging is performed by adding a cylindrical lens CL (RCX cylindrical lens 10m focal length, CVI Melles Griot) before L4 in order to create an astigmatism, whereby the detected spot shape depends on the fluorophore depth<sup>4</sup> – most microscope bodies have a polarizer insertion slider immediately below the filter cube wheel that can be cleverly adapted as a cavity to insert the cylindrical lens (see **Sup. Fig. 2**).

## Supplementary Note: Design and operation of QuickPALM

### *Particle detection, localization and visualization*

Particle detection and localization takes advantage of all available CPUs on the processing computer through the use of a thread manager (see “Thread Manager” in **Sup. Note Fig. 1**) that distributes the processing jobs between available free CPUs or buffers the acquisition while waiting for these to become free.

Within each thread a new unprocessed image is collected (see “Open next image” in **Sup. Note Fig. 1**) and the noise is characterized by calculating the standard deviation on a small area of 13x13 pixels centered on the minimum intensity pixel of the image. It is assumed that due to the stochastic nature of a PALM or STORM image there is a low probability of having a blinking molecule in the immediate neighborhood of this point. A band-pass filter is then applied to provide noise reduction and background correction on the overall image (see “Filtering” in **Sup. Note Fig. 1**). Initially the image is convolved with a Gaussian kernel of sigma equal to 0.5 pixels and subtracted to a convolution of the original image with a Gaussian kernel of sigma with twice the maximum FWHM given by the user, thus both reducing the noise frequencies and background of the overall image without any visible decrease of the localization accuracy.

The image is then searched for the maximum intensity pixel, the surrounding pixels to this point are selected if within a square window of size twice the maximum *FWHM* whose values are above a relative threshold to the local peak intensity (see “Get brightest spot” in **Sup. Note Fig. 1**). The local SNR is calculated as the division between the mean intensity of the selected pixels and the noise standard deviation. If this value is below the minimum SNR given by the user then the process for this image is halted (see “Compare against SNR” in **Sup. Note Fig. 1**).

Before the spot is registered as a potentially valid particle it needs to pass the following tests: image edge – if a part of the intensity profile of the spot is obscured by the image edge; saturation/clamping – if the intensity of the local spot is not saturated; already analyzed region overlapping – if any of the pixels of the spot overlap with the region of an already previously analyzed spot on the same image. If these tests are correctly passed the algorithm proceeds to calculate the center of the spot coordinates ( $c_x$ ,  $c_y$ ) as given by the center of mass formulas:

$$c_x = \frac{\sum_{i,j} s_{i,j} x_{i,j}}{\sum_{i,j} s_{i,j}}$$
$$c_y = \frac{\sum_{i,j} s_{i,j} y_{i,j}}{\sum_{i,j} s_{i,j}}$$

where  $i$ ,  $j$  are the  $x$ -axis and  $y$ -axis indices for each pixel within the spot,  $x_{i,j}$  and  $y_{i,j}$  are the coordinates of the pixel in nanometers and  $s_{i,j}$  the intensity of the pixel (see “Get center of mass” in **Sup. Note Fig. 1**). The spot shape is then characterized by calculating the parameters:

$$\begin{aligned}\sigma_l &= \sum_{i,j} s_{i,j} (c_x - x_{i,j}) / \sum_{i,j} s_{i,j}, \text{ where } (i,j) \in \{(i,j) \mid x_{i,j} < c_x\} \\ \sigma_r &= \sum_{i,j} s_{i,j} (x_{i,j} - c_x) / \sum_{i,j} s_{i,j}, \text{ where } (i,j) \in \{(i,j) \mid x_{i,j} \geq c_x\} \\ \sigma_a &= \sum_{i,j} s_{i,j} (c_y - y_{i,j}) / \sum_{i,j} s_{i,j}, \text{ where } (i,j) \in \{(i,j) \mid y_{i,j} < c_y\} \\ \sigma_b &= \sum_{i,j} s_{i,j} (y_{i,j} - c_y) / \sum_{i,j} s_{i,j}, \text{ where } (i,j) \in \{(i,j) \mid y_{i,j} \geq c_y\}\end{aligned}$$

if the spot arises from a single diffraction limited particle and if the PSF is symmetric then the particles can approximate to a Gaussian PSF model where in the absence of astigmatism  $\sigma_l \approx \sigma_r \approx \sigma_a \approx \sigma_b$  or otherwise in its presence  $\sigma_l \approx \sigma_r$  and  $\sigma_a \approx \sigma_b$ . We can calculate the particle x-, y-axis symmetry as

$$S_x = 1 - \frac{|\sigma_l - \sigma_r|}{\sigma_l + \sigma_r}; \quad S_y = 1 - \frac{|\sigma_a - \sigma_b|}{\sigma_a + \sigma_b}$$

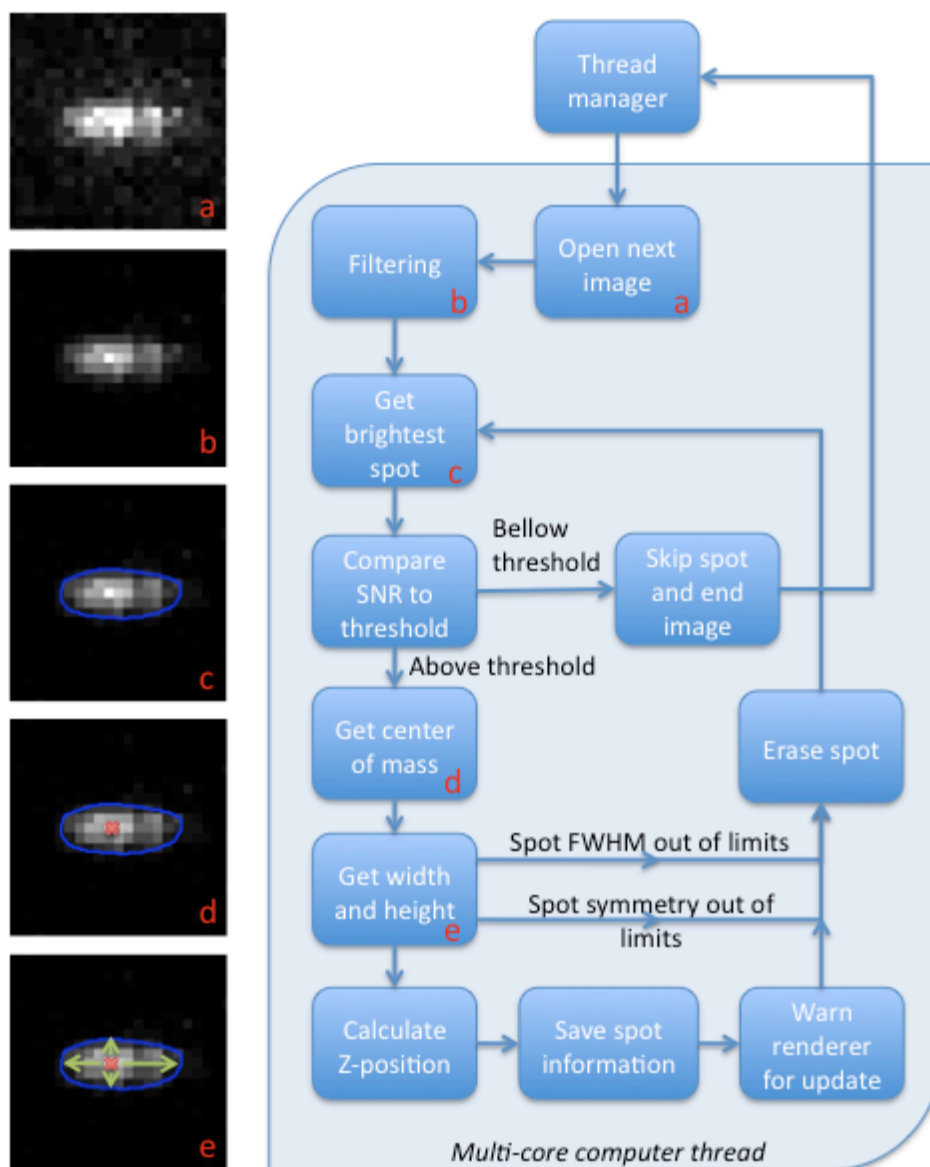
for a single diffraction limited particle, one expects  $S_x \approx 1$  and  $S_y \approx 1$  with or without astigmatism. The lateral *FWHM* along each axis (see “Get width and height” in **Sup. Note Fig. 1**) can be defined as

$$\begin{aligned}FWHM_x &= 2.354(\sigma_l + \sigma_r)/2 \\ FWHM_y &= 2.354(\sigma_a + \sigma_b)/2\end{aligned}$$

in the absence of astigmatism one expects

$$FWHM_x \approx FWHM_y \approx 2.354(\sigma_0/2) \text{ with } \sigma_0 = 0.225(\lambda/NA);^5$$

it then becomes possible to test if the particle obeys a symmetry limit or if the *FWHM* values are within assigned margins given by the user in the graphical interface. The z-position of the particle is extracted by comparing the width minus height (*WmH*) of the particle calculated as  $WmH = FWHM_x - FWHM_y$  against the values on a z-calibration table (**Sup. Note Fig. 2**) through linear interpolation of the closest *WmH* values on the table and associated *Z*-coordinates (see “Calculate Z-position” in **Sup. Note Fig. 1**). Finally if all tests are passed, the information for the spot is saved (“Save spot information” in **Sup. Fig. S1**).

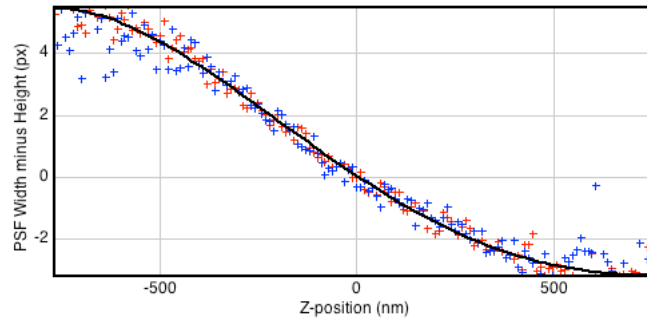


**Supplementary Note Figure 1.** Flow-chart of particles detection, localization and visualization within QuickPALM. Images in left column schematically represent the corresponding steps on the flow-chart labeled with the same inset letter.

### *3D particle localization by comparison with an experimental calibration table*

In order for QuickPALM to localize particles in the z-axis it needs to have prior-information on the astigmatic distortion, this is done by first acquiring a sequence of calibration images with the astigmatic lens<sup>4</sup> featuring sub-diffraction beads. Ideally these images are acquired at regular 10 nm *Z* intervals with the help of a piezo *Z*-motor. It should be possible to observe the width and height change of the *PSF* as a function of *Z*. QuickPALM is able to generate this calibration table, however, the user needs to first manually select which beads to use for calibration with the help of the “ROI Manager”. After this selection QuickPALM calculates the position, width and height of each selected bead through the “Get center of mass” and “Get width and

height” methods discussed before and generates a plot of *Width-Height* vs. *Z* (**Sup. Note Fig. 2**).



**Supplementary Note Figure 2.** Example plot of the width minus height change for bead particles corrupted by astigmatism as a function of the z-position as calculated by QuickPALM. Crosses are measured values for each selected bead, the curve represents a 4<sup>th</sup> order polynomial fit to the data. The fitted values are saved as a calibration table and later used by the “Get Z-position” method previously described to estimate the z-position for each detected particle.

#### *Drift calculation and correction*

Drift correction is accomplished after the user has pre-defined one or more regions of interest around isolated spot clusters corresponding to either landmark beads added to the sample or individual molecules (**Sup. Note Fig. 3a**). The algorithm then calculates the distribution center  $c_{r,w}$  in each axis (**Sup. Note Fig. 3b**) for the selected clusters indexed by  $r$  ( $w$  represents either the x-, y- or z-axis):

$$c_{r,w} = \frac{\sum_t s_{r,t} w_{r,t}}{\sum_t s_{r,t}}$$

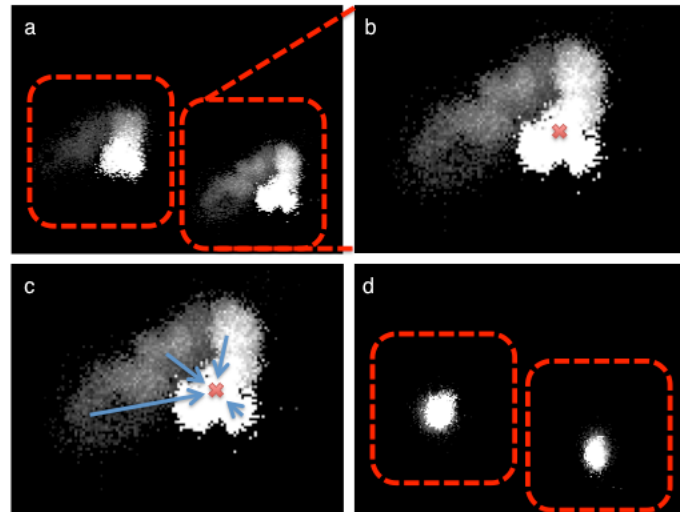
$$d_{w,t} = \frac{\sum_r s_{r,t} (c_{r,w} - w_{r,t})}{\sum_t s_{r,t}}$$

where  $t$  is the time-point index for each detected spot within the cluster,  $s_{r,t}$  the intensity for that spot and  $w_{r,t}$  the localization of spot center. The joint displacement between each element of the cluster and its center is also calculated (**Sup. Note Fig. 3c**) as  $d_{w,t}$ . Due to the possibility of missing detections, the displacement track  $d_{w,t}$  might not contain the displacement information for all time-points. In order to correct this, we linearly interpolate the missing values and iteratively update both the cluster centers and displacements as follows:

$$\hat{c}_{r,w}^{i+1} = \frac{\sum_t s_{r,t} (w_{r,t} + \hat{d}_{w,t}^i)}{\sum_t s_{r,t}}$$

$$\hat{d}_{w,t}^{i+1} = \frac{\sum_r s_{r,t} (\hat{c}_{r,w}^{i+1} - w_{r,t} - \hat{d}_{w,t}^i)}{\sum_r s_{r,t}}$$

where  $\hat{c}_{r,w}^{i+1}$  and  $\hat{d}_{w,t}^{i+1}$  are the corresponding cluster center and joint displacement estimations for the  $i$ -th iteration. The updates are performed until convergence is achieved. The particle position data is then corrected by subtracting the corresponding displacement value to each particle position (**Sup. Note Fig. 3d**).



**Supplementary Note Figure 3.** Drift correction with QuickPALM through the selection of individual spot clusters. **(a)** Identification and selection of individual spot clusters caused by the repetitive detection of beads or fluorophore clusters over time. **(b)** Calculation of the center of mass of the spot cluster. **(c)** Estimation of the displacement of each spot in regards to the cluster center. **(d)** Plot of the spot clusters after drift correction.

## Supplementary Discussion: Overview of the QuickPALM performance

During a typical image acquisition of 512x512 frames in a PALM/STORM experiment, the frame-rate hard-limit imposed by the readout speed of the camera, such as in the case of the EM-CCD technology, is on the order of 32ms. QuickPALM has a typical processing time of 30-50ms that may vary depending on the sample complexity and processing computer characteristics (**Fig. 1a**). Notwithstanding, this standard processing speed allows real-time super-resolution image reconstruction, albeit at a minor loss in localization accuracy compared to Gaussian fitting methods<sup>4</sup>. In practice, our software automatically processes incoming low-resolution images streamed on the hard drive during image acquisition and accumulates the computed positions into a real-time super-resolution reconstruction. Without real-time reconstruction, imaging parameters such as activation/excitation intensities often need to be optimized by trial and error after multiple suboptimal experiments. Our method allows the dynamic inspection of sample behavior and the adjustment of acquisition parameters “on the fly” for optimal imaging.

Real-time reconstruction and the integration of software for parallel processing and acquisition, in conjunction with an open source platform, allows super-resolution imaging modalities to be broadly adopted and extended. Since processing and reconstruction can occur in real-time and on a separate machines, data-driven decisions can be used in real-time to control actuators. For example, spatial light modulators could be used to locally optimize the activation laser power and ensure uniform blinking probabilities, thus minimizing acquisition time, as required for live super-resolution imaging<sup>6,7</sup>. In a further example, initial super-resolution images reconstructed from a limited number of frames may identify the presence of an event of interest and inform the decision to continue PALM/STORM imaging at this location with real-time visualization - or search for another region-of-interest. This would be an important feature to study events such as host-pathogen interactions in high-throughput screening approaches<sup>8</sup>.

## References

1. S. Kaech and G. Banker, *Nat Protoc* **1** (5), 2406 (2006).
2. G. A. Banker and W. M. Cowan, *Brain Res* **126** (3), 397 (1977).
3. M. Heilemann, S. van de Linde, M. Schuttpelz et al., *Angew Chem Int Ed Engl* **47** (33), 6172 (2008).
4. B. Huang, W. Wang, M. Bates et al., *Science* **319** (5864), 810 (2008).
5. B Zhang, J Zerubia, and JC Olivo-Marin, *Applied Optics* **46** (10), 1819 (2007).
6. H. Shroff, C. G. Galbraith, J. A. Galbraith et al., *Nat Methods* **5** (5), 417 (2008).
7. S. Manley, J. M. Gillette, G. H. Patterson et al., *Nat Methods* **5** (2), 155 (2008).
8. R. Henriques and M. M. Mhlanga, *Biotechnol J* **4** (6), 846 (2009).



# Curriculum Vitae

## **Ricardo Henriques**

PhD finalist at Instituto de Medicina Molecular - Institut Pasteur

**Email:** [rhenriques@fm.ul.pt](mailto:rhenriques@fm.ul.pt)

**Nationality:** Portuguese

**Birth Date:** May 20<sup>th</sup>, 1980

## **Education**

### **Faculdade de Medicina da Universidade de Lisboa**

PhD candidate, Biology, Physics, 2008 – 2011 (expected)

Thesis theme: Achieving Real-Time Super-Resolution Fluorescence Microscopy

### **Faculdade de Ciências da Universidade de Lisboa**

Diploma, Physics Engineering, 1998 – 2005

Thesis theme: Imaging Collagen Rich Tissues by Second-Harmonic Generation

## **Scientific and Professional Experience**

### **Manager of the BioImaging Facility at Instituto de Medicina Molecular (Lisbon, Portugal)**

2006 – 2008 (2 years)

Responsible for the Institute BioImage Unit and for the training of post-graduate students in the most recent microscopy techniques. Administrator of the microscopy systems in the Institute, including several last generation confocal microscopes.

### **Microscopy Technician at Instituto Gulbenkian de Ciência (Oeiras, Portugal)**

2005 – 2006 (1 year)

Responsible for teaching post-graduate students in the usage of the Institute's microscope systems. Software developer for cellular imaging and quantification. Manager of the majority of the Institute's microscopes including a two-photon microscope system.

### **Software Engineer at pyLabs.com - Information technologies (Oeiras, Portugal)**

2002 – 2003 (1 year)

Development of web application software including a framework to manage small companies and a webmail system. Development of code in the Python/Zope language and integration with MySQL servers.

## Peer-reviewed Publications

### 2011

J.Y. Tinevez, N. Perry, J. Schindelin, **R. Henriques**, H. Soares, S. Spencer (2011) *TrackMate: from single-molecule to full cell tracking made easy*, Cytometry Part A, in preparation.

H. Soares, **R. Henriques**, O. Alarcon, F. Porrot, O. Schwartz, M. Alarcon, M.I. Thoulouze, A. Alcover (2011) *HIV unveils calcium and synaptotagmin-7 regulated exocytosis of signaling molecules required for immunological synapse signal amplification*, Nature Immunology, submitted.

M. Lelek\*, F.D. Nunzio\*, **R. Henriques**, P. Charneau, N. Arhel, C. Zimmer (2011) *Super-resolution imaging of HIV in infected cells with FLAsH-PALM*, PNAS, submitted.

C.S.S. Gomes-Santos, M.A. Itoe, C. Afonso, **R. Henriques**, R. Gardner, N. Sepúlveda, P.D. Simões, H. Raquel, P. Almeida, L.F. Moita, F. Frischknecht and M.M. Mota (2011) *Highly dynamic host actin reorganization events around developing plasmodium inside hepatocytes*, FASEB Journal, submitted.

C. Griffiths\*, **R. Henriques**\*, M.M. Mhlanga (2011) *PALM and STORM: a super-resolution molecular view into living cells*, Biotechnology International, vol. 23 (1) pp. 8-10.

**R. Henriques**, C. Griffiths, E.H. Rego, M.M. Mhlanga (2011) *PALM and STORM: unlocking live-cell super-resolution*, Biopolymers vol. 95(5):322-331.

### 2010

**R. Henriques**, M. Lelek, E.F. Fornasiero, F. Valtorta, C. Zimmer, M.M. Mhlanga (2010) *QuickPALM: 3D real-time photoactivation nanoscopy image processing in ImageJ*, Nature Methods; 7(5): 339-40.

### 2009

**R. Henriques**, M.M. Mhlanga (2009) *PALM and STORM: what hides beyond the Rayleigh limit?*, Biotechnology journal; 4(6): 846-57.

J. Caetano-Lopes, A.M. Nery, **R. Henriques**, H. Canhão, J. Duarte, P.M. Amaral, M. Vale, R.A. Moura, P.A. Pereira, P. Weinmann, S. Abdulghani, M. Souto-Carneiro, P. Rego, J. Monteiro, S. Sakagushi S, M.V. Queiroz, Y.T. Kontinen, L. Graça, M.F. Vaz, J.E. Fonseca (2009) *Chronic arthritis directly induces quantitative and qualitative bone disturbances leading to compromised biomechanical properties*, Clinical and experimental rheumatology; 27(3): 475-82.

# Curriculum Vitae

L.B. Barreiro, **R. Henriques**, M.M. Mhlanga (2009) *High-throughput SNP genotyping: combining tag SNPs and molecular beacons*, Methods in molecular biology (Clifton, N.J.); 578: 255-76.

J. Rino, J. Braga, **R. Henriques**, M. Carmo-Fonseca (2009) *Frontiers in fluorescence microscopy*, The International journal of developmental biology; 53(8-10): 1569-79.

## Oral communications in Scientific Meetings or Courses

### 2011

11<sup>th</sup> International ELMI meeting on Advanced Light Microscopy  
**From TIRF microscopy to super-resolution with ImageJ.**  
Alexandroupolis, Greece

### 2010

EMBO II Practical Course on 3D Developmental Imaging  
**Super-resolution microscopy: make it blink.**  
Instituto Gulbenkian de Ciência. Oeiras, Portugal

Microscopy – From theory to application  
**Principles of light microscopy.**  
Institut Pasteur, Paris

EMBO IV Practical Course on Light Microscopy in Living Cells  
**Image processing with ImageJ.**  
Instituto Gulbenkian de Ciência. Oeiras, Portugal

### 2008

EMBO Practical Course on 3D Developmental Imaging  
**Image processing with ImageJ.**  
Instituto Gulbenkian de Ciência. Oeiras, Portugal

### 2007

EMBO III Practical Course on Light Microscopy in Living Cells  
**Image processing with ImageJ.**  
Instituto Gulbenkian de Ciência. Oeiras, Portugal

Image visualization, processing and analysis course  
**Introduction to programming with ImageJ.**  
Instituto de Medicina Molecular. Lisboa, Portugal

Image visualization, processing and analysis course  
**Hands on Image Processing.**  
Instituto de Medicina Molecular. Lisboa, Portugal

3D Microscopy and Live Imaging course.

**Fast confocal imaging.**

Instituto de Medicina Molecular. Lisboa, Portugal

Advanced image processing and analysis workshop

**Free 3D reconstruction software.**

Instituto Gulbenkian de Ciência. Oeiras, Portugal

Introduction to Light Microscopy course

**Principles of light interaction with matter.**

Instituto de Medicina Molecular. Lisboa, Portugal

**2006**

6th International ELMI Meeting and Workshop on Advanced Light Microscopy

**Imaging Collagen Rich Tissues by Second Harmonic Generation.**

Ofir, Portugal

## Poster communications

**2011**

Biophysical Society 55th Annual Meeting

**Super-resolution imaging of HIV in infected cells with FIAH-PALM.**

Baltimore, Maryland.

**2010**

Gordon research conferences – Single molecule approaches to biology

**QuickPALM: 3D real-time photoactivation nanoscopy image processing in ImageJ.**

Il Ciocco Hotel & Resort, Italy

**2006**

International Summer School on Molecular Imaging

**Imaging Collagen Rich Tissues by Second Harmonic Generation**

European Molecular Biology Laboratory, Heidelberg, Germany

Malaria: Functional Genomics to Biology to Medicine

**Identification of Host Factors Required for Liver Stage Infection by *Plasmodium* using RNA Interference.**

Keystone Symposia, Taos, USA

## Participation in meetings, workshops and courses

**2004**

ERASMUS - Thin films as seen by local probes.

KFKI Research Institute for Particle and Nuclear Physics, Budapest, Hungary

# Curriculum Vitae

**1994**

Nord Anglia International English Course

Nord Anglia International, York, England

## Specialities

Optical Microscopy, Fluorescence Microscopy, Photo-Activated Localization Microscopy (PALM), Stochastic Optical Reconstruction Microscopy (STORM), Multi-photon Microscopy (MPM, 2PFM), Second-Harmonic Generation (SHG) microscopy, fluorescent molecular-probes development, computer-assisted image processing, artificial vision, adaptive sampling, robotics, instrumentation, spectroscopy and photometry.

## Languages

**Portuguese** (Native or bilingual proficiency)

**English** (Expert proficiency)

**Spanish** (Limited working proficiency)

**French** (Limited working proficiency)

**Italian** (Elementary proficiency)

## Expertize

**Fluorescence Microscopy** (Expert, 7 years experience)

**Confocal Microscopy** (Expert, 7 years experience)

**Super-resolution Microscopy** (Expert, 4 years experience)

**Computer Vision** (Expert, 7 years experience)

**Digital Image Processing** (Expert, 7 years experience)

**Python** (Expert, 14 years experience)

**Borland C++** (Beginner, 2 years experience)

**C++** (Intermediate, 2 years experience)

**Matlab** (Advanced, 5 years experience)

**Java** (Advanced, 5 years experience)

**Linux** (Expert, 14 years experience)

## Volunteering

Volunteer mentor in the Physics Engineering graduate school (1999-2003), helping new students at Faculdade de Ciências Universidade de Lisboa (Lisbon, Portugal).

## 6 References

1. E. Abbe, *Arch Mikroskop Anat* **9**, 413 (1873).
2. A. Pertsinidis, Y. Zhang, S. Chu, *Nature* **466**, 647 (Jul 29).
3. E. Betzig *et al.*, *Science* **313**, 1642 (Sep 15, 2006).
4. S. T. Hess, T. P. Girirajan, M. D. Mason, *Biophys J* **91**, 4258 (Dec 1, 2006).
5. M. Rust, M. Bates, X. Zhuang, *Nature Methods* **3**, 793 (2006).
6. M. Heilemann *et al.*, *Angew Chem Int Ed Engl* **47**, 6172 (2008).
7. J. Fölling *et al.*, *Angew. Chem. Int. Ed* **46**, 6266 (2007).
8. A. Egner *et al.*, *Biophysical Journal* **93**, 3285 (2007).
9. H. Bock *et al.*, *Applied Physics B: Lasers and Optics* **88**, 161 (2007).
10. J. Pawley, *Handbook of Biological Confocal Microscopy*. (Springer, New York, 2006).
11. A. Koster, J. Klumperman, *Nature Reviews Molecular Cell Biology* **4**, (2003).
12. S. Hell, *Science* **316**, 1153 (2007).
13. R. E. Thompson, D. R. Larson, W. W. Webb, *Biophys J* **82**, 2775 (May, 2002).
14. T. Basché, *Single-Molecule Optical Detection, Imaging and Spectroscopy*. (John Wiley & Son Ltd, 1997).
15. L. Novotny, B. Hecht, *Principles of Nano-Optics*. (Cambridge University Press, 2006).
16. C. Cremer, T. Cremer, *Microscopica acta* **81**, 31 (1978).
17. S. Hell, E. Stelzer, *Optics Communications* **93**, 277.
18. S. Hell, J. Wichmann, *Optics Letters* **19**, 780 (1994).
19. Y. Malkki *et al.*, *Eur J Clin Nutr* **49 Suppl 3**, S321 (Oct, 1995).
20. M. Gustafsson, D. Agard, J. Sedat, 1995.
21. A. Egner, S. Hell, *Trends in Cell Biology* **15**, 207 (2005).
22. R. Heintzmann, C. Cremer, *Optical Biopsies and Microscopic Techniques III*, 185 (1999).
23. B. Bailey, D. Farkas, D. Taylor, F. Lanni, *Nature* **366**, 44 (1993).
24. M. GUSTAFSSON, *Journal of Microscopy* **198**, 82 (2000).
25. L. Schermelleh *et al.*, *Science* **320**, 1332 (2008).

26. L. Shao *et al.*, *Biophysical Journal* **94**, 4971 (2008).
27. R. Heintzmann, T. Jovin, C. Cremer, *Journal of the Optical Society of America A* **19**, 1599 (2002).
28. M. Gustafsson, *Proceedings of the National Academy of Sciences* **102**, 13081 (2005).
29. M. Schrader *et al.*, *Bioimaging* **3**, 147 (1995).
30. T. Klar, S. Jakobs, M. Dyba, A. Egner, S. Hell. (National Acad Sciences, 2000), vol. 97, pp. 8206-8210.
31. R. Schmidt *et al.*, *Nature Methods* **5**, 539 (2008).
32. X. Nan, P. Sims, X. Xie, *Chemphyschem: a European journal of chemical physics and physical chemistry* **9**, 707 (2008).
33. D. H. Burns, J. B. Callis, G. D. Christian, E. R. Davidson, *Applied Optics* **24**, 154 (1985).
34. N. Bobroff, *Review of Scientific Instruments* **57**, 1152 (1986).
35. S. Hell, J. Soukka, P. Hanninen, *Bioimaging* **3**, (1995).
36. J. Gelles, B. Schnapp, M. Sheetz, *Nature* **331**, 450 (1988).
37. A. Yildiz *et al.*, *Science* **300**, 2061 (2003).
38. E. Betzig, *Optics Letters* **20**, 237 (Feb 1, 1995).
39. A. Van Oijen, J. Köhler, J. Schmidt, M. Müller, G. Brakenhoff, *Chemical Physics Letters* **292**, 183 (1998).
40. M. P. Gordon, T. Ha, P. R. Selvin, *Proceedings of the National Academy of Sciences of the United States of America* **101**, 6462 (Apr 27, 2004).
41. X. H. Qu, D. Wu, L. Mets, N. F. Scherer, *Proceedings of the National Academy of Sciences of the United States of America* **101**, 11298 (Aug 3, 2004).
42. K. A. Lidke, B. Rieger, T. M. Jovin, R. Heintzmann, *Optics Express* **13**, 7052 (Sep 5, 2005).
43. E. Betzig *et al.* (American Association for the Advancement of Science, 2006), vol. 313, pp. 1642-1645.
44. S. Hess, T. Girirajan, M. Mason, *Biophysical Journal* **91**, 4258 (2006).
45. B. Huang, W. Wang, M. Bates, X. Zhuang, *Science* **319**, 810 (Feb 8, 2008).
46. M. Juetten *et al.*, *Nature Methods* **5**, 527 (2008).
47. G. Patterson, J. Lippincott-Schwartz. (2002), vol. 297, pp. 1873-1877.
48. M. Schneider, S. Barozzi, I. Testa, M. Faretta, A. Diaspro, *Biophysical Journal* **89**, 1346 (2005).

49. S. T. Hess *et al.*, *Proc Natl Acad Sci U S A* **104**, 17370 (Oct 30, 2007).
50. S. Habuchi, H. Tsutsui, A. B. Kochaniak, A. Miyawaki, A. M. van Oijen, *PLoS ONE* **3**, e3944 (2008).
51. H. Shroff *et al.*, *Proc Natl Acad Sci U S A* **104**, 20308 (Dec 18, 2007).
52. M. Andresen *et al.*, *Nat Biotechnol* **26**, 1035 (Sep, 2008).
53. M. Bates, B. Huang, G. T. Dempsey, X. Zhuang, *Science* **317**, 1749 (Sep 21, 2007).
54. M. Fernandez-Suarez, A. Y. Ting, *Nat Rev Mol Cell Biol* **9**, 929 (Dec, 2008).
55. D. Sinnecker, P. Voigt, N. Hellwig, M. Schaefer, *Biochemistry* **44**, 7085 (May 10, 2005).
56. J. Folling *et al.*, *Nat Methods* **5**, 943 (Nov, 2008).
57. J. Reymann *et al.*, *Chromosome Research* **16**, 367 (May, 2008).
58. D. Baddeley, I. D. Jayasinghe, C. Cremer, M. B. Cannell, C. Soeller, *Biophys J* **96**, L22 (Jan, 2009).
59. K. A. Lukyanov, D. M. Chudakov, S. Lukyanov, V. V. Verkhusha, *Nat Rev Mol Cell Biol* **6**, 885 (Nov, 2005).
60. F. V. Subach *et al.*, *Nat Methods* **6**, 153 (Feb, 2009).
61. D. M. Chudakov, S. Lukyanov, K. A. Lukyanov, *Nat Protoc* **2**, 2024 (2007).
62. S. A. McKinney, C. S. Murphy, K. L. Hazelwood, M. W. Davidson, L. L. Looger, *Nat Methods* **6**, 131 (Feb, 2009).
63. H. Shroff, C. G. Galbraith, J. A. Galbraith, E. Betzig, *Nat Methods* **5**, 417 (May, 2008).
64. T. B. McAnaney *et al.*, *Biochemistry* **44**, 5510 (Apr 12, 2005).
65. J. Biteen *et al.*, *Nature Methods*, (2008).
66. R. M. Dickson, A. B. Cubitt, R. Y. Tsien, W. E. Moerner, *Nature* **388**, 355 (Jul 24, 1997).
67. R. Henriques, M. M. Mhlanga, *Biotechnol J* **4**, 846 (Jun, 2009).
68. S. Manley *et al.*, *Nat Methods* **5**, 155 (Feb, 2008).
69. J. Fuchs *et al.*, *Nat Methods* **7**, 627 (Aug).
70. S. R. Adams *et al.*, *J Am Chem Soc* **124**, 6063 (May 29, 2002).
71. E. G. Guignet, J. M. Segura, R. Hovius, H. Vogel, *Chemphyschem* **8**, 1221 (Jun 4, 2007).
72. A. Ojida *et al.*, *J Am Chem Soc* **128**, 10452 (Aug 16, 2006).
73. A. Gautier *et al.*, *Chem Biol* **15**, 128 (Feb, 2008).



74. L. W. Miller, Y. Cai, M. P. Sheetz, V. W. Cornish, *Nat Methods* **2**, 255 (Apr, 2005).
75. D. Stephens, V. Allan, *Science* **300**, 82 (2003).
76. M. Popp, J. Antos, G. Grotenbreg, E. Spooner, H. Ploegh, *Nature Chemical Biology* **3**, 707 (2007).
77. T. Proft, *Biotechnology letters* **32**, 1.
78. Z. Zhou *et al.*, *ACS Chemical Biology* **2**, 337 (2007).
79. M. Howarth *et al.*, *Nature Methods* **3**, 267 (2006).
80. M. Fernandez-Suarez *et al.*, *Nature biotechnology* **25**, 1483 (2007).
81. M. Fernandez-Suarez *et al.*, *Nat Biotechnol* **25**, 1483 (Dec, 2007).
82. H. Baruah, S. Puthenveetil, Y. A. Choi, S. Shah, A. Y. Ting, *Angew Chem Int Ed Engl* **47**, 7018 (2008).
83. D. J. Stephens, V. J. Allan, *Science* **300**, 82 (Apr 4, 2003).
84. C. L. Rieder, A. Khodjakov, *Science* **300**, 91 (Apr 4, 2003).
85. S. van de Linde *et al.*, *Photochem Photobiol Sci* **8**, 465 (Apr, 2009).
86. M. Bates, B. Huang, G. Dempsey, X. Zhuang, *Science* **317**, 1749 (2007).
87. M. Rust, M. Bates, X. Zhuang, *Nature Methods* **3**, 793 (2006).
88. M. Sauer, *Proceedings of the National Academy of Sciences of the United States of America* **102**, 9433 (2005).
89. J. Vogelsang *et al.*, *Angewandte Chemie International Edition* **47**, 5465 (2008).
90. J. Högbom, *Astronomy and Astrophysics Supplement* **15**, 417 (1974).
91. Y. Kalaidzidis, *Eur J Cell Biol* **86**, 569 (Sep, 2007).
92. K. Jaqaman *et al.*, *Nat Methods* **5**, 695 (Aug, 2008).
93. A. Serge, N. Bertaux, H. Rigneault, D. Marguet, *Nat Methods* **5**, 687 (Aug, 2008).
94. M. Nagorni, S. Hell, *Journal of Structural Biology* **123**, 236 (1998).
95. S. Hell, *Nature Biotechnology* **21**, 1347 (2003).
96. P. Lemmer *et al.*, *Applied Physics B: Lasers and Optics* **93**, 1 (2008).
97. M. Tokunaga, N. Imamoto, K. Sakata-Sogawa, *Nature Methods* **5**, 159 (2008).
98. S. Wolter *et al.*, *J Microsc* **237**, 12 (Jan, 2010).
99. P. N. Hedde, J. Fuchs, F. Oswald, J. Wiedenmann, G. U. Nienhaus, *Nat Methods* **6**, 689 (Oct, 2009).
100. R. Henriques *et al.*, *Nat Methods* **7**, 339 (May).

101. C. S. Smith, N. Joseph, B. Rieger, K. A. Lidke, *Nat Methods* **7**, 373 (May, 2010).
102. T. Quan *et al.*, *Opt Express* **18**, 11867 (May 24, 2010).
103. N. Stuurman, Amodaj N., Vale, R.D., *Microscopy Today*. **15**, 42 (2007).
104. B. Huang, S. A. Jones, B. Brandenburg, X. Zhuang, *Nat Methods* **5**, 1047 (Dec, 2008).
105. S. Kaech, G. Banker, *Nat Protoc* **1**, 2406 (2006).
106. G. A. Banker, W. M. Cowan, *Brain Res* **126**, 397 (May 13, 1977).
107. B. Zhang, J. Zerubia, J. Olivo-Marin, *Applied Optics* **46**, 1819 (2007).
108. S. Tyagi, F. R. Kramer, *Nat Biotechnol* **14**, 303 (Mar, 1996).
109. S. Tyagi, D. P. Bratu, F. R. Kramer, *Nat Biotechnol* **16**, 49 (Jan, 1998).
110. E. Condon, *Physical Review* **32**, 858 (1928).
111. J. Rino, J. Braga, R. Henriques, M. Carmo-Fonseca, *Int J Dev Biol* **53**, 1569 (2009).
112. K. Willets, P. Callis, W. Moerner, *J. Phys. Chem. B* **108**, 10465 (2004).
113. P. W. Atkins, Trapp, C.A. & Paula, J.D., *Physikalische Chemie*. (Wiley-VCH, Weinheim).
114. Y. Harada, K. Sakurada, T. Aoki, D. Thomas, T. Yanagida, *Journal of molecular biology* **216**, 49 (1990).
115. T. Förster, *Annalen der Physik* **437**, 55 (1948).
116. R. Haugland, J. Yguerabide, L. Stryer, *Proceedings of the National Academy of Sciences of the United States of America* **63**, 23 (1969).
117. L. Stryer, *Annual Review of Biochemistry* **47**, 819 (1978).
118. S. A. Marras, *Mol Biotechnol* **38**, 247 (Mar, 2008).
119. M. Zuker, *Nucleic acids research* **31**, 3406 (2003).
120. I. Bonnet *et al.*, *Nucleic Acids Res* **36**, 4118 (Jul, 2008).
121. J. A. Steyer, W. Almers, *Nat Rev Mol Cell Biol* **2**, 268 (Apr, 2001).
122. C. Steinhauer, C. Forthmann, J. Vogelsang, P. Tinnefeld, *J Am Chem Soc* **130**, 16840 (Dec 17, 2008).
123. P. Lemmer *et al.*, *J Microsc* **235**, 163 (Aug, 2009).
124. D. Dong *et al.*, *J Biotechnol* **145**, 310 (Feb 1).
125. D. Horejsh *et al.*, *Nucleic Acids Res* **33**, e13 (2005).
126. S. A. Marras, F. R. Kramer, S. Tyagi, *Nucleic Acids Res* **30**, e122 (Nov 1, 2002).

127. C. Choi, L. G. Hudson, P. Savagner, D. F. Kusewitt, *Methods Mol Biol* **326**, 173 (2006).
128. I. Testa *et al.*, *Biophys J* **99**, 2686 (Oct 20, 2010).
129. M. S. Hayden, S. Ghosh, *Genes & development* **18**, 2195 (2004).
130. N. Perkins, T. Gilmore, *Cell Death & Differentiation* **13**, 759 (2006).
131. A. S. Baldwin, Jr., *Annu Rev Immunol* **14**, 649 (1996).
132. M. S. Hayden, S. Ghosh, *Genes Dev* **18**, 2195 (Sep 15, 2004).
133. M. Karin, Y. Ben-Neriah, *Annu Rev Immunol* **18**, 621 (2000).
134. C. Scheidereit, *Oncogene* **25**, 6685 (Oct 30, 2006).
135. M. S. Hayden, S. Ghosh, *Cell* **132**, 344 (Feb 8, 2008).
136. S. Yamaoka *et al.*, *Cell* **93**, 1231 (Jun 26, 1998).
137. E. D. Tang, C. Y. Wang, Y. Xiong, K. L. Guan, *J Biol Chem* **278**, 37297 (Sep 26, 2003).
138. E. Laplantine *et al.*, *EMBO J* **28**, 2885 (Oct 7, 2009).
139. Z. J. Chen, *Nat Cell Biol* **7**, 758 (Aug, 2005).
140. A. Israel, *Trends Immunol* **27**, 395 (Sep, 2006).
141. H. Sebban, S. Yamaoka, G. Courtois, *Trends Cell Biol* **16**, 569 (Nov, 2006).
142. L. Hicke, H. L. Schubert, C. P. Hill, *Nat Rev Mol Cell Biol* **6**, 610 (Aug, 2005).
143. J. H. Hurley, S. Lee, G. Prag, *Biochem J* **399**, 361 (Nov 1, 2006).
144. N. D. Perkins, *Nat Rev Mol Cell Biol* **8**, 49 (Jan, 2007).
145. H. Sebban, S. Yamaoka, G. Courtois, *Trends in Cell Biology* **16**, 569 (2006).
146. F. Cordier *et al.*, *J Biol Chem* **284**, 2902 (Jan 30, 2009).
147. F. Agou *et al.*, *J Biol Chem* **279**, 27861 (Jul 2, 2004).
148. S. Tegethoff, J. Behlke, C. Scheidereit, *Mol Cell Biol* **23**, 2029 (Mar, 2003).
149. C. K. Ea, L. Deng, Z. P. Xia, G. Pineda, Z. J. Chen, *Molecular cell* **22**, 245 (2006).
150. C. J. Wu, D. B. Conze, T. Li, S. M. Srinivasula, J. D. Ashwell, *Nat Cell Biol* **8**, 398 (Apr, 2006).
151. A. Kovalenko *et al.*, *Nature* **424**, 801 (Aug 14, 2003).
152. G. Shtengel *et al.*, *Proc Natl Acad Sci U S A* **106**, 3125 (Mar 3, 2009).
153. A. G. York, A. Ghitani, A. Vaziri, M. W. Davidson, H. Shroff, *Nat Methods* **8**, 327 (Apr, 2011).
154. T. A. Planchon *et al.*, *Nat Methods*, (Mar 4).

155. J. Huiskens, J. Swoger, F. Del Bene, J. Wittbrodt, E. H. Stelzer, *Science* **305**, 1007 (Aug 13, 2004).
156. T. Quan *et al.*, *Opt Express* **18**, 11867 (May 24).
157. R. A. Hoebe *et al.*, *Nat Biotechnol* **25**, 249 (Feb, 2007).
158. R. A. Hoebe, H. T. Van der Voort, J. Stap, C. J. Van Noorden, E. M. Manders, *J Microsc* **231**, 9 (Jul, 2008).
159. A. B. Berger *et al.*, *Nat Methods* **5**, 1031 (Dec, 2008).
160. G. G. Cabal *et al.*, *Nature* **441**, 770 (Jun 8, 2006).
161. A. Raj, P. van den Bogaard, S. A. Rifkin, A. van Oudenaarden, S. Tyagi, *Nat Methods* **5**, 877 (Oct, 2008).
162. A. Raj, A. van Oudenaarden, *Cell* **135**, 216 (Oct 17, 2008).
163. A. Raj, C. S. Peskin, D. Tranchina, D. Y. Vargas, S. Tyagi, *PLoS Biol* **4**, e309 (Oct, 2006).
164. W. J. Blake *et al.*, *Mol Cell* **24**, 853 (Dec 28, 2006).
165. W. J. Blake, K. A. M., C. R. Cantor, J. J. Collins, *Nature* **422**, 633 (Apr 10, 2003).
166. C. S. Osborne *et al.*, *Nat Genet* **36**, 1065 (Oct, 2004).
167. S. Lewenza, M. M. Mhlanga, A. P. Pugsley, *J Bacteriol* **190**, 6119 (Sep, 2008).
168. L. Siksou *et al.*, *J Neurosci* **27**, 6868 (Jun 27, 2007).